Reductive Activation of Nitric Oxide and Nitrosobenzene at a Dinickel(II) Dihydride Complex

and

New Pyrazole-Based Diiron Compounds

Dissertation

zur Erlangung des mathematisch-naturwissenschaftlichen Doktorgrades

„Doctor rerum naturalium"

der Georg-August-Universität Göttingen

im Promotionsprogramm BioMetals

der Georg August University School of Science (GAUSS)

vorgelegt von

Eleonora Ferretti

aus Pisa

Göttingen 2018

Betreuungsausschuss

Prof. Dr. Franc Meyer
Institut für Anorganische Chemie, Georg-August-Universität Göttingen

Prof. Dr. Inke Siewert
Institut für Anorganische Chemie, Georg-August-Universität Göttingen

Prüfungskommitee

Referent: **Prof. Dr. Franc Meyer**
Institut für Anorganische Chemie, Georg-August-Universität Göttingen

Korreferent: **Prof. Dr. Inke Siewert**
Institut für Anorganische Chemie, Georg-August-Universität Göttingen

Prof. Dr. Kai Tittmann
Schwann-Schleiden-Forschungszentrum, Abteilung Molekulare Enzymologie,
Georg-August-Universität Göttingen

Prof. Dr. Lutz Ackermann
Institut für Organische und Biomolekulare Chemie, Georg-August-Universität Göttingen

Dr. Alexander Breder
Institut für Organische und Biomolekulare Chemie, Georg-August-Universität Göttingen

Dr. Matthias Otte
Institut für Anorganische Chemie, Georg-August-Universität Göttingen

Datum der mündlichen Prüfung: 17.09.2018

Part of this thesis have been published after the original submission in the following journal article:

E. Ferretti, S. Dechert, S. Demeshko, M. C. Holthausen, F. Meyer, *Angew. Chem. Int. Ed.* **2019**, *58*, 1705-1709.

Table of contents

1 Introduction

1.1 Nickel-Based Enzyme Systems

Nickel is a chemical element found in group 10 of the periodic table, whose chemistry and biochemical properties are comparable to cobalt. Nowadays, the biochemistry of nickel is gaining attention, as a variety of nickel-dependent enzymes play a role in processes essential for life. Furthermore, these enzymes often reveal complicated multi-metal catalytic sites, which are fascinating to chemists and physicists. The electronic configuration of elemental nickel is (Ar) $3d^8 4s^2$ and the common oxidation states in which it can be found are 0 or +II, although the uncommon +I and +III states are also possible. When in aqueous solution, the oxidation state +II is the most stable, associated mainly with square planar (diamagnetic, $S = 0$) or tetrahedral (paramagnetic, $S = 1$) geometries. Nevertheless, Ni^I and Ni^{III} have been also spectroscopically characterized in biological systems.[1]

Despite the fact that the majority of the known metalloenzymes contain iron, copper and zinc, an extensive number of nickel-containing enzymes are object of studies. Some important examples include superoxide dismutase (SOD), urease, methyl coenzyme M reductase (MCR), acetylcoenzyme A synthase (ACS), carbon monoxide dehydrogenase and NiFe hydrogenase (H_2ase).[2] An overview of their active site cofactors and the related small molecules which they interact with is depicted in Figure 1. Most of these systems provide the right environment for reversible, two-electron redox processes that are able to convert dihydrogen, carbon monoxide or carbon dioxide and other small molecules. A description of the most relevant systems mentioned above will be given in the next sections.
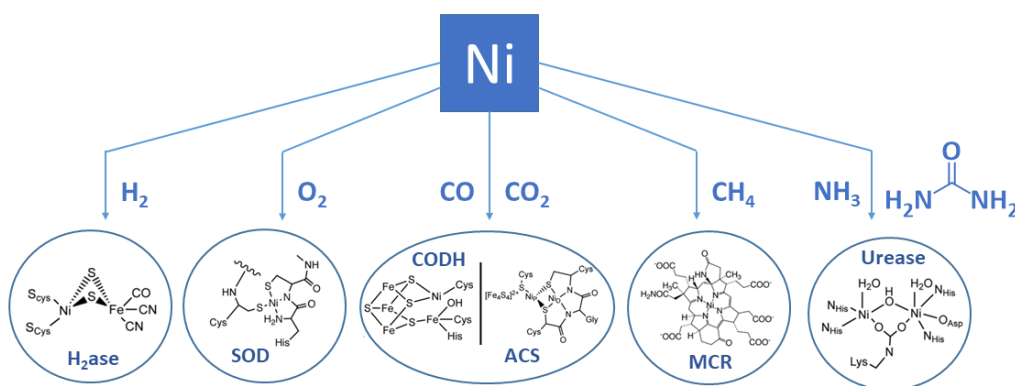
Figure 1. Some nickel-containing enzyme systems involved in small molecule transformations.

Thus, nickel scaffolds seem to be suitable platforms for small molecule transformations, and it seems feasible that the reactivity of this metal ion in a certain chemical environment could be expanded to other relatively inert compounds such as N_2, S_8, or NO. Despite the latter being quite reactive in comparison to the others, studies regarding its reactivity are of biological and chemical significance.

1.1.1 NiFe-Hydrogenase

Hydrogenases are a family of enzymes that promote reversibely the conversion between H_2 and protons as represented in Scheme 1:

$$H_2 \quad + \quad A_{ox} \quad \longrightarrow \quad 2H^+ \quad + \quad A_{red} \qquad \textbf{(1)}$$

$$2H^+ \quad + \quad D_{red} \quad \longrightarrow \quad H_2 \quad + \quad D_{ox} \qquad \textbf{(2)}$$
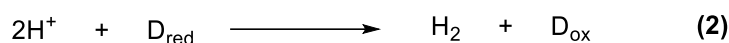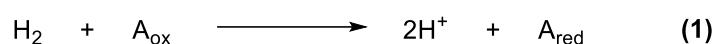
Scheme 1. Redox processes catalyzed by hydrogenase enzymes (A = electron acceptor; D = electron donor).

The oxidation of molecular H_2 (Eq. 1) is coupled with species that accept electrons such as oxygen, carbon dioxide and others, while the reduction of protons (Eq. 2) coincides with the oxidation of electron donors (e.g. ferredoxin).[3] Hydrogenases are divided into sub-categories based on the nature of the active site of the enzyme and are known as [FeFe], [NiFe] and Fe-only hydrogenases. While the first two compounds behave as redox catalysts, the Fe-only hydrogenase is able to reversibly cleave H_2 in a heterolytic fashion. Additional details for this compound will be given in section 1.4.1.
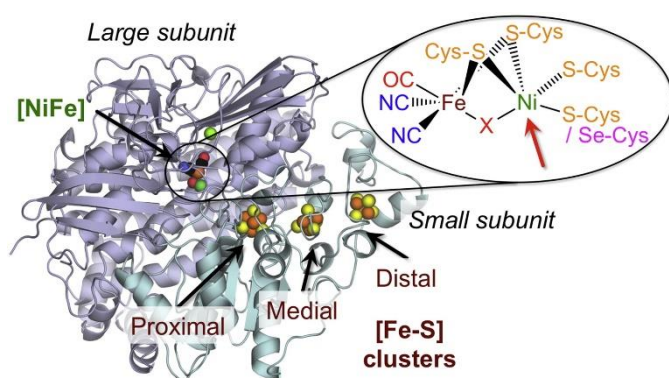
Figure 2. Structure of the [NiFe] hydrogenase with its active site, [4Fe-4S] proximal and distal clusters and [3Fe-4S] medial cluster. Image taken from reference 4.

X-ray crystallography and spectroscopic tools allowed for the structural determination of the active site of the [NiFe] hydrogenase, which was found to be a Ni/Fe/S compound with CO, CN and cysteine ligands, as shown in Figure 2.[4]

Mechanistic studies showed that the nickel ion participates in redox processes, while the iron center does not change its coordination sphere

and oxidation state during catalysis, remaining Fe^{II}.

Nowadays, the catalytic cycle followed by this enzyme is reasonably well understood, but the use of such systems for different technological applications (e. g. potential application for utilizing dihydrogen as an energy source) remains a great challenge.[5] One of the many reasons for that is the high sensitivity of the enzymes and their reaction intermediates towards dioxygen, even though the [NiFe] hydrogenase is believed to be the most robust among the hydrogenases enzymes. Studies illustrated that [NiFe] hydrogenases are capable of donating electrons for O_2 reduction under O_2 attack, which in turn produces water that protects the active site from reactive oxygen compounds.[6] This mechanism is particularly useful as a self-defense for the entire system, as it can reversibly switch these states on and off at a very slow rate upon reduction. However, this is only effective for small amounts of O_2.

Biologists, chemists and scientists from different fields are currently interested in overcoming all these problems, due to the high potential of hydrogenases for biotechnological applications. In fact, the understanding of such compounds might help the development of new biological energy sources that are able to produce hydrogen.[7] Soluble [NiFe] hydrogenases turned out to be versatile species that are relatively easy to handle and purify in comparison to other enzymes, with a high activity for H_2 oxidation and a resistance towards O_2 and CO. Such features are also useful for catalysis. For instance, the enzyme can be used either in solution or as part of a solid matrix to form an enzyme electrode and to obtain a catalyst for hydrogen oxidation with a power density higher than that achievable by standard Pt compounds.[8]

1.1.2 Acetyl-Coenzyme A Synthase (ACS)

Acetylcoenzyme A synthase (ACS) is a nickel based enzyme that is found in the metabolic processes of cells, along with carbon monoxide dehydrogenase (CODH). These systems together create a bifunctional system (ACS/CODH) that primarily works for the conversion of carbon dioxide to acetyl-CoA in anaerobic organisms such as archaea and bacteria.[9] The acetyl-CoA functions in turn as the provider of acetyl groups that are oxidized to carbon dioxide and chemical energy in the form of adenosine triphosphate (ATP) by all aerobic organisms through the "Krebs cycle".[10]

Figure 3. Structure of the active site of the Acetyl-CoA Synthase (ACS).

The structure of the active site of this system is shown in Figure 3. The ACS active site is a dinuclear nickel compound with both metal centers in the oxidation state +II, and bridged through one nickel ion (Ni_P) to an [Fe_4S_4] cluster. The presence of additional cysteine and amide donor leaves both nickel ions in a square-planar coordination environment. Studies regarding the activity of this enzyme suggested that, despite the fact that the proximal nickel ion can easily be replaced by copper or zinc,[11,12] its specific reactivity is limited to the presence of nickel only. Moreover, under certain conditions, the substitution of Ni with Cu can inhibit the enzyme.[13]

Studies that aim to understand the mechanism of action of this biological system for the synthesis of the acetyl-CoA led to two different pathways known as the paramagnetic and diamagnetic mechanism (Scheme 2).[14] The main difference that distinguishes them is given by the oxidation state of the nickel center (Ni_P) that is considered to be the substrate binding site, which undergoes a series of redox transformation steps. In the paramagnetic mechanism, the Ni^{II} ion is activated to Ni^I by certain cofactors that promote its reduction and binding of CO from the CODH or the methyl group from other specific proteins. Subsequently, the acetyl-CoA is formed after a series of reaction steps. However, this kind of pathway remains debatable because of its unbalanced electron count and the issues experienced to detect the putative Ni^I species by means of electron paramagnetic resonance spectroscopy (EPR).[15]

The diamagnetic mechanism proposes the formation of a Ni^0 intermediate compound instead of a Ni^I species. In this case, the methyl and CO group are added and a metal-acetyl compound is produced, followed by a series of reactions that lead to the final product.[16] Although this mechanism is electronically balanced, there is still no solid evidence for the formation of a Ni^0 intermediate, along with the fact that such complex is unprecedented in biological systems.

However, ongoing research is addressing all these questions and the mechanisms described above are still not considered implausible hypotheses.
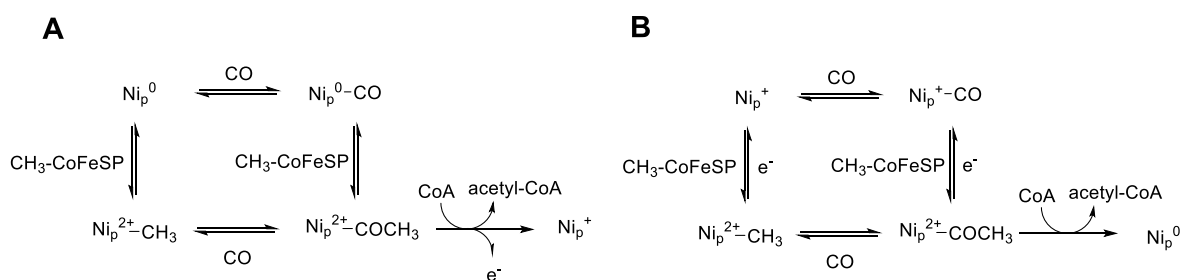
Scheme 2. Proposed diamagnetic (A) and paramagnetic (B) mechanisms of action of ACS. CFeSP = corrinoid-iron sulfur protein that catalyzes the transfer of a methyl group.

1.1.3 Nickel Superoxide Dismutase (Ni-SOD)

Another category of nickel-based enzymes that is worth mentioning is the nickel superoxide dismutase (SOD). This class of enzymes is essential for protecting cells from the so-called oxidative damage by catalyzing the disproportionation of the superoxide radical $(O_2)^-$, which is cytotoxic, to hydrogen peroxide and molecular oxygen, as shown in Scheme 3.[17]

$$O_2^{\bullet-} + E^{ox} \longrightarrow O_2 + E^{red} \quad \textbf{(1)}$$

$$O_2^{\bullet-} + 2H^+ + E^{red} \longrightarrow H_2O_2 + E^{ox} \quad \textbf{(2)}$$
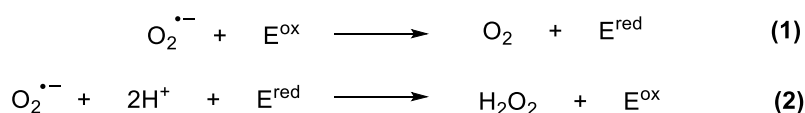
Scheme 3. Reaction pathway for the disproportionation of the superoxide radical catalyzed by Ni-SOD.

The presence of superoxide is unavoidable as it comes from the immune response of animal macrophages and it is implicated in aging processes, inflammatory disease, and a variety of pathological conditions.[18]

The Ni-SOD enzyme was isolated for the first time in 1996 from certain bacteria[17] and is now found primarily in prokaryotic organisms. This biological system is formed by six identical subunits, each of them containing a single nickel ion active site. A unique environment of ligands surrounds the nickel center, which gives its powerful features to the entire system. In fact, Ni-SOD is the only SOD enzyme that bears different ligands other than histidine, water and aspartate. Cysteine and thiolate ligands are also present, and allow the molecule for tuning the reduction potential of the nickel cofactor to that necessary for the desired superoxide disproportionation.[19] In particular, the value must lie within the potential of the two half-reactions of superoxide (Scheme 4). Therefore, the ideal value would be approximately around 360 mV *vs.* the normal hydrogen electrode (NHE).[20]

$$O_2 + e^- \rightleftharpoons O_2^{\bullet-} \qquad E_1^{0'} = -0.16 \text{ V vs NHE} \quad \textbf{(3)}$$

$$O_2^{\bullet-} + 2H^+ + e^- \rightleftharpoons H_2O_2 \qquad E_2^{0'} = +0.89 \text{ V vs NHE} \quad \textbf{(4)}$$
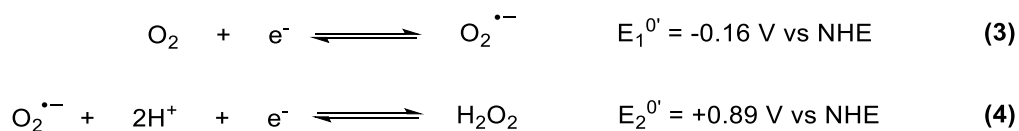
Scheme 4. Stepwise reduction of dioxygen to hydrogen peroxide.
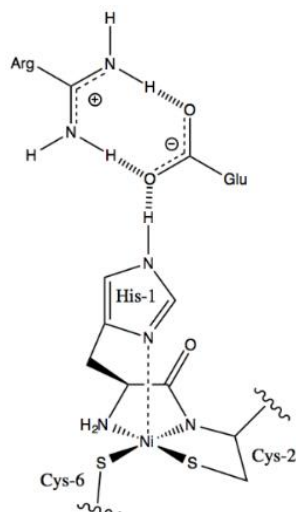
Figure 4. Structure of the active site of the nickel-SOD enzyme.

Figure 4 shows the molecular structure of the active site of the nickel superoxide dismutase enzyme. When it is found in its oxidized form, the Ni^{III} ion is in a square pyramidal geometric environment. However, it is still not completely clear whether or not the histidine-1 moiety can act as the axial ligand in its reduced form. In case this does not occur, then the geometry of the Ni^{II} center is square planar.

The mechanism by which the Ni-SOD enzyme operates involves a reduction/oxidation process where an electron is transferred between the Ni^{II}/Ni^{III} redox couple in the active site. This highly efficient pathway called "ping-pong" mechanism shows similarities with other SOD enzymes such as Cu or Mn based ones. As shown in Scheme 5, the superoxide radical reduces or oxidizes the nickel cofactor in an alternating sequence. The presence of the nickel cofactor itself facilitates the electron transfer steps that occur very quickly.[19]

Despite the fact that the reaction mechanism appears to be straightforward, several aspects still need to be clarified. First of all, the way the proton is transferred remains unclear. Probably an H^+ ion is bound to the active site of the enzyme, which leads to the conclusion that the interaction with the superoxide radical occurs in its protonated form HO_2. How the disproportionation reaction is carried out is still under debate,[21] since the second coordination sphere should be involved, but other evidences suggest a possible $H\cdot$ or H^+ quantum tunneling event, a supposition supported by an Arrhenius analysis. This is because the catalytic mechanism is so fast, that large changes or structural rearrangements are unlikely to occur.

$$O_2^- \ + \ Ni^{III}SOD \ \longrightarrow \ Ni^{II}SOD \ + \ O_2 \qquad (5)$$

$$O_2^- \ + \ 2H^+ \ + \ Ni^{II}SOD \ \longrightarrow \ H_2O_2 \ + \ Ni^{III}SOD \qquad (6)$$
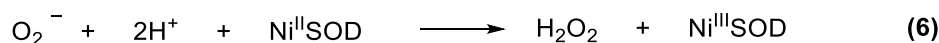
Scheme 5. Mechanism of action of Ni-SOD.

1.2 Nitric Oxide

Nitric oxide (NO) is a potentially toxic, diatomic gas whose chemistry was intensively studied over the past 30 years.[22] This interest emerged from the recognition that NO and its derivatives play an important role in several pivotal regulatory pathways. Its highly lipophilic character allows the molecule to diffuse through cell membranes without specific transporters, serving as physiological messenger molecule in the human body.[23] As a consequence, it can affect a variety of processes, ranging from regulation of blood pressure, immune system or nerve impulses.[24] Additionally, NO can be found as necessary intermediate in bacterial denitrification.[25] Gaseous NO is a radical, having an unpaired electron in one of its π^* orbitals. Therefore, it exhibits an active chemistry in both oxidation, readily forming NO^+ compounds, and reduction, where NO^- species are produced.[26] Overall, these different redox forms that bear 10 electrons (NO^+), 11 electrons (NO) and 12 electrons (NO^-) can also be considered in analogy with the different oxidation states of dioxygen in O_2, $(O_2)^-$ and $(O_2)^{2-}$ which also have essential biochemical functions, although these two series are not strictly isoelectronic.[27]

Coordination complexes of nitric oxide (nitrosyl complexes) have been known for centuries, and the usual binding mode is found to be via the nitrogen atom to the metal center. In the case of a terminal nitrosyl compound, two formal geometries can be adopted, known as linear or bent (Figure 5, I and II).[28]
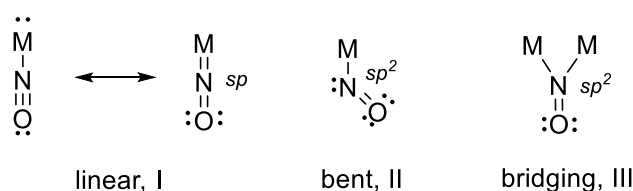
Figure 5. Coordination geometries for metal nitrosyl complexes.

These designations shown in Figure 5 represent a simplified interpretation with respect to the ligand charge and metal oxidation state assignment, but only consider the electron pair located either on the metal, or on the ligand. Therefore, this formalism does not intend to substitute for a detailed bonding description.

In general, the bonding situation would be more accurately described by MO theory, considering a σ orbital from the nitrogen atom that forms a bond to the metal. The metal center can then backdonate its electron density from the $d\pi$ orbitals to one of the π^* orbitals of NO, as represented in Scheme 6.[29]

σ_{2p}^*

π_{2p}^*

2p

σ_{2p}

2p

π_{2p}

σ_{2s}^*

2s

2s

σ_{2s}

ground state NO

N atomic orbitals

O atomic orbitals
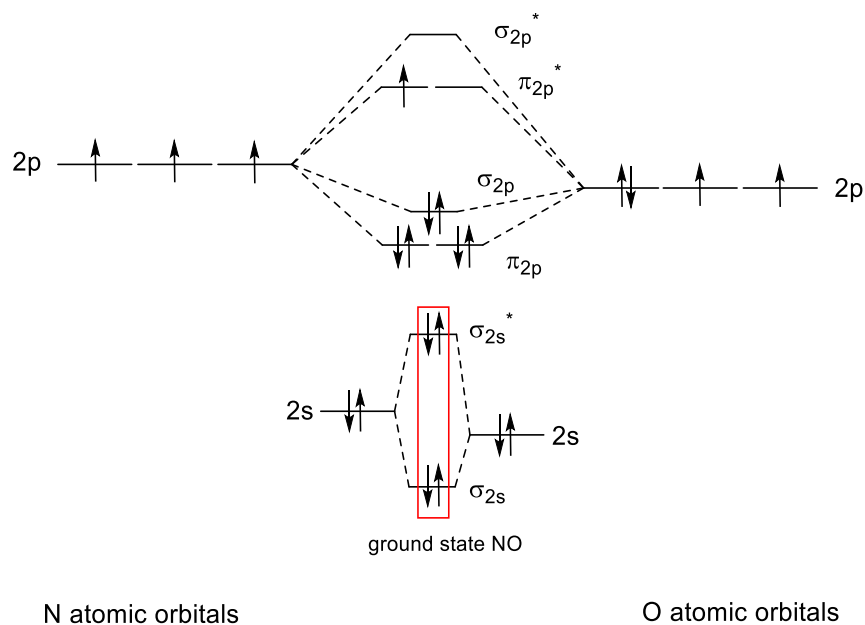
Scheme 6. MO scheme for nitric oxide radical (NO).

According to model studies on an iron nitrosyl complex, the HOMO $d_{xz}(Fe)/p_x(N)$ orbital has a strong π-antibonding character and the effect can be reduced when the nitrosyl ligand bends its geometry.[30] However, it is worth mentioning that the generalization of the binding of NO to metal centers is extremely difficult, as a series of different interactions and ligand environments could drastically change the system's properties.

Especially for the description of highly covalent bonds in M-NO complexes, a special notation called "Enemark-Feltham notation" was introduced. It can be used to rationalize the number of d-type electrons present in a given complex, as the number of π^* electrons of the NO ligand moiety is added to the number of d electrons of the metal.[31] For instance, for a Fe^{II} mononitrosyl complex, a $\{Fe(NO)\}^7$ species could be formulated, considering six d-electrons from the metal center and one electron from nitric oxide.

1.3 Nitric Oxide Reactivity Studies with Nickel Complexes (and more)

1.3.1 Synthesis and Reactivity of Nickel Nitrosyl Complexes

An overview of some fascinating natural systems that involve nickel ions was given in the previous sections. The biocatalytic transformations that they perform are certainly of great interest not only to understand how these enzymatic processes work, but also to be able to mimic them for industrial applications. Indeed, their efficiency and selectivity are usually higher than those of artificially reproduced systems, due to the use of abundant metal-catalysts and low activation barriers. However, many difficulties are faced during the studies of natural systems, because of the high reactivity and instability of reaction intermediates that are necessary to characterize. Therefore, model compounds are fundamental for understanding mechanisms, interactions and properties of a particular system, as their use can be extended to non-biological conditions, to a variety of different temperatures and/or pressures.

Driven by its biological importance, the coordination chemistry of nitric oxide expanded rapidly over the past years, especially for first row transition metals like iron, cobalt, nickel and copper. The work on nickel complexes towards this gas was also motivated by the interest in organic synthesis or catalytic NO reduction.[32]

A $\{Ni(NO)\}^{10}$ configuration in the Enemark-Feltham notation was reported so far for all nickel nitrosyl complexes (Ni-NO). Despite this similarity, nickel nitrosyl complexes exhibit a wide range of reactivity, ranging from dissociation to reduction and disproportionation. In general, the coordination environment and the electronic structure of the compounds has a major effect on its reactivity.

For instance, WARREN's group reported the synthesis of a three-fold coordinated Ni-NO complex that is able to react with organonitroso species such as RNO (R = Et, Mes) to afford a complex where a new N-N bond formed between the nitrosyl group and the RNO substrate.[33] The same complex could also be formed by oxidative nitrosylation of a dinuclear $[LNi]_2(RNO)$ compound by gaseous nitric oxide or after insertion of NO into a Ni^{II}-alkyl precursor at low temperature.[34] This kind of reactivity pathway was also interesting because of the unusual electrophilic behavior of RNO, which led to the consequent nucleophilic character of the starting material Ni-NO complex. Therefore, a $Ni^{II}(NO)^-$ electronic structure was expected, in contrast to the typical $Ni^0(NO^+)$ configuration for linear nickel nitrosyl compounds.[35] Further details on the coordination chemistry of nitrosobenzene will be given in the next section 1.3.3.

HAYTON and co-workers also studied the reactivity of nickel nitrosyl compounds, and reported more recently the characterization of a [Ni(NO)(bipy)]⁺ cation complex that acted as a strong Lewis acid to bind Lewis bases and afford [(bipy)Ni(NO)L]⁺ type complexes, increasing its coordination number.[32] The reactivity of the [Ni(NO)(bipy)]⁺ compound was also studied towards oxidants and the one-electron oxidation with AgPF₆ led to the homolysis of the Ni-NO bond and evolution of NO gas, in contrast to the expected but still unprecedented isolation of a {Ni(NO)}⁹ compound. Similarly, a square planar Ni^II complex was isolated along with the production of NO when TEMPO was used as the oxidant (Scheme 7).[36] Although it was clear that the {Ni(NO)}⁹ configuration is highly unstable, the {Ni(NO)}^{10/9} couple could be used as means for NO delivery.
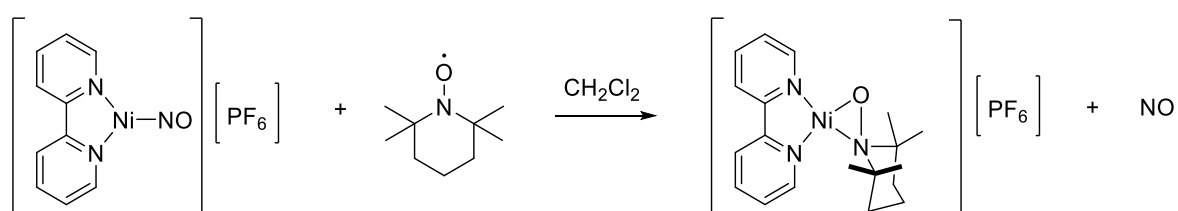
Scheme 7. Release of NO by one-electron oxidation from the [Ni(NO)(bipy)]⁺ complex.[36]

Other compounds reported by the same group involve pseudo-tetrahedral geometries, like in the [Ni(NO)(CH₃NO₂)][PF₆] complex, where it was shown that the nitromethane ligand undergoes substitution upon treatment with MeCN, piperidine and even arenes.[37] The latter case was rather interesting, as the arene group showed a η⁶ binding mode, which is rare for Ni(arene) compounds.[38]

In contrast with the pseudo tetrahedral geometry usually adopted by four-coordinated nickel nitrosyl compounds, the addition of NO to (PNP)Ni (PNP = (^tBu₂PCH₂SiMe₂)₂N) afforded (PNP)Ni(NO), which features a distorted square planar geometry, probably originated from the rigidity of the PNP ligand backbone.[39] Additionally, a bent Ni-N-O linkage was found, suggesting a Ni^I(NO·) or Ni^II(NO⁻) electronic structure (Figure 6). Based on preliminary calculations, the Ni^II(NO⁻) configuration seemed to be more reasonable.

A   **B**

(PNP)Ni^II—N〜O   (PNP)Ni⁰—N≡O
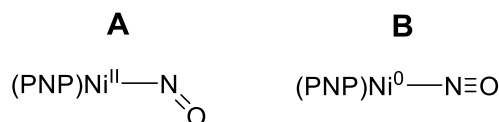
Figure 6. Possible configurations of a Ni(PNP) nitrosyl complex. For the bent configuration (A), calculations suggested the presence of a Ni^II(NO⁻) electronic structure.[39]

In 2007, the first five-coordinated nickel nitrosyl compounds were structurally characterized by PARKIN[40] with [BseMe]Ni(PPh$_3$)(NO) (Bse = bis(2-seleno-1-methylimidazolyl)borate) and RABINOVICH[41] with (BmR)Ni(PPh$_3$)(NO) (BmR = bis(mercaptoimidazolyl)borate; R = Me, ^{t}Bu) complexes. Both compounds showed a significant bending of the Ni-NO linkage, probably due to either a non-C$_3$ symmetry around the nickel ion, or as consequence of a B-H bond interaction with the metal center.

The previously mentioned three-coordinate nickel nitrosyl [Ni(NO)(bipy)]$^+$ was found to be a suitable for the synthesis of five-coordinate nickel nitrosyl compounds, just by adding excess of bipy or Me$_2$phen to the starting material to obtain the corresponding [Ni(NO)(bipy)(Me$_2$phen)]$^+$ complex.[32] In this cases, the Ni-N-O bond angle of about 130° for both species suggested the presence of a nitroxyl (NO moiety with formal charge of -1; NO$^-$) ligand. The assignment was further supported by the relatively low NO stretching vibration determined by IR spectroscopy. Surprisingly, when the [Ni(NO)(bipy)(Me$_2$phen)][PF$_6$] compound was isolated and exposed to acids such as acetylacetone (acac), no reaction was observed. On the other hand, [Ni(NO)(bipy)$_2$][PF$_6$] converted into [Ni(acac)(bipy)$_2$][PF$_6$], N$_2$O, and water under the same conditions. It was also proved that the NO reduction that occurs in the reaction proceeds via a hyponitrite intermediate, as a (bipy)Ni(κ^2-N$_2$O$_2$) could be isolated and structurally characterized (Scheme 8).[32] Further studies in order to shed light into the reaction mechanism indicated that the N-N bond formation occurred by the coupling of two nitroxyl ligands via a bimetallic intermediate.
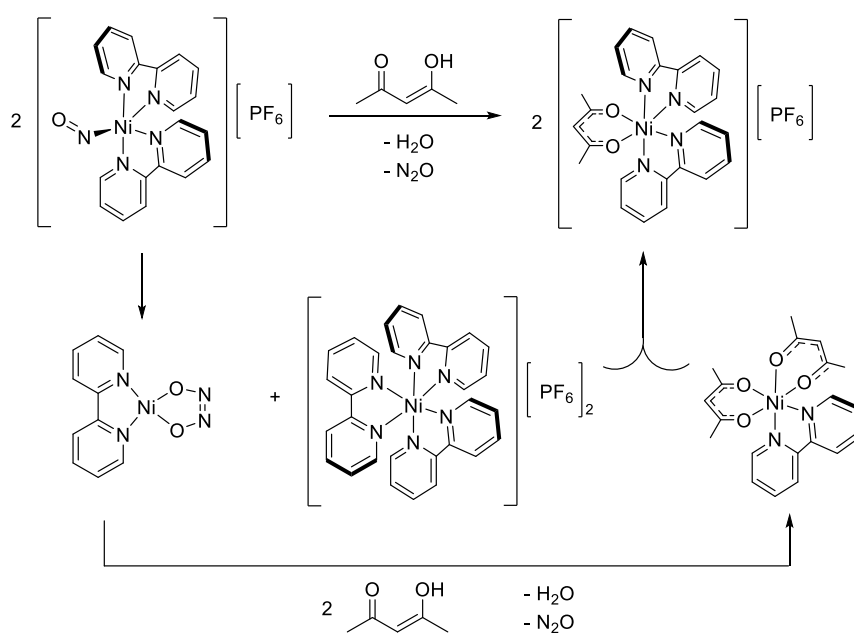
Scheme 8. Reduction of nitric oxide mediated by the [Ni(NO)(bipy)$_2$][PF$_6$] complex.

This last example regarding the possibility of isolating intermediates occurring during the reduction of nitric oxide is of high interest among chemists, and such reactivity will be further discussed in the next section 1.3.2.

1.3.2 Some Aspects Regarding Hyponitrite in the Nitric Oxide Reduction

The interest in the aforementioned hyponitrite reaction intermediates is explained by the biological importance of NO reduction. In nature, this process is a key step of the total inorganic nitrogen cycle,[42,43] where the oxidation state of this small molecule changes upon conversion into other compounds, as represented in Scheme 9.
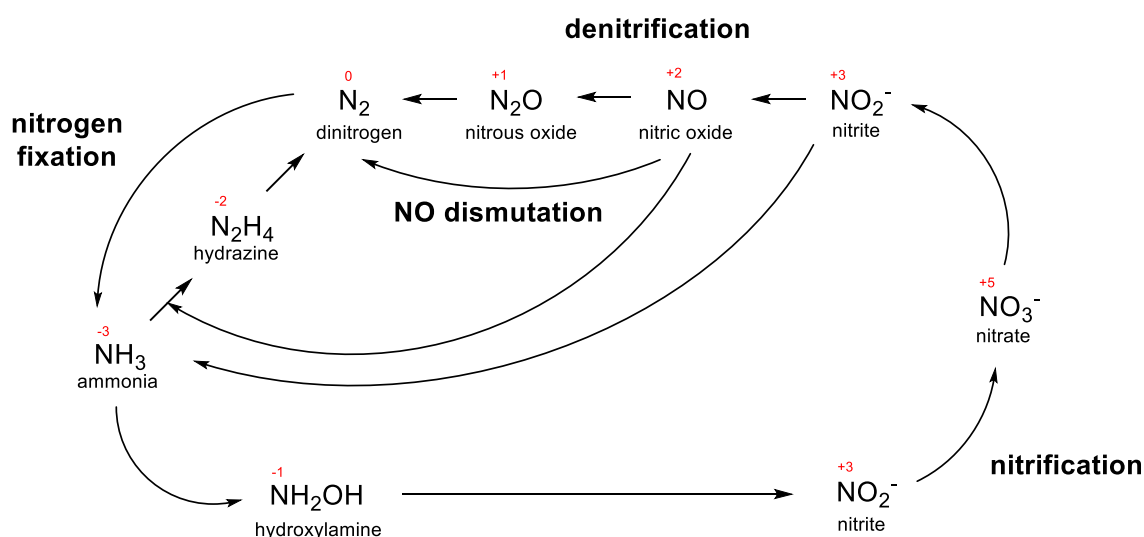
Scheme 9. The total inorganic nitrogen cycle. Each step is mediated by a specific metalloenzyme.

In particular, NO reduction is part of the bacterial denitrification process that reduces nitrate to dinitrogen in four steps, each of them catalyzed by a specific enzyme. The two-electron reductive coupling of two molecules of NO leads to the formation of N_2O, and the process is usually mediated by nitric oxide reductases (NORs) and non-heme flavodiiron reductases (FNORs) that additionally provide two protons in order to complete the reaction as follows:[44]

$$2\,NO \;+\; 2\,e^- \;+\; 2\,H^+ \longrightarrow N_2O \;+\; H_2O$$

These species are able to bind NO to generate the corresponding nitrosyl adducts, where a hyponitrite-like {N_2O_2} moiety is proposed as common intermediate in the catalytic cycle. However, the mechanism by which these systems mediate the conversion of NO to N_2O

and water is still under debate.[45] Recently, a computational study suggested a series of intermediates with bound hyponitrite that could be reasonable at the dinuclear active site of FNORs, as shown in Scheme 10.[46]
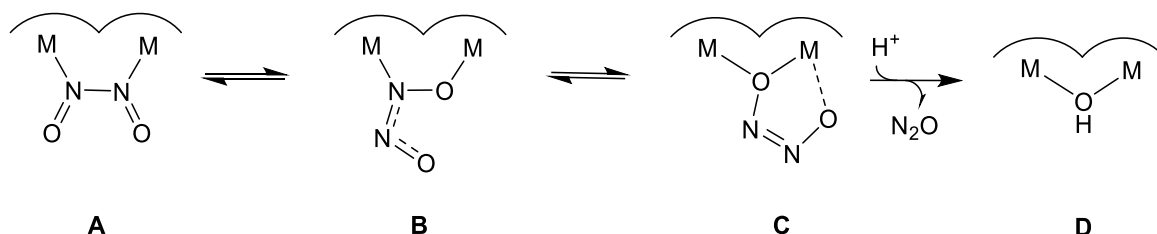
Scheme 10. Calculated reaction pathway to generate N_2O after N-N coupling of two NO molecules.

A structural rearrangement after the initial N-N bond formation in a *cis*-$[N_2O_2]^{2-}$ intermediate (A) is suggested to take place in order to generate the corresponding *cis*-isomer (B) where the hyponitrite moiety is bound through both nitrogen and oxygen atoms. A further rotation of the unit would then progress to the formation of an only O-bound species (C) that allows for facile N_2O release and formation of the hydroxo species (D) in the presence of protons. However, so far there is no experimental evidence of a reaction intermediate of type B or C that could strongly suggest such type of hyponitrite binding mode in the process of N_2O formation.

Besides the biological motivation in understanding fundamental aspects of the nitric oxide reduction, the reaction is also necessary for controlling NO_x emissions that are constantly produced by vehicles. Currently, the catalysts that allow for such reaction are highly efficient but also very expensive, as noble metals (e.g. Pt and Rh) are used.[47] Therefore, the interest in replacing such materials with cheaper, earth-abundant elements is growing.[47,48,49] Nevertheless, the attention in learning about the mechanism of heterogeneous NO reduction in catalytic converters was considerable even before these challenges were faced.[50,51] More recent experimental works suggested that the formation of a hyponitrite moiety is also plausible for metal centers different than the iron containing active sites found in the enzymatic process, pointing at an analogy with the heterogeneous catalysis.[52] Although many studies in this regard were already performed, not many molecular metal complexes that contain a hyponitrite motif were reported so far. However, it is clear that this unit can adopt a variety of different binding modes to metal centers, and they were found mainly in Pt,[53] Co,[54] and Ni compounds.[32]

Given the current vagueness surrounding the mechanism of nitric oxide reduction, it is clear that further studies in this area are rewarding.

1.3.3 Organonitroso Nickel Compounds

The interest in the chemistry of nitroxyl (HNO) increased its importance due to the remarkable properties and biological relevance of this molecule.[55] In fact, HNO displays an acid-base equilibrium HNO $\rightarrow$ NO$^-$ + H$^+$ with pKa = 11.4 that is spin-forbidden,[56] along with its instability that leads to dimerization and production of nitrous oxide and water. To overcome the problem, the use of stable analogues may serve for gaining knowledge on HNO, otherwise difficult to study. To this end, nitrosoarenes are organic compounds that form by oxygenating aromatic amines at the nitrogen position and are often used to model HNO chemistry.[57] Furthermore, nitrosobenzene is known to have a greater affinity for hemoglobin over dioxygen[58] so that it can be considered of biological relevance itself.
Along with the biological importance of this class of compounds, Cu and Ni organonitroso complexes were found to take part in reactions of synthetic importance, such as the allylic CH amination reactions and nitrene transfer, respectively.[59]

Previously reported organonitroso complexes were able to show the different degrees of activation of the bound molecule upon changing the nature of the metal ion and the entire ligand scaffold. In general, it was found that bimetallic complexes exhibited greater activation of the NO bond in comparison with their monometallic analogous.[34,60] For instance, when two nacnac Ni^I fragments coordinate a nitrosobenzene molecule, a dinuclear Ni complex was finally obtained (Figure 7, c). In this case, a N-O distance of 1.44 Å was found, which was longer than in free nitrosobenzene (d(NO) = 1.21-1.23 Å).[61]
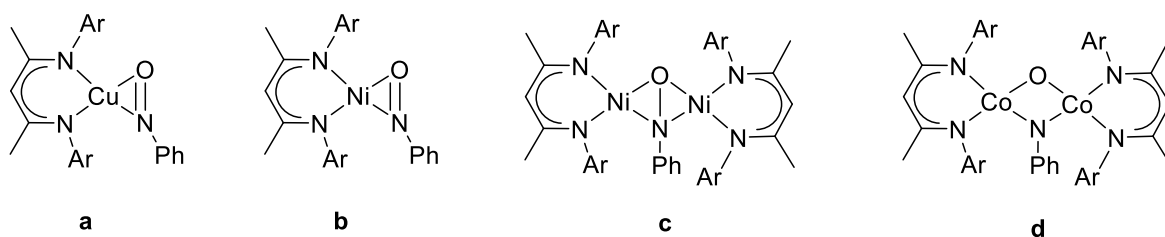
Figure 7. Examples of β-diketiminate organonitroso complexes.

The dinuclear Co^I bis(nacnac) system (Figure 7, d) represents a limiting case for NO bond activation, where the ArN-O bond is completely cleaved by the high electron density on the system, and the organic moiety bears both Co-N-Co and Co-O-Co bridging units.
Interestingly, further studies on mononuclear nickel nacnac systems described the redox non-innocence of the organonitroso group,[62] suggesting an analogy with the transformations between bound superoxide[63] and peroxide ligands.[64] Binding of nitrosobenzene to an electron-deficient nacnac Ni^I complex resulted in one electron

reduction of the PhNO ligand to form a (PhNO)$\cdot^-$ radical species coordinated to a Ni^{II} square planar metal center, which served as H-atom abstractor and afforded the corresponding protonated compound after reaction with a diene. The (PhNO)$\cdot^-$ ligand moiety could be further reduced to obtain a formal (PhNO)$^{2-}$ group related with the reactivity of oxygenated species, even though dioxygen and nitrosobenzene possess different ground states. The described transformations are represented in Scheme 11.
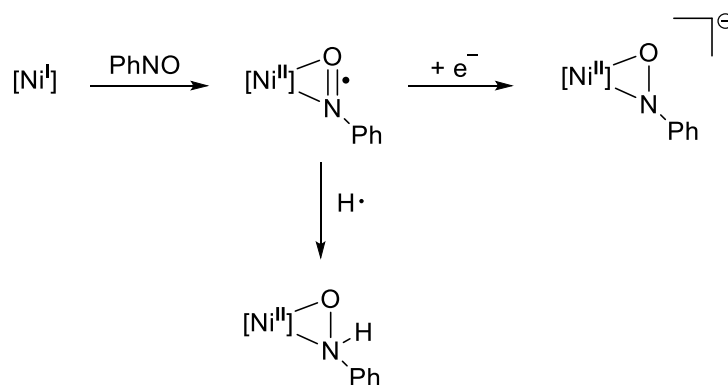
Scheme 11. Redox conversions of PhNO on a mononuclear nickel complex based on a β–diketiminato ligand.

1.4 Biological Role of Iron

Iron is an element that is involved in a large number of biological systems where it plays various key roles, and its importance can be illustrated by some examples. First of all, the bacterium *Escherichia Coli* (E. Coli), a facultative anaerobic, coliform bacterium commonly found in the lower intestine of endotherm organisms and used as a general model system for bacteria, owns a high number of genes that are used to express proteins involved in iron uptake.[65] Moreover, the way to determine the potential for growth of a tumor in medicine is represented by the measurement of the density of transferrin receptors, which are required for iron uptake and in turn cellular growth and division.[66]

The chemistry of iron in aqueous solutions is in general governed by its oxidation states +II and +III, whose metal complexes can undergo acid-base reactions and electron transfer.[67] Additionally, iron is the fourth most abundant metal on Earth and the most abundant in humans, where the bulk of iron is bound in the oxygen transporting protein hemoglobin[68] in the red blood cells and to the muscle oxygen storage protein myoglobin.[69] Binding of dioxygen to these iron-containing heme cofactors is essential to circumvent the low solubility of O_2 in blood that could prevent its transport to the other body tissues.

To perform other kinds of reactions in biological systems, iron containing enzymes often display intermediate species that also involve unusual oxidation states of the metal center, such as Fe^I or high valent Fe^{IV} and Fe^V in oxidative processes. For instance, hydrogenases are a family of enzymes which are able to catalyze the reversible oxidation of dihydrogen H_2, and the iron-only form is believed to catalyze the heterolytic cleavage of H_2. Here, Fe^I species are postulated to be part of this process.[70] More details in this regard will be discussed in section 1.4.1.

Furthermore, the activation of the diatomic N_2 molecule performed by bacteria involves the nitrogenase enzyme that converts N_2 to NH_3.[71] Interestingly, these enzymes are able to break the dinitrogen bond at room temperature (25°C) and atmospheric pressures, although this process is extremely energy intensive.[72] The FeMo cofactor is recognized to be the binding site of N_2 for its activation, although the mechanism by which this process occurs is still under debate. However, biochemical studies support the evidence that a possible mechanism proceeds through diazene and hydrazine intermediates en route to ammonia formation.[73] Details regarding the dinitrogen fixation will be given in section 1.4.2.

1.4.1 Iron Hydride Complexes in Nature

As described in the previous section, iron is considered of ubiquitous biological relevance. Typically, model studies of the active site of iron-based enzymes address many key questions to deeply understand how these complex species work and why specific metal centers or ligand properties are so necessary for biocatalysis.

Iron hydrides are more often mentioned as important intermediates that play a role in the catalytic cycles of biological systems. Bacteria, archaea and other unicellular eukaryotes accommodate certain hydrogenase enzymes which are able to catalyze reactions involving molecular hydrogen. Furthermore, it is suggested that Fe-H species are formed at their active sites during these transformations.[74] These intermediates are obviously highly reactive, and their isolation appears rather challenging. Research in this regard moved many steps forward, and success was achieved in understanding partially several enzymatic mechanisms.

As already mentioned in section 1.1.1, hydrogenases are able to reversibly combine electrons and protons to give dihydrogen at high rates. Within the different types of this family of enzymes, the Fe-only hydrogenase features a different mechanism in terms of electron delivery from one side of the active site to others, and in terms of redox couples involved in the process.[75]

Formation of metal hydride species or dihydrogen bonds seems to be obvious when talking about evolution or uptake of H_2 in this system. However, direct spectroscopic evidence that supports this hypothesis was not achieved. It was possible to observe indirectly the formation of this species when detecting the presence of HD during enzymic turnover in atmosphere of D_2.[76] Based on previous results, it is known that the cofactor methylenetetrahydromethanopterin (methylene-H4MPT) can accept hydride units from H_2 in the process. For this reason, Fe-only hydrogenase is also named H_2-forming methylene-H4MPT dehydrogenase because it can reversibly reduce [methylene-H4MPT]$^+$ to [methylene-H4MPT].[77] Interestingly, this hydrogenation process occurs instead of production (oxidation) of H_2, in contrast with the observations made for the other kind of hydrogenases.[78] According to recent findings, it is proposed that the molecular hydrogen is first heterolytically cleaved, and the produced hydride is then transferred to the acceptor.[79]

Iron hydrides are not limited to the hydrogenases category of enzymes described above, but they can also be found as proposed species that form during the conversion of dinitrogen into ammonia promoted by nitrogenase. Nitrogenase is composed of two proteins, a Fe protein that supplies the system with electrons, and the heterotetrameric MoFe protein, which uses the received electrons to convert N_2 to NH_3. When the reduction of N_2 occurs at the FeMo-cofactor, the reductive elimination of H_2 from two iron hydride units is proposed to be linked to N_2 binding, as shown in Figure 8.[80]
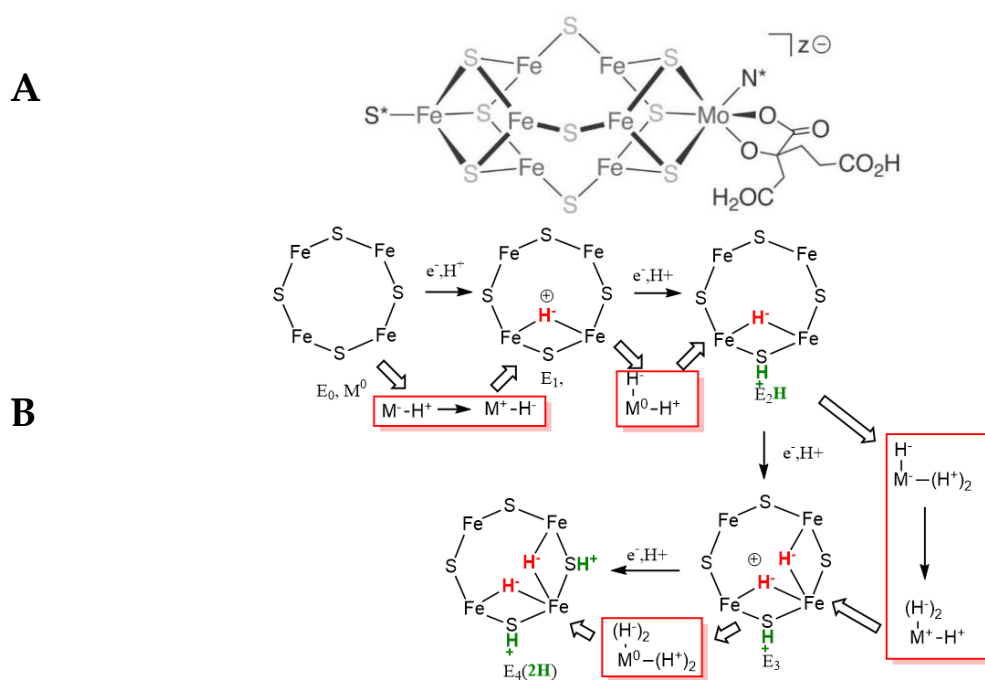

Figure 8. Representation of the FeMo-cofactor (A) and E_n states of the active site when the first four protons and electrons are stored. This is then followed by reductive elimination of H_2 from $E_4(4H)$ (not shown).[80]

The picture illustrates that four protons and four electrons are collected in the FeMo-cofactor as two Fe-H units, forming a series of states that are represented as E_n, with n = number of delivered electrons/protons. This mechanism brings to the protonation of iron-hydride species and reductive elimination of H_2 from the E_4 state, while the whole process results kinetically and thermodynamically reversible.

One discouraging side of nitrogenase research is that some important aspects are still unknown. For instance, the hydride iron units could be either terminal (Fe-H) or bridging (Fe-H-Fe). Computational studies on simplified models tried to give an answer to such questions by evaluating the relative energies of these different coordination modes.[81] Furthermore, ENDOR analysis of the E_4H_4 state showed the presence of a rhombic tensor resulting from the coupling of the ^1H nuclear spin and the unpaired electron spin, while the same experiment on isolable iron hydride compounds confirmed an axial tensor for terminal hydrides and a rhombic for Fe-H-Fe units.[82] Thus, terminal hydrides are more consistent to be part of the E_4 state of the FeMo cofactor. However, other hypotheses that are based on synthetic modeling studies suggest that the actual active form of the enzyme has transient terminal hydrides.[83]

1.4.2 Iron Intermediates in Nitrogen Fixation

The biologically available nitrogen (fixed nitrogen) is a critical limiting element for life. Although nitrogen gas (N_2) is one of the most predominant elements in the Earth's atmosphere, plant growth and food production only depend on its reduced forms. Therefore, this gas must be converted into other compounds by natural processes (e.g. lightning), by biological nitrogen fixation, or added as ammonia and/or nitrate fertilizers obtained through industrial processes such as the Haber-Bosh process, which requires drastic conditions of high temperature and pressure. As the worldwide population is constantly increasing, the optimization of agricultural practices and sustainability is obviously gaining of importance.[84]

Microorganisms are able to generate ammonia at physiological conditions through the enzyme nitrogenase, already mentioned in the previous section. However, the energy demand is quite high also in the enzymatic reaction, namely in form of ATP hydrolysis (P_i = inorganic-phosphate containing product):[85]

$$N_2 + 8H^+ + 16MgATP + 8e^- \longrightarrow 2NH_3 + H_2 + 16MgADP + 16P_i$$
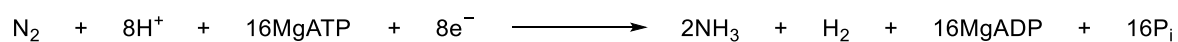
Nowadays, the exact mechanism of biological nitrogen fixation is a matter of debate, and two main proposals are currently considered as reasonable.

The "distal" or "alternating" pathways invoke distinct reaction intermediates that will be discussed.[86] On the one hand, the distal pathway[87,88] bases its assumptions on inorganic model complexes of molybdenum or tungsten. These systems are able to mediate the fixation of N_2 under catalytic conditions and several proposed intermediates in the pathway were independently synthetized. The mechanism originated from the idea that N_2 binding takes place at the Mo atom of the FeMoco, but N_2 binding at the central Fe belt of the FeMoco now seems more likely. In that mechanism, the distal nitrogen of the coordinated N_2 is hydrogenated in a three step reaction, where one equivalent of NH_3 is liberated, along with the formation of a nitride species. This remaining nitride function takes part in other three hydrogenation steps in order to yield the second ammonia molecule. A simplified version of this mechanistic pathway is shown in Scheme 12.
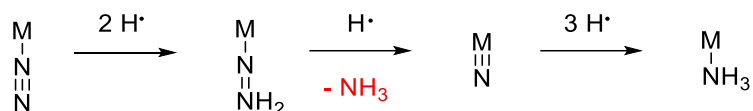
Scheme 12. Proposed distal pathway for N_2 reduction.

Many studies suggest that the whole process is focused on the metallic region as main site for substrate binding, supporting the so-called alternating pathway.[89] In this case, the N-N bond is protonated and reduced by following an alternating sequence of steps through a diazenido (N_2H^-), diazadiene (N_2H_2), hydrazido ($N_2H_3^-$) and hydrazine (N_2H_4) series of intermediates, as shown in Scheme 13. During the fifth and last hydrogenation, the N-N bond cleavage occurs.
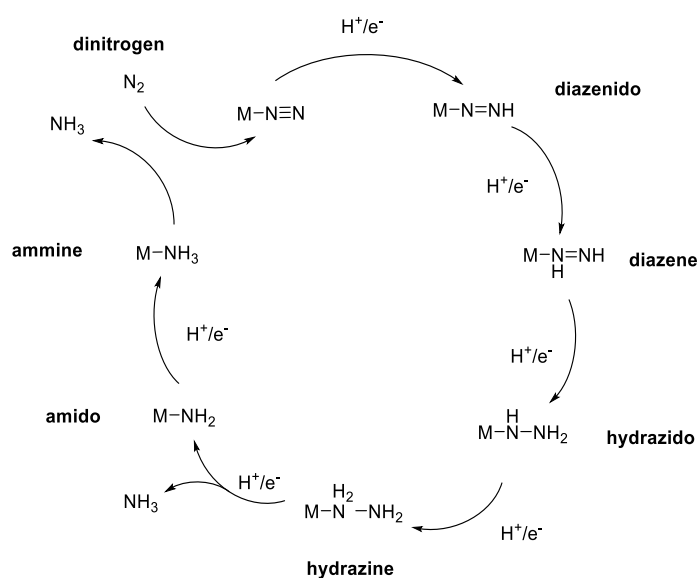
Scheme 13. Alternating pathway for N_2 reduction. The FeMoco binding site is abbreviated with M.

This type of mechanism is supported by the fact that compounds like hydrazine or diazene are substrates of nitrogenase and are released when the enzyme is hydrolyzed under turnover conditions in acid or basic conditions.[90] In addition, research on iron model complexes showed that cleavage of dinitrogen[91] or its catalytic fixation[92] are possible, supporting even more the fact that the activation of the molecule occurs at the iron site of the FeMo cofactor.

Although the alternating mechanism seems to be most likely similar to the real reaction pathway for the nitrogen fixation supported by nitrogenase, it is clear that a considerable number of N_xH_y species must be taken into account in each step of the cycle, leading to a number of questions that still need an answer. For instance, more information regarding the binding mode of the nitrogen and its reduced forms at the metal center is needed. Therefore, synthetic studies provided and still provide useful indications for possible mechanistic scenarios. Moreover, such model systems could be used for developing compounds, which are able to reduce dinitrogen under mild conditions, relevant for the industrial production of ammonia and related compounds.

More details regarding some iron-based synthetic models for N_2 reduction of importance for this thesis work will be given in the next section.

1.4.3 Iron Model Complexes

Synthetic model complexes are generally used to provide understanding into the viability of different structures and mechanisms of enzymes.[93,94] Yet, the chemistry of iron complexes that are found in a coordination environment similar to the FeMo-cofactor was little known until a few years back. Nevertheless, current advancements in synthetic iron complexes, including iron hydride systems, which are related to the N_2 reduction pathway, allowed for advances in this field. As already mentioned in the previous sections, iron hydrides are believed to best describe the E_4H_4 state of nitrogenase, and most of the conclusions are made by means of model studies. The majority of the isolated iron-hydride species are coordinated by strong-field organometallic or phosphine co-ligands, with a low spin electronic configuration and diamagnetic centers,[95,96] while the iron atoms of the enzyme nitrogenase experience a weak field – given by a sulfide donor set, and coordination number less than five – that is electronically different.[97] Therefore, new iron-sulfur hydride complexes reminiscent of the FeMoco active sites were prepared.

For instance, a low-coordinate $Fe(\mu\text{-}H)_2Fe$ dimer that bears a weak field ligand environment was isolated by the HOLLAND group.[98] The compound was shown to react with relevant substrates for nitrogenase activity, such as CO_2, cyanide, azides and alkynes.[99,100] Other

interesting reported compounds include a family of $Fe_3(\mu\text{-}H)_3$ clusters, stabilized by a tris(β-diketiminato) scaffold, which only reacted with CO_2 and not with other nitrogenase substrates.[101] However, these iron hydride species did not contain S functionalities. More recently, diiron hydrides placed in an environment rich of carbon and sulfur were synthetized by QU and co-workers.[102] Another interesting result was achieved again by the HOLLAND group,[103] which isolated a dinuclear iron complex (**I**) with sulfide and hydride bridging units that could potentially model a coordination mode for hydrides in FeMoco, as represented in Scheme 14 (A).
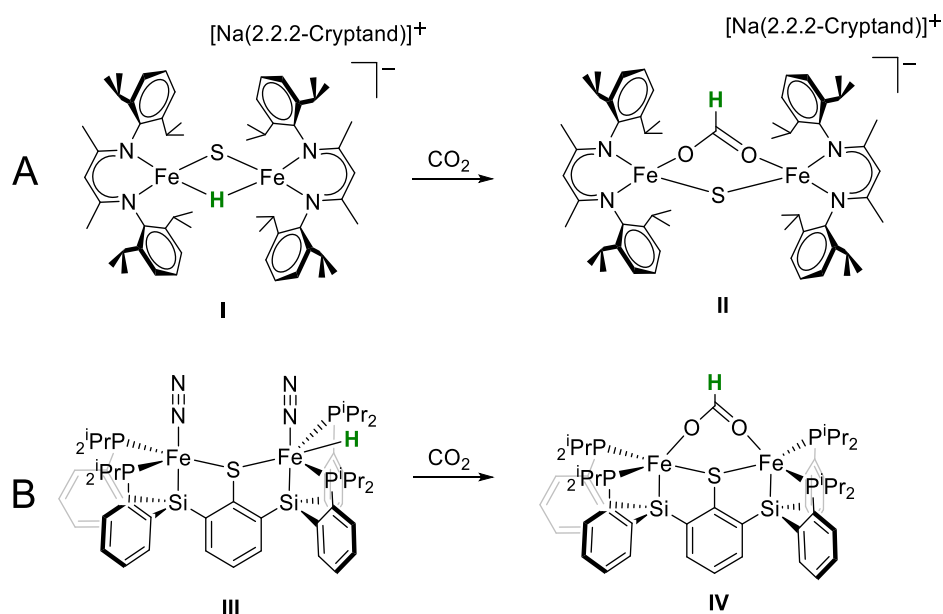
Scheme 14. Iron hydride complexes that are shown to reduce carbon dioxide.

Moreover, the ability of compound (**I**) to reduce carbon dioxide to obtain the corresponding bridging formate complex (**II**) mimics the behavior of nitrogenase.[104,105] Also complex (**III**) represented in Scheme 14 (B) bears a terminal hydride, and it was shown to reductively bind CO_2, to form a thiolate bridged formate compound (**IV**).[106] Therefore, it could be assumed that hydrides in both terminal and bridging configuration are active in sulfur supported Fe-H complexes.

The starting diiron hydride complex (**I**) (Scheme 14, A) was also tested towards reduction by two electrons under an atmosphere of dinitrogen, as the reductive elimination of two hydrides from the E_4H_4 state of nitrogenase is proposed (Scheme 15).[103] Evolution of H_2 was observed, along with the formation of a diiron(0)-N_2 complex (**V**), supporting a parallel pathway to the reductive elimination. Since the complex only has one hydride, it is not possible to liberate H_2 in an intramolecular reaction. Therefore, together with the fact that

the yields of the final N_2-bridged compound and dihydrogen are relatively low, the reactivity mechanism seems still to be uncertain.
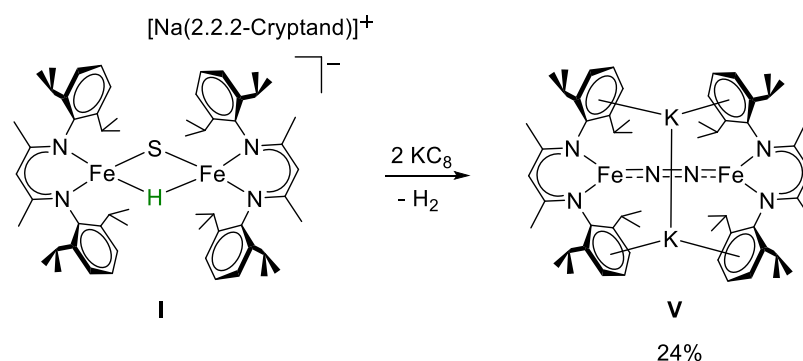
Scheme 15. Reduction of complex **I** that leads to release of H_2 and formation of the diiron(0)-N_2 complex **V** in low yields.[103]

Further studies conducted by the HOLLAND group focused on designing mono- and dinuclear iron compounds that feature only one or two key properties of the nitrogenase hydride intermediate. Weak field ligands and a coordination number lower than five were reached by using extremely bulky β-diketiminate ligands (Figure 9).[107,108] Additional details regarding the advantages of β-diketiminate ligands for the synthesis of coordination chemistry compounds will be given in the following section. The use of these ligands was fundamental in order to isolate the first examples of iron-hydrides with a coordination number less than five.[98,109]
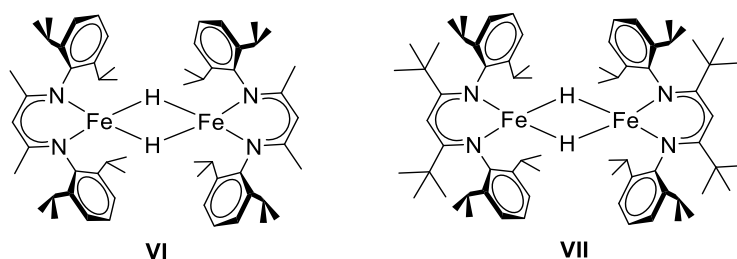
Figure 9. Bulky β-diketiminate low coordinated iron hydride complexes. Both compounds have a tetrahedral geometry at each iron ion.[109]

Another important aspect regarding nitrogenase is certainly represented by the description of how the N_2 molecule binds to the active site where it can be reduced and activated. These processes are now well conclusively proved with iron model complexes, and recent highlights in this regard include the cleavage of N_2 to two nitrides[110,111] and additional mononuclear systems that can catalytically convert N_2 to ammonia.[112,113] In these last cases,

it was also observed that phosphine ligands are suitable scaffolds for the functionalization of N_2 on iron centers[114,115,116] so that potential reduction intermediates like Fe-N_xH_y could be studied.[116,117,118,119,120,121]

Ammonia was produced by a metal complex with tripodal trisphosphine ligands with axial donors such as Si, C or B and the yield increased in the order of Si < C < B.[119] Studies that used the B-based ligand allowed for the characterization of an Fe≡N-NH$_2$ intermediate, which models the distal pathway for N_2 reduction.[117] On the other hand, Si-supported ligands gave rise to a reduction pathway that involves Fe=N-NH$_2$ and Fe-NH$_2$NH$_2$ compounds.[118]

Already more than 25 years ago, multidentate thioether/thiolate ligands were used to isolate and characterize hydrazine, diazene and ammonia complexes.[122,123] The hydrazine moiety with this ligand scaffold coordinated to two iron centers and displayed a *trans* coordination mode. The system was further stabilized by the presence of a hydrogen bonding interaction with the S-ligand, resembling the active site of FeMoco. Unfortunately, it was not possible to isolate any dinitrogen complex with this system, as systems with S donors were not observed to bind N_2. Moreover, N_2 reduction catalyzed by these compounds was never observed, although some were capable of catalytically reducing hydrazine.[124,125]

It is worth mentioning that sulfide iron complexes that are able to bind relevant N_xH_y substrates for nitrogenase are still quite rare, especially in comparison with the corresponding thiolato complexes. In a notable contribution, a coordinatively unsaturated diiron sulfide complex was used to bind hydrazine in a μ-η^1:η^1 fashion, as shown in Figure 10.[126,127] However, the compound undergoes decomposition at room temperature and a full characterization or reactivity studies were not possible.
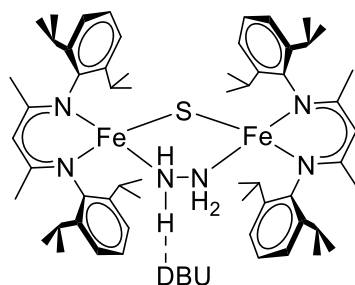
Figure 10. Iron-N_2H_4 in a sulfur environment.[127]

When a substituted hydrazine was used, greater stability was observed.[127] A mixed-valence system was also studied with ENDOR spectroscopy in order to compare the hyperfine

parameters with those of a nitrogenase intermediate. Although the system represents an interesting scaffold, binding of dinitrogen was not observed without loss of sulfide.

It is clear that more model complexes that are able to stabilize Fe-N_xH_y intermediates would be beneficial to enhance the knowledge in the coordination chemistry of these compounds. The second part of this work will focus on the isolation of new iron supported intermediates relevant for the nitrogen fixation process.

1.5 β-diketiminate Ligand Scaffolds

1.5.1 General Properties

In recent times, the β-diketiminate class of ligands gained popularity, in view of their ability to strongly bind metals and generate rare coordination environments, and to facilitate the use of reactive organometallic reagents or catalysts.[128,129] These monoanionic bidentate ligands are generally known as "nacnac", or [{ArNC(R)}₂CH] (where Ar = aryl and R = methyl or another bulkier group) (Figure 11), and differ from the analogous skeleton of the acac (acetylacetonate) group by the presence of nitrogen donor atoms instead of oxygen donor atom.

Comparing the two classes of ligands, the β-diketiminate group offers additional steric protection at the metal center, and the steric and electronic parameters can easily be tuned by changing the nature of the substituents.[130] Therefore, it is of no surprise that the nacnac scaffolds are able to form metal complexes with most elements of the periodic table, ranging from the main groups,[131] to transition metals,[132,133,134] lanthanides[135] or actinides.[136]
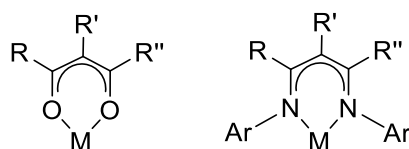
Figure 11. Schematic diagram of an acac (left) and a nacnac ligand (right).

The first reported complexes bearing a β-diketiminate scaffold were synthetized at the end of the 1960s,[137] where it was shown that tuning the steric properties of the R moieties on the nitrogen group led to a modification of the Ni^{II} ion's geometry from square-planar to tetrahedral. It was also shown that in general, the employment of small N-substituents such as H, Me or SiMe₃ allowed higher coordination numbers at the metal centers, whereas complexes with bulkier N-substituents usually prefer low coordination numbers.

More recently, the versatility of such ligand scaffolds was exploited to obtain striking results in the field of small molecule activation. For instance, Scheme 16 shows an example of dinitrogen reduction by a molecular iron-potassium complex reported by HOLLAND group.[110] In this work, the structural characteristics of an iron-based N_2-cleaving system were demonstrated, suggesting cooperation between the iron centers to obtain N-N cleavage (Scheme 16, C). Formation of ammonia from the resulting iron nitride complex **VI** was also possible through reaction with dihydrogen.

Interestingly, previous studies performed by the same group indicated that dinitrogen activation could be obtained with analogous systems that differed by their steric hindrance, and the N-N bond strength upon binding could be tuned accordingly.[138,139]
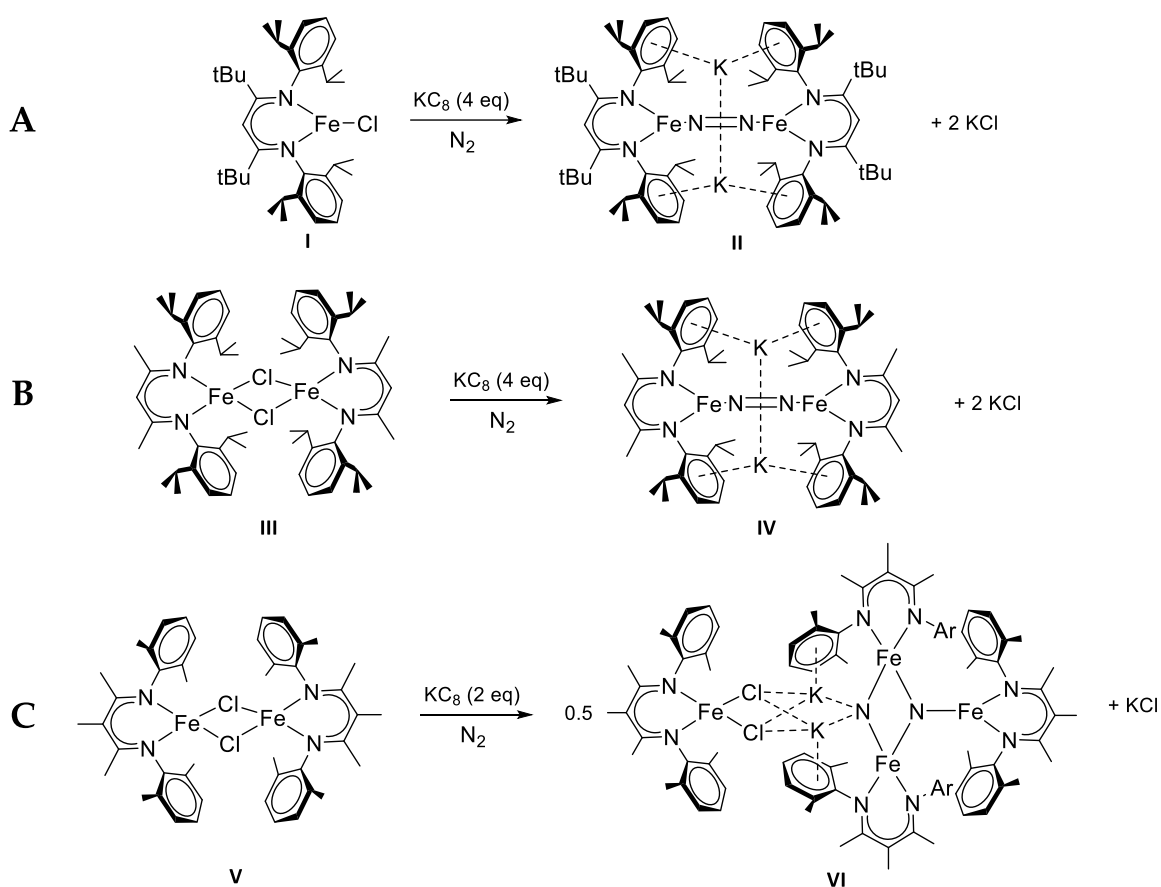
Scheme 16. Iron nacnac metal complexes with various steric bulk give different products upon reduction.

In fact, the N-N bond length was found to be 1.23 Å when N_2 activation was achieved with a mononuclear iron nacnac system bearing two bulky tert-butyl groups **II** (Scheme 15, A), and similar bond weakening was observed in analogous dimers containing the less hindering methyl groups in the nacnac backbone **IV** (Scheme 15, B).

In order to achieve metal-metal cooperation and to provide more sophisticated scaffolds for selective reactivity pathways, several approaches were used in the past to connect at least two β-diketiminate units, yielding the corresponding bis(β-diketiminato) ligand system (Figure 12). Different rare earth metal complexes based on these linked nacnac ligands were prepared, and subsequent structural characterization of the complexes revealed that the geometry and the coordination mode of the ancillary ligand were profoundly influenced by the linker.[140]

Furthermore, bis(β-diketiminato) complexes containing chiral linkers were successfully used for controlling the stereoselectivity in further reactions. For instance, diisopropylphenyl side-arm groups could be employed to obtain multinuclear Mg, Ca and Zn complexes, which were able to catalyze CO_2 copolymerization and other substrates.[141]
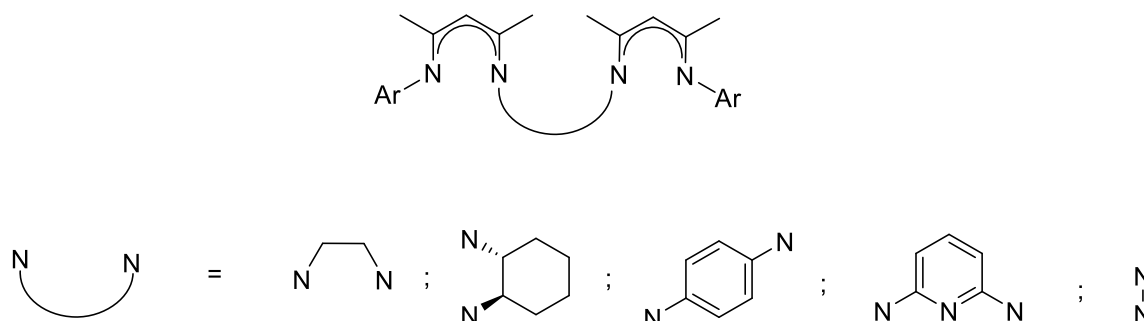
Figure 12. Some examples of bis(nacnac) ligand systems with different linker units.

In the context of this thesis work, particular interest is given to the ligand that bears a pyridine linker.[142] Reactivity studies were conducted with this ligand by LIMBERG and co-workers to establish new nickel and iron complexes.[143,144] Notably, it was possible to obtain mixed valent Ni^I-Ni^{II} complexes that featured a hydride in the bridging position (Scheme 17), relevant for potential hydrogen storage.[143]
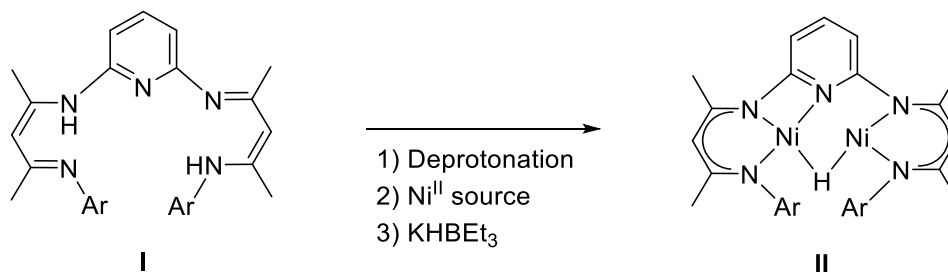
Scheme 17. Formation of a Ni^I-Ni^{II} complex with bridging hydride using a bis(nacnac) scaffold.[143]

1.5.2 Introduction to a Pyrazolate-Bridged Bis(β-diketiminate) Ligand System

As presented in the previous section, β-diketiminate compounds represented a breakthrough in coordination chemistry, since they are highly capable of stabililizing reactive intermediates and are suitable for most of the elements in the periodic table.
Therefore, it is of no surprise that huge progress was achieved with these compounds in hand, especially in the field of small molecule activation. Compounds [FeCl(^{t}Bu-nacnac)] **I** and [FeCl(Me-nacnac)]$_2$ **III** (Scheme 16, A-B) clearly show the advantages of using these systems. The possibility of tuning both steric and electronic properties of such complexes enabled for unprecedented reactivity with respect to small molecule activation and the opportunity to study unique bonding situations and structures. Thus, the combination of two (or even more) nacnac units through a suitable linker can potentially expand the chemistry of these compounds, but in comparison with the monodentate analogues, it remains still less explored.

Previous work by MANZ[145] established the synthesis of a new ligand system **H₃L** similar to the one used by LIMBERG, where two DIPP-substituted β-diketiminate moieties were linked by a pyrazolate bridging unit to yield a trianionic, hexadentate scaffold **L³⁻** with two binding pockets in close proximity (Figure 13).[146]

Compared to LIMBERG's system where a pyridine acts as linker, the usage of a pyrazole provides the advantage of an additional N-donor function and an additional negative charge, which results in a stronger chelating effect, promoting the formation of new stable highly preorganized bimetallic systems.[147,148]

H₃L
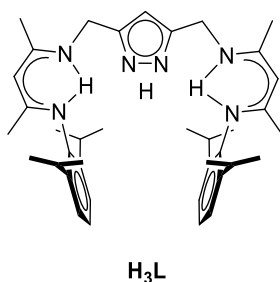
Figure 13. Bis(nacnac) system developed by MANZ and employed during this thesis work.

Deprotonation of **H₃L** and subsequent addition of NiBr₂(DME) led to the isolation of the first dinickel complex **1** of this type (Scheme 18). Subsequent treatment of **1** with KHBEt₃ followed by workup allowed for the synthesis of the corresponding dinickel dihydride compound **2**. Interestingly, two terminal Ni-H units were found in close proximity within the bimetallic pocket, in contrast to the system developed by LIMBERG where only one μ-H

was found.[143] In the case of complex **2**, the presence of a bridging hydride was prevented by a large metal-metal separation imposed by the pyrazolate bridge in the ligand system.
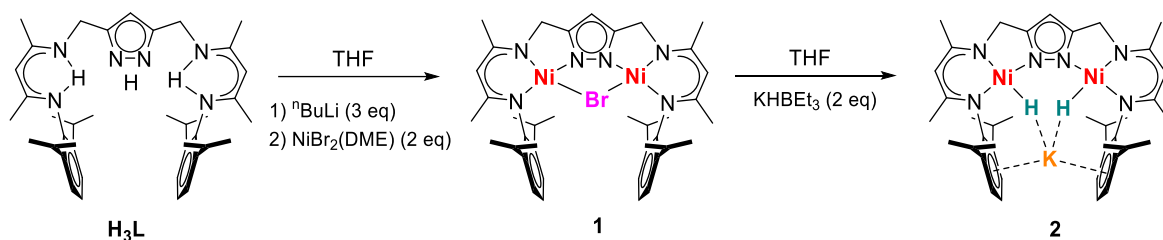
Scheme 18. Stepwise synthesis of the dinickel dihydride system **2** featuring two nacnac units spanned by a pyrazolate bridge.

Complex **2** and its main properties could be intensely studied by MANZ and DUAN by an interplay of different spectroscopic techniques which revealed its tendency to eliminate H_2 and reductively activate substrates by two electrons whilst gaining on metal-metal cooperativity.[146,146]

By means of ^{1}H-NMR experiments it was possible to establish that the H_2 elimination occurs in a concerted way, as shown in Scheme 19. In fact, addition of D_2 at atmospheric pressure to a degassed solution of **2** in THF-d_8 rapidly led to the formation of the deuterated analogue $K[LNi_2(D)_2]$ (**2-D**). Subsequent removal of D_2 and addition of H_2 to the solution reversed the situation, leading to the formation of **2**. This particular process could be followed by ^{2}H-NMR spectroscopy, as represented in Figure 14, which showed the formation of D_2 (signal at 4.57 ppm) and concomitant disappearance of the signal of Ni-D at -24.0 ppm. HD formation was not observed for long times, suggesting that the H_2/D_2 exchange synchronously involves both Ni-H moieties in complex **2**.
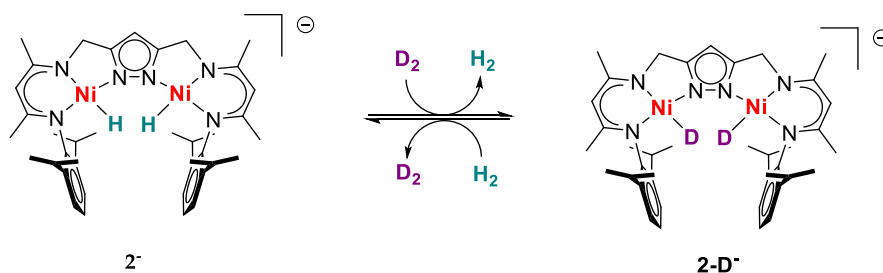
Scheme 19. Pairwise H_2/D_2 exchange observed in complex **2**.

Furthermore, density functional theory (DFT) calculations showed that the energy barrier for the elimination of H_2 is rather low, suggesting that the complex could easily form H_2 within the cleft and formally leave two reducing equivalents on the LNi_2 core for substrate

binding, unmasking the real Ni^I character of the molecule. Therefore, complex **2** can be potentially used as storage scaffold for electrons, and subsequent reductive substrate binding reminiscent of the nitrogenase system that was described in the previous sections. Additionally, what makes **2** such an interesting compound is its advantage of avoiding the isolation of highly reduced intermediates like a dinickel(I) species, that is obviously highly reactive and in turn more difficult to handle.
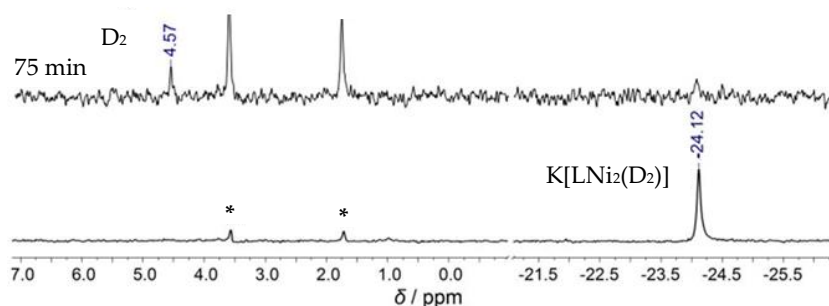
Figure 14. ^{2}H-NMR experiments that shows exclusive formation of D_2 (top spectrum) upon treatment of **2-D** with H_2 (bottom spectrum).[146]

Prior to this thesis work, reactivity studies regarding the mechanism of activation of different substrates were already initiated.[145,146] Additionally, DUAN studied the reactivity of complex **2** towards dioxygen. When one equivalent of O_2 was used, a μ-1,2-peroxo dinickel intermediate **VII** was obtained, whereas excess O_2 led to the isolation of a μ-1,2-superoxo species **VIII**. These compounds could be structurally characterized and chemically and electrochemically interconverted into each other at a very low potential ($E_{1/2}$ = −1.22 V *vs.* Fc$^+$/Fc), as depicted in Scheme 20.[149]
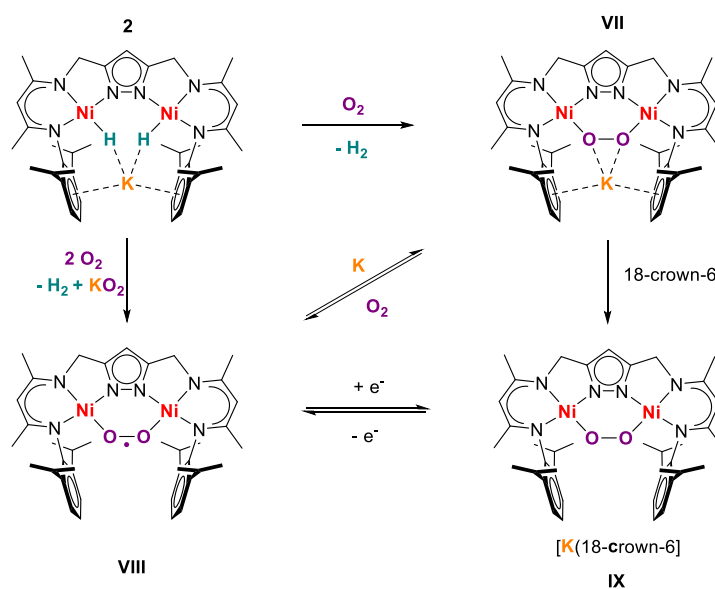
Scheme 20. Interconversion of O_2 on complex **2**.

2 Thesis Outline

β-diketiminate scaffold are becoming more and more important, as they are often involved in a variety of applications, ranging from catalysis to the synthesis of new model complexes for small molecule activation. Nowadays, a moderate number of new bis(β-diketiminate) systems have been synthetized, even though their chemistry still remains little developed.

This work is based on the recent achievements in the synthesis of a new bis(β-diketiminate) ligand scaffold **H₃L** and the first examples of a new family of binuclear nickel complexes of that ligand.[145,146] The main objective of this thesis deals with the synthesis and characterization of novel nickel and iron complexes of **H₃L**, which are relevant for understanding the transformation of important small molecules.
In particular, the aim of this work can be mainly divided in two parts. On the one hand, the bimetallic nickel(II) dihydride complex **2** is further employed for the reductive binding and transformations of nitric oxide (Chapter 3-5). The focus hereby is set on understanding the cooperative effects of the two nickel centers for the stabilization of new intermediates. On the other hand, the bis(nacnac) ligand system **H₃L** developed by MANZ is employed to obtain new diiron complexes (Chapter 6-7). Scheme 21 summarizes the different goals which are part of this thesis work.

In the first part of this thesis, the reactivity of complex **2** towards nitric oxide is planned to be studied. The fascinating features of **2** are exploited in Chapter 3 in order to reductively bind gaseous nitric oxide and to gain insights into the mechanism of this reaction. The isolation of a reaction intermediate, namely a hyponitrite complex, is described, along with its reactivity studies inspired by the nitric oxide reductase enzyme.

Furthermore, new strategies are employed to obtain a novel nitroxyl compound and will be described in Chapter 4. The redox properties of the new obtained complexes are investigated to allow for a better understanding of the reactivity pathways.
Chapter 5 describes the reactivity between **2** and nitrosobenzene. Such motivation comes from the general interest in using nitrosoarenes as stable analogues of nitroxyl (HNO), a redox active nitric oxide derivative of biological importance.

Inspired by the chemistry of mononuclear iron β-diketiminate complexes mentioned in Chapter 1, and their relevance as model systems for the biological dinitrogen fixation, the synthesis of new binuclear iron complexes of **H₃L** is explored in the second part of this

thesis work. The results are mainly described in Chapter 6. With a diiron(II) complex in hand, the possibility of isolating new diiron dihydride systems is planned to be studied by following the route suggested by MANZ for the nickel analogous complex.

Finally, the reactivity of the new diiron complex towards hydrazine is investigated in Chapter 7 to synthetize new model complexes for intermediates of the dinitrogen fixation. The characterization of the obtained product is pursued in order to confirm analogies and discover differences with the literature reported mononuclear iron compounds.
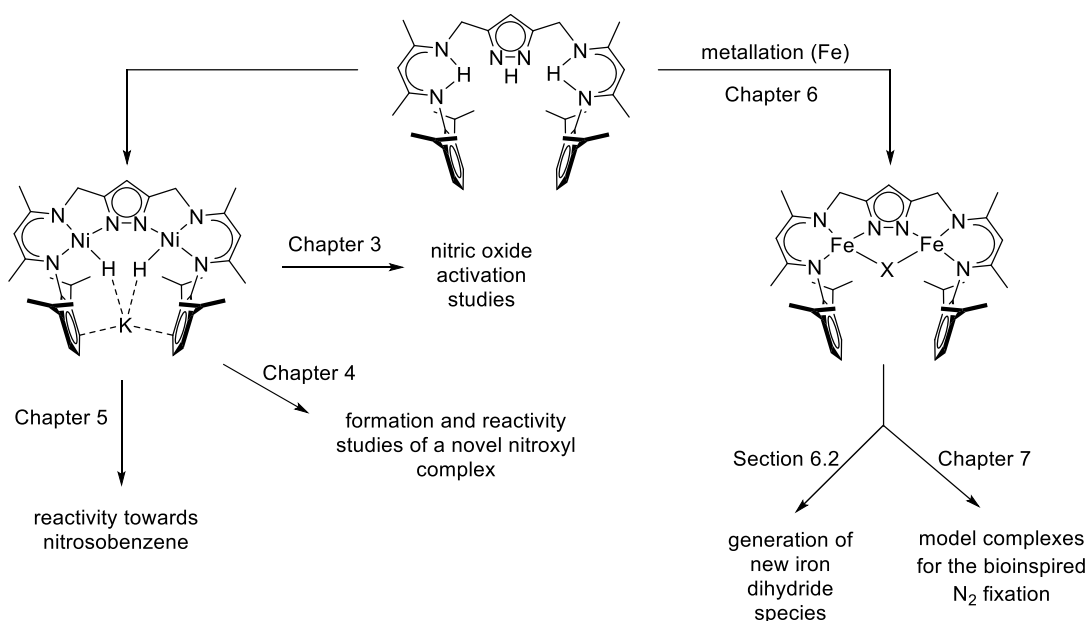
Scheme 21. General topics studied within this thesis work and related chapters.

3 Reactivity of a Dinuclear Nickel(II) Dihydride Complex Towards Nitric Oxide

3.1 Motivation

As described in Chapter 1, the interest in the coordination chemistry of nitric oxide (NO) increased over the last few decades. Certainly, one of the main reason is given by its environmental and biological importance, as crucial enzymes (e.g. flavodiiron proteins) carry out the two-electron reduction of NO to the less toxic nitrous oxide (N_2O). This process was intensively studied by spectroscopic techniques to gain insight into the reaction mechanism. However, synthesis of complexes that are able to bind and activate NO are fundamental for comparison. Previously reported diiron-dinitrosyl model systems showed the ability to produce N_2O under reductive conditions or exposure by light, as described by LEHNERT[150,151,152] and LIPPARD/MOËNNE-LOCCOZ.[153]

The reactivity of gaseous nitric oxide with mononuclear and dinuclear iron complexes was also studied in the MEYER group. A unique {Fe(NO)}[7] species (Figure 15, A) stabilized by a tetracarbene macrocycle was isolated and reversibly converted to its reduced/oxidized analogues so that the first complete series of {Fe(NO)}[6/7/8] was reported. However, initial reactivity experiments of the {Fe(NO)}[6] towards acids did not lead to formation of N_2O.[154] Further diiron complexes that showed reactivity towards NO were isolated. When a [{Fe(NO)}[7]]$_2$ dimer (Figure 15, B) was chemically reduced, the transfer of only one electron triggered subsequent ligand scrambling reactions, and a mixture of {Fe(NO)$_2$}[9] and $Fe^{II}Fe^{II}$ species in a 1 : 1 ratio were obtained, in contrast to the expected two-electron reduction and release of N_2O.[155] Finally, SCHOBER described the synthesis and structural characterization of an additional dinuclear iron nitrosyl compound, which was able to produce N_2O upon reduction (Figure 15, C).[156]
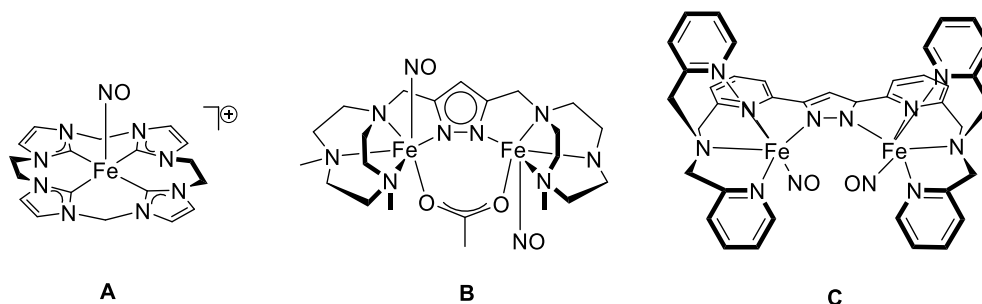
Figure 15. Mononuclear and dinuclear iron nitrosyl complexes developed in MEYER group.

Motivated by the interest in the activation, binding and coordination chemistry of NO, as well as the determination of reaction intermediates in FNORs-type reactions, the reactivity of the dinuclear nickel(II) dihydride compound **2** was studied by treating the complex with different amounts of gaseous NO. This strategy was adopted in order to find the optimal conditions for the synthesis of new bimetallic nickel nitrosyl compounds. As mentioned in Section 1.5.2, complex **2** represents a masked dinickel(I) synthon providing two reducing equivalents, so that a certain degree of NO activation should be expected. However, particular care in the purification of the gas was crucial for the successful binding of the investigated molecule, as NO often contains NO_x impurities that derive from several reactions (Scheme 22). In fact, the disproportionation of NO leads to N_2O and NO_2 and the equilibrium is shifted towards these products at high pressure. Therefore, commercial NO (high pressure bottles) commonly contains N_2O and N_2O_3 impurities (Scheme 22, Eq. 1-2). Moreover, NO easily reacts with dioxygen to form NO_2 (Eq. 3) or NO_2^- (Eq. 4) in water.[157]

$$3NO \rightleftharpoons N_2O + NO_2 \qquad \textbf{(1)}$$

$$NO + NO_2 \rightleftharpoons N_2O_3 \qquad \textbf{(2)}$$

$$2NO + O_2 \rightleftharpoons 2NO_2 \qquad \textbf{(3)}$$

$$2NO + O_2 + H_2O \rightleftharpoons 4NO_2^- + 4H^+ \qquad \textbf{(4)}$$
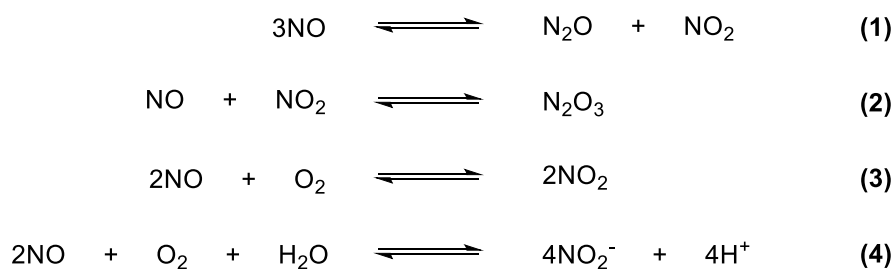
Scheme 22. Formation of NO_x impurities from commercial nitric oxide.

Although the mechanism for the formation of these species still needs to be completely understood, it is clear that the N_xO_y species that originate are in turn powerful oxidants and/or nitrosylating agents.

In particular, the presence of N_2O needed to be strictly avoided for the NO reactivity studies on complex **2**. Further details in this regard will be given in Section 3.3. A general method for the purification of NO is described in the Experimental part, whilst the scheme for the experimental set up is shown in the Appendix (Section 10.2, Figure 16).

3.2 Isolation of a *cis*-Hyponitrite Intermediate

When the dinickel dihydride(II) complex **2** was treated with exactly two equivalents of pure nitric oxide at room temperature (Scheme 23), the color of the solution changed from orange to deep red within a few minutes, accompanied by evolution of H_2 (detected by headspace GC-MS analysis).
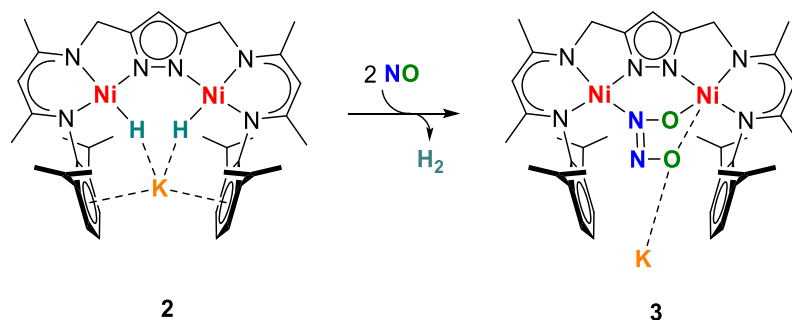
Scheme 23. Preparation of complex $KLNi_2(N_2O_2)$ from the dihydride precursor **2**.

This indicated the formation of the species $KLNi_2(N_2O_2)$ **3**, which was initially analyzed by ESI mass spectrometry (Figure 16). The spectrum essentially shows just one signal, with a mass to charge ratio and isotopic distribution pattern consistent with that calculated for complex $[LNi_2(NO)_2]^-$ (m/z = 781.4), suggesting that two NO molecules were incorporated upon reaction and the integrity of the core was maintained in solution. However, this observation could not provide any information about the binding mode of the NO moiety.
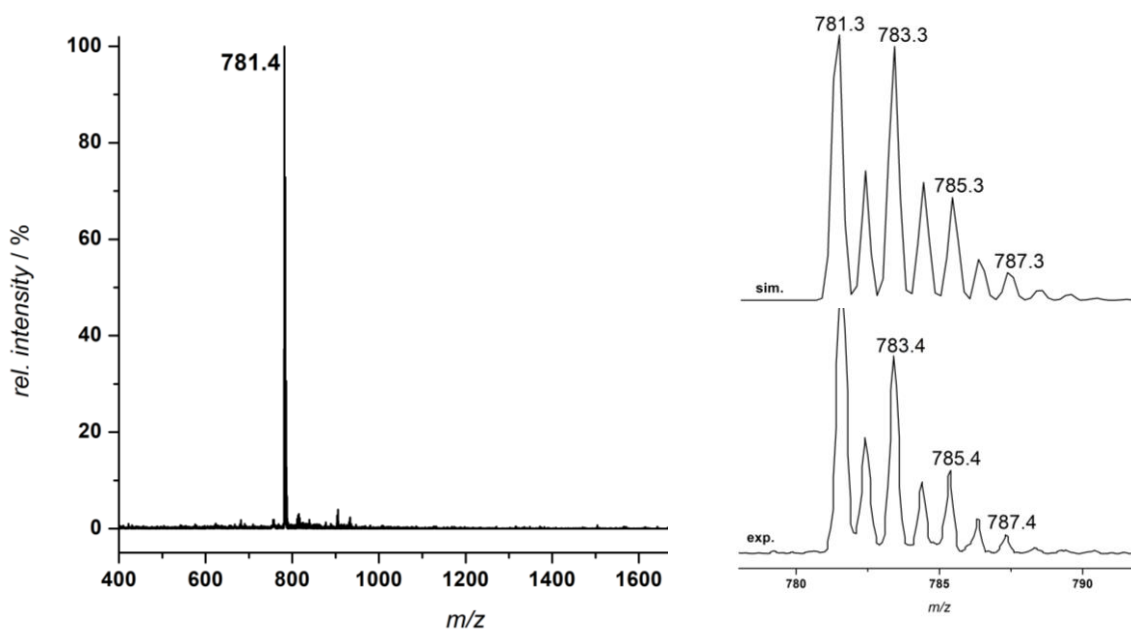
Figure 16. Negative mode ESI mass spectrum of complex **3** in THF/MeOH. The insets show experimental and simulated isotopic distribution for $[LNi_2(NO)_2]^-$.

Definitive elucidation was provided by X-ray diffraction analysis. Single crystals were obtained by storing a concentrated solution of **3** in diethyl ether/pentane at -30°C for two days. The result of the structural identification of complex **3** is shown in Figure 17, selected bond lengths and angles are reported in Table 1.
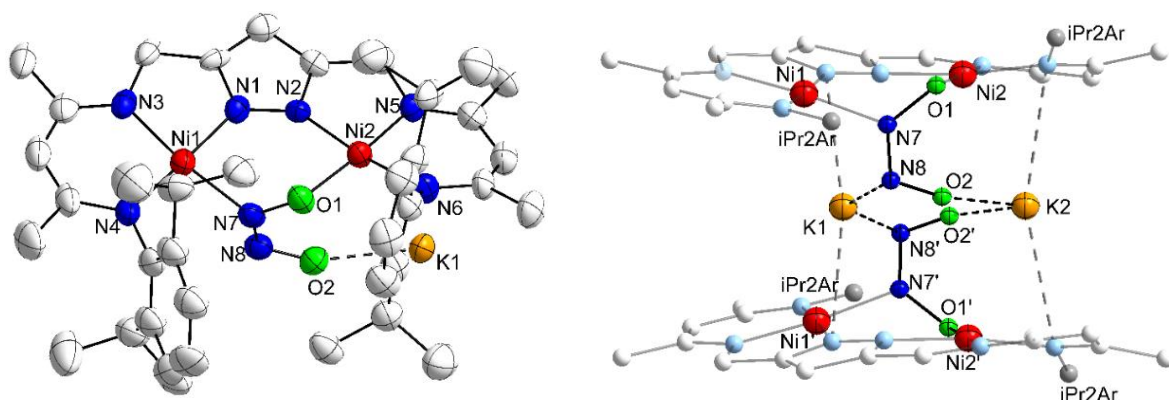
Figure 17. Molecular structure of complex **3** (left), and dimeric arrangement of the hyponitrite complex stabilized by interaction with potassium cations (right). Hydrogen atoms and solvent molecules are omitted for clarity. In the representation of **3** on the right also the N-bound aryl groups are omitted.

Table 1. Selected bond lengths and angles in complex **3**.

Bond length / Å		Angle / °	
Ni(1)-N(7)	1.908(5)	N(1-Ni(1)-N(4)	75.5(2)
Ni(1)-N(1)	1.859(5)	N(3)-Ni(1)-N(7)	164.8(2)
Ni(1)-N(3)	1.891(5)	N(1)-Ni(1)-N(3)	83.4(2)
Ni(1)-N(4)	1.877(5)	N(4)-Ni(1)-N(3)	95.9(2)
Ni(2)-N(2)	1.871(5)	N(1)-Ni(1)-N(7)	84.4(2)
Ni(2)-O(1)	1.884(4)	N(5)-Ni(2)-O(1)	174.4(2)
Ni(2)-N(5)	1.881(5)	N(2)-Ni(2)-N(6)	172.5(2)
Ni(2)-N(6)	1.900(5)	N(2)-Ni(2)-N(5)	83.8(2)
N(7)-O(1)	1.349(6)	O(1)-Ni(2)-N(2)	90.9(2)
N(7)-N(8)	1.290(7)	N(5)-Ni(2)-N(6)	93.2(2)
Ni(2)···O(2)	2.7994(5)	O(1)-N(7)-N(8)	120.0(5)
Ni(1)···Ni(2)	3.8753(10)	N(7)-N(8)-O(1)	117.9(5)

3 crystallizes in the monoclinic space group $C/2_c$, and is a dimeric structure in the solid state. Both nickel centers are coordinated in a slightly distorted square planar geometry with a Ni···Ni distance of 3.8753(10) Å. The N_2O_2 moiety that is bridging between the two metal centers via a *cis*-"end on" configuration is a four-electron hyponitrite ligand $[N_2O_2]^{2-}$. Only one of the two NO groups participates in the binding and consequently, both nickel ions are found in square-planar environment and are considered in the formal oxidation state +2. The hyponitrite group shows a O(1)-N(7) and O(2)-N(8) distance of 1.3497(7) Å and 1.3026(6) Å, respectively, and the N(7)-N(8) bond length of 1.289(10) Å is consistent with a double bond. These distances compare well with other *cis*-hyponitrite salts, e.g. $Na_2N_2O_2 \cdot 5H_2O$.[158] Complex **3** represents a rare example of a structurally characterized

dinuclear nickel *cis*-hyponitrite compound and, to the best of our knowledge, the first type-B hyponitrite complex (Chapter 1, Scheme 10) that originates from the reductive N-N coupling of two NO molecules on a bimetallic scaffold. Other similar complexes are the tetranuclear[159] [{(NO)$_2$Co(μ-ONO)Co(NO)$_2$}$_2$(μ-ONNO)] that resembles in part the bonding environment in **3** with O-N-N-O bond lengths of 1.316 Å, 1.265 Å and 1.316 Å and the ruthenium complex[160] [Ru$_2$(CO)$_4$(μ-H)(μ-PBu$^t_2$)(μ-dppm)(μ-η^2-ONNO)] with 1.356 Å, 1.264 Å and 1.317 Å. The type-B coordination seems to be stabilized by the interaction of the terminal N(8)-O(2) unit with potassium cations [d(O(2)···K(2)) = 2.563(4) Å]. In fact, the dimeric aggregate found in the solid state is formed by two [LNi$_2$(N$_2$O$_2$)]$^-$ monomers that are linked via K$^+$ (Figure 17, right). As a result, the hyponitrite bridging unit is almost perpendicularly oriented to the dinickel scaffold, as suggested by the angle between the Ni(1)-N(1)-N(2)-Ni(2) and the O(1)-N(7)-N(8)-O(2) planes of 84.5(1)°.

Isolated solid red material of complex **3** was also characterized by IR spectroscopy (Figure 18), which revealed the presence of a distinct peak at 1138 cm^{-1} that was assigned to the N-O vibration.
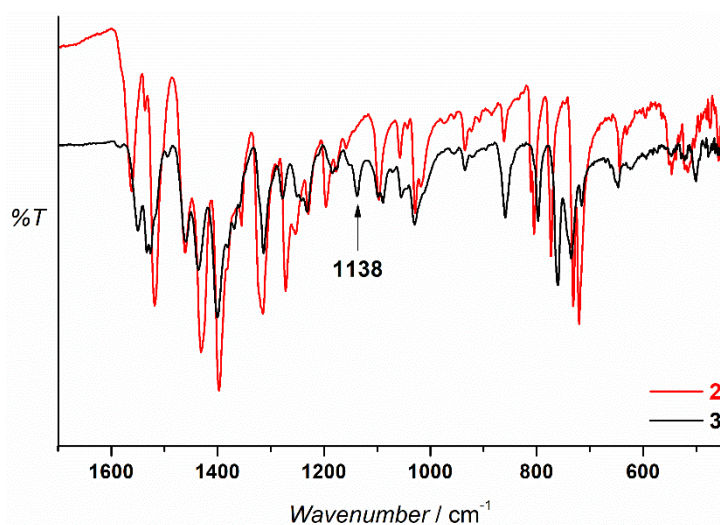
Figure 18. IR-ATR spectrum of solid material of the hyponitrite complex KLNi$_2$(N$_2$O$_2$) **3** (black line). The NO stretching vibration is observed at 1138 cm^{-1}, as it is not present in the spectrum of the starting material **2** (red line).

Furthermore, the data compare well with the reported *trans*-Na$_2$N$_2$O$_2$ ($\tilde{v}$(NO) = 1143 cm^{-1}).[161] To assign undoubtedly the stretching vibration, the synthesis of the corresponding labeled ^{15}NO analogue **3-^{15}NO** was attempted. Gaseous ^{15}NO was produced in situ by treating an aqueous solution of labeled Na^{15}NO$_2$ with ascorbic acid. However, it was not possible to obtain the desired compound, as only copious amount of the corresponding stable dinickel

hydroxo-bridged complex $LNi_2(OH)$ **4** were isolated.[146] This compound is known to form easily when traces of water are present in the reaction environment, or as decomposition product. Despite all efforts in order to keep a rigorous anhydrous, oxygen-free reaction environment and to purify the reaction precursors (e.g. double distillation of the ^{15}NO gas produced in situ), the synthesis of **3**-^{15}NO for IR characterization has not been achieved so far.

Nevertheless, the assignment of the band at 1138 cm^{-1} to a N=N double bond stretching vibration should be excluded. Indeed, it occurs at low frequencies, especially when compared to the fundamental frequency of the N-N bond of the hyponitrite ion (HO-N=N-O$^-$) for sodium, silver and mercury salts of the hyponitrous acid which is found at 1392 cm^{-1}.[162] A similar value for the N=N vibration was found at 1332 cm^{-1} for a hyponitrite complex in a nitric oxide reductase isolated from *P. denitrificans* cells.[163] These values are surprisingly low for a N=N stretching since the same vibration mode was found at 1576 cm^{-1} in azomethane,[164] but it could be explained by the presence of a resonance effect.

3.2.1 Structural Rearrangement in Solution

The diamagnetic nature of the hyponitrite compound **3** was also confirmed by variable temperature magnetic susceptibility experiments of a solid sample (Appendix, Figure 1), and by ^1H-NMR spectroscopy in solution. Interestingly, the ^1H-NMR of **3** dissolved in THF-d^8 and recorded at room temperature shows an unexpected situation (Figure 19). Indeed, the number of observed resonances is lower than the one expected by the analysis of the structure in the solid state. This apparent C_{2v} symmetry of the $[LNi_2(N_2O_2)]^-$ core implicates either a more symmetric structure of **3** in solution, or a fast fluxional process on the NMR time scale that involves the $[N_2O_2]^{2-}$ unit.

Therefore, an additional variable temperature ^1H-NMR experiment was performed in the range 298 K – 218 K. According to the results shown in Figure 20 (signals highlighted in orange), a splitting of signals was observed upon cooling. Unfortunately, the general broadness of the resonances at low temperature accompanied by the presence of a second species (mainly the hydroxo-bridged complex **4**) obviated any quantitative analysis. Several issues were encountered during the synthesis and purification of compound **3**. Details in this regard will be discussed in the next Section 3.3.

Nevertheless, the presence of a dynamic process of the hyponitrite moiety at the dinickel core in solution can be evaluated by computational studies, in association to a putative role of **3** in the generation of N_2O, relevant for the reaction pathway proposed for FNORs.[46]

Therefore, a collaboration with the group of Prof. Dr. Max Holthausen at the Goethe University in Frankfurt am Main was started. DFT calculations studies to obtain a possible process for the rearrangement of complex **3** in solution are currently ongoing.
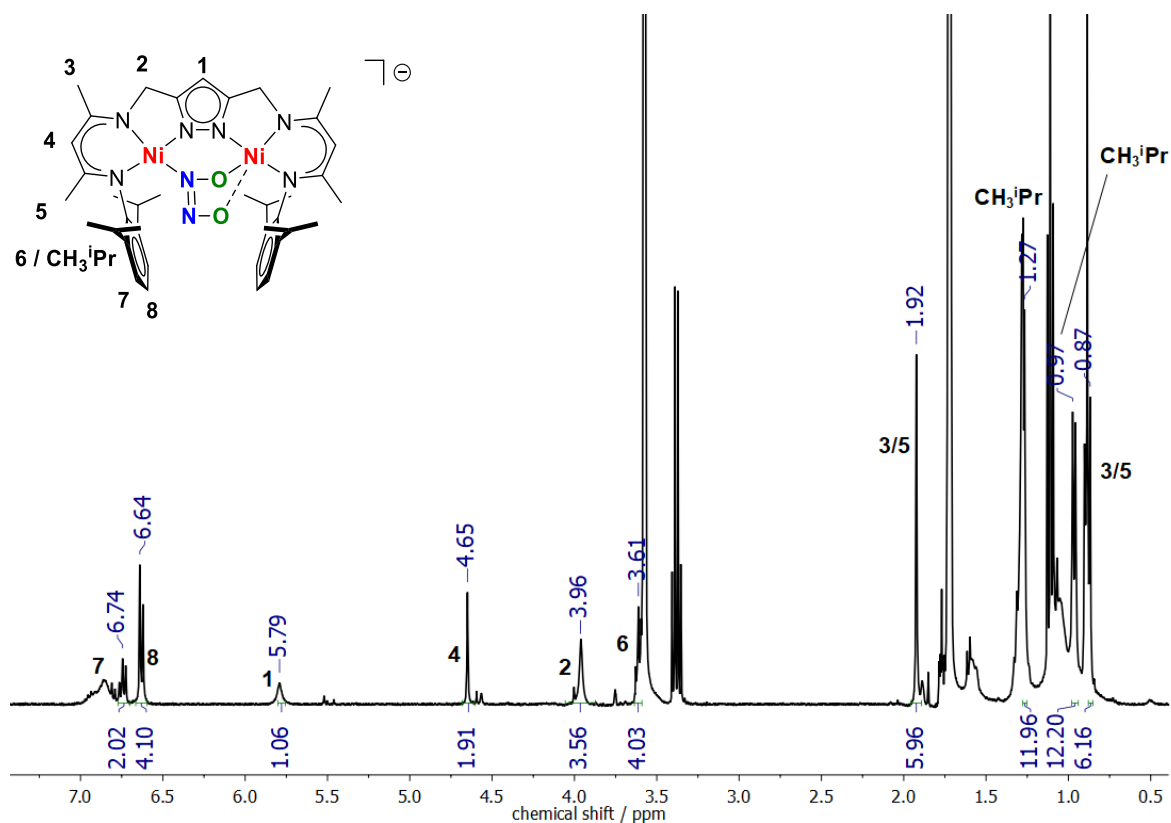
Figure 19. ^{1}H-NMR spectrum of crystalline material of **3** in THF-d$_8$ at room temperature, showing an apparent C$_{2v}$ symmetry.
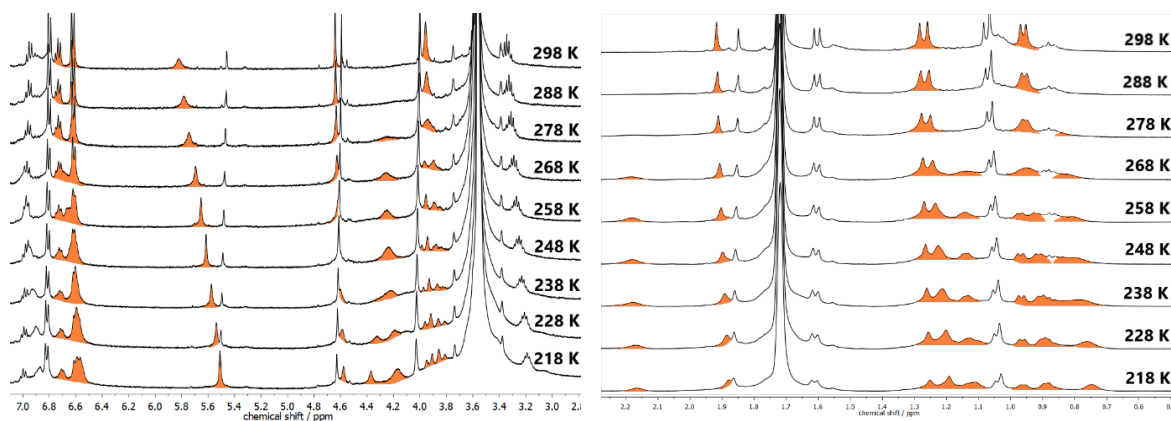
Figure 20. Variable temperature ^{1}H-NMR of compound **3** in THF-d$_8$ at room temperature. Upon cooling, a splitting of the signals of **3** was observed (highlighted in orange). Quantitative analysis was prevented by the presence of the hydroxo-bridged compound **4**, whose signals partially overlap with those corresponding to **3**.

However, a hypothesis can be made at this stage in the absence of theoretical evidences that may better explain the experimental observations. It is reasonable to assume that the hyponitrite moiety (N$_2$O$_2$)$^{2-}$, which binds the two nickel centers in the solid state both with

the nitrogen and the oxygen atoms, rearranges its configuration in solution via a rotation of the group that leads to a symmetric molecule (Scheme 24). The binding of the $(N_2O_2)^{2-}$ can be assumed either through the nitrogen atoms or the oxygen. Hence, these compounds could explain to some extent the ^{1}H-NMR spectrum at room temperature. Furthermore, the presence of the potassium cation K^+ in solution may be the key for the stabilization of the hyponitrite moiety with consequent isolation of the compound.
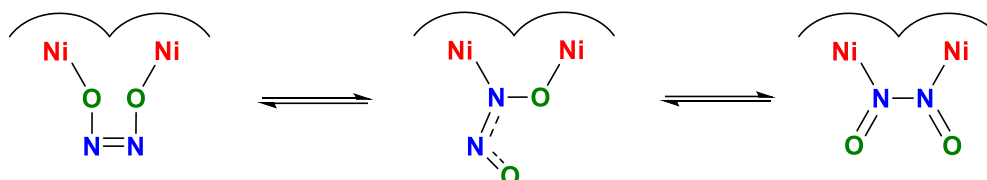
Scheme 24. Proposed rearrangement of the hyponitrite moiety at the dinickel core in solution.

3.3 Decomposition of the Hyponitrite Complex 3

As already mentioned in Section 3.1, the purification of nitric oxide from a commercial source is necessary for the successful synthesis of the hyponitrite complex $KLNi_2(N_2O_2)$ **3**. In fact, NO spontaneously disproportionates and subsequently releases N_2O and nitrogen dioxide (NO_2) when stored at high pressures over time.

In general, it is possible to remove NO_x impurities by taking advantage of their different boiling points and reactivity. Impurities generally have much higher boiling points with respect to NO (-164°C) and can be easily removed by simple distillation of NO from a column where it is condensed with the undesired compounds. On the other hand, removal of N_2O is in general more difficult due to its lower boiling point and its inertness, and it is usually best achieved by passing the NO steam through a column of activated silica at low temperature or through repeated distillations of the gas. Despite all the efforts and progress, the complete purification of the NO reagent along with its anhydrification still remains challenging. The major problem seems to be represented by traces of N_2O that prevented the clean conversion of complex **2** to the hyponitrite **3**.

When an orange solution of the dinickel dihydride complex **2** was treated with anhydrous N_2O, the color rapidly changed to brown-green and a further reaction took place, along with evolution of H_2. The reaction was monitored by ^{1}H-NMR spectroscopy, which displays that the characteristic Ni-H resonance at -24.2 ppm (Figure 21, top) rapidly disappears, and a signal at -7.24 ppm is observed (Figure 21, bottom). This was assigned to the clean formation of the nickel hydroxo-bridged complex **4** (Scheme 25). Probably, N_2O acted as

oxidant transferring its O-atom to the respective nickel centers and forming an highly reactive $LNi_2(O)$ species, most likely through release of N_2. Eventually, the huge affinity of this very basic oxo intermediate towards protons led to exclusive isolation of **4**, even though the source of protons still remains unknown.
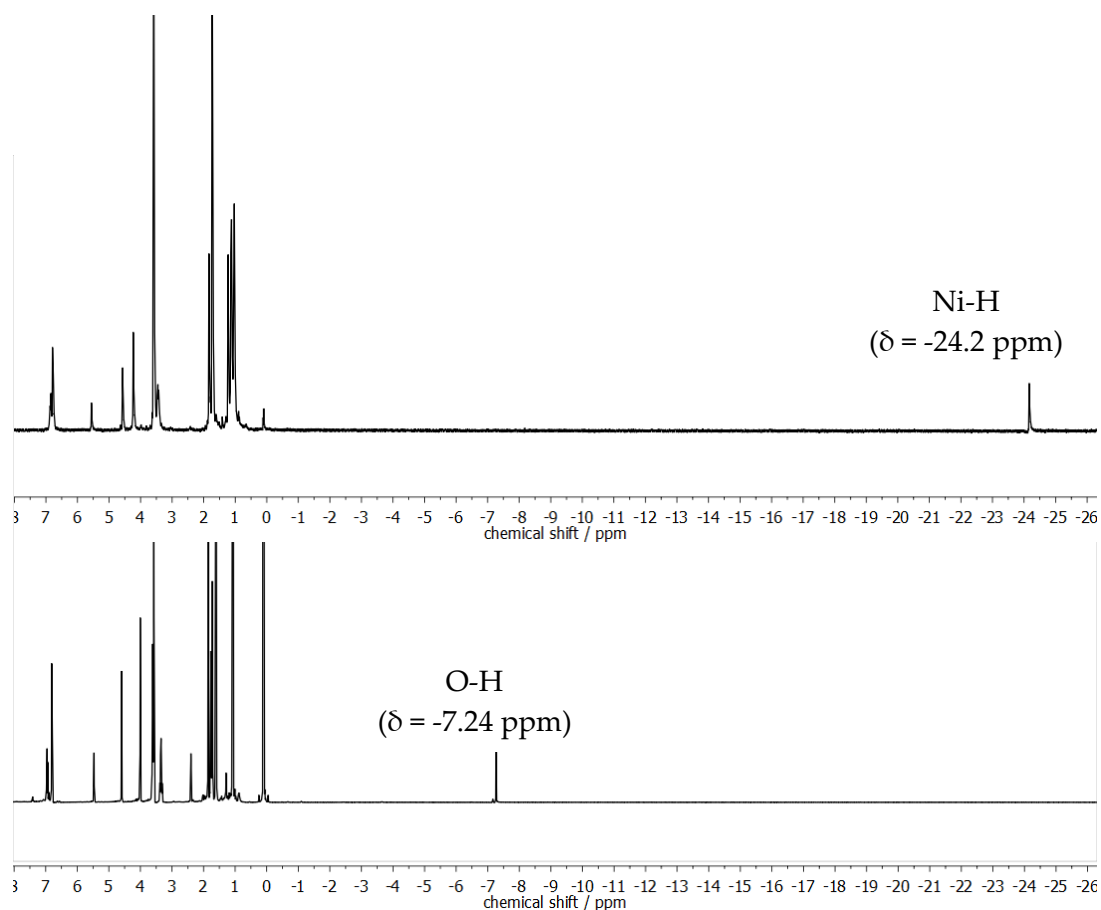
Figure 21. ^{1}H-NMR spectrum of the starting material complex **2** (top) and after treatment with an excess of N_2O (bottom).
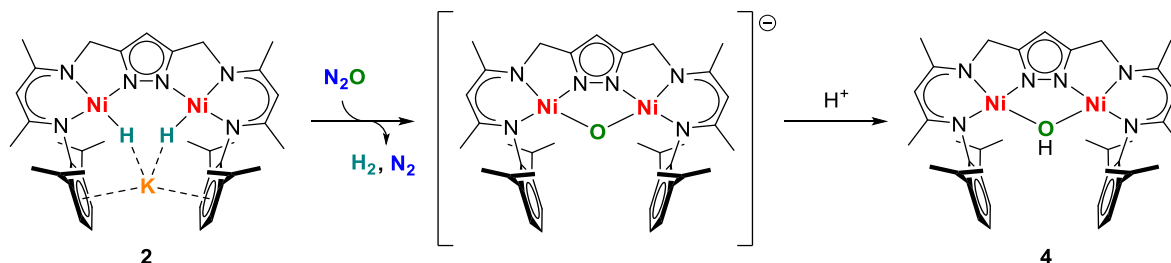
Scheme 25. Clean conversion of the starting material **2** to the nickel hydroxo-bridged complex **4** upon treatment with N_2O at room temperature.

Such reactivity was already observed by DRIESS and coworkers (Scheme 26),[63] where treatment of the (β-diketiminato)nickel(I) complex **A** with pure N_2O led to the isolation of a corresponding (β-diketiminato)hydroxonickel(II) compound **B**, under release of N_2.
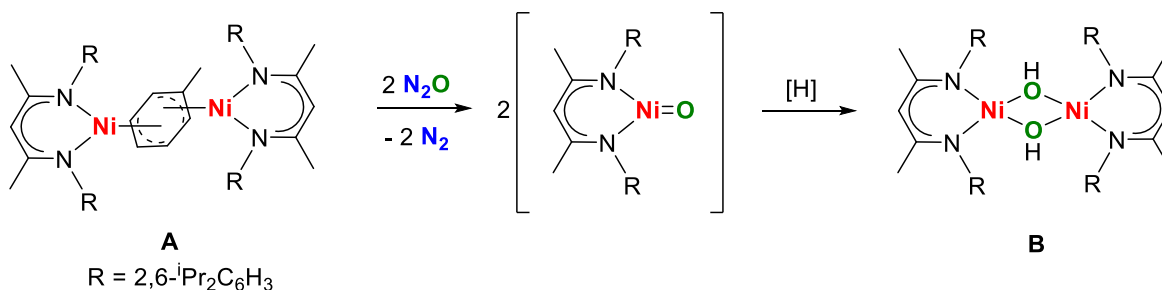
Scheme 26. Isolation of the nickel(II) hydroxo complex **B** after treating the nickel(I) precursor **A** with N_2O by DRIESS and coworkers.[63]

Further problems were encountered when the stability of the hyponitrite complex **3** was assessed. Indeed, the treatment of a solution of **3** in THF with excess NO led to an unidentified mixture of products based on the ^{1}H-NMR spectrum. However, it was possible to assign the major product contained in the reaction mixture to the well-known hydroxo complex **4**. Interestingly, the gas phase of the reaction vessel containing complex **3** and excess NO was analyzed after the reaction was complete, and presence of gaseous N_2O was confirmed by its characteristic band centered at 2224 cm^{-1}, while the excess of NO appeared at 1876 cm^{-1} (Figure 22).
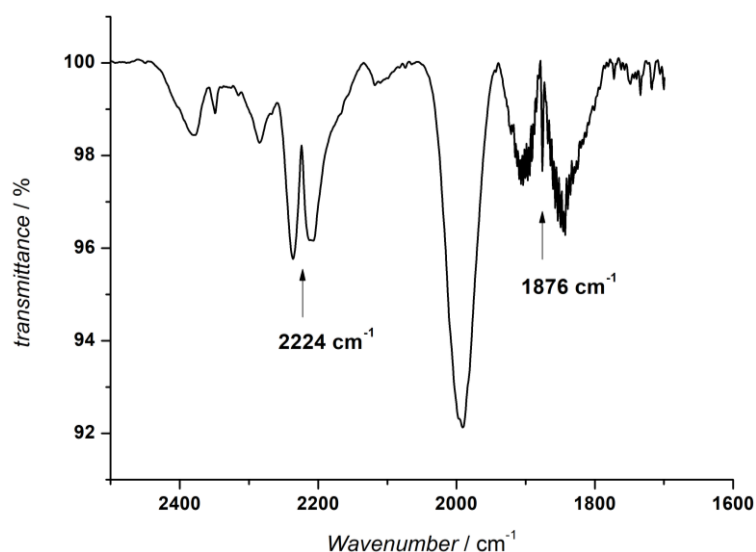
Figure 22. Gas phase IR spectrum of complex **2** treated with excess NO. Formation of N_2O was confirmed by the presence of the peak at 2224 cm^{-1}.

This evidence suggested that the formed hyponitrite complex **3** is susceptible to decomposition in the presence of excess NO, and spontaneous release of nitrous oxide and formation of complex **4** is observed. However, by following the experimental evidences the reaction equation is unbalanced (Scheme 27), so that the mechanism of this process remains unclear.

Overall, these findings suggest that optimal conditions need to be used in order to maximize the yield of the hyponitrite compound **3** and avoid formation of hydroxo-bridged **4**, which is in general extremely hard to separate from the desired product due to similar solubility properties, even by repeated crystallizations. Although manual separation of the obtained crystals was helpful to increase the purity of **3**, it was not possible to completely prevent the presence of **4** in the crystalline material of **3**.

Two main factors have to be considered: traces of water and N_2O usually contained in the commercial NO tanks must be eliminated and particular care should be taken to control the correct amount of NO as well as the rate of its addition in the reaction vessel.

All the possible side-reactions that were observed are represented in Scheme 27:
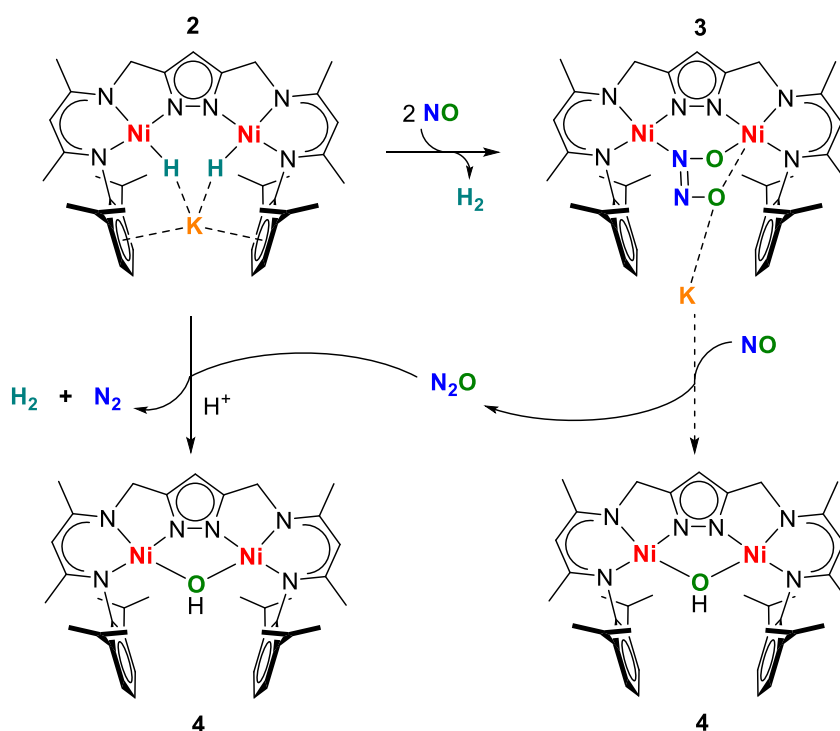
Scheme 27. Decomposition pathways for complex **2** and **3** that lead to the formation of **4**.

3.4 Protonation of the Hyponitrite Complex 3

The hyponitrite compound **3** represents the product of the formal two-electron reduction of two NO molecules, followed by N-N coupling and binding to the dinickel core. The nickel dihydride precursor **2** proved to be again a suitable scaffold for donating redox equivalents stored as hydrides. As mentioned in Chapter 1, NO can be reduced by enzymes that are able to provide protons and electrons to convert the molecule to N_2O and H_2O. To test whether the *cis*-"end-on" hyponitrite binding mode found in complex **3** can represent a possible intermediate for NO reduction in FNORs, the reactivity towards a source of protons was studied.

A red solution of complex **3** in THF was then treated with two equivalents of lutidinum triflate at room temperature (Scheme 28), and the headspace of the reaction vessel was analyzed via IR spectroscopy.
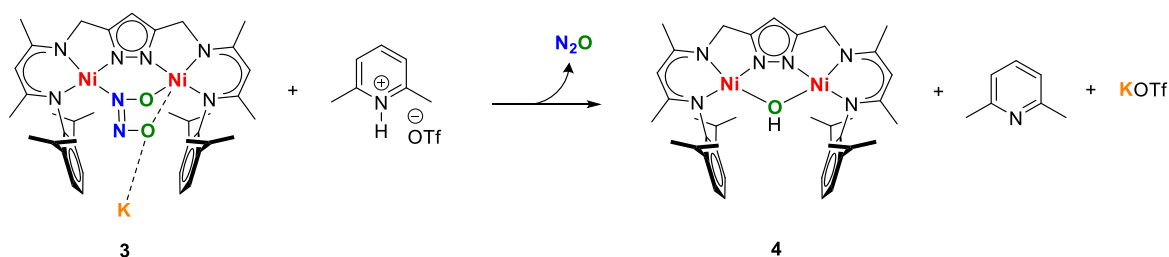
Scheme 28. Evolution of nitrous oxide from **3** upon treatment with [LuH][OTf].

As expected, the characteristic signal of N_2O in the gas phase was observed as an absorption band centered at 2224 cm^{-1}, split in two single peaks at 2236 cm^{-1} and 2212 cm^{-1} (Figure 23, red line). A blank experiment in order control the stability of **3** and to exclude formation of N_2O upon decomposition was also performed. Thus, the gas phase IR spectrum of complex **3** in solution was analyzed, and only bands belonging to THF in the atmosphere were detected in these conditions (Figure 23, black line), confirming the stability of the complex in solution. The signal was only detected after treatment of complex **3** with lutidium triflate.
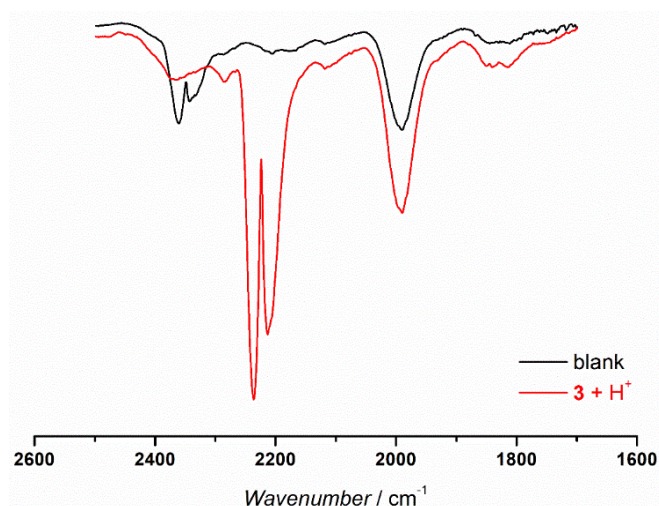
Figure 23. IR gas phase of complex **3** dissolved in the solvent (black line) and after reaction with the acid (red line) recorded at room temperature. The peak centered at 2224 cm^{-1} confirmed the formation of N$_2$O.

In order to check whether the amount of N$_2$O formed quantitatively with respect to the mole fraction of molecules of complex **3**, a calibration curve was established. Gaseous N$_2$O from a lecture bottle was used for this purpose. Different known amounts of gas were injected into a vessel and the gas phase IR spectrum was recorded. Details regarding the measurements and experimental setup are given in the Experimental part and the Appendix, respectively. The calibration was repeated three times and an average data set for each volume was obtained. The volume of injected N$_2$O was plotted in dependence of the integral area of the respective signal. The resulting plot is shown in Figure 24.
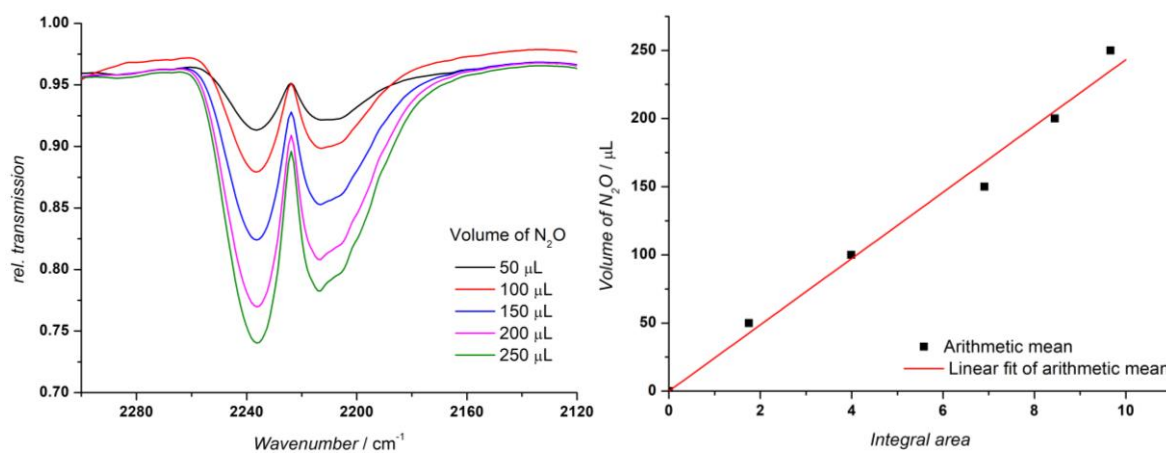
Figure 24. Gas phase IR spectrum of different concentrations of N$_2$O (left) obtained by injecting different volumes of N$_2$O into a vessel connected to an IR cell and calibration curve for the quantification of N$_2$O produced (right). The black dots represent the average of the collected data for each concentration and a linear dependence of the integral area of the N$_2$O signals with the injected volumes was assumed.

By using a known amount of complex **3**, 68.4% of the expected N_2O with respect to the complex concentration upon treatment with the acid was observed. Possible problems that did not lead to the quantitative reaction could be represented by the fact that a very small amount of **3** and acid were used to probe the evolution of N_2O, so that the mass error is substantial. Furthermore, the KBr windows of the IR gas cell could not be sufficiently tight and this might have led to a loss of gas prior to the measurement after transfer to the spectrometer. Nevertheless, it is reasonable to consider that the main reaction that occurs is represented by the formation of N_2O and H_2O, as the amount of detected gas was above 50%.

The formation of water was also supported by the analysis of the reaction mixture after the reaction was completed by ^{1}H-NMR, as shown in Figure 25.
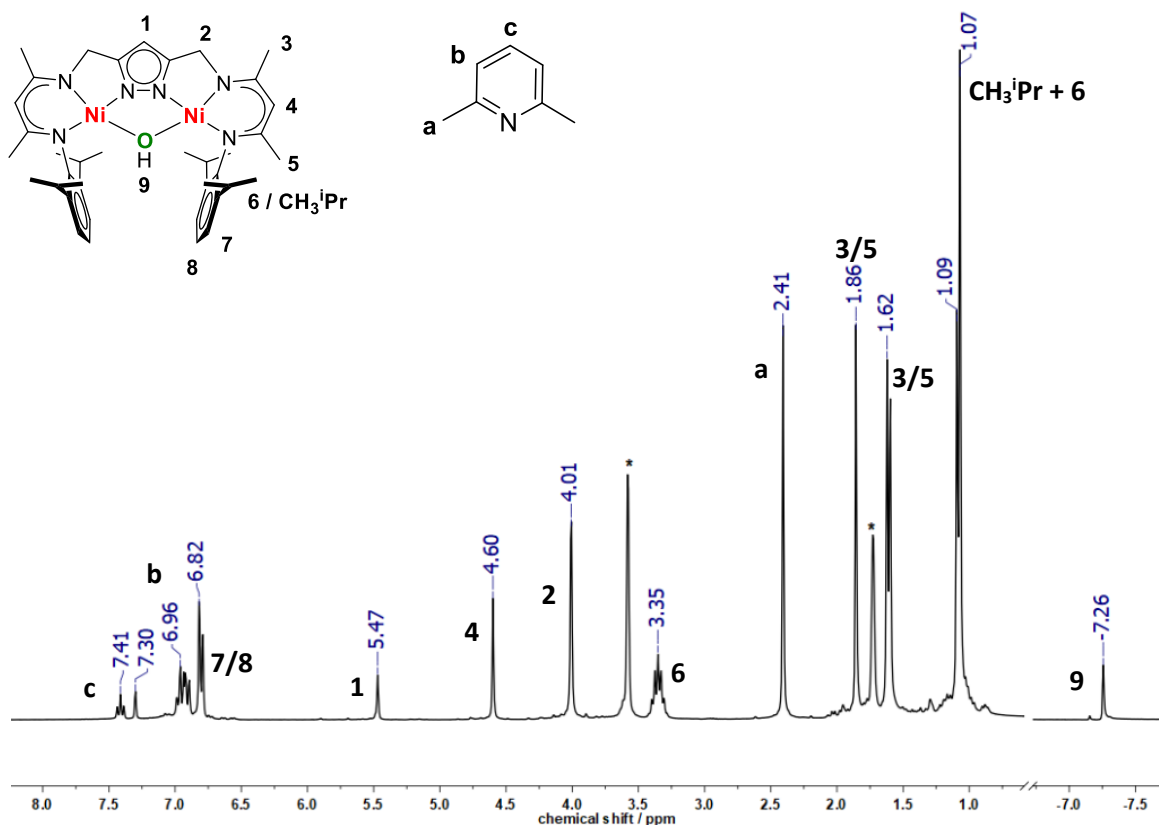
Figure 25. ^{1}H-NMR spectrum of a solution of complex **3** in THF-d$_8$ at room temperature after treatment with [LuH][OTf].

The ^{1}H-NMR spectrum clearly indicates that the hydroxo-bridged nickel complex **4** was mainly formed (O*H* resonance at -7.24 ppm), as a result of the reaction between complex **3** and water. Furthermore, proton donation from the acid leads to the formation of the corresponding free base whose presence was observed by detection of the aromatic peaks

of 2,6-Lutidine at 7.34 ppm and 6.96 ppm, and a singlet assigned to the methyl groups at 2.41 ppm.

In conclusion, the experiments described above suggest that complex **3** could be considered as an intermediate in the two-electron reduction of nitric oxide to nitrous oxide using protons and doesn not undergo NO disproportionation. Such reactivity is reminiscent of the nitric oxide reductase enzyme that catalyses the same process involved in biological denitrification.

Similar reaction pathways were already observed for nickel and platinum complexes, which were sentitive to acids, heat or light and produced N_2O and a transient metal oxido compound, as shown in Scheme 29.[53]
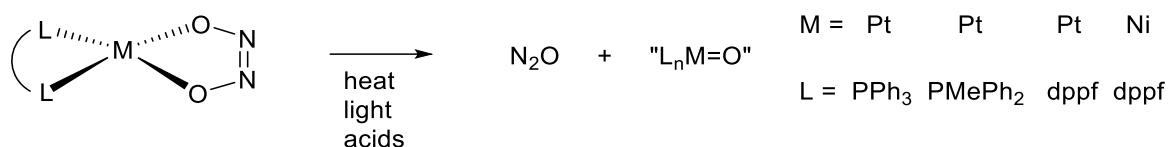
Scheme 29. Elimination of N_2O from group 10 hyponitrite complexes.[53]

Furthermore, a similar hyponitrito-bridged cobalt complex which bears a planar hyponitrite moiety with a *cis* configuration was shown to produce nitrous oxide and the corresponding aquapentammine cobalt(III) compound upon treatment with acids, as represented in Scheme 30.[165]
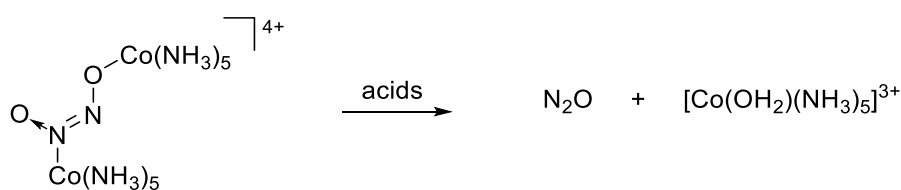
Scheme 30. Elimination of N_2O from an asymmetric hyponitrito-bridged cobalt complex.

3.5 Summary

In this chapter, the reactivity of the dinuclear nickel(II) dihydride complex **2** towards nitric oxide was examined. Two electrons were provided by the complex in order to reductively couple two molecules of NO and subsequently isolate the new dinickel compound **3** that features a hyponitrite moiety. The complex represents a rare example of a *cis*-hyponitrite unit that is bound end-on to the two metal centers and the only structurally characterized type-B $[N_2O_2]^{2-}$ complex. Its characterization by means of several spectroscopic techniques led to interesting observations. For instance, a dynamic process is present in solution as indicated by the ^{1}H-NMR spectrum of **3**, which does not reflect the symmetry of the molecule in the solid state. Currently, DFT studies aim to shed light into such process.

Furthermore, complex **3** reacts in the presence of an excess of NO, decomposing to the hydroxo-bridged complex **4** along with formation of N_2O. Thus, particular care must be taken when controlling the amount of NO employed during the synthesis of **3** as nitrous oxide would convert the starting material **2** to the corresponding hydroxo-bridged complex **4**, drastically decreasing the total yield of the reaction. Rapid reaction of **2** with N_2O to give mainly complex **4** has been demonstrated in independent experiments, although the mechanism of this reaction is still unclear.

Finally, it was found that the hyponitrite compound **3** reacts with protons to form N_2O and H_2O, showing a NOR-type reactivity. The amount of gas produced was detected and quantified by means of headspace IR spectroscopy.

4 Insight into the Formation of the Hyponitrite Complex 3: a Novel Nitroxyl-Bridged Dinickel Complex

In Chapter 3, the dinuclear nickel(II) dihydride complex **2** was shown to reductively couple two equivalents of nitric oxide to give a bound hyponitrite, $[N_2O_2]^{2-}$. This complex was further characterized in solution and in the solid state, which confirmed the $[N_2O_2]^{2-}$ group to be bound in the *cis* configuration and N,O-bridging. Furthermore, the hyponitrite complex **3** showed a NOR-type reactivity, releasing nitrous oxide and water upon treatment with a suitable acid.

This chapter focuses on the formation of the hyponitrite complex itself, in particular on the binding of the first equivalent of nitric oxide and the formation of the corresponding nitrosyl compound. Such species are considered to be the key step in nitric oxide activation promoted by complex **2**, as reducing equivalents are provided.

Compound **2** was initially treated with one equivalent of gaseous NO in order to gain insight into the mononitrosylation reaction (Scheme 31). The reaction was carried out both at room temperature as well as low temperatures, and the outcome was mainly analyzed by ^{1}H-NMR spectroscopy. The results showed that a mixture of products was formed regardless of the experimental conditions. Unfortunately, no traces of a putative nitrosyl compound were detected, as only the precursor **2**, the hyponitrite complex **3**, and the hydroxo-bridged compound **4** were observed.
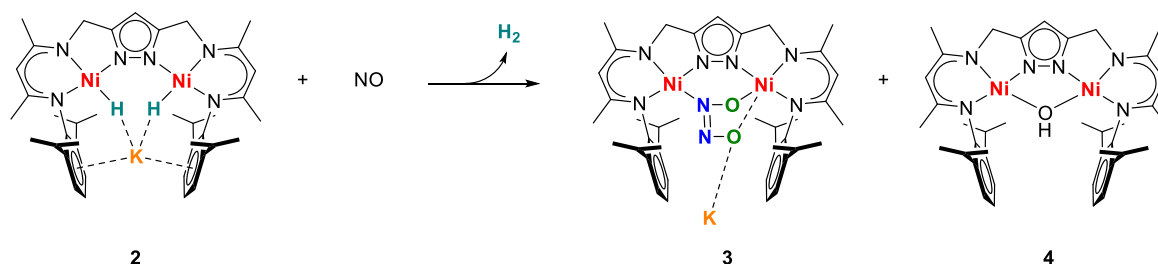
Scheme 31. Reaction of **2** with one equivalent of NO$_{(g)}$. A mixture of compounds mainly containing **3** and **4** was obtained.

One possible explanation for such behavior is due to the intrinsic property of **2** discussed in Chapter 1. Specifically, the nickel dihydride complex **2** stores two redox equivalents in two metal hydrides, and can release H_2 for reductive substrate binding. Thus, when two electron are transferred to one equivalent of NO radical, a putative 13-electron $(NO)^{2-}$ dianion that is highly activated should form. This may be extremely reactive towards any

substrate, namely surrounding molecules of NO and/or traces of water. Consequently, only mixtures of products were obtained. Therefore, modification of the reaction conditions was necessary in order to cleanly synthetize a new nitroxyl species. The synthesis and characterization of the novel nitroxyl complex will be discussed in the following sections.

4.1 Synthesis of a Nitroxyl Complex

As mentioned in the previous section, usage of gaseous NO afforded only a mixture of products. Consequently, a new strategy to obtain the desired nitroxyl compound was employed. To that end, NO$^+$ was used as NO source since the dihydride precursor **2** is able to reduce substrates by two electrons.

Treatment of a solution of **2** with nitrosonium tetrafluoroborate NOBF$_4$ at -20°C resulted in a dark purple reaction mixture (Scheme 32). ESI-MS analysis of the crude product revealed one major peak corresponding to [LNi$_2$(NO) + H]$^+$ (*m/z* = 752.3) (Appendix, Figure 2). The same product could also be obtained by using the NO-transfer reagent Ph$_3$CSNO. Crystallization upon slow diffusion of Et$_2$O and pentane into the THF solution led to the formation of dark red crystals of the air sensitive LNi$_2$(NO) (**5**) in moderate yields (ca. 40%). The molecular structure of **5** is shown in Figure 26 and selected structural parameters are reported in Table 2.
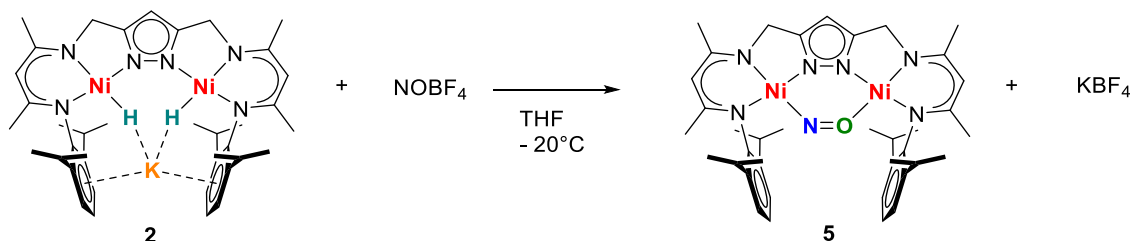
Scheme 32. General scheme for the synthesis of complex **5**.
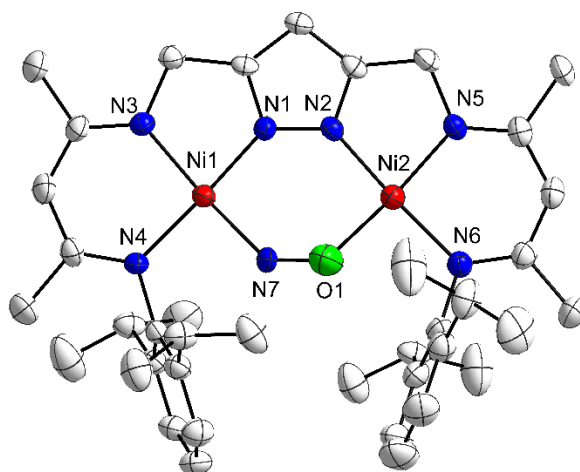
Figure 26. Molecular structure of **5** (50% probability thermal ellipsoid); hydrogen atoms are omitted for clarity.

Table 2. Structural parameters, bond lengths [Å] and angles [°] for complex **5**.

Bond length / Å		Angle / °	
Ni(1)-N(7)	1.834(3)	N(7)-Ni(1)-N(1)	92.89(14)
Ni(1)-N(1)	1.842(3)	N(1)-Ni(1)-N(3)	82.75(14)
Ni(1)-N(3)	1.913(3)	N(7)-Ni(1)-N(4)	90.04(14)
Ni(1)-N(4)	1.925(3)	N(3)-Ni(1)-N(4)	94.39(14)
Ni(2)-N(2)	1.842(3)	N(1)-Ni(1)-N(4)	176.96(13)
Ni(2)-O(1)	1.849(4)	N(2)-Ni(2)-O(1)	91.93(15)
Ni(2)-N(5)	1.897(3)	N(2)-Ni(2)-N(5)	83.25(14)
Ni(2)-N(6)	1.917(3)	O(1)-Ni(2)-N(6)	91.54(15)
N(7)-O(1)	1.197(4)	N(5)-Ni(2)-N(6)	93.84(14)
Ni(1)⋯Ni(2)	3.8151(7)	Ni(1)-N(7)-O(1)-Ni(2)	2.142(61)

Complex **5** crystallizes in the monoclinic space group $P2_1/c$. Both nickel centers are found in an ideal square planar environment with a metal-metal distance of 3.81 Å, consistent with other dinuclear nickel β-diketiminato complexes isolated throughout this thesis work. The distance N(7)-O(1) of 1.20 Å is longer than the bond length found in free gaseous nitric oxide (1.15 Å),[166] suggesting a reduction of the molecule at the metal centers, consistent with a formal charge of -1 for a nitroxyl unit. The Ni(1)-N(7) and Ni(2)-O(1) distances of 1.83 Å and 1.85 Å, respectively, are in agreement with other similar nickel complexes which feature a Ni-N or Ni-O(sp^3) character.[145,167] Furthermore, the analysis of the torsion angle ∢(Ni(1)-N(7)-O(1)-Ni(2)) of 2.14° confirms that the NO unit lies in plane with the six membered N(1)N(2)Ni$_2$NO ring. The nature of the interaction of the diatomic molecule with each metal center can then be classified as "end on", with a bridging μ-η^1:η^1 NO⁻ unit which,

to the best of our knowledge, represents the first structurally characterized example of this binding motif. However, the precise determination of the position and occupancy of nitrogen and oxygen atoms is challenging, due to the difficulty in distinguishing between the two atoms using X-ray diffraction. Moreover, DUAN[168] and MANZ[145] showed that binding and subsequent reduction of dinitrogen N_2 can be achieved by complex **2** in certain reaction conditions. In order to distinguish between the two molecules, further spectroscopic methods for the characterization of **5** were necessary. The results are presented in the following section.

4.1.1 Spectroscopic Characterization of 5

To confirm the presence of the nitroxyl unit between the two metal centers in **5**, labeled $^{15}NOBF_4$ was synthetized in a two-step reaction[169] and the corresponding **5**-^{15}NO compound was prepared. An IR spectrum of both compounds was recorded, and the characteristic N-O stretching frequency was then analyzed, as shown in Figure 27.
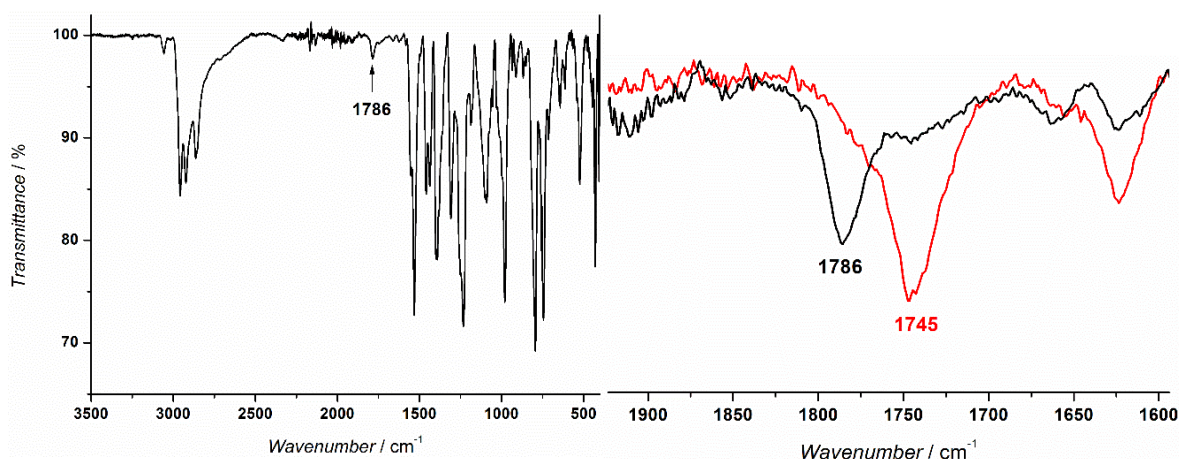
Figure 27. IR spectrum of complex **5** (left) and NO stretching band (right) of **5** (black line) and **5**-^{15}NO (red line).

A weak and relatively broad band at 1786 cm^{-1} was observed in the IR-ATR spectrum of the solid material (Figure 27, left), which slightly shifted to 1781 cm^{-1} in THF solution (Appendix, Figure 3). Although this value is in agreement with reported terminal nickel nitroxyl compounds,[170,171] direct comparison is not possible since complexes bearing nitroxyl units that display such a binding mode have not been reported so far.

The NO vibration of the corresponding ^{15}NO-labeled compound showed the expected isotopic shift to lower energies by 41 cm^{-1}, which is consistent with the calculated value of 32 cm^{-1} (Details are given in the Experiental part), unambiguously confirming the binding of NO (Figure 27, right). This finding also excluded the formation of the dinitrogen

LNi$_2$(μ-η^1:η^1-N$_2$) compound, which displays a corresponding N-N stretching frequency at 1896 cm^{-1} (1838 cm^{-1} for the ^{15}N$_2$ labeled compound).[145]

EPR and SQUID measurements corroborated the diamagnetic properties of **5**, which could be studied in solution by NMR spectroscopy. The ^{1}H-NMR spectrum of **5** recorded in THF-d$_8$ at room temperature revealed a resonance pattern that is consistent with an asymmetric complex, as shown in Figure 28. In fact, two singlets at 5.33 ppm and 5.10 ppm corresponding to the C*H* protons of the nacnac backbone, each with a normalized integral of one were observed. Similarly, two signals both with a normalized integral of two, were observed at 4.32 ppm and 4.24 ppm, corresponding to the C*H*$_2$ groups. Only one resonance associated with the isopropyl C*H* group was observed at 3.22 ppm, whereas the second C*H* group was partially hidden by the solvent residual signal at 3.61 ppm (signal 11 in Figure 28), but determined by means of ^{1}H-^{1}H-COSY experiments.

^{15}N-NMR spectroscopy was also conducted on **5**-^{15}NO in THF-d$_8$, illustrating a single signal at 735.3 ppm, which corresponds to the ^{15}N-O resonance, as show in Figure 29. Until now, no ^{15}N resonances for μ-η^1:η^1 NO-bridging ligands in nickel complexes were reported, so a direct comparison was not possible. However, the nitrogen resonates at high frequencies (low fields) but falls well within the range of other reported bent nitrosyl complexes between 350 ppm and 900 ppm, and it can be easily distinguished from linear nitrosyl compounds where the nitrogen resonance is usually found in the range 50 ppm – 200 ppm.[172]
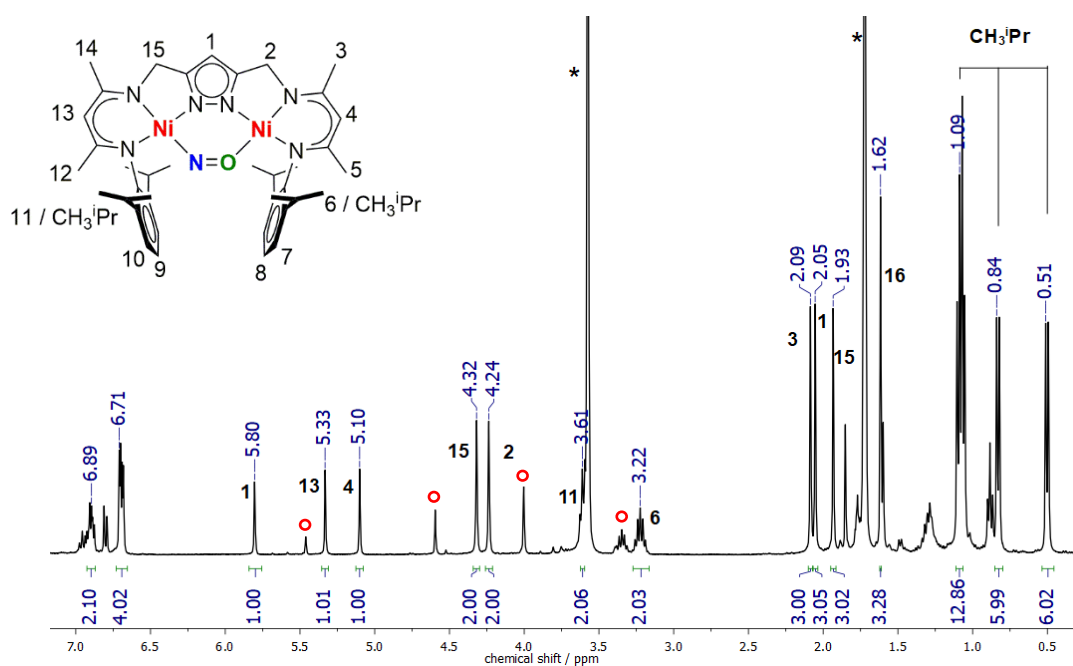
Figure 28. ^{1}H-NMR spectrum of **5** in THF-d$_8$ recorded at room temperature. Residual solvent peaks are marked with an asterisk (*). Traces of **4** present as impurity are marked with a red circle.
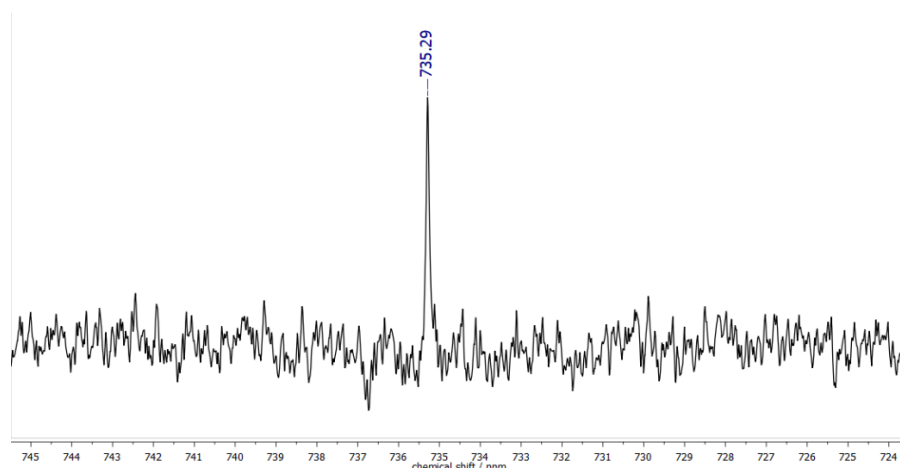
Figure 29. ^{15}N-NMR spectrum of **5** in THF-d$_8$ recorded at room temperature.

The UV/vis spectrum of **5** (Figure 30) recorded in THF at room temperature showed a prominent absorption at 261 nm which is slightly shifted in comparison with the characteristic ligand to nickel charge transfer (MLCT) band of the dinickel dihydride precursor **2** (270 nm, ε = 15600). In addition, two other absorptions were observed at 352 nm and 500 nm. The first is consistent with a charge transfer from the pyrazole ligand to the Ni(+II) metal centers and also observed for other nickel(II) pyrazole-bridged β-diketiminato complexes,[149] whereas the latter is assigned to a NO$^-$ π^* → Ni(+II) charge transfer (CT) feature.
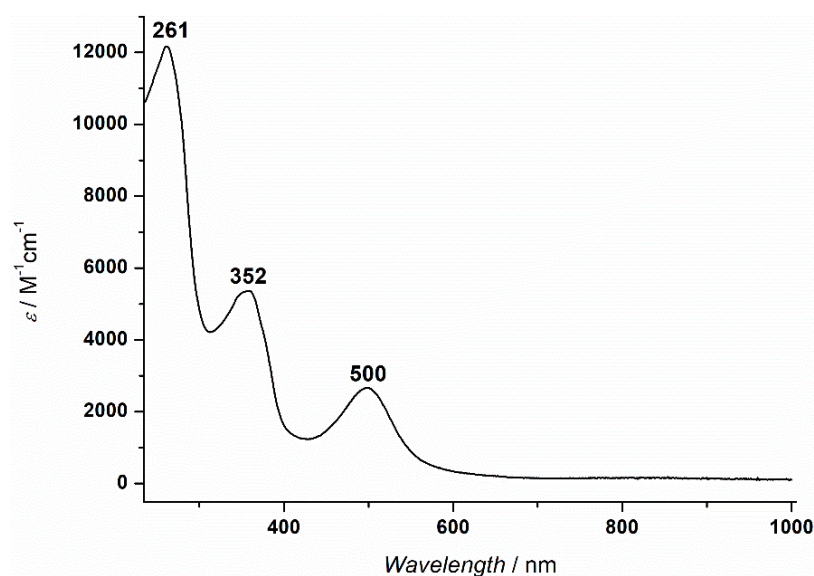
Figure 30. UV/vis spectrum of **5** recorded in THF at room temperature.

In conclusion, the electronic properties of complex **5** were investigated with different approaches using complementary methods that yielded consistent results. In particular, ^{1}H-NMR spectroscopy, ^{15}N-NMR spectroscopy, IR spectroscopy, EPR spectroscopy, and SQUID measurements confirmed the two electron reduction of the nitrosonium cation NO$^+$ promoted by complex **2**. As a result, a bridging nitroxyl NO$^-$ moiety with a formal charge of -1 is coordinated between the two nickel ions, as shown in the X-ray crystal structure obtained for **5**. Although a similar binding mode for NO was not reported so far and direct comparison with literature was only possible to a certain extent, **5** represents an interesting compound with unique electronic properties which were further investigated.

4.1.2 Redox Properties of 5

As already mentioned in the previous section, the properties of complex **5** were investigated in order to obtain information regarding possible intermediates that form during the first step of nitric oxide activation mediated by **2**. In principle, the dihydride precursor **2** should provide the necessary redox equivalents to one equivalent of gaseous NO to form an hypothetical [LNi$_2$(NO)]$^-$ species which could be in turn attacked by another NO radical molecule, leading to the corresponding [LNi$_2$(N$_2$O$_2$)]$^-$ **3** species. The nitroxyl complex **5** is the result of the two electron reduction of NO$^+$, and it should be theoretically possible to further reduce it to obtain a formal (NO)$^{2-}$ bridging unit. Thus, studies aiming at the reduction of **5** have been conducted starting with cyclic voltammetry experiments. The possible redox processes were examined with particular regard to the reduction and detailed investigations into the nature of the products were performed.

Cyclic Voltammetry

Cyclic voltammetry (CV) studies were performed on **5** in THF with Bu$_4$NPF$_6$ (0.1 M) as the electrolyte, values were referenced to the ferrocene/ferrocenium redox couple, which was used as the internal standard. All voltammograms were recorded under inert conditions in a glovebox at room temperature. The resulting CV is shown in Figure 31.
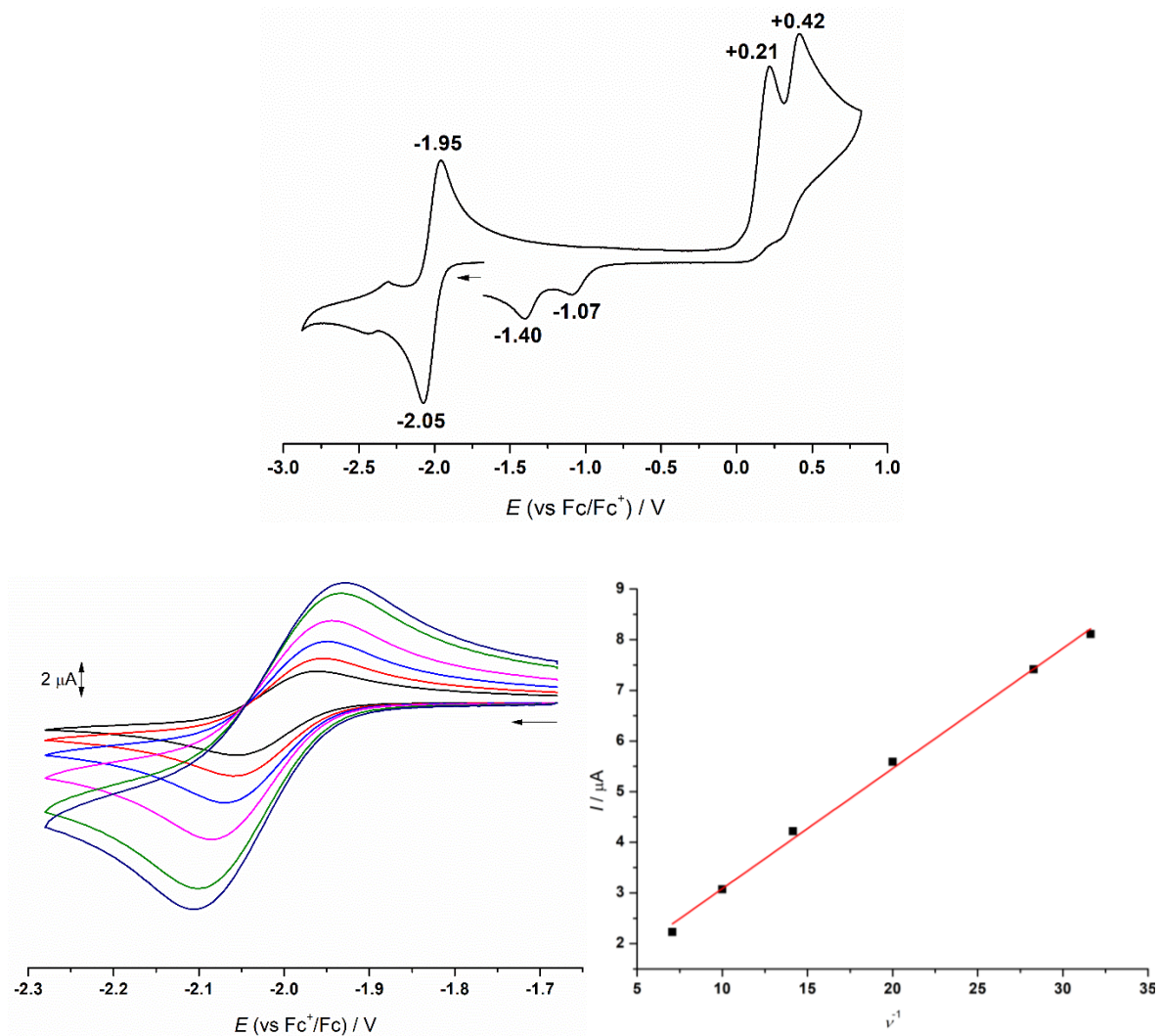
Figure 31. Top: cyclic voltammogram (vs Fc/Fc⁺) of **5** (THF, 0.1 M Bu₄NPF₆) at a scan rate of 100 mV/s. Bottom (left)): fully reversible reduction wave ($E_{1/2}$ = -2.0 V) at 50 mV/s (black), 100 mV/s (red), 200 mV/s (blue), 400 mV/s (magenta), 800 mV/s (green), and 1000 mV/s (dark blue). Bottom (right): Reversible electron transfer indicated by the Randles-Sevcik plot that verifies the linearity between the peak current (anodic) and the square root of the scan rate.

The cyclic voltammogram of **5** (Figure 31, top) can be divided into two distinct sets of signals. The reductive regime shows mainly one cathodic wave centered at −2.0 V (vs Fc/Fc⁺) that fulfills the criteria for a reversible process (Figure 31, bottom).

Considering the structure of **5**, it stands to reason that the first reduction reversibly generates a [LNi₂(NO)]⁻ species. A second reversible reduction with lower intensity was also observed at −2.3 V, but its nature was not further investigated as it originates from a small amount of the hydroxo-bridged complex **4** that forms during decomposition.

In contrast, the oxidative region of the cyclic voltammogram shows two anodic waves. The first one appears at +0.21 V, and the second at +0.42 V. Both processes are notably separated and are considered fully irreversible. Along with these two oxidations, two associated irreversible reductions are present at −1.07 V and −1.4 V. Although it is not possible to determine which part of the molecule is affected by these processes, it is reasonable to assume that the (NO)⁻ moiety is involved in the process. In fact, it is expected that oxidation of both metal centers from Ni^{II} to Ni^{III} and the ligand scaffold L^{3-} occur at higher potentials. The oxidation of the (NO)⁻ unit formally leads to NO· that most likely partially dissociates from the complex that in turn leads to decomposition of **5** and subsequent re-oxidation at lower potentials.

The information obtained by CV was not sufficient in order to establish whether the reversible reduction centered at −2.0 V could be considered ligand based (i.e. at the nitroxyl bridging moiety) or at the metal centers at this stage. Therefore, further experiments were conducted.

Spectroelectrochemistry

The reversible redox process ($E_{1/2}$ = −2.0 V) observed in the cyclic voltammogram of **5** was then monitored by UV/vis spectroscopy to gain further insight into the nature of the [LNi₂(NO)]⁻ species. These investigations were performed under inert conditions in a dinitrogen glovebox using a quartz cuvette with the same conditions adopted from cyclic voltammetry. However, the experimental setup was different, as a platinum net was used as the working electrode, platinum wire as the counter electrode, and a silver wire placed in a sample holder with a septum to avoid direct contact with the solution as the pseudo reference electrode.

When a steady reducing potential at −2.2 V (*vs.* Fc/Fc⁺) was applied, continuous changes in all major features in the UV/vis spectrum of **5** were observed, as shown in Figure 32. The spectra were recorded every 10 seconds until no further changes were detected, and subsequent application of a steady re-oxidizing potential at −1.3 V resulted in the stepwise recovery of the initial spectrum. The reaction was completed in about 30 minutes, and the results are summarized as follows: the LMCT-like band at 261 nm slightly loses in intensity, while the NO⁻ π* ➔ Ni(+II) CT band at 500 nm experiences a loss of at least half of its intensity. Meanwhile, the band at 352 nm slightly decreases and splits into two well separated absorptions at 332 nm and 367 nm.
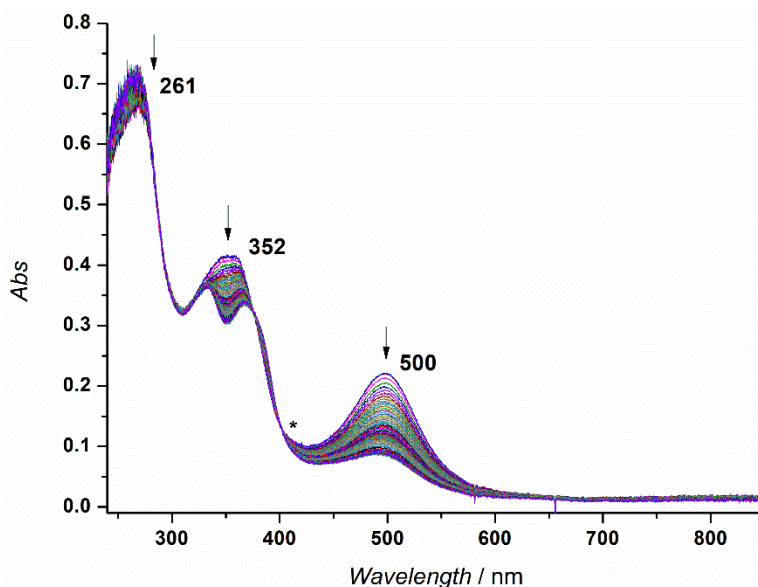
Figure 32. UV/vis spectra of **5** following the electrochemical reduction to give [LNi₂(NO)]⁻ in THF.

Comparison of the UV/vis of a related nickel(I) complex (isolated and characterized by DUAN, see Appendix, Figure 3) shows spectral features that are reminescent of the final UV/vis spectrum obtained spectrochemically for complex **5**. The band below 300 nm is still present, while two absorptions at 323 nm and 375 nm fall well within the range for the nitroxyl complex **5**, although the intensities are significantly different.

Overall, the mechanism behind the reduction of **5** is still inconclusive. Nevertheless, purely on the basis of the UV/vis spectra it can be preliminarly deduced that the reduction of **5** mainly involves the metal centers.

4.2 Chemical Reduction of 5

The reversible reduction wave in the cyclic voltammogram of **5** inspired us to attempt its chemical reduction and subsequent isolation of the final product. The nitroxyl complex **5** was then chemically reduced to gain insights into the electronic structure of the corresponding [LNi₂(NO)]⁻ species. For this purpose, decamethylcobaltocene (Co(Cp*)₂) was chosen as the reducing agent, with a $E^0 = -2.0$ V *vs.* Fc/Fc⁺ in THF.

Treatment of a cherry red THF solution of **5** with one equivalent of Co(Cp*)₂ at -10°C (Scheme 33) immediately led to a green-brown solution, which was stirred for about 10 minutes and analyzed by EPR spectroscopy. The same procedure was applied for the **5**-¹⁵NO labeled analogue. The resulting EPR spectra of both compounds are reported in Figure 33.
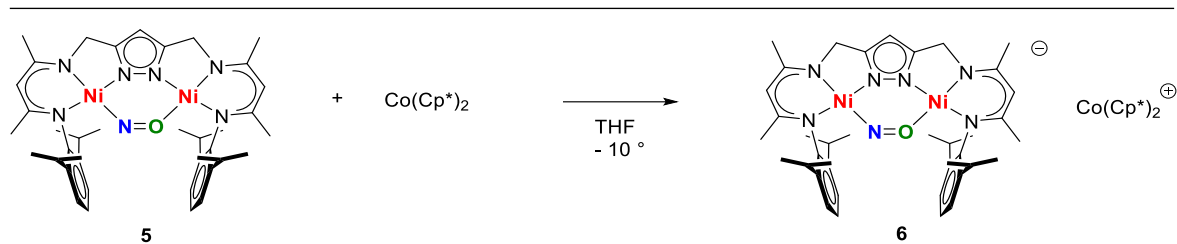
Scheme 33. Reduction of **5** with decamethylcobaltocene.
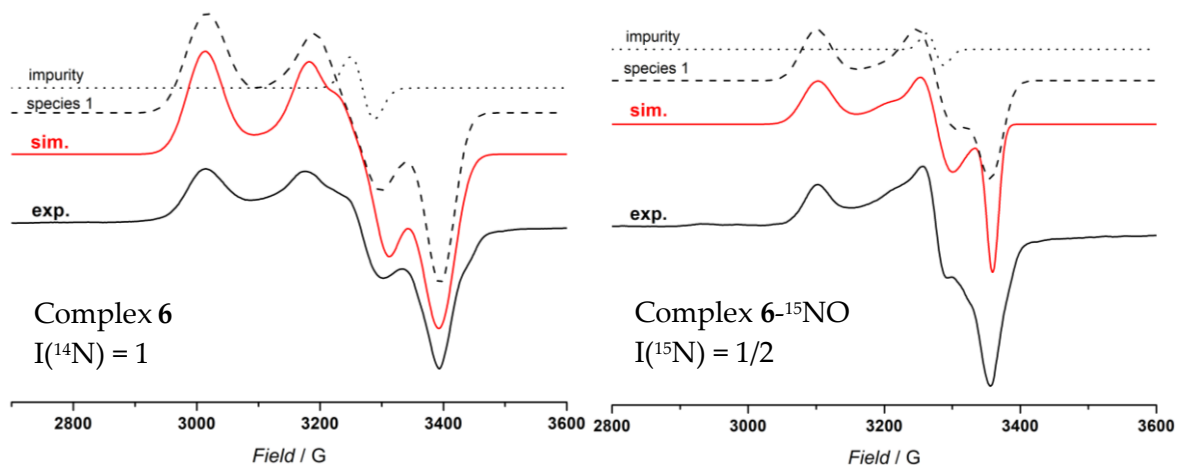
Figure 33. Experimental X-band EPR spectra (black line) of **6** (left) and **6**-¹⁵NO (right) recorded at 153 K in frozen THF solution. The corresponding simulations are represented by the red line.

The X-band EPR spectrum of the reaction mixture of **6** revealed a signal with a biaxial anisotropy of the g factor, which is typical for compounds with one unpaired electron. The simulation afforded g-values of 2.171, 2.069, 2.007 and corresponding hyperfine coupling constants of 40 MHz, 65 MHz, and 1 MHz. The presence of a sharp but relatively small organic impurity (3%) was found with g = 2.085. Interestingly, the EPR spectrum of **6**-¹⁵NO showed essentially identical parameters (g = 2.175, 2.058, 2.007; A(¹⁵N) = 40 MHz, 65 MHz, 1 MHz, 1% organic impurity g = 2.058), suggesting that upon reduction the spin density is mainly located on the metal center. The NO bridging group may also be involved with a minor contribution but the partial spin density that would give rise to two different line patterns for **6** and **6**-¹⁵NO is probably hidden by the intrinsic line broadening. Nevertheless, the large g-anisotropy clearly indicates a Ni-centered reduction for complex **5**.

Unrestricted DFT calculations (ORCA, B3LYP functional, RIJCOSX approximation, def2-tzvp and def2-tzvp/j basis sets) were then performed in order gain insight on the electronic structure of the metal-based reduced compound **6** from **5** and Co(Cp*)₂. The energy-minimized DFT calculated molecular structure of **6**⁻ shows that the electron density

on the singly occupied molecular orbital (SOMO) is mostly delocalized on one of the two nickel centers and the nitroxyl unit, along with slight involvement of the ligand scaffold. The Mulliken population analysis indicates that the unpaired spin density is consistently located on the nickel ions (46% on Ni1 and 14% on Ni2), whereas a minor contribution from the NO group is given (16% N, 5% O), as shown in Figure 34.
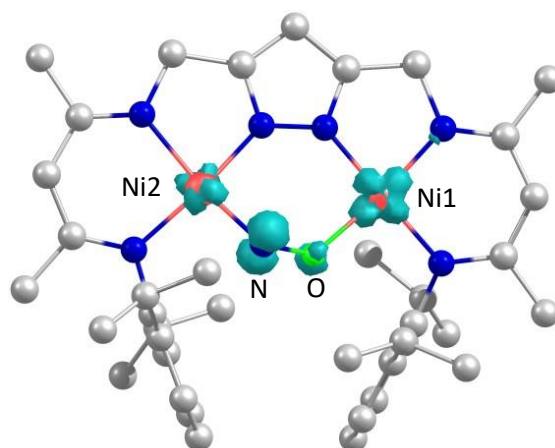
Figure 34. Spin density plot of **6** derived from Mulliken population analysis: Ni1 = 0.456907; Ni2 = 0.135684; O = 0.057954; N = 0.167033.

To confirm that the reduction of **5** with $Co(Cp^*)_2$ led predominantly to a metal-centered reduction, IR spectroscopy was again employed to analyze how the process influences the strength of the NO bond. The IR spectra of the crude powder material of **6** and **6**-[15]NO were measured, and the results are shown in Figure 35.
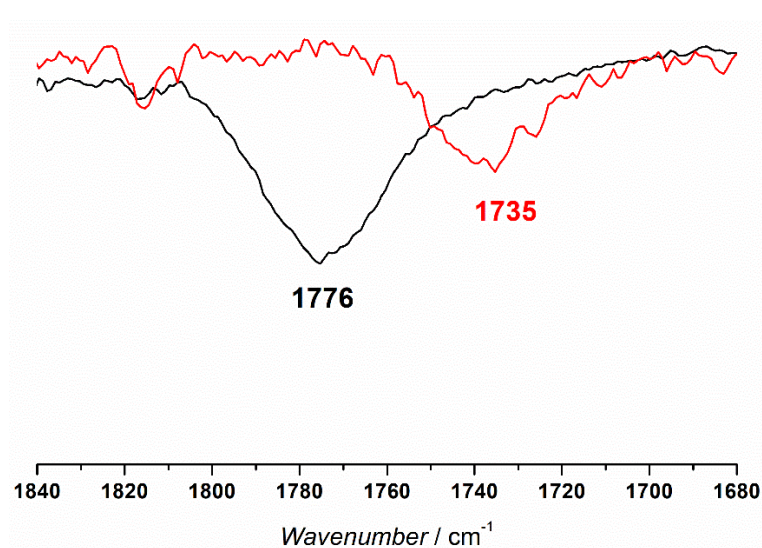
Figure 35. IR-ATR stretching frequency of NO in **6** (black line) and **6**-[15]NO (red line).

The NO stretching frequency of **6** was observed at 1776 cm^{-1}, which shifted to 1735 cm^{-1} in **6**-^{15}NO, and consistent with the calculated value of 1744 cm^{-1}. These data could be compared with the value obtained for the oxidized starting material **5** (Figure 25) observed at 1786 cm^{-1} (1745 cm^{-1} for **5**-^{15}NO) and it could be concluded that the NO peak shifted by only 10 cm^{-1} upon reduction, unambiguously confirming that the nitroxyl bridging ligand was barely affected and the process is predominantly metal-based.

At the same time, the UV/Vis spectrum of **6** was recorded in THF at room temperature (Appendix, Figure 5), but it did not provide any evidence for a metal-based reduction since the expected bands observed during spectroelectrochemical measurements (Figure 32) were hidden by the presence of the UV-vis active [Co(Cp*)$_2$]$^+$ counterion in solution.

Unfortunately, it was not possible to obtain single crystals for **6** suitable for X-ray diffraction studies, and due to the moderate amount of isolated material, no further experiments were conducted.

4.3 Effect of Lewis Acids on the Electronic Structure of 6

4.3.1 Reduction of 5 and Interaction with Alkali Metals

Redox-inactive metal alkali cations are known to play crucial roles in modulating the electron density distribution of a given molecule. Consequently, the coordination of these ions to metal complexes may significantly influence their reactivity towards different substrates.[173] Moreover, metal cations (in particular K$^+$) have been previously reported to be particularly suitable for binding to dinuclear nickel complexes of the present ligand scaffold **L**$^{3-}$,[146,149] since the K$^+$ ion is held between the aryl substituents of the ligand scaffold via cation-π interactions. Thus, reaction of complex **5** in the presence of an alkali metal ion may lead to a species with a higher stability than **6**, as well as provide a higher possibility to obtain single crystalline material for structure determination.

To assess the effect of the alkali metal cation, electrochemical experiments on **5** were performed again, but in the presence of K$^+$ cations. For this purpose, KB(Ar^F)$_4$ (potassium tetrakis[3,5-bis(trifluoromethyl)phenyl]borate) was synthetized[174] and used due to its good solubility in THF, in contrast to potassium triflate (KOTf) or potassium tetrafluoroborate (KBF$_4$). Solvents like MeCN, MeOH or DCM are not suitable for the nitrosyl complex **5** since they solely lead to immediate decomposition of the compound.

The cyclic voltammogram of **5** was measured under the same conditions described in
Section 4.1.2, but with an excess of $KB(Ar^F)_4$ (about five equivalents) in solution. The results
of the experiment are shown in Figure 36.
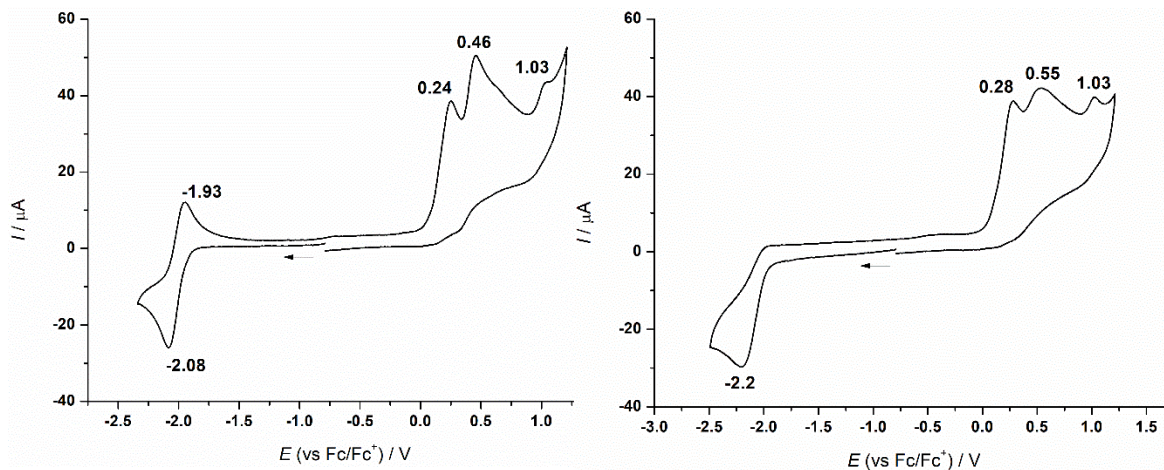
Figure 36. Cyclic voltammogram of **5** (1 mM in THF, 0.1 NBu_4PF_6) versus Fc/Fc^+ (left) and in presence of $KBAr^F$
(right).

The outcome of the experiment showed that in the presence of K^+ cations, the reversible
reduction centered at −2.0 V corresponding to the reduction from $[LNi_2(NO)]$ to $[LNi_2(NO)]^-$
vanishes and the complex is reduced at more negative potential of $E^p = −2.2$ V. Furthermore,
the reversibility of the process was lost, indicating that the alkali cation binds to the complex
and modifies the reduction step. Interestingly, no re-oxidation was observed after changing
the direction of the potential scan after the irreversible reduction. One possible explanation
may be that the process occurs at higher potentials, and it may be hidden by the other
oxidation processes that already take place in the absence of K^+. In fact, the potential of
second irreversible oxidation increased to +0.55 V when $KB(Ar^F)_4$ is added to the solution,
in comparison to the case in absence of K^+ where the value was found at +0.46 V.

Based on these experiments, the best way to describe the interaction that occurred in the
conditions employed for the experiment is displayed in Scheme 34.
This particular binding motif of the potassium cation was already shown for the nickel(II)
dihydride complex **2** and the corresponding μ-1,2 peroxo compound **VII** (Chapter 1,
Scheme 20).[146][146,149] In the case of **5**, reduction in the presence of $KB(Ar^F)_4$ may lead to a K^+
ion being sandwiched between the aryl rings of the aromatic arms, supported by attractive
$K^+\cdots(NO)^-$ interactions.
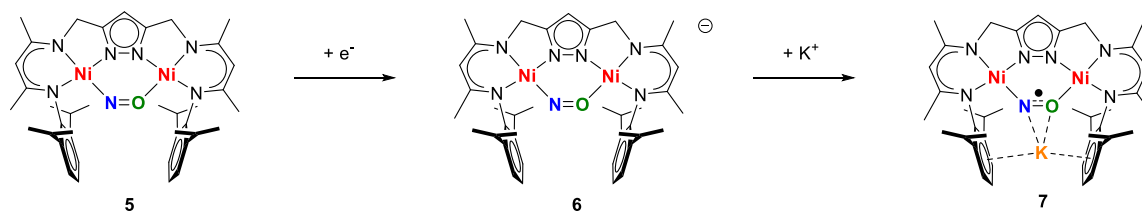
Scheme 34. Proposed binding of K⁺ after reduction of the nitrosyl complex **5**.

Furthermore, it is worth noting that the interation between complex **5** and the K⁺ was not observed in solution, as indicated by titration of **5** with different amounts of KB(ArᶠF)₄ followed by ¹H-NMR spectroscopy (Figure 37). The position of the proton resonances corresponding to **5** did not change upon increasing the concentration of K⁺, suggesting that the alkali cation does not interact with the complex in solution but only plays a role in the stabilization of the reduced analogue **6** to afford compound **7**.
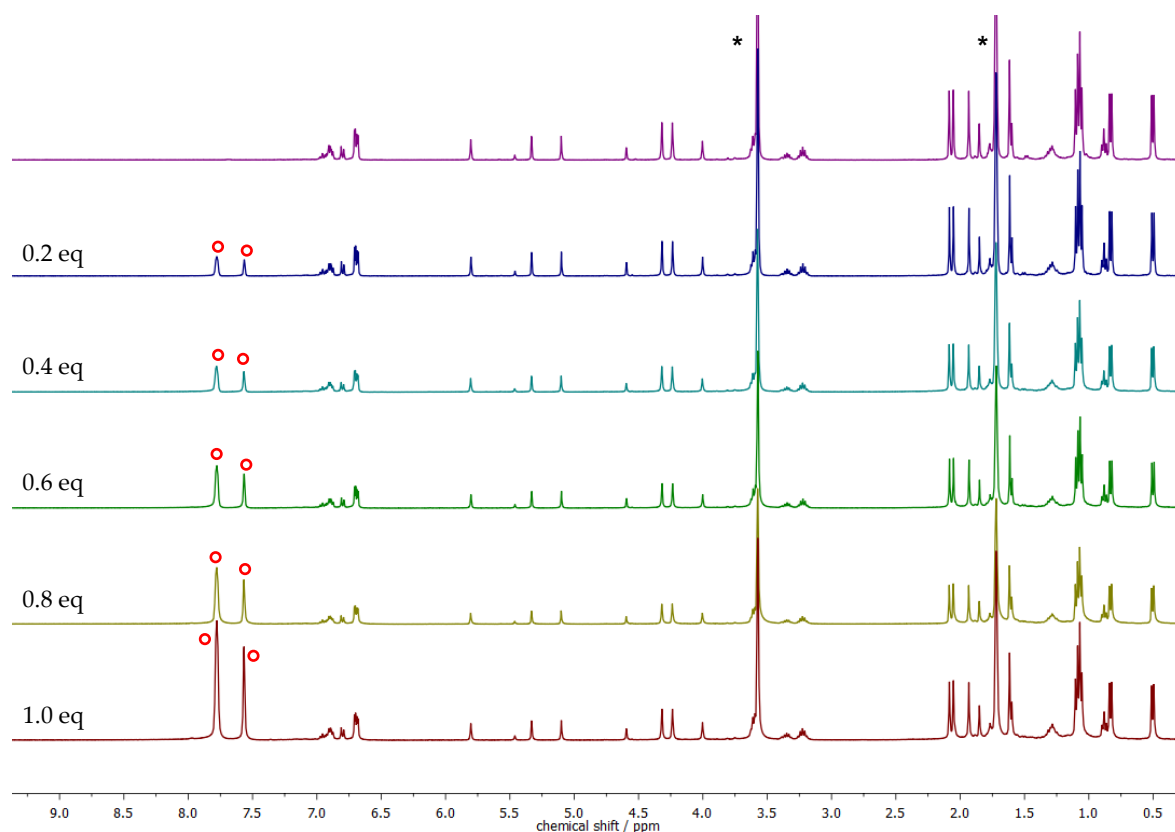
Figure 37. Titration of **5** with KB(ArᶠF)₄ in 0.2 eq steps followed by ¹H-NMR spectroscopy recorded in THF-d₈ at room temperature. Residual solvent peaks are marked with an asterisk (*). Increasing amounts of KB(ArᶠF)₄ are marked with a red circle.

Spectroelectrochemical reduction was also performed and the results were compared with the data obtained in the absence of the alkali metal cation. The investigations were

performed under the same conditions reported in section 4.1.2. Monitoring of the reaction
and related UV/vis spectra are shown in Figure 38.
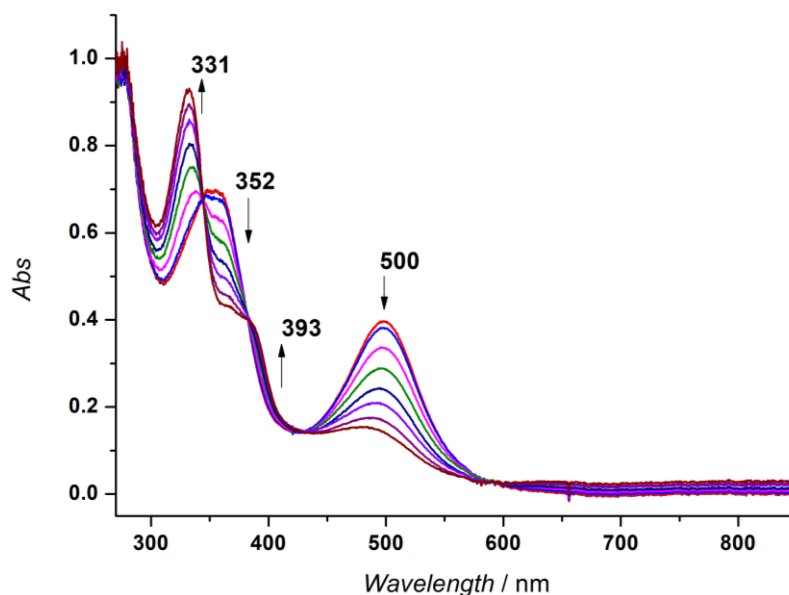
Figure 38. UV/vis spectra of **5** following its electrochemical reduction in presence of K⁺ (one scan every 10
seconds).

In contrast to the changes upon reduction in the absence of K⁺, the process was extremely
fast, concluding in about four minutes. In addition, significant differences were observed
for the bands at 332 nm and 352 nm. From previous experiments, these bands were shown
to be particularly sensitive to reduction (Figure 30), suggesting that the process involves the
same subunits as those involved in the absence of K⁺, namely the NO⁻ π^* → Ni(+II) orbitals.
However, in the latter case the absorption band at 332 nm significantly increased in
intensity while the band at 352 nm decreased along with the NO-specific band at 500 nm.
Unfortunately, no specific considerations regarding the modification of the electronic
structure can be made solely on the basis of the electrochemical experiments. Nevertheless,
it is clear that the interaction with the alkali metal cations dramatically influenced the
system upon reduction. In the following section, additional experiments to gain
information on how the reduction of complex **5** is influenced in these conditions will be
presented.

4.3.2 Chemical Reduction of 5 in the Presence of Potassium Cation

Since the interaction of the (NO)⁻ bridging unit with the potassium cation could stabilize the reduced product, reduction of **5** with Co(Cp*)$_2$ in the presence of KB(Ar^F)$_4$ was attempted. Sadly, it was not possible to obtain single crystals suitable for X-ray diffraction, as a large amount of salt had to be used in order to successfully replace the [Co(Cp*)$_2$]$^+$ cation with K$^+$. This was further supported by the fact that only the starting material **5** could be crystallized when working with stoichiometric amount of reagents. Consequently, another strategy was employed to avoid undesired inorganic salts in solution, and possibly a cleaner reaction pathway as well.

To that end, K·benzophenone was chosen as the reducing agent that contains potassium ions, and has the optimal reducing potential for complex **5** ($E_{1/2}$ = −2.3 V (*vs.* Fc/Fc$^+$) in THF).[175] A freshly prepared solution of K·benzophenone in THF was added to a solution of **5** in THF, which afforded an immediate dark green solution (Scheme 35). Crystals of the complex were obtained by layering the THF solution of **7** with a mixture of diethyl ether and hexane. Unfortunately, they were not optimal for X-ray diffraction analysis, as shown in Figure 39. While the crystallographic data were of poor quality, they still establish the connectivity of the atoms.
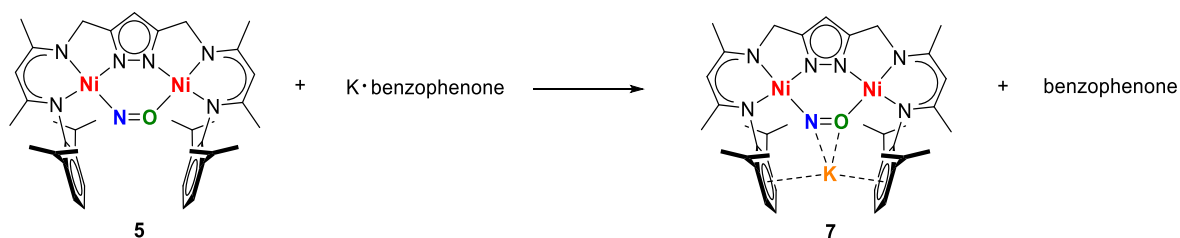
Scheme 35. General reaction scheme for the synthesis of **7**.
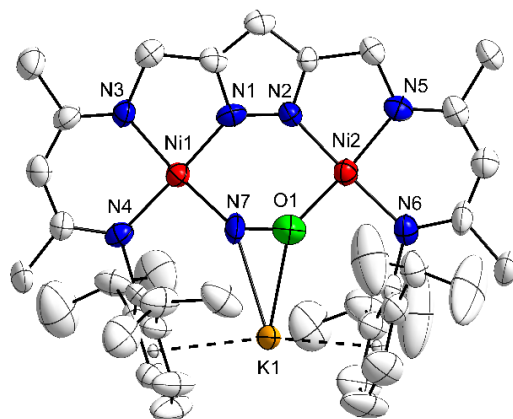
Figure 39. Low resolution molecular structure of KLNi$_2$NO **7**. Hydrogen atoms are omitted for clarity.

Refinement of the molecular structure indicates the co-crystallization of the starting material LNi$_2$NO **5** and its reduced analogue **7** in a 75 : 25 ratio. As shown by CV experiments, reduction of **5** occurs at very low potentials, so that its re-oxidation is highly favorable. Thus, this process may slowly take place during the crystallization, leading to the isolation of both compounds. Nevertheless, the results suggest an effective interaction of the potassium cation with the NO bridging unit, which is reduced by one electron compared to **5** and formally bears a charge of -2. Complex **7** represents a rare example of a radical dianion of nitric oxide (NO)$^{2-}$ since only one example has been reported so far (Scheme 36, compound **II**), and **7** is the first complex containing nickel.[176] Modifications of the crystallization method to obtain better crystals for X-ray diffraction analysis are still ongoing.
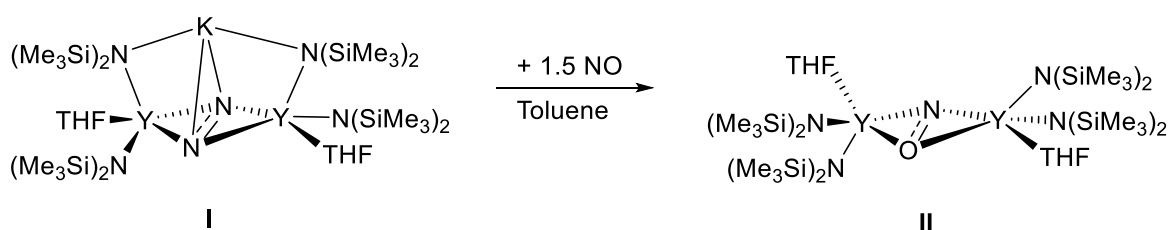
Scheme 36. Synthesis of the (NO)$^{2-}$ complex **II** from an (N$_2$)$^{3-}$ precursor **I**.[176]

To further investigate the nature of the electronic structure of compound **7**, and to assay the effect of the potassium cation on the complex, EPR measurements were performed.

While crystals of **7** were dissolved in THF and immediately frozen, the corresponding ^{15}NO labeled analogue was prepared in situ by treating a THF solution of **5**-^{15}NO with 0.8 equivalents of K·benzophenone under strictly inert conditions, and frozen after a few minutes of stirring. Excess of **5**-^{15}NO with respect to the benzophenone radical reducing agent was used intentionally to avoid interferences with the EPR measurement. A slight excess of complex **5**-^{15}NO would not affect the experiment because of its diamagnetic properties. X-band EPR spectra of both compound were recorded at 150 K, the results are shown in Figure 40.
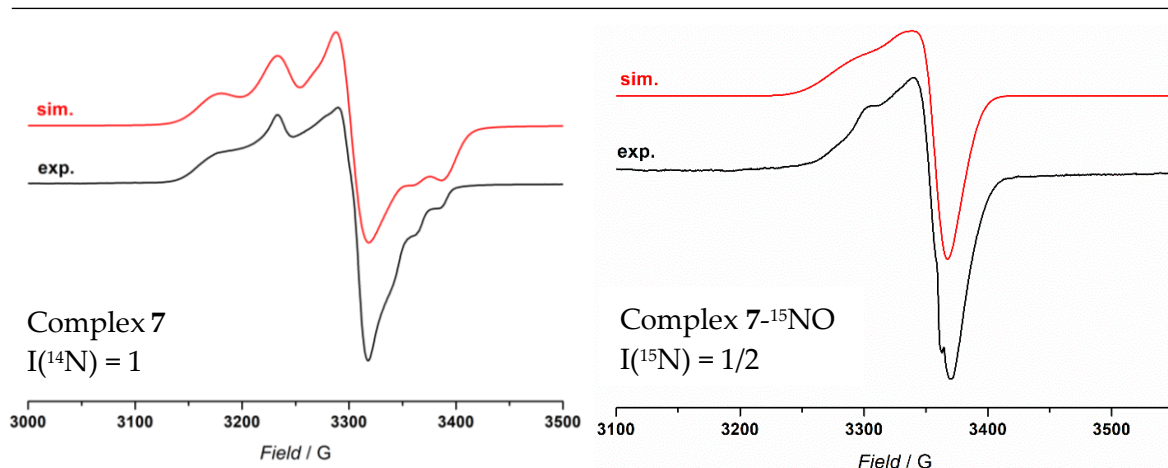
Figure 40. EPR spectra of single crystals of **7** (left) and **7**-[15]NO (right) recorded in THF at 150 K. The red traces represent the simulations.

Complex **7** shows an almost isotropic spectrum with g values of $g_1 = 2.084$, $g_2 = 2.059$, and $g_3 = 2.003$ ($A_1 = 167$ MHz, $A_2 = 80$ MHz, and $A_3 = 73$ MHz) as might be expected for a mostly organic radical. On the other hand, **7**-[15]NO displays g values of $g_1 = 2.047$, $g_2 = 2.011$, and $g_3 = 2.001$ ($A_1 = 15$ MHz, $A_2 = 25$ MHz, and $A_3 = 70$ MHz). The two compounds clearly show different electronic properties, although a different number of lines is expected in case the spin density is located entirely on the bridging ligand. However, a broadness of the signal can also be observed, which indicates a partial spin density distribution and unresolved hyperfine coupling to the nitrogen atom. Consequently, the hyperfine coupling constant A(N) obtained from the simulations may be inaccurate.

Nonetheless, the data qualitatively support the conclusion that the reduction of **5** in the presence of K^+ takes place at the NO bridging unit, in which the spin density is mainly delocalized onto the organic moiety. This indicates a different electronic distribution compared to compound **6** (reduced in absence of alkali metal cations). In that case, a major contribution of a metal-centered reduction was observed, as a result of the presence of the bulkier cation $[Co(Cp^*)_2]^+$, which could not be held in the aryl binding pocket of the ligand. Thus, the spin density in **6** remains on the metal that has Ni^I character.

To support the evidence of a ligand-centered reduction of **5** mediated by the presence of metal alkali cations and subsequent formation of a $(NO)^{2-}$ radical complex, the NO stretching frequency was further analyzed by IR spectroscopy.

Spectra of **7** and **7**-[15]NO were recorded for solid material, and the NO stretching frequencies were directly compared, as shown in Figure 41.
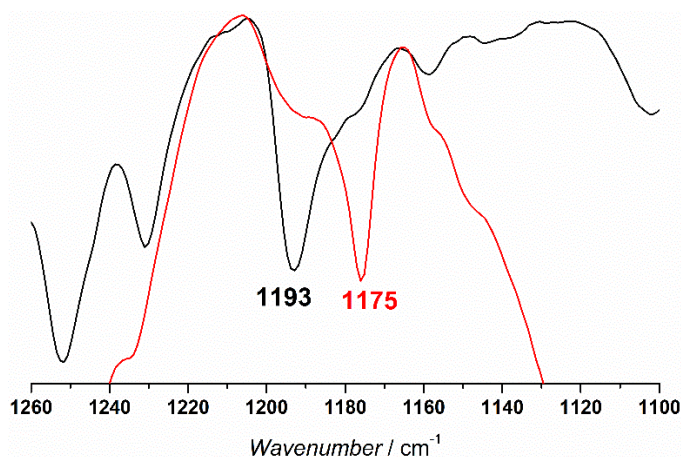
Figure 41. NO stretching frequency of **7** (black) and **7**-^{15}NO (red).

As expected, the NO bond strength was dramatically influenced by the reduction process, as the NO stretching frequency at 1786 cm^{-1} found in **6** decreased to 1193 cm^{-1} (1175 cm^{-1} for **7**-^{15}NO) with an isotopic shift of 18 cm^{-1} consistent with the value expected from theoretical calculated value of 1171 cm^{-1}. The data compare well with literature where the determined $\tilde{v}$(NO) observed for the only other example of a radical dianion of nitric oxide was found at 958 cm^{-1}.[176]

4.4 Conversion of 7 into the Hyponitrite Complex 3

One electron reduction of the NO$^-$ bridging group of **5** by K·benzophenone formally led to the isolation of the corresponding NO^{2-} radical complex **7**, which was characterized with a variety of spectroscopy methods. It was already mentioned that the nickel dihydride complex **2** is able to provide two electrons for the reduction of gaseous nitric oxide. Although it was not possible to directly isolate any compound following this procedure, due to the high reactivity of the product and the difficulties in keeping the reaction conditions strictly inert, the alternative procedure that follows the stepwise reduction of NO$^+$ to NO$^-$ by complex **2**, and to NO^{2-} by a suitable reducing agent was successful.

Therefore, to support that **7** represents an intermediate during the direct reduction of NO by **2**, the reactivity of **7** towards nitric oxide was tested. Compound **7** was then synthesized and treated in situ with one equivalent of NO, and the reaction mixture was analyzed by ESI mass spectrometry. The spectrum is shown in Figure 42.
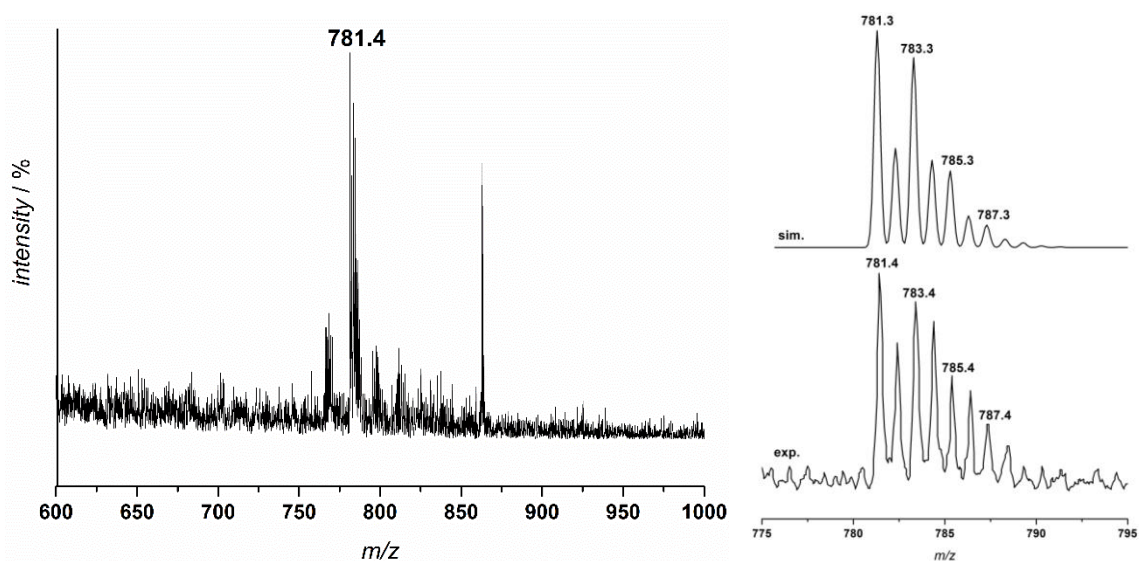
Figure 42. ESI-MS(-) of the reaction mixture of **7** treated with one equivalent of NO. The insets shows the experimental peak assigned to the hyponitrite anion **[3 − K⁺]⁻** (top) and its simulation (bottom).

A major peak at m/z = 781.4 was observed in the ESI mass spectrum, corresponding to the formation of the anionic hyponitrite complex **[3 − K⁺]⁻**. Interestingly, analogous results were obtained also when complex **6** was treated with one equivalent of NO, confirming the delocalization of the electron density on the Ni-NO-Ni subunit. The other decomposition product, which was observed during the synthesis of **[3 − K⁺]⁻**, corresponds to the well-known hydroxo compound **4**. Unfortunately, all attempts to avoid its formation were not successful so far.

Formation of a $(NO)^{2-}$ complex seemed to be necessary in order to obtain the hyponitrite compound **3**. In fact, an additional experiment where the nitrosyl complex **5** was treated with one equivalent of nitric oxide did not lead to the formation of **3**, according to mass spectrometry. However, a new reaction pathway was observed, which will be discussed in the next section of this chapter.

4.5 Reactivity Studies on the End-On Nitroxyl Complex 5

The disproportionation of NO is a thermodynamically favored process (ΔG^0 = −24.6 kcal) but, due to NO being kinetically inert, a metal catalyst is usually required. The reaction requires at least three molecules of NO in order to produce N_2O and NO_2 (Scheme 37), and it has been well documented that copper, iron and other metals are able to promote the reaction.[177,178]

$$3 \ NO \longrightarrow N_2O \ + \ NO_2$$

Scheme 37. Simple disproportionation of nitric oxide to give nitrous oxide and nitrogen dioxide.

Similarly to the case of the NO reduction mediated by acids mentioned in Section 3.4, also the disproportionation of NO implies that the key step is represented by the N-N bond formation between two NO molecules. Therefore, the reactivity of **5** in the presence of an excess of NO was studied.

Initially, solutions of **5** in THF were treated with about a five-fold excess of nitric oxide and the gas phase of the resulting reaction mixture was analyzed by IR spectroscopy. The formation of N_2O was clearly detected at 2224 cm^{-1}, whereas the excess of gaseous nitric oxide was observed at 1876 cm^{-1} (Figure 43, black trace).
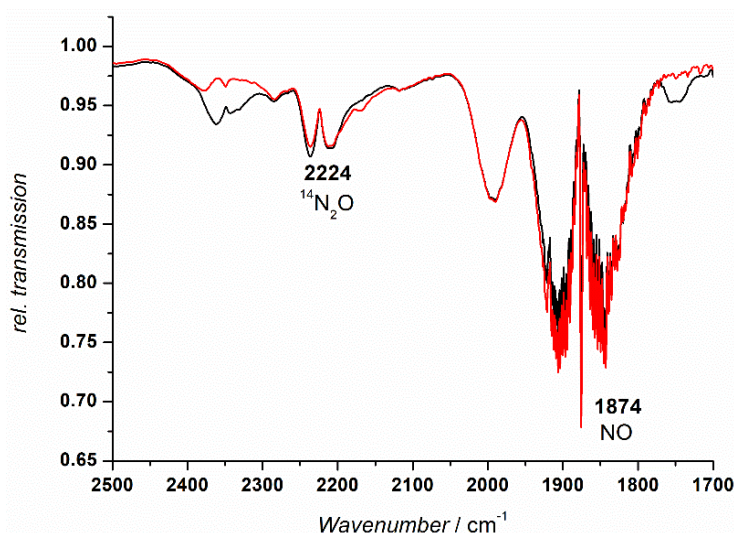
Figure 43. Right: gas phase IR spectrum of the reaction mixture corresponding to **5** treated with an excess of [14]NO (black) and **5**-[15]NO treated with [14]NO (red).

Crystalline material was isolated from the reaction mixture and X-ray diffraction analysis confirmed that disproportionation of NO led to the formation of a nitrito complex $LNi_2(NO_2)$ **(8)**, according to Scheme 38. The molecular structure of **8** is represented in Figure 44. Selected bond lengths and angles are tabulated in Table 3.
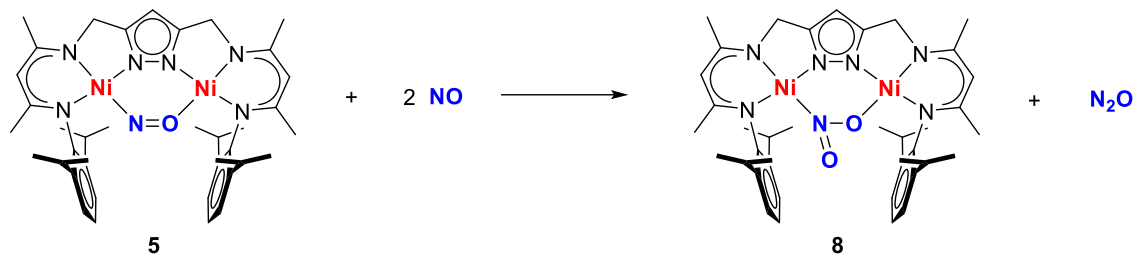
Scheme 38. Disproportionation of nitric oxide mediated by **5**.
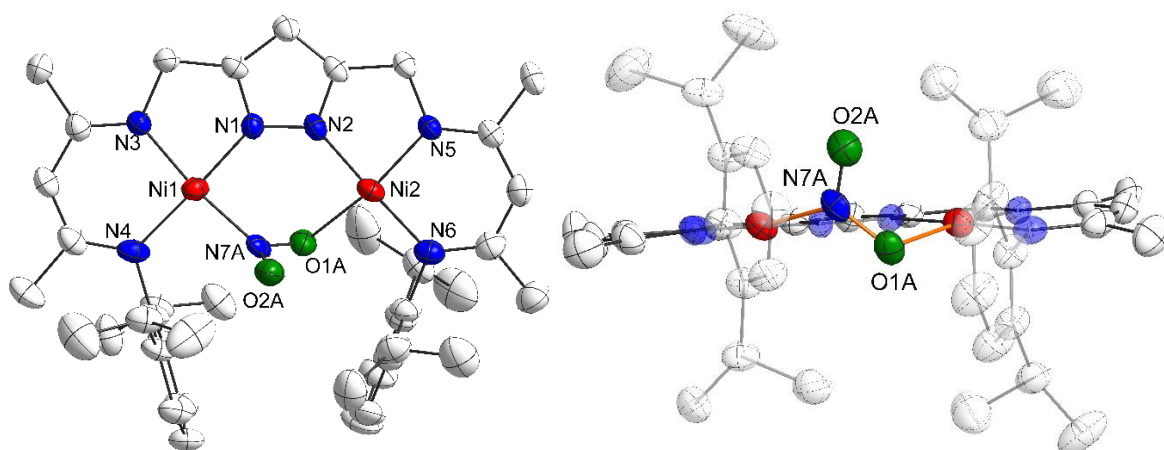
Figure 44. Left: X-ray molecular structure of compound **8**. The complex co-crystallizes with **4**. Right: front view of the molecular structure of **8**. The torsion angle ∢(Ni(1)-N(7A)-O(1A)-Ni(2)) is highlited in orange.

Table 3. Selected bond length (Å) and angles (°) for compound **8**.

Bond length / Å		Angle / °	
Ni(1)-N(1)	1.836(4)	N(1)-Ni(1)-N(3)	82.74(16)
Ni(1)-N(3)	1.876(4)	N(3)-Ni(1)-N(4)	88.96(7)
Ni(1)-N(4)	1.891(4)	N(1)-Ni(1)-N(7A)	89.3(3)
Ni(1)-N(7A)	1.847(8)	N(1)-Ni(1)-N(4)	177.66(17)
Ni(2)-N(2)	1.843(4)	N(3)-Ni(1)-N(7A)	167.6(3)
Ni(2)-N(5)	1.874(4)	N(2)-Ni(2)-N(5)	83.08(16)
Ni(2)-N(6)	1.882(4)	N(5)-Ni(2)-N(6)	95.18(17)
Ni(2)-O(1A)	1.191(8)	N(6)-Ni(2)-O(1A)	92.0(3)
N(7A)-O(1A)	1.314(10)	N(2)-Ni(2)-N(6)	177.55(17)
N(7A)-O(2A)	1.198(9)	N(5)-Ni(2)-O(1A)	169.4(3)
Ni(1)···Ni(2)	3.799(9)	O(1A)-N(7A)-O(2A)	117.1(7)
		Ni(1)-N(7A)-O(1A)-Ni(2)	89.82(67)

Characterization of the complex in the solid state showed that the crystals contained both the nitrito complex **8** and the μ-hydroxo complex **4** in roughly 60 : 40 ratio. Formation of **4**

probably resulted from the degradation of both **5** and **8**, which typically occurs when the solutions are left at room temperature under a slight excess of NO atmosphere for prolonged periods.

8 crystallizes in the monoclinic space group $P2_1/c$ with four molecules per unit cell. The nickel ions are both found in a roughly square planar geometry, as expected for a ls-d^8 nickel(II) center. The metal-metal distance of 3.79 Å is very similar to that of the starting material **5**, as are the Ni-N distances for both metal centers, which range from 1.83 Å to 1.89 Å. A $[NO_2]$ bridging unit is bound between the two nickel ions, which displays a formal charge of -1, by virtue of the neutral nature of the complex. Similarly to compound **5**, the bridging nitrite moiety shows a μ-η^1:η^1 binding mode, and is located out of plane with respect to the dinickel-ligand scaffold as indicated by the torsion angle $\sphericalangle$(Ni(1)-N(7A)-O(1A)-Ni(2)) of 86.8°. The Ni(1)-N(7A) and Ni(2)-O(1A) distances are 1.84 Å and 1.91 Å, respectively, and did not show any significant change in comparison with **5**. The N(7A)-O(2A) distance of 1.19 Å is consistent with double bond character, while the d(N(7A)-O(1A)) = 1.31 Å is much longer, indicating single bond character. While many binding motifs of nitrite groups have already been reported for several metal complexes,[179,180,181] the coordination mode of the $(NO_2)^-$ moiety in **8** is unprecedented.

Liquid Injection Field Desorption (LIFDI) and mass spectrometry also showed a signal at m/z = 768, confirming the formation of the nitrito complex **8**. Therefore, the disproportionation of NO by compound **5** takes place as already represented in Scheme 38. To offer first insights into such reactivity, scrambling experiments were conducted. Treatment of **5**-^{15}NO with a large excess of ^{14}NO and subsequent stirring for two hours led to the following results: the analysis of the IR gas phase of the reaction mixture indicated the formation of $^{14}N_2O$ (band at 2224 cm^{-1}), while LIFDI measurements suggested the formation of LNi$_2$(^{14}NO$_2$). Formation of ^{15}NO labeled products was not observed, suggesting that in presence of a large excess of ^{14}NO, exchange between the ^{15}NO moiety of the complex and the gas occurs. The experiment was then repeated using a lower amount of ^{14}NO (ca. five equivalents) and stirring for not more than 30 minutes. In these conditions, the IR of the gas phase mixture still showed exclusive formation of $^{14}N_2O$, and $^{14}N^{15}$NO was not observed, as shown in Figure 43 (right, red trace). On the other hand, the LIFDI spectrum of the reaction mixture showed formation of the corresponding labeled LNi$_2$(^{15}NO$_2$) compound without traces of LNi$_2$(^{14}NO$_2$) (Figure 45).
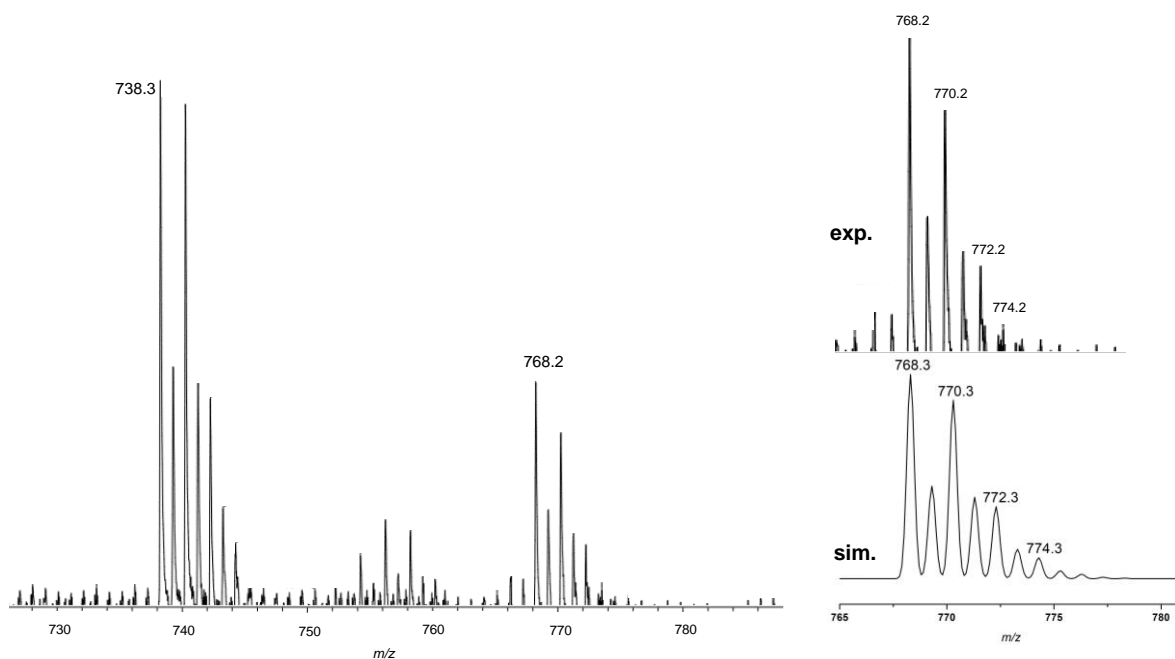
Figure 45. LIFDI of **5**-^{15}NO treated with ^{14}NO shows formation of LNi$_2$(^{15}NO$_2$) (*m/z* = 768.2). The peak at *m/z* = 738.3 corresponds to the hydroxo complex **4**.

The same experiments were conducted starting from LNi$_2$(^{14}NO) **5** and ^{15}NO. The gas was prepared in situ by treating an aqueous solution of Na^{15}NO$_2$ with ascorbic acid. From these experiments, release of ^{15}N$_2$O was detected in the IR spectrum with the characteristic doublet at 2154 cm^{-1}, and the formation of the corresponding LNi$_2$(^{14}NO$_2$) compound was confirmed by LIFDI analysis (*m/z* = 767.3).
The results are shown in Figure 46.
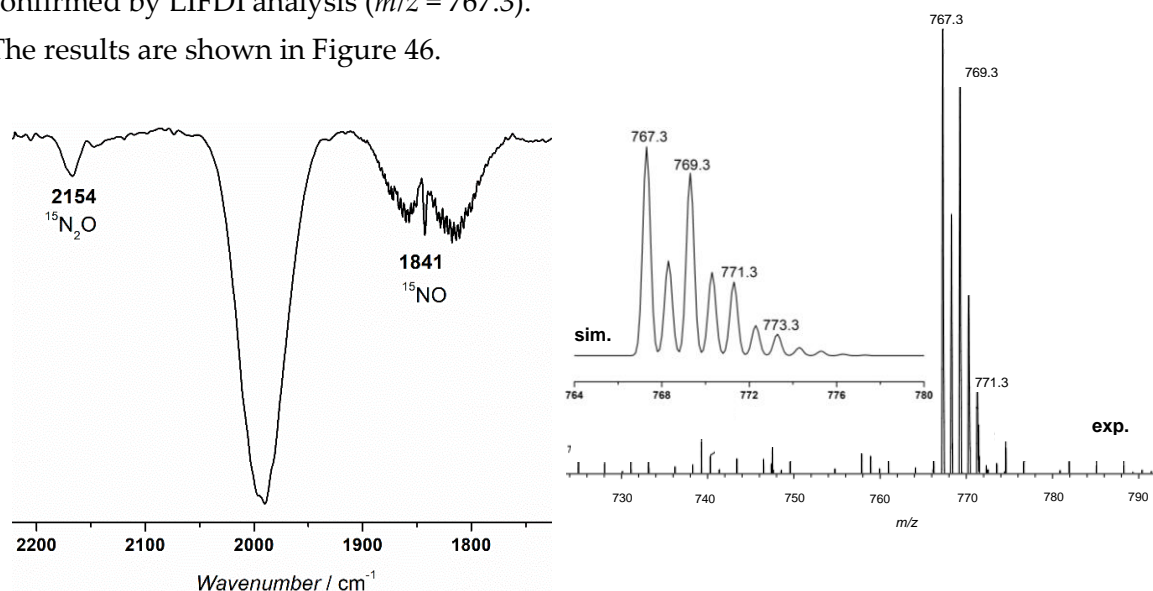
Figure 46. The gas phase IR spectrum of the reaction mixture containing **5** and an excess of ^{15}NO (left) shows formation of ^{15}N$_2$O, and LIFDI-MS of shows formation of LNi$_2$(^{14}NO$_2$) (*m/z* = 767.3) (right).

The reactivity pathway deduced from the scrambling experiments can then be summarized in Scheme 39. Previous studies on the mechanism of mononuclear copper,[182] manganese[180] and iron[181] complexes indicated that the disproportionation of NO occurs via at least two possible pathways that involve either a hyponitrite (N_2O_2) formation or a dinitrosyl intermediate as initial key step of the reaction. The possible reaction mechanism is depicted in Scheme 40.
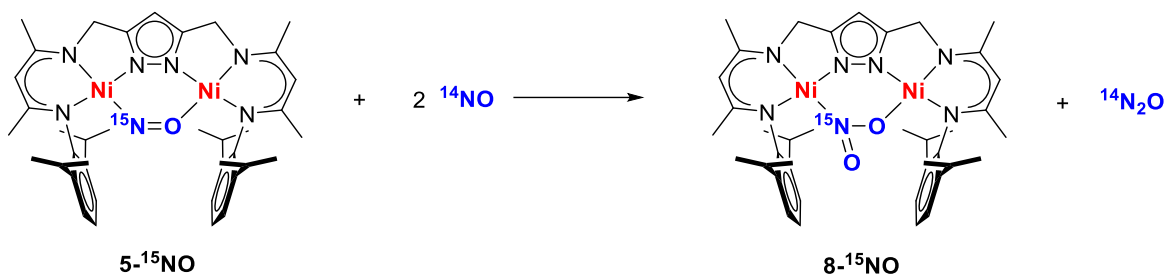
Scheme 39. Reaction pathway for the disproportionation of NO suggested by [14]NO/[15]NO labeling studies.
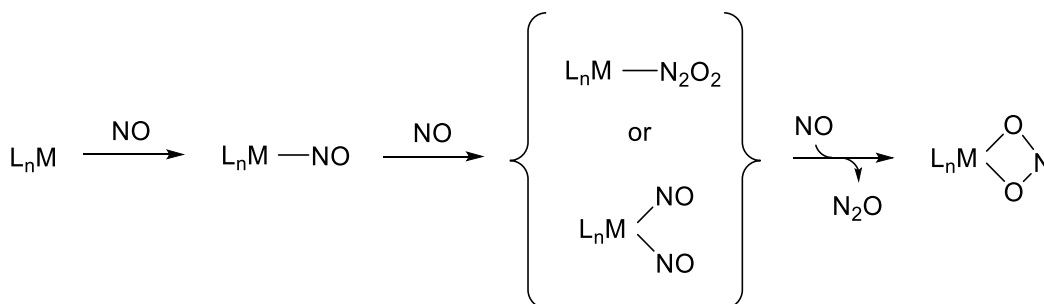
Scheme 40. Mechanistic pathway for the disproportionation of NO catalyzed by mononuclear metal complexes.

Indeed, similar mechanisms are suggested for these systems where an electrophilic attack by a second molecule of NO onto an initial M-NO adduct to give a $M(NO)_2$ species is assumed. This first step is followed by N-N coupling and O-atom transfer to NO to give $(NO_2)^-$ coordinated to the metal center, with and subsequent release of N_2O.

Hence, it is reasonable to propose a similar reaction pathway for the interaction of the nitrosyl complex **5** with excess NO. The NO-exchange step that was detected in complex **5** could support the existence of a dinitrosyl intermediate along the reaction pathway. However, further reactivity studies and DFT calculations are necessary in order to support the interpretation of the data and to elucidate the mechanism.

4.6 Summary

In this chapter, the synthesis of a new dinickel nitroxyl compound **5** was presented and its electronic properties were studied in order to gain insights into the reductive coupling of two molecules of NO that led to the formation of the corresponding hyponitrite complex **3**, presented in Chapter 3. Complex **5** is the result of the two-electron reduction of NO$^+$ mediated by the dinickel dihydride starting material **2**, and its structural characterization revealed an unprecedented binding mode for the nitroxyl N,O-bridging moiety.

The redox properties of **5** were investigated, and it was shown that the complex could be reversibly reduced to a [LNi$_2$(NO)]$^-$ radical species, which was chemically isolated by direct treatment of **5** with a suitable reducing agent. When Co(Cp*)$_2$ was used, compound **6** was formed, whose electronic structure revealed a localization of the unpaired electron mostly on the metal centers. Therefore, a mostly metal center reduction occurs and the compound attains a nickel(I) character. On the other hand, the introduction of metal alkali cations significantly influences the electrochemical behavior of complex **5**. For instance, cyclic voltammetry studies on **5** in the presence of KB(Ar^F)$_4$ revealed much lower reducing potentials and the process becomes irreversible. On the other hand, chemical reduction of **5** with potassium benzophenone allowed for the isolation of the new species KLNi$_2$(NO) **7** which was characterized in solution and in the solid state. **7** represents a rare example of a dinickel complex with a (NO)$^{2-}$ bridging unit. Furthermore, EPR analysis showed that the presence of the potassium ion, which is held between the two aryl groups of the ligand scaffold, shifts electron density within the [LNi$_2$(NO)]$^-$ complex and the unpaired electron now mostly resides on the NO bridging moiety, suggesting a more ligand centered reduction of complex **5**.

Consequently, both compounds **6** and **7** were both shown to be involved in the NO reduction process to form the hyponitrite compound **3**. The aforementioned results are summarized in Scheme 41.

Finally, the reactivity of the nitroxyl compound **5** was tested using NO. In the presence of excess NO, the compound showed to be active for NO disproportionation that led to formation of the corresponding compound LNi$_2$(NO$_2$) **8** and N$_2$O. By means of gas phase IR spectroscopy, LIDFI mass analysis and labelling studies, further insights into the reaction mechanism were obtained. Additional DFT calculation would then be beneficial to unambiguously explain the reactivity pathway.
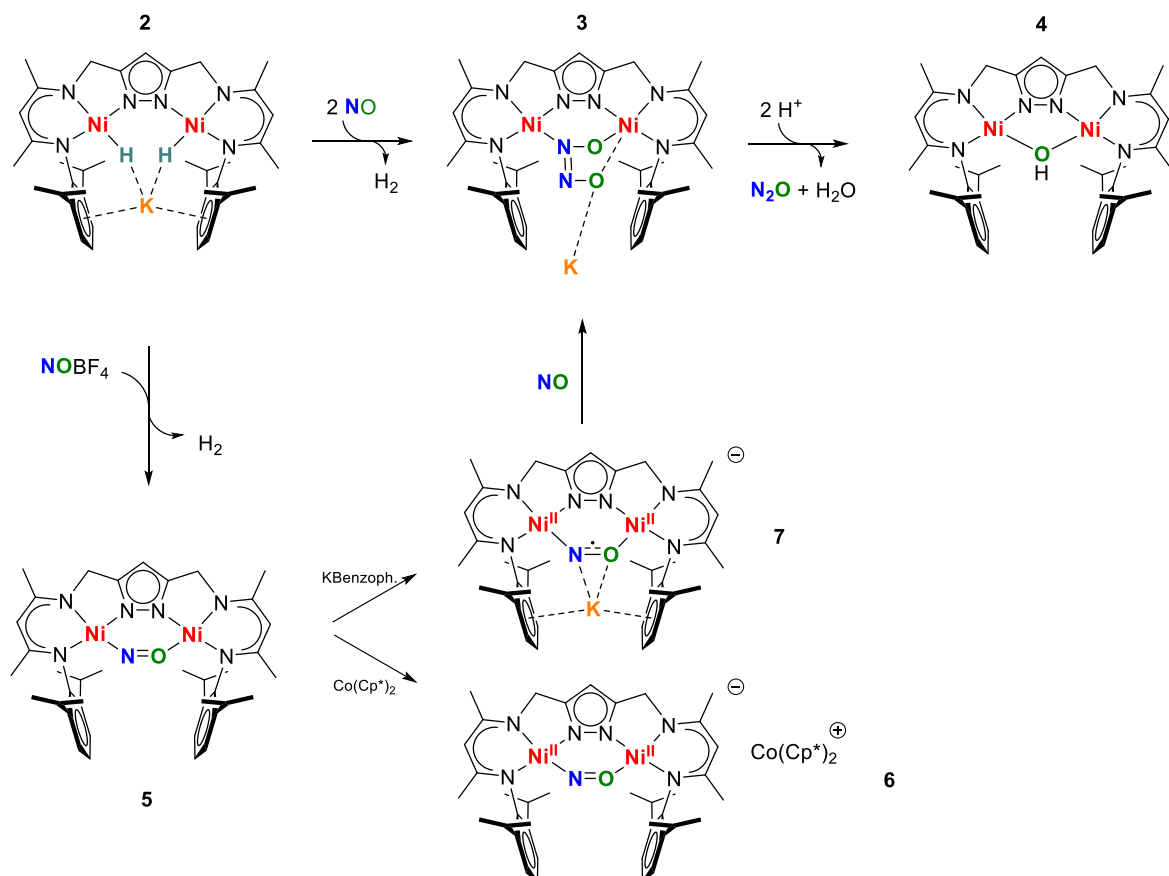
Scheme 41. Summary of the redox transformations of NO on the **L³⁻** based dinickel scaffold.

5 Reductive Binding of Nitrosobenzene at a Dinickel(II) Dihydride Complex

5.1 Synthesis of a Nitrosobenzene-Bridged Adduct

The previous chapters described the ability of complex **2** to reductively bind a small molecule such as nitric oxide and to be a suitable scaffold for its subsequent redox transformations. The possibility of interconverting the oxidation state of the NO unit at the nickel centers, and finally to trigger the reduction process to give the final products nitrous oxide N_2O and water, represents an additional step in understanding the coordination chemistry of NO. Motivated by the importance of NO reactivity in biological systems, the chemistry of organonitroso compounds was studied since related species are thought to be endogenously produced and involved in a variety of conversions, which are connected to the redox chemistry of NO_x species.[183] Furthermore, the structural diversity[184] of these compounds as well as their possible application for catalytic reduction (e.g. reductive carbonylation)[185] encourage to expand the knowledge on such systems.

The nickel nitrosobenzene systems described in Chapter 1 illustrate the ability of Ni^I sources to reductively bind the organic molecule which can be in turn reduced by one electron. Further studies in this regard would aim to better understand this reactivity, and take advantage of metal-metal cooperativity. Therefore, inspired by the relative ease for H_2 elimination and rich chemistry of **2**, the reactivity towards nitrosobenzene (PhNO) was investigated. Treatment of an orange THF solution of the dinickel dihydride complex **2** at room temperature with one equivalent of nitrosobenzene led to evolution of dihydrogen and a fast color change from red to black (Scheme 42). The outcome of the reaction was initially studied by recording an ESI-MS spectrum, which showed two peaks at $m/z = 851.3$ and $m/z = 867.3$. These signals were assigned to $[LNi_2(PhNO) + Na]^+$ and $[LNi_2(PhNO) + K]^+$ (Appendix, Figure 6), respectively, indicating the successful formation of the new dinickel complex $KLNi_2(PhNO)$ **9**. The compound was further characterized by means of several spectroscopic techniques, included single crystal X-ray diffraction.

Complex **9** proved fairly stable in the solid state under strictly inert conditions, which allowed for its straightforward characterization. However, further analyses in solution were hindered by the general poor solubility of the compound in most of the organic solvents commonly used for nickel complexes based on the L^{3-} scaffold (i.e. THF, MeCN).
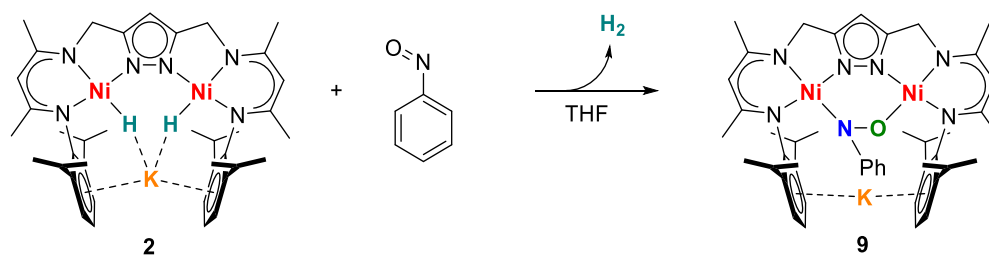
Scheme 42. General synthetic strategy for the isolation of a new dinickel nitrosobenzene complex KLNi$_2$(PhNO) **9** from the dihydride precursor **2**.

In order to overcome the problem, the general solubility of the compound was enhanced by treating a black THF suspension of complex **9** with one equivalent of [2.2.2]-cryptand at room temperature (Scheme 43). The three-dimensional internal pocket of the cryptand supplied a suitable binding site for the potassium cation K$^+$, which was easily removed from the cavity between the two aryl rings of the ligand scaffold. After purification, compound **10** was isolated as a dark green crystalline material in high yield, and was characterized in solution and in the solid state. A comparison of the main features and additional reactivity studies of the above mentioned complexes are presented in the following sections.
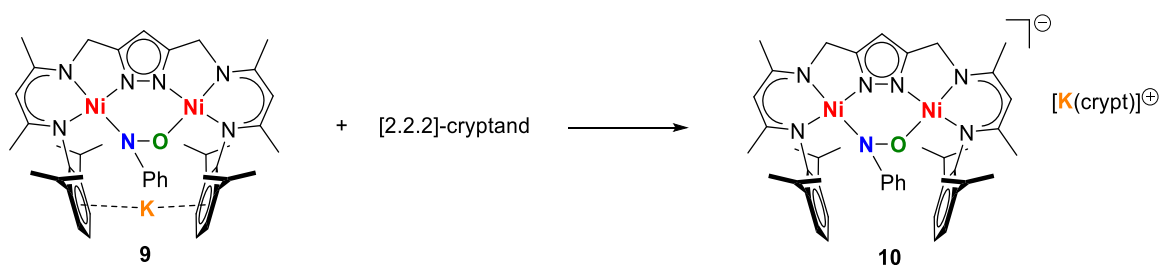
Scheme 43. The potassium cation K$^+$ can be removed from the cavity in complex **9** by treatment with [2.2.2]-cryptand to obtain compound **10**.

5.1.1 Structural Characterization

Evidence for the successful activation of nitrosobenzene at the dinickel centers was obtained from X-ray crystallography. The molecular structures of compounds **9** and **10** are shown in Figure 47, and characteristic bond lengths and angles are reported in Table 4 and Table 5, respectively, to allow a direct comparison between the two complexes.
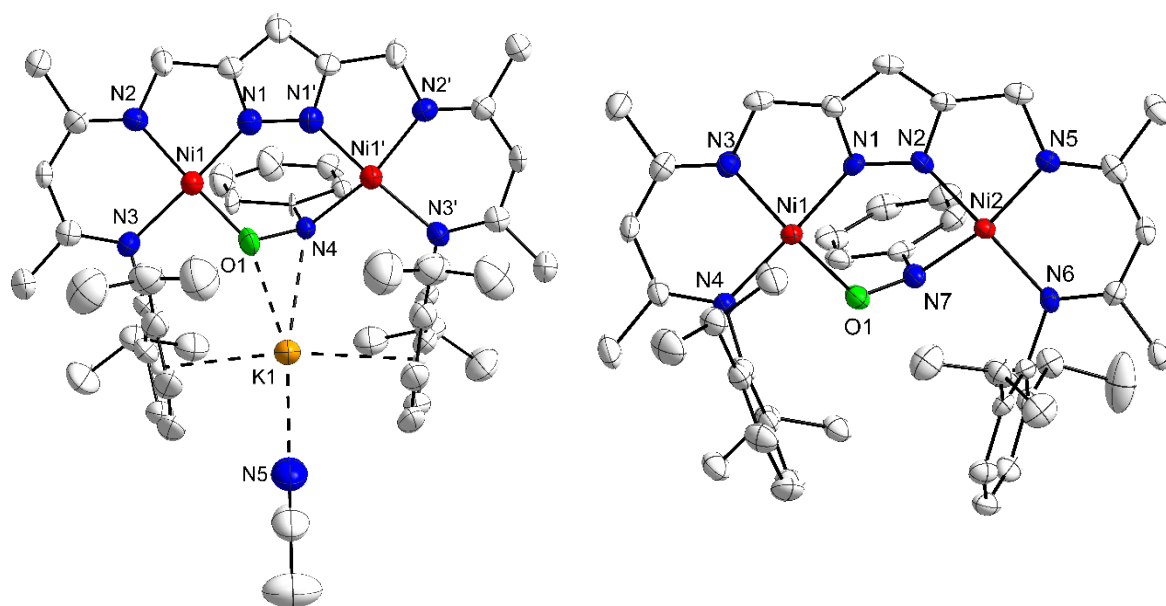
Figure 47. Thermal displacement ellipsoid (50% of probability) of the molecular structure of compound KLNi$_2$(PhNO) **9** (left) and [K(crypt)][LNi$_2$(PhNO)] **10** (right). Hydrogen atoms, solvent molecules and counterion were omitted for clarity.

Table 4. Selected bond lengths of KLNi$_2$(PhNO) **9** and [K(crypt)][LNi$_2$(μ-PhNO)] **10**.

KLNi$_2$(μ-PhNO), 9		[K(crypt)][LNi$_2$(μ-PhNO)], 10	
Bond length / Å			
Ni(1)-N(1)	1.862(5)	Ni(1)-N(1)	1.861(3)
Ni(1)-N(2)	1.913(5)	Ni(1)-N(3)	1.908(4)
Ni(1)-N(3)	1.931(5)	Ni(1)-N(4)	1.909(3)
Ni(1)-O(1)	1.798(10)	Ni(1)-O(1)	1.865(3)
Ni(1')-N(1')	1.862(5)	Ni(2)-N(2)	1.842(4)
Ni(1')-N(2')	1.912(5)	Ni(2)-N(5)	1.917(5)
Ni(1')-N(3')	1.930(5)	Ni(2)-N(6)	1.909(3)
Ni(1')-N(4)	1.992(9)	Ni(2)-N(7)	1.895(3)
N(4)-O(1)	1.486(14)	N(7)-O(1)	1.374(4)
Ni(1)···Ni(1')	3.921(8)	Ni(1)···Ni(2)	3.826(7)

Table 5. Selected angles of KLNi2(PhNO) **9** and [K(crypt)][LNi2(μ-PhNO)] **10**.

KLNi2(μ-PhNO), 9		[K(crypt)][LNi2(μ-PhNO)], 10	
	Angle / °		
N(1)-Ni(1)-N(2)	80.03(2)	N(1)-Ni(1)-N(3)	82.48(1)
N(1)-Ni(1)-O(1)	93.81(3)	N(1)-Ni(1)-O(1)	93.86(1)
N(2)-Ni(1)-N(3)	92.70(2)	N(3)-Ni(1)-N(4)	93.41(1)
N(2)-Ni(1)-O(1)	174.19(35)	N(3)-Ni(1)-O(1)	175.26(14)
N(1)-Ni(1)-N(3)	172.49(24)	N(1)-Ni(1)-N(4)	170.82(14)
N(1′)-Ni(1′)-N(3′)	172.49(24)	N(2)-Ni(2)-N(5)	82.99(14)
N(2′)-Ni(1′)-N(4)	160.16(30)	N(2)-Ni(2)-N(7)	87.78(14)
N(4)-Ni(1′)-N(3′)	98.20(31)	N(7)-Ni(2)-N(6)	95.60(14)
Ni(1)-O(1)-N(4)	119.85(67)	Ni(1)-O(1)-N(7)	119.77(23)
O(1)-N(4)-Ni(1′)	120.65(65)	O(1)-N(7)-Ni(2)	121.92(25)

Black crystals of **9** suitable for X-ray diffraction were obtained by slow diffusion of diethyl ether and pentane into a THF/MeCN solution of **9** at -30°C. Complex **9** crystallizes in the monoclinic space group $P2_1/m$ and the two nickel(II) ions exhibit a distance of 3.92 Å, which is consistent with those found for analogous nickel complexes of pyrazolate-based ligand L^{3-} systems.[148] However, the metal-metal distance is relatively large, in comparison with other nickel compounds based on ligand systems similar to L^{3-} (3.60 Å, 3.43 Å).[186] The nitrosobenzene moiety is N,O-bridging between the two nickel centers in a μ-η^1:η^1 binding mode. As a result, while the Ni(1) atom is coordinated in an ideal square-planar fashion (∡ N(2)-Ni(1)-O(1) = 174° and ∡ N(1)-Ni(1)-N(3) = 172°), the environment around Ni(1′) is slightly distorted (∡ N(2′)-Ni(1′)-N(4) = 160° and ∡ N(1′)-Ni(1′)-N(3′) = 172°). In fact, due to the steric demand of the diisopropylphenyl side arm of the ligand, the aromatic ring of the PhNO substrate in **9** is essentially pushed out of the ideal Ni-N-N-N plane, moving also the nitrogen atom. Nevertheless, these parameters are in agreement with both nickel centers being in the oxidation state of +2. This results in a formal charge on the PhNO bridging moiety of -2, consistent with the two electron reduction of nitrosobenzene promoted by compound **2**. Consequently, the N(4)-O(1) distance of 1.486(14) Å indicates a significant reduction of the NO bond order, with respect to that in reported free nitrosoarenes compounds, which possess N-O distances of 1.13 Å - 1.29 Å.[61]

Single crystals suitable for X-ray diffraction of **10** were grown by slow diffusion of pentane into a solution of **10** in THF at -30°C. The complex crystallizes in the monoclinic space group $P2_1/c$, with a Ni(1)···Ni(2) distance of 3.826(7) Å, which is roughly 0.1 Å shorter than that found for **9**. Overall, the nitrosobenzene adduct **10** possesses average Ni-N$_{nacnac}$ and Ni-N$_{pz}$

distances that are similar to those found in complex **9**. However, two major structural differences can be found by comparing the two compounds **9** and **10** in the solid state: the potassium counterion in **10** is no longer held in the cavity, but is separated from the [LNi$_2$(PhNO)]$^-$ complex anion and encapsulated by the cryptand. Interestingly, the N(7)-O(1) distance in **10** of 1.374(4) Å is close to those in previously reported mononuclear β-diketiminate Cu complexes (1.333 Å - 1.336 Å)[34] (Chapter 1, Figure 7a) but it becomes significantly shorter than in **9** and other dinuclear β-diketiminate Ni analogues (Chapter 1, Figure 7c). This suggests that the position of the potassium cation (held between the side arms in **9** or encapsulated by the cryptand in **10**) influences the electronic structure of the anion, and the N-O distance in **9** and **10** results to be significantly different.

An overview of nitrosobenzene complexes relevant for this thesis work is given in Table 6, which reports the characteristic N-O bond distance for the corresponding metal complex and the related binding mode of the organic moiety. Furthermore, the IR values for the corresponding NO vibrations (Ph^{14}NO/Ph^{15}NO) are shown, and the parameter will be discussed in detail in Section 5.1.3.

Table 6. Geometric and spectroscopic features of relevant nitrosobenzene PhNO complexes reported so far. The compounds described in this work are included.

Ligand/Complex	Counterion	Binding mode	d(N-O) / Å	IR $\tilde{\nu}$(N-O)/ cm^{-1} (Δ[^{15}NO])	Reference
PhNO	-	-	1.21-1.23[a]	1506	[59]
[LNi$_2$(μ-PhNO)]$^-$ (**9**)	K$^+$	μ-η^1:η^1	1.48	907 (894)	this work
[LNi$_2$(μ-PhNO)]$^-$ (**10**)	[Kcryptand]$^+$	μ-η^1:η^1	1.37	973 (954)	this work
(CF$_3$-nacnac)Ni(PhNO) Fig. 7 **(b)**	b	η^2	1.32	968 (950)	[62]
[(CF$_3$-nacnac)Ni(PhNO)]$^-$	[K(18-crown-6)]$^+$	μ-η^2:η^2	1.38	765 (751)	[62]
[(nacnac)Ni]$_2$(ArNO) Fig. 7 **(c)** Ar = 3,5-Me$_2$C$_6$H$_3$	b	μ-η^2:η^2	1.44	-	[34]
[(nacnac)Ni]$_2$(PhNO)	b	μ-η^2:η^2	-	915 (901)	[34]
(nacnac)Cu(PhNO) Fig. 7 **(a)**	b	η^2	1.33	1113 (1093)	[34]
[(nacnac)Cu]$_2$(PhNO)	b	μ-η^2:η^1	1.37	1040 (1029)	[34]
[(Cp*Rh)$_2$(μ-Cl)(PhNO)]$^+$	[BF$_4$]$^-$	μ-η^2:η^2	1.422	1001	[187]
[{Cp*Ru(S(iPr))}$_2$(PhNO)]$^+$	[OTf]$^-$	μ-η^1:η^1	1.35	-	[188]
[{Cp*Rh(S(iPr))}$_2$(PhNO)]$^+$	[BPh$_4$]$^-$	μ-η^1:η^1	1.33	-	[188]
[{Cp*Ir(S(iPr))}$_2$(PhNO)]$^+$	[BPh$_4$]$^-$	μ-η^1:η^1	1.34	-	[188]
[CpCo(PhNO)]$_2$	b	μ-η^2:η^1	1.38	1047	[189]

[a] Free nitrosoarenes exist in both monomeric and dimeric form. [b] Neutral complex

5.1.2 NMR Spectroscopy

NMR experiments with samples of crystalline material of **9** were prevented by the poor solubility in THF-d_8. Thus, **10** was used for the characterization of the nitrosobenzene-bridged adduct in solution, and the resulting ^{1}H-NMR spectrum is shown in Figure 48. The formation of a complex with a lower symmetry with respect to the starting material **2** is reflected by the large number of proton resonances, which is consistent with the molecular structure of **10** in the solid state obtained by X-ray diffraction analysis. The resonances of the spectrum were assigned to the corresponding protons based upon their relative intensities, the coupling of the neighboring protons observed by ^{1}H-^{1}H COSY NMR spectroscopy (Figure 49), and on comparison with the related complex LNi_2(NO) **5**.

For instance, the characteristic CH-pyrazole resonance at 5.22 ppm and two distinct resonances at 4.39 and 4.36 ppm that belong to the CH protons of the nacnac backbone (signals 6 and 7 in Figure 48) were observed. In addition, a total of eight doublets that integrate for three protons each were found for the methyl groups of the isopropyl substituents in the range between 0.12 ppm and 2.17 ppm.

Interestingly, the resonances assigned to the methylene groups (CH_2), which produce a single signal in the case of the symmetric complex **2**, show a signal pattern that may result from the virtual coupling between the neighboring protons (Figure 50). However, the spectrum appears to be complex for interpretation, so that the only useful information is the integration, chemical shift and general appearance. The coupling constants obtained by the only distinguishable multiplet could indeed be in error because of second order effects.
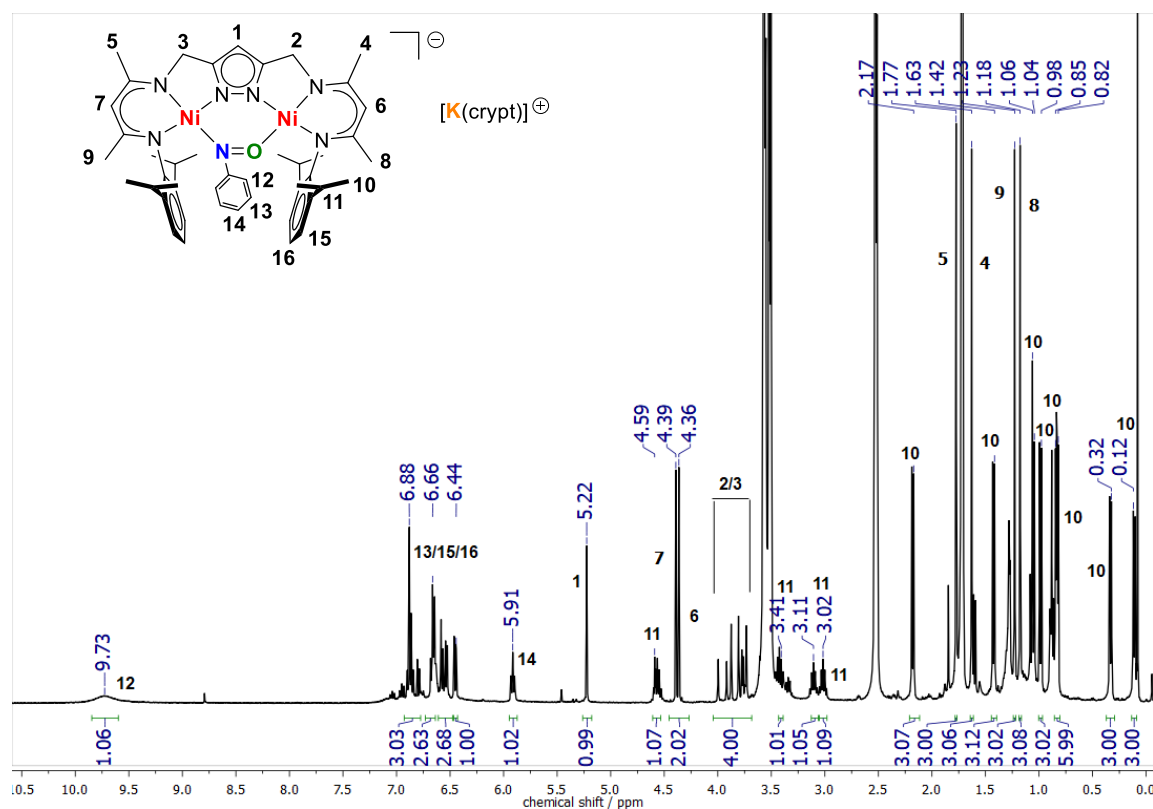
Figure 48. ^{1}H-NMR spectrum of **10** in THF-d$_{8}$ recorded at room temperature.
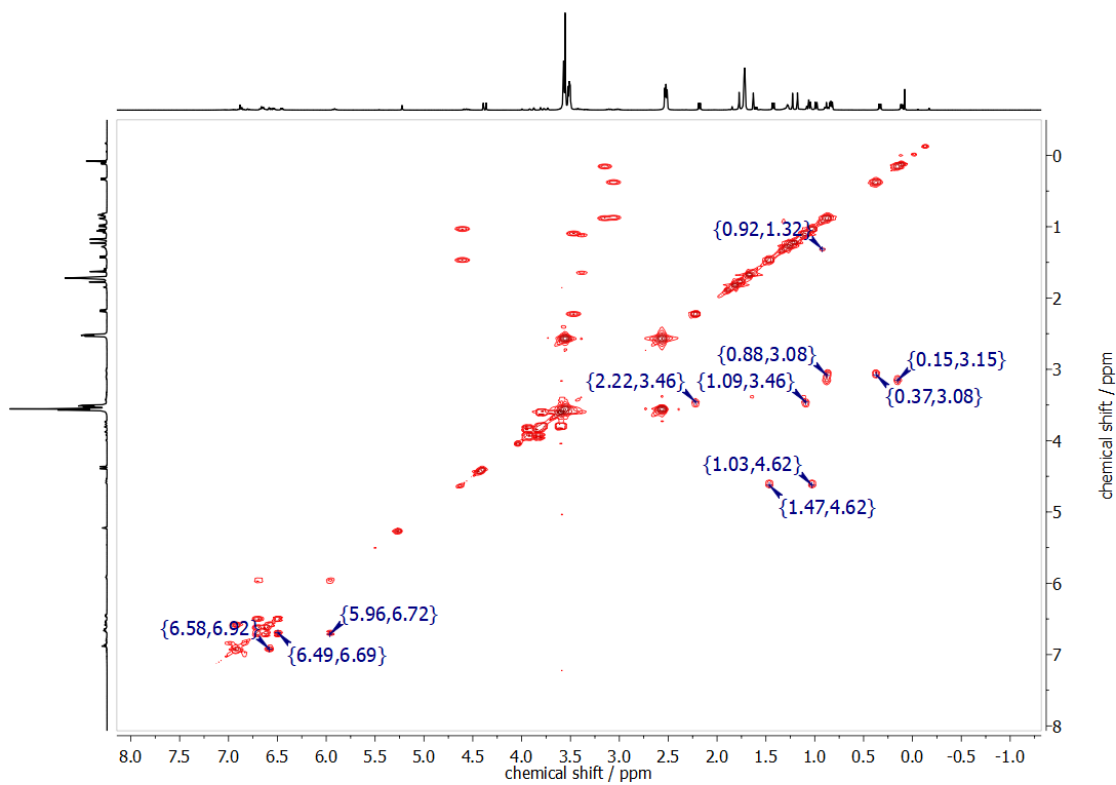
Figure 49. ^{1}H-^{1}H COSY spectrum of **10** in THF-d$_{8}$ recorded at room temperature.
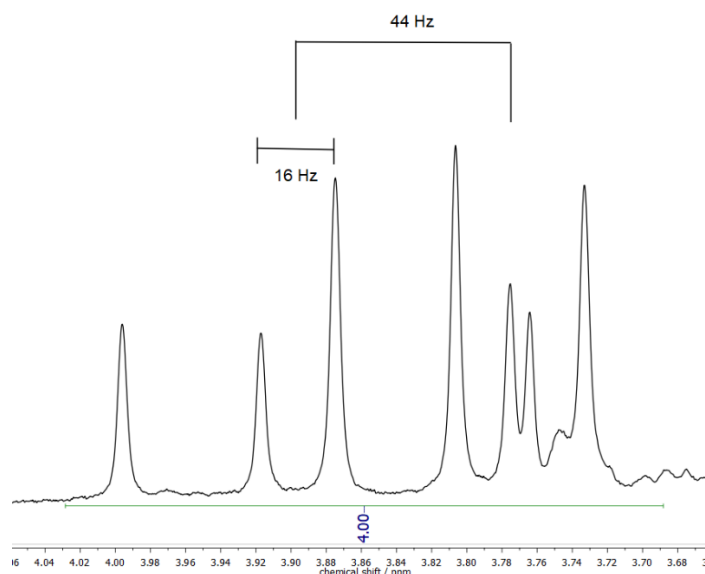
Figure 50. Multiplet attributable to the CH_2 groups observed in the ^{1}H-NMR spectrum of complex **10**.

In the region of the spectrum corresponding to the aromatic protons, a number of resonances with integrations that are almost consistent with the expected protons were observed. Interestingly, the triplet at 5.91 ppm may be assigned to the *para-H* of the phenyl substituent at the nitrogen atom of the bridging unit (signal 14), indicating a significant shielding of this proton with respect to the other aromatic signals. A possible explanation for such behavior is the position of an aryl ring of the ligand side arms that could be placed close to *para-H*. As a result, the aromatic π-system's ring current effectively shields the *para-H* atom and leads to a high fields shifted resonance.

On the other hand, the signal at 9.73 ppm is assigned to the *ortho-H* of the same phenyl group and is significantly deshielded with respect to the other aromatic protons, probably due to the electron withdrawing effect of the nitrogen atom. Furthermore, the signal shows a pronounced broadness at room temperature, making its integration difficult. This observation originates from a dynamic effect in solution, which can be associated with the rotation of the phenyl substituent at the nitrogen atom of the bridging moiety. A similar process that involves the rotation of an aryl group around the $C(sp^2)$-$C(sp^2)$ was already reported.[145,190] For instance, this effect was observed for a mononuclear cationic ruthenium complex with a η[2] coordination mode,[190] and also by MANZ for the related dinuclear nickel(II) system (**A**) represented in Figure 51.[145]

A
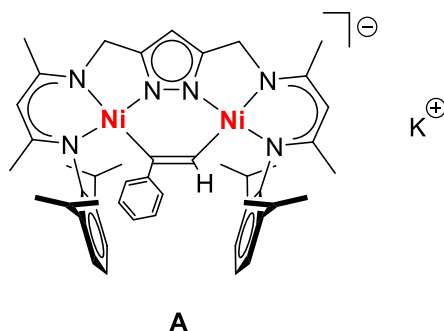
Figure 51. Complex K[LNi$_2$(μ-η^1:η^1-CHCPh)] **(A)** reported by Manz that shows a dynamic process in solution associated with the rotation of the phenyl ring.

To study the rotational barrier for this system, variable temperature ^{1}H-NMR experiments were performed in the range 308-218 K, focusing on the resonance peak at 9.73 ppm assigned to the two *ortho-H* (H$_a$, H$_e$) of the phenyl substituent (signal 12 in the ^{1}H-NMR spectrum). The results are shown in Figure 52.
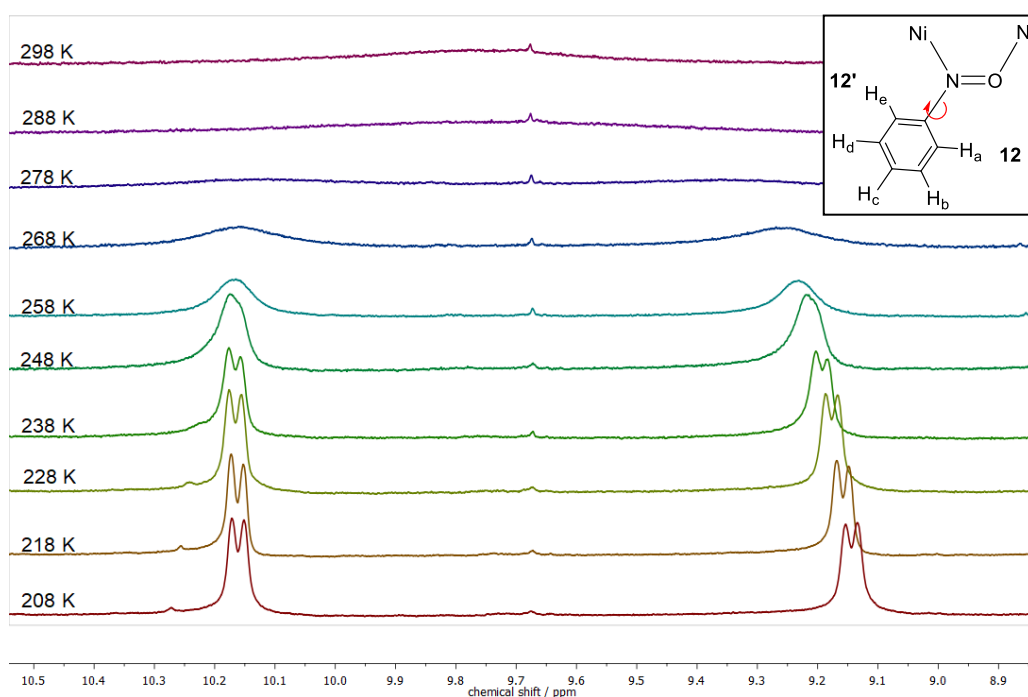
Figure 52. Temperature dependent ^{1}H-NMR experiments (400 MHz) of complex **10** in THF-d^8 in the range 298 K - 208 K. H$_a$ and H$_e$ represent the two hydrogen atoms in ortho position of the phenyl ring.

Line shape analysis was used in order to extract the activation parameters from the evaluation of the rotational rate constants.[191] Since the line broadening for the two protons becomes too pronounced for temperatures higher than 288 K due to a large chemical shift difference of $\Delta\delta \approx 450$ Hz, those values were not considered.

For the considered spectra, the frequencies ν_A and ν_B and the signal width at half-height $\Delta\nu_{\frac{1}{2}}$ were determined in order to calculate the rate constants k for the exchange at each temperature. The data were divided into groups corresponding to slow and intermediate exchange, coalescence temperature and fast exchange and the equations (5.1)-(5.4) were used:

Slow exchange
$$k = \pi[(\Delta\nu_e)_{\frac{1}{2}} - (\Delta\nu_0)_{\frac{1}{2}}] \tag{5.1}$$

Intermediate exchange
$$k = \frac{\pi}{\sqrt{2}}(\Delta\nu_0^2 - \Delta\nu_e^2)^{1/2} \tag{5.2}$$

Coalescence
$$k = \pi\frac{\Delta\nu_0}{\sqrt{2}} \tag{5.3}$$

Fast exchange
$$k = \frac{\pi\Delta\nu_2^0}{2}[(\Delta\nu_e)_{\frac{1}{2}} - (\Delta\nu_0)_{\frac{1}{2}}]^{-1} \tag{5.4}$$

where $(\Delta\nu_e)_{\frac{1}{2}}$ is the half-height width of the observed signals, whereas $(\Delta\nu_0)_{\frac{1}{2}}$ is considered the half-height width obtained from the spectrum measured at the lowest temperature of 208 K (zero exchange). At the coalescence temperature, $\Delta\nu_0$ represents the peak separation in Hz. The calculated rate constants for each temperature are shown in Table 7.

Table 7. Rate exchange constants calculated from the experimental NMR spectra.

T / K	k / s^{-1}
208	0
218	0.25
228	1.06
238	5.56
248	23.40
258	46.84
268	429.92
278	665.02
283 (Tc)	903.54
288	1060.04

Thermodynamic parameters could be obtained by considering the Arrhenius equation (5.5), which was used to plot $\ln(k)$ *vs.* 1/T, as shown in Figure 51 (a). A linear fit was then applied, and the activation energy could be extrapolated from the slope equal to E_a/R. In addition, the Eyring equation (5.6) and the further transformations (5.7) and (5.8) were considered to plot $\ln(k/T)$ *vs.* (1/T), as illustrated in Figure 53 (b). Application of a linear fit provided the slope $(-\frac{\Delta H^{\ddagger}}{R})$ and intercept $(23.76 + \frac{\Delta S^{\ddagger}}{R})$ values which in turn yielded the activation enthalpy and activation entropy.

$$\ln k = -\frac{E_a}{RT} + \ln A \tag{5.5}$$

$$k = \kappa \frac{k_b T}{h} \exp(-\frac{\Delta G^{\ddagger}}{RT}) \tag{5.6}$$

$$\Delta G^{\ddagger} = RT(23.76 - \ln\left(\frac{k}{T}\right)) \tag{5.7}$$

$$\ln\left(\frac{k}{T}\right) = 23.76 - \left(\frac{\Delta H^{\ddagger}}{R}\right)\frac{1}{T} + \left(\frac{\Delta S^{\ddagger}}{R}\right) \tag{5.8}$$

with

T absolute temperature

R universal gas constant ($8.3144 \; J \cdot K^{-1}$)

A frequency factor

k_b Boltzmann constant ($1.3805 \cdot 10^{-23} \; J \cdot K^{-1}$)

h Planck constant ($6.6256 \cdot 10^{-34} \; J \cdot s$)

κ transmission coefficient (usually equal to 1)
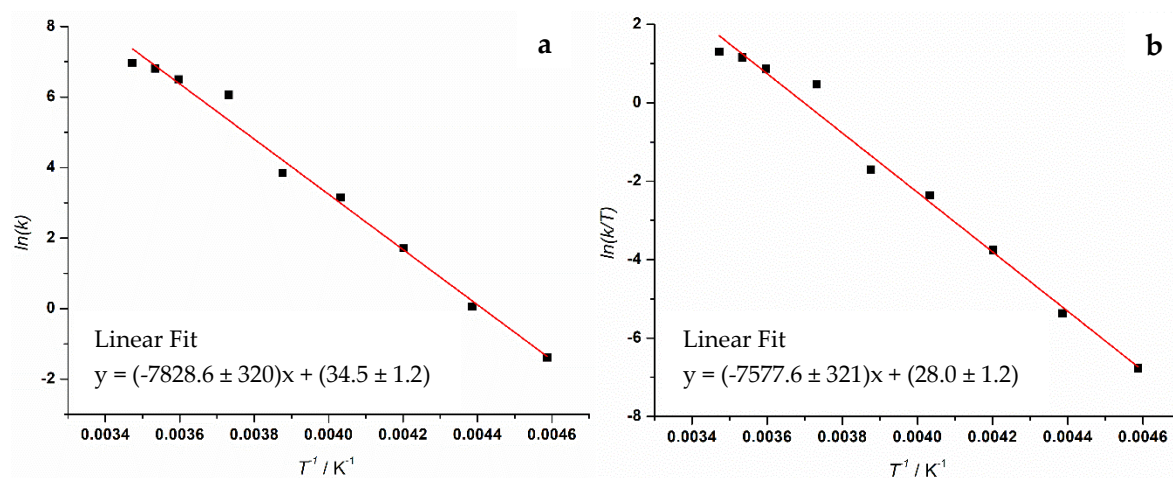
Figure 53. Arrhenius (a) and Eyring (b) plot for the obtained exchange constants. The linear fit is represented by the red line.

The values for the activation enthalpy and entropy could be derived from the linear fit, and the corresponding free activation energy was calculated using the equation (5.8). Table 8 summarizes the determined activation parameters.

$$\Delta G^{\ddagger} = \Delta H^{\ddagger} - T\Delta S^{\ddagger}$$

Table 8. Activation parameters determined by the variable temperature NMR experiment.

E_a		$\Delta H^{\ddagger}$		$\Delta S^{\ddagger}$		$\Delta G_{298}^{\ddagger}$	
kJ mol^{-1}	kcal mol^{-1}	kJ mol^{-1}	kcal mol^{-1}	J K^{-1} mol^{-1}	cal K^{-1} mol^{-1}	kJ mol^{-1}	kcal mol^{-1}
65.1±2.7	15.6±0.6	62.7±2.7	15.0±0.6	35±9	8.3±2.1	52.1±1.0	12.5±0.3

Comparable results for the rotational barrier of the phenyl group in a $\mu\text{-}\eta^1\text{:}\eta^1$ nitrosobenzene complex were not found since this binding mode observed for the organic molecule remained unprecedented until now. Nevertheless, the obtained values were correlated to an anionic platinum nitrosobenzene compound, which NMR studies were initiated in order to find out whether the large barrier of free rotation in similar compounds could be altered by coordination to a metal center.[192] A similar value of free energy activation was found for a Pt nitrosobenzene complex para-substituted with an amino function (54.6 kJ mol^{-1} at 303 K), whereas a significant lower energy value was found for a –OMe substituent (39.7 kJ · mol^{-1} at 223 K). The value of 52.1 kJ · mol^{-1} at 298 K obtained for compound **10** is then of similar magnitude to that of the free organonitroso ligand.[193] Those data suggest that the coordination of the nitrosobenzene group to the nickel ions does not effect the barrier for rotation of the phenyl ring with respect to the N=O group. In addition, the value is in agreement with the one found for compound **A** (Figure 51) of 57 kJ · mol^{-1} at 298 K obtained by MANZ.[145]

Finally, to complete the NMR characterization of the complex, a ^{15}N-^{1}H HMBC spectrum of the labeled **10**-^{15}NO compound was recorded in order to indirectly observe the nitrogen atom resonance belonging to the NO group of the nitrosobenzene ligand (Figure 54). At room temperature, a NH cross correlation between the proton of the phenyl group in ortho position with respect to the nitrogen and the ^{15}N atom was observed. The ^{15}N resonance at -213.8 ppm was found in the range of other similar nickel complexes based on **L**$^{3-}$ ligand system.[145]
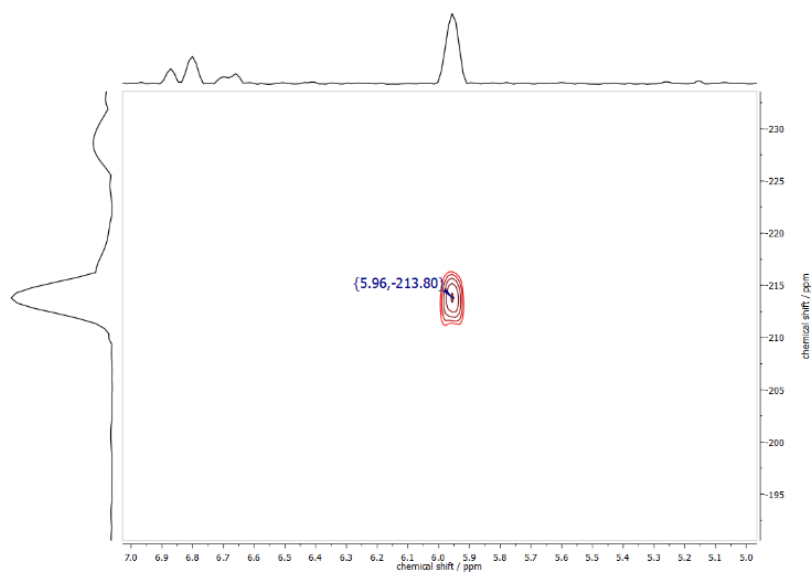
Figure 54. ^{1}H-^{15}N HMBC spectrum (400 MHz) of **10**-^{15}NO.

5.1.3 IR and UV/vis Spectroscopy

A characteristic parameter for nitrosoarene compounds is the N-O stretching frequency, which can be determined via IR spectroscopy. In fact, this value can be directly correlated with the bond strength, giving additional information about the N-O bond order. The IR spectrum of compound **9** is shown in Figure 55 (red line).
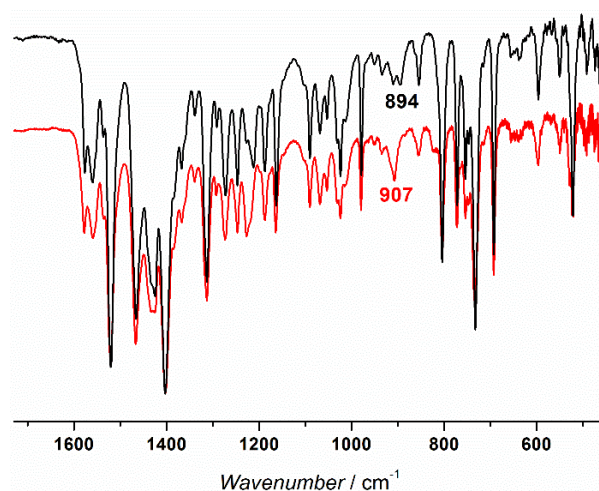
Figure 55. IR spectra of compound **9** (red line) and **9**-^{15}NO (black line). The characteristic NO stretching frequency can be observed at 907 cm^{-1} (894 cm^{-1} for **9**-^{15}NO).

As already observed in the X-ray structure of species **9**, the N-O bond order dramatically decreased upon binding to the nickel ions. Therefore, it was not possible to undoubtedly

assign the NO vibration, as the band could be hidden by other vibrations in the fingerprint region of the spectrum. The NO IR stretching frequency was then obtained by recording an IR spectrum of the corresponding labeled ^{15}NO nitrosobenzene adduct. The compound Ph^{15}NO could be easily prepared from the commercially available Ph^{15}NH$_2$, and was used to synthetize the analogous **9**-^{15}NO. The IR spectrum of **9**-^{15}NO is shown in Figure 55 (black line). Coordination to the two nickel centers reduced the NO stretching frequency to 907 cm^{-1} (897 cm^{-1} for **9**-^{15}NO, the calculated value is 890 cm^{-1}), with respect to the free, monomeric PhNO (1506 cm^{-1})[194] and consistent with previously reported nickel diketiminate compounds (Table 6).

The same procedure was applied to the corresponding complex **10**. Comparison of the NO stretching frequency would help to assess the effect of the potassium cation on the bond strength. The IR spectra of **10** and **10**-^{15}NO are represented in Figure 56. The NO stretching frequency lies at 973 cm^{-1} (954 cm^{-1} for **10**-^{15}NO, the calculated value is 955 cm^{-1}), with a shift of 66 cm^{-1} with respect to compound **9**. Such decrease suggests that the positive charge of the potassium cation held in the cavity between the two aryl substituents of each ligand side arm withdraws the electron density of **9** mainly on the N-O group of the bridging unit. Similarly to the reduced nitroxyl complex **7** described in Chapter 4, this effect can be tuned by the presence/absence of the potassium cation which, in the case of compound **10**, does not interact with the nitrosobenzene bridging unit. Thus, the negative charge of the compound is probably more delocalized between the NO moiety and the nickel centers, and the N-O bond results to be strengthen.
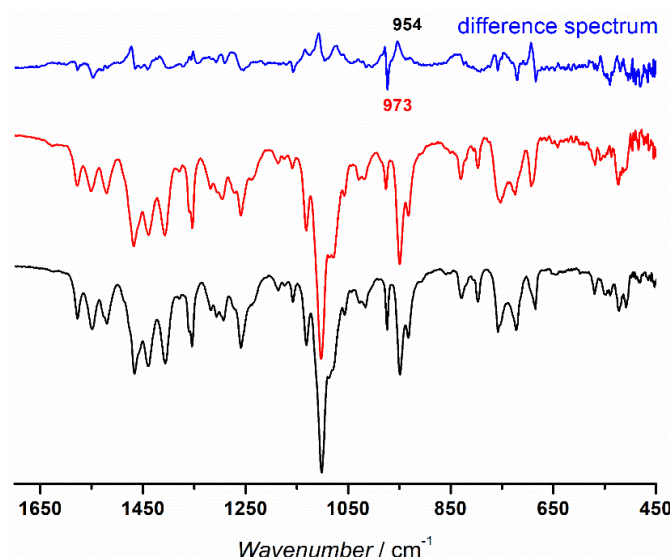
Figure 56. IR spectra of compound **10** (red line) and **10**-^{15}NO (black line). The characteristic NO stretching frequency can be observed at 973 cm^{-1} (954 cm^{-1} for **10**-^{15}NO) as shown by the resulting difference spectrum (blue line.

Compound **9** and **10** were also analyzed by UV/vis spectroscopy in THF solution at room temperature. Figure 57 shows the result for compound **9**, which is essentially identical to the spectrum of complex **10**, suggesting that the potassium cation does not interact with the NO bridging unit and the aryl groups in solution. The band at 271 nm does not change its position with respect to the starting material **2**. The most interesting feature is represented by the two broad bands at 611 nm and 721 nm, respectively. These two transitions are tentatively assigned to a $(PhNO)^{2-}$ $\pi^* \rightarrow Ni^{II}$ charge transfer processes, similarly to what it was observed for the nitroxyl complex **5**.
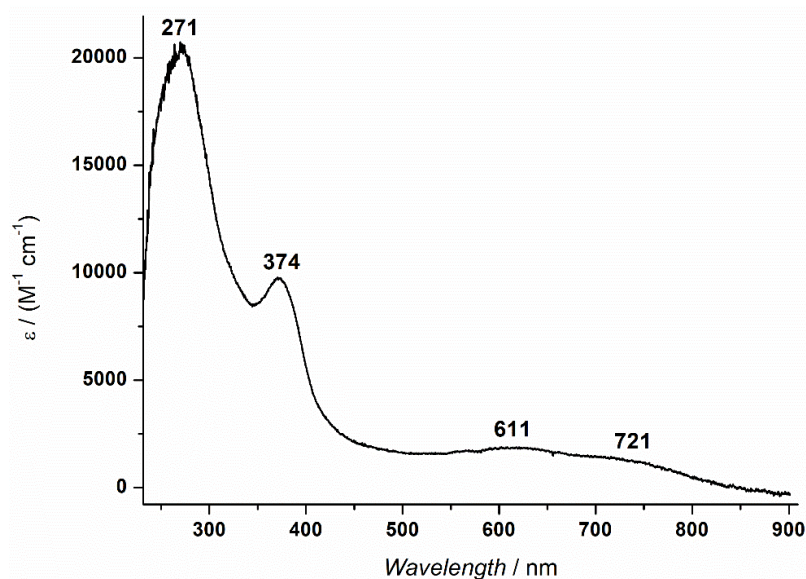
Figure 57. UV/vis spectrum of compound **9** (c = 3 · 10^{-5} M) in THF at room temperature.

5.2 Redox Properties of Complex 9

Cyclic Voltammetry

In order to gain insights into the redox properties of **9**, the cyclic voltammogram of the complex was recorded at room temperature. As shown in Figure 58, two main electron transfers between -2.0 V and +0.5 V *vs.* the ferrocene/ferrocenium couple could be observed. The first anodic process at -1.53 V is reversible, whereas the second at +0.03 V is fully irreversible.
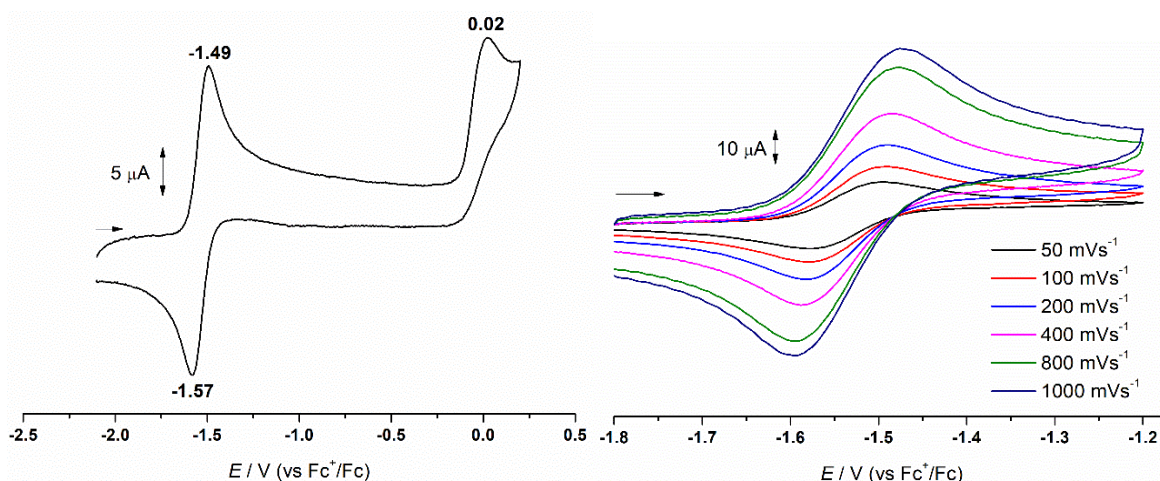
Figure 58. Cyclic voltammogram of **9** in THF (left), 0.2M [^{n}Bu$_4$N][PF$_6$] at 100 mVs^{-1} at 25°C. The reversible peak was measured at different scan rates (right).

The first reversible oxidation process occurs at very low potentials, suggesting that complex **9** could be easily oxidized by one electron to a formally neutral species [LNi$_2$(PhNO)]^0. When the potassium cation K$^+$ is removed between the two phenyl groups like in **10**, the same oxidation process preserves its reversible features and slightly shifts to −1.58 V (Appendix, Figure 7), indicating that the presence of the cation does not influence the redox properties of the compound in solution. The redox potential for **9** is much different from the one found for a related mononuclear nickel complex which bears a end-on nitrosobenzene ligand moiety (Figure 7, complex **b**).[62] In that case, the PhNO group is found in its singly reduced form (PhNO)$^-$, and it could be reversibly reduced at −0.89 V. Furthermore, it was found by means of complementary techniques that the process was exclusively centered at the PhNO group, indicating the redox non-innocence of this ligand moiety at the nickel centers.

Spectroelectrochemistry

The reversible oxidation of **9** observed during cyclic voltammetry experiments was also monitored by UV/vis spectroscopy, as shown in Figure 59. The complex was dissolved in THF at room temperature, and spectroelectrochemistry measurements were performed using [Bu$_4$N][PF$_6$] as the electrolyte. Application of a steady oxidizing potential at −1.0 V (*vs.* Fc/Fc$^+$) led to full conversion of the compound within 20 minutes. The most prominent feature is given by the disappearance of the NO-specific broad bands at 611 nm and 721 nm, indicating that the PhNO unit could be affected by the process. On the other hand, the bands at 271 nm and 374 nm experienced only little changes in intensity and did not shift

their position. This might further support the idea that both the nickel centers and the β-diketiminate ligand scaffold are not involved in the oxidation process, and the redox process occurs at the PhNO moiety.
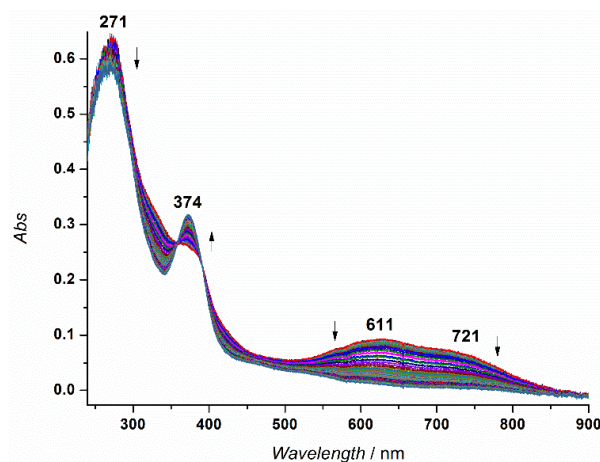
Figure 59. Spectroelectrochemical oxidation of compound **9** in THF.

5.3 Chemical Oxidation

Motivated by the presence of a reversible oxidative wave in the cyclic voltammetry studies, chemical oxidation of compound **9** was attempted. [Fe(Cp*)$_2$][PF$_6$] was chosen as mild oxidant (E^0 = −0.59 V in MeCN; −0.48 V in CH$_2$Cl$_2$)[175] and a deep green THF solution of **9** was treated with it at room temperature (Scheme 44). Color change to dark red within minutes indicated the successful synthesis of the oxidized complex LNi$_2$(μ-PhNO) **11** which was isolated as a red powder after work-up.
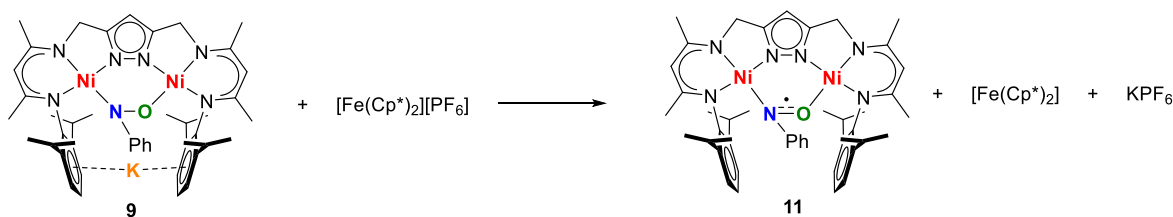
Scheme 44. Synthetic strategy for the oxidation of **9** to give LNi$_2$(PhNO) **11**.

As the removal of one electron would lead to a radical species, the complex was firstly analyzed by EPR spectroscopy. X-band EPR spectroscopy of compound **11** was performed in THF both at room temperature and in frozen solution. In addition, the corresponding

labeled compound **11**-[15]NO was synthetized following the same procedure, starting from **9**-[15]NO, and the EPR spectra were also measured for comparison. Figure 60 shows the results of those measurements together with simulated spectra, and parameters obtained from the simulation are reported in Table 9.
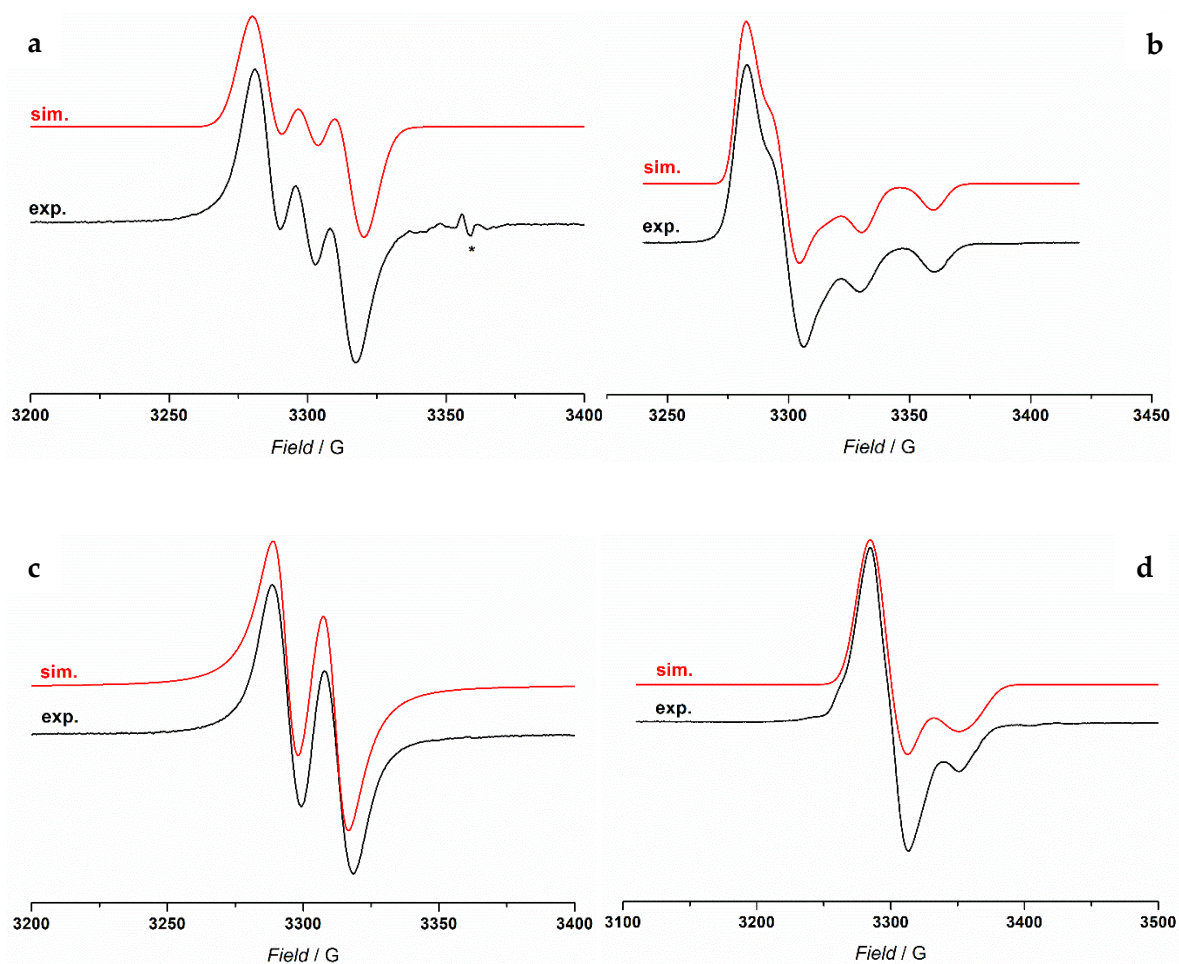
Figure 60. X-band EPR spectra measured in THF of **11** at room temperature (a) and in frozen solution at T = 153 K (b). The same experiment was repeated for **11**-[15]NO at room temperature (c) and in frozen solution (d). Impurities are denoted with an asterisk (*) and were not considered in the simulation.

Table 9. EPR simulation parameters for chemically prepared samples **11** and **11**-[15]NO.

	T = 298 K		T = 153 K					
	g_{iso}	A_{iso} (MHz)	g_1	g_2	g_3	A_1 (MHz)	A_2 (MHz)	A_3 (MHz)
KLNi$_2$(μ-PhNO) **11**	2.040	40	2.051	2.036	2.024	15	30	83
KLNi$_2$(μ-Ph-[15]NO) **11**-[15]NO	2.039	49.1	2.054	2.042	2.022	14	20	80

The X-band spectra of **11** and **11**-^{15}NO in THF at 298 K show a characteristic isotropic signal with S = ½, and strong coupling to a $^{14/15}$N nucleus, confirming a ligand centered radical (I(^{14}N) = 1; I(^{15}N) = ½). The spectrum of **11** shows a signal centered at g_{iso} = 2.040 that consists of three lines (Figure 60, a), and hyperfine coupling A_{iso}(^{14}N) = 40 MHz. On the other hand, the corresponding signal for **11**-^{15}NO shows the expected two lines centered at g_{iso} = 2.039 and A_{iso}(^{15}N) = 49 MHz (Figure 60, c). Interestingly, the ratio of the isotropic hyperfine coupling constants A(^{15}N)/A(^{14}N) = 1.22 is close to 1.40, which represents the expected ratio of the gyromagnetic ratios for the corresponding nuclei, suggesting a certain degree of accuracy for the values obtained from the simulation.

When the measurements were repeated at T = 153 K, the frozen-glass X-band EPR spectrum of **11** showed a slightly rhombic pattern with three rather similar g values (g_1 = 2.049, g_2 = 2.034, g_3 = 2.024) and strong anisotropy of the hyperfine coupling corresponding to the ^{14}N nucleus of the nitrosobenzene (A(^{14}N)$_1$ = 15 MHz, A(^{14}N)$_2$ = 30 MHz, A(^{14}N)$_3$ = 83 MHz) (Figure 60, b). Consistent with what was observed in the measurements at room temperature, also in this case the data are similar to the free electron value (g_e = 2.0023)[195] and support a ligand-centered radical on the PhNO moiety of the complex. Finally, two lines were observed in the spectrum of **11**-^{15}NO with g values of 2.054, 2.042 and 2.022, associated with hyperfine coupling constants for the ^{15}N nucleus of A(^{15}N)$_1$ = 14 MHz, A(^{15}N)$_2$ = 20 MHz, A(^{15}N)$_3$ = 80 MHz (Figure 60, d).

These observations are supported by DFT calculations on complex **11**, which show that the spin density on the SOMO is mainly located on the nitrosobenzene group (Figure 61). The Mulliken population analysis of **11** indicates that the total spin density on the PhNO accounts for more than 80%, whereas a small contribution is given by the metal centers (Ni1 = 9%; Ni2 = 17%).
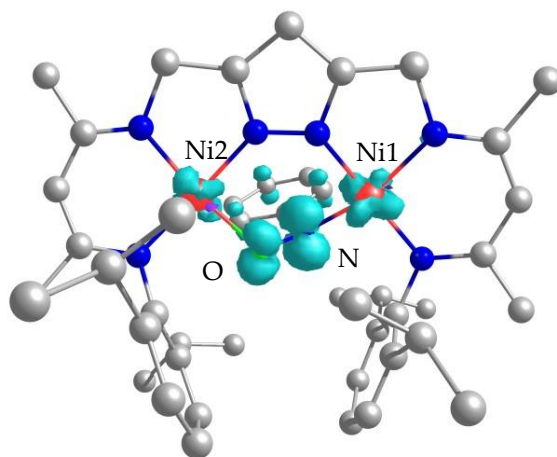
Figure 61. Spin density plot for the oxidized complex **11**.

These data compare well with the aforementioned mononuclear nacnac Ni[II] nitrosobenzene compound (Figure 7, compound **b**) which undergoes the same type of reactivity and shows a localization of the spin density exclusively on the PhNO group for the corresponding radical species.[62]

It is also worth mentioning that the presence of the oxidized species **11** was already detected when performing EPR experiments on the reduced forms **9** and **10**, along with their [15]NO labeled analogues. However, NMR spectroscopy, IR spectroscopy and UV/vis spectroscopy on **9** and **10** confirmed the presence of a diamagnetic species. Thus, it is reasonable to assume that the oxidized complex **11** represents only a minor impurity in those cases, even though its amount was not quantified. As indicated by cyclic voltammetry experiments in section 5.2, oxidation of **9** (or **10**) occurs at very low potentials and it might be possible that traces of dioxygen or any kind of mild oxidant in solution would lead to a partial conversion to the corresponding radical complex **11**.

11 was further characterized in solution, and a UV-vis spectrum of the compound in THF at 298 K was recorded, as shown in Figure 62 (a). Overall, two major bands at 270 nm and 378 nm are displayed, which resemble the features found for the complex during spectroelectrochemical analysis of the oxidation of **9** (Figure 59). This suggests a full conversion to **11**, as the typical broad absorptions at 611 nm and 721 nm found for the reduced compound have completely disappeared. Furthermore, extinction molar coefficients of **11** were determined by recording concentration dependent UV/vis spectra (Figure 62, b). The concentration of each solution was plotted against the maximum value for each absorption and a linear fit was applied (Figure 62, c). Extinction coefficients of 19607 $M^{-1}cm^{-1}$ and 7826 $M^{-1}cm^{-1}$ were calculated for the bands at 270 nm and 378 nm, respectively. The values are in line with those of previously reported dinuclear nickel systems based on the **L**[3-] scaffold.[146,149]
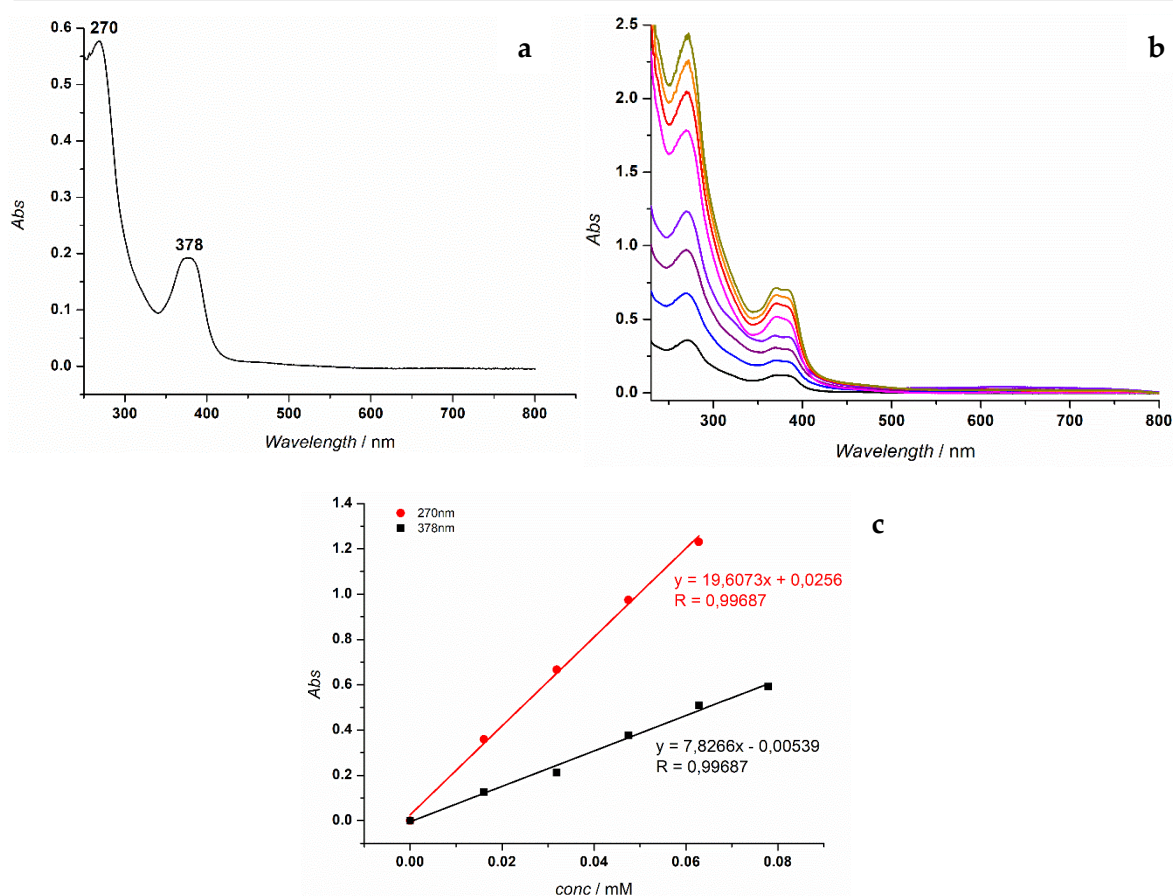
Figure 62. a) UV-vis spectrum of **11** recorded at room temperature in THF. b) UV-vis spectra of **11** at different concentrations. c) Beer's law plot of **11** shows λ_{max} / nm (ε / M^{-1} cm^{-1}) = 270(19607), 378(7826).

IR spectroscopy was further employed to assess the effect of the ligand centered oxidation on the NO bond strength. ATR-IR spectra of solid compounds **11** and **11**-^{15}NO were measured and compared in order to obtain the NO stretching frequency values. As shown in Figure 63 (left), it was not possible to unambiguously determine the position of the band by comparison of the two complexes. Therefore, a difference spectrum was plotted (Figure 63, right), which possibly indicates the stretching frequency for the NO group at 1080 cm^{-1}. This value shifts of 27 cm^{-1} upon labeling the compound to 1053 cm^{-1}, consistent with the calculated value of 1043 cm^{-1}. In comparison to the starting material, where the NO stretching vibration for **9** was found at 973 cm^{-1}, it is clear that transfer of one electron to the [Fe(Cp*)$_2$]$^+$ reagent affects the NO bond strength which increases its order resulting in a higher wavenumber observed in the spectrum.

Finally, the vibrational features in the IR spectrum could also be reproduced with adequate agreement to the experimental results by means of DFT calculations, where the NO stretching frequency was predicted at 1110 cm^{-1} (Experimental part, Figure 95).
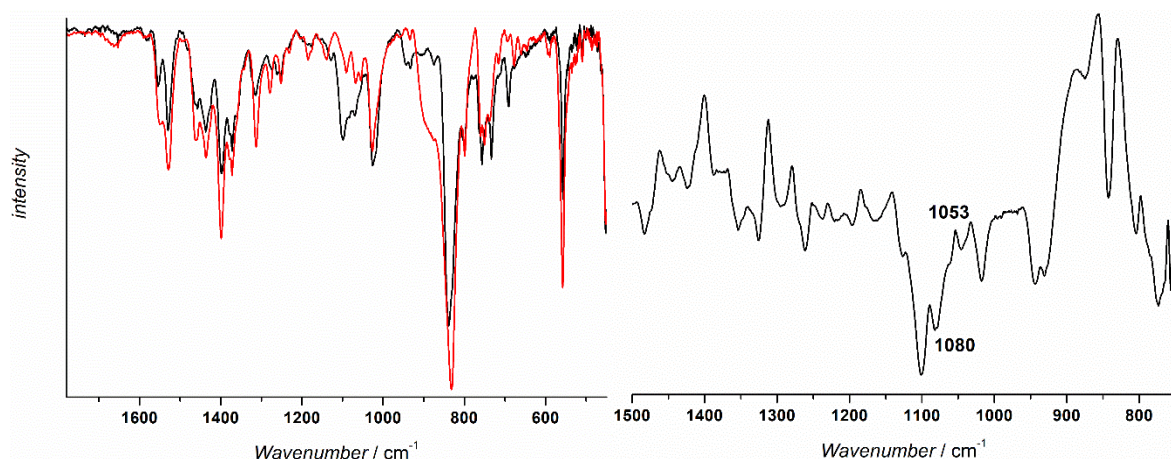
Figure 63. IR spectra of compound **11** (red line) and **11**-^{15}NO (black line) (left) and difference spectrum of both compounds (right) that shows the NO stretching vibration at 1080 cm^{-1} for **11**.

Unfortunately, it was not possible to obtain single crystals of **11** suitable for X-ray diffraction analysis in order to shed light into the structural features of LNi$_2$(μ-PhNO). Despite being a rather stable species, especially in comparison with its reduced form KLNi$_2$(μ-PhNO) **9**, the compound is highly soluble in most moderately polar and apolar solvents such as THF, Et$_2$O, toluene, benzene and, to a certain extend, even in hexane or pentane. Therefore, optimization of the crystallization conditions to find a suitable solvent mixture is still ongoing.

5.4 Reactivity Studies on Complex 9

The protonation of the PhNO moiety is of current interest since the resulting PhNHO compound is reminiscent of the biologically active HNO. As mentioned in Chapter 1, this species is highly reactive and in turn difficult to study, so that the isolation of a more stable analog would be beneficial in order to gain insight into the chemistry of HNO.

Thus, protonation of the (PhNO)$^{2-}$ group of complex **9** was achieved by treating a THF suspension of **9** with [LuH][OTf], according to Scheme 45.
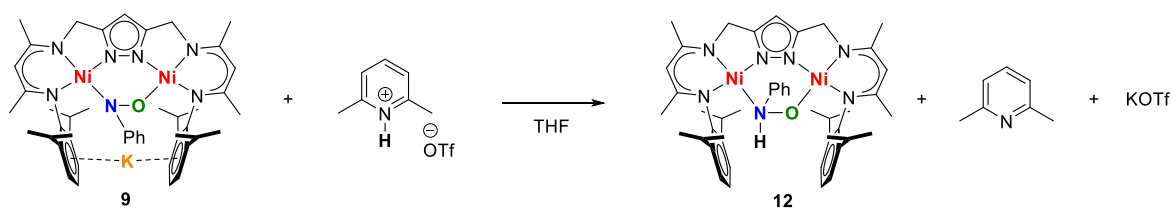
Scheme 45. Synthetic strategy for the protonation of **9** to give LNi$_2$(PhNHO) **12**.

Single crystals of **12** suitable for X-ray diffraction analysis were obtained by diffusion of hexane onto a concentrated THF solution of **12** at room temperature within a few days. The molecular structure of **12** is represented in Figure 64, and selected structural parameters are listed in Table 10.
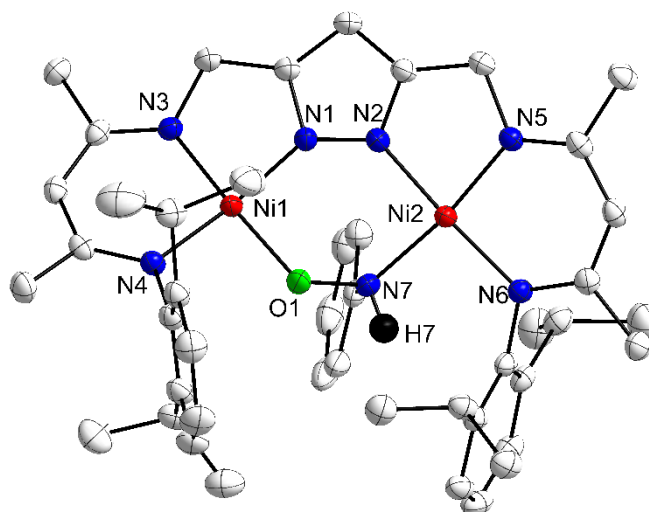
Figure 64. Thermal displacement ellipsoid (50% of probability) of the molecular structure of compound LNi$_2$(PhNHO) **12**.

Table 10. Selected structural parameters for complex **12** in the solid state.

Bond length / Å		Angle / °	
Ni(1)-N(1)	1.8410(16)	N(1)-Ni(1)-N(3)	83.23(7)
Ni(1)-N(3)	1.8696(13)	N(3)-Ni(1)-N(4)	167.07(7)
Ni(1)-N(4)	1.9023(16)	N(1)-Ni(1)-O(1)	92.56(6)
Ni(1)-O(1)	1.8696(13)	N(4)-Ni(1)-O(1)	90.80(6)
Ni(2)-N(7)	1.9450(16)	N(2)-Ni(2)-N(5)	82.64(7)
Ni(2)-N(5)	1.8857(16)	N(5)-Ni(2)-N(6)	94.05(7)
Ni(2)-N(6)	1.9141(15)	N(6)-Ni(2)-N(7)	94.25(7)
Ni(2)-N(2)	1.8560(16)	N(2)-Ni(2)-N(7)	89.04(7)
N(7)-O(1)	1.464(2)	Ni(1)-O(1)-N(7)	119.32(10)
N(7)-H(7)	0.867(25)	Ni(2)-N(7)-O(1)	117.36(11)
Ni(1)···Ni(2)	3.8866(6)	Ni(1)-O(1)-N(7)-Ni(2)	77.15(14)

Complex **12** crystallizes in the monoclinic space group *P*2$_1$/*n* with four molecules in the unit cell. Both nickel ions are found in a slightly distorted square planar geometry and exhibit a metal-metal distance of 3.88 Å, which is consistent with dinickel complexes based on the ligand system **L**$^{3-}$.[145] The nitrosobenzene bridging unit retains its μ-η^1:η^1 binding mode with

respect to the starting material **9**, and an additional proton is connected to the moiety through the nitrogen atom with a resulting N(7)-H(7) distance of 0.86 Å. The N(7)-O(1) distance of 1.46 Å is slightly shorter than the one found in **9**, indicating an oxidation of the PhNO group upon protonation. The potassium cation K^+ is no longer interacting with the aryl groups of the ligand scaffold and the complex is considered neutral. These data are consistent with the two nickel ions being in the oxidation state of +2.

Isolated solid material of **12** was studied by IR spectroscopy, and the data were compared with the labeled **12**-[15]NO complex, which was prepared by following the same synthetic strategy for **12** and starting from **9**-[15]NO. The IR spectra of **12** and **12**-[15]NO are shown in Figure 65.
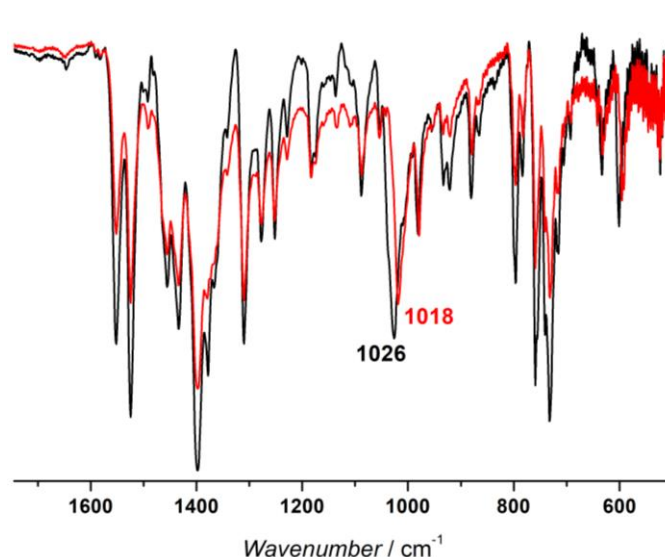
Figure 65. IR spectra of compound **12** (black line) and **12**-[15]NO (red line). The characteristic NO stretching frequency can be observed at 1026 cm^{-1} (1018 cm^{-1} for **9**-[15]NO).

The oxidation of the PhNO moiety upon protonation observed in the X-ray structure of **12** is also reflected by the NO stretching frequency, which increased to 1026 cm^{-1} (1018 cm^{-1} for **12**-[15]NO) with respect to compound **9** (907 cm^{-1}, 894 cm^{-1} for **9**-[15]NO). The calculated isotope shift of 19 cm^{-1} is slightly higher that the experimental value of 8 cm^{-1}. Furthermore, it is worth noting that the N-H vibration was not observed neither for **12** nor for **12**-[15]NO (Appendix, Figure 8).

Currently, further experiments for the complete characterization of **12** are ongoing.

5.5 Summary

Building on the results of previous studies, the ability of the dinuclear nickel(II) dihydride system **2** to reductively bind and activate substrates was also investigated in detail using nitrosobenzene. The adducts which resulted were showing a two-electrons reduction of the NO bond, as expected. Spectroscopic techniques were used for characterization, which provided significant insights in the case of the each system. An overview of the reactions and compounds reported in this chapter is given in Scheme 46.

Characterization in the solid state of the dinickel(II) nitrosobenzene adduct KLNi2(μ-PhNO) **9**, which results from reaction of the dinickel dihydride complex **2** with one equivalent of nitrosobenzene, showed that the potassium cation can still be accomodated in the cavity between the aryl groups of the ligand side arms, weakly interacting with the PhNO bridging unit. The cation could be easily removed from that position to obtain the corresponding [LNi2(μ-PhNO)][K(crypt)] **10** complex, whose properties were compared to those of **9**. Notably, experimental evidences suggest that binding of K$^+$ in the ligand cavity plays a role in tuning the negative charge of the complex mostly on the bridging unit or delocalized on the complex, as reflected by the difference in the NO bond distances in the solid state. On the other hand, the solution properties did not seem to be influenced by the presence of the alkali metal cation.

Furthermore, redox properties of both reduced compounds **9** and **10** were studied. This procedure led to the observation of a reversible oxidation wave in cyclic voltammetry experiments, thereby providing an indicator for the possibility of oxidizing this species by one electron. Using these results, chemical oxidation was performed, in combination with [15]NO isotopic labeling experiments. This gave strong evidence that the oxidation takes place exclusively at the nitrosobenzene bridging unit to yield compound LNi2(μ-PhNO) **11**. A redox non-innocence of the nitrosobenzene moiety was already reported in the literature,[62] and further confirmed for the new dinuclear nickel complexes described herein.

Finally, protonation of the reduced compound **9** led to LNi2(μ-PhNHO) **12** which was characterized by means of X-ray crystallography. This showed that the proton is connected to the nitrogen atom of the PhNO bridging unit leading to a partial oxidation of the NO bond.

Detailed computational analysis of the reduced **9** (and **10**) and oxidized **11** is a topic of future interest. Such studies are needed to confirm the interpretation of the experimental evidences described above. The theoretical investigation could potentially provide

significant insights into the electronic structure of the complexes, as well as analyze the effect of the potassium binding to the nitrosobenzene unit.
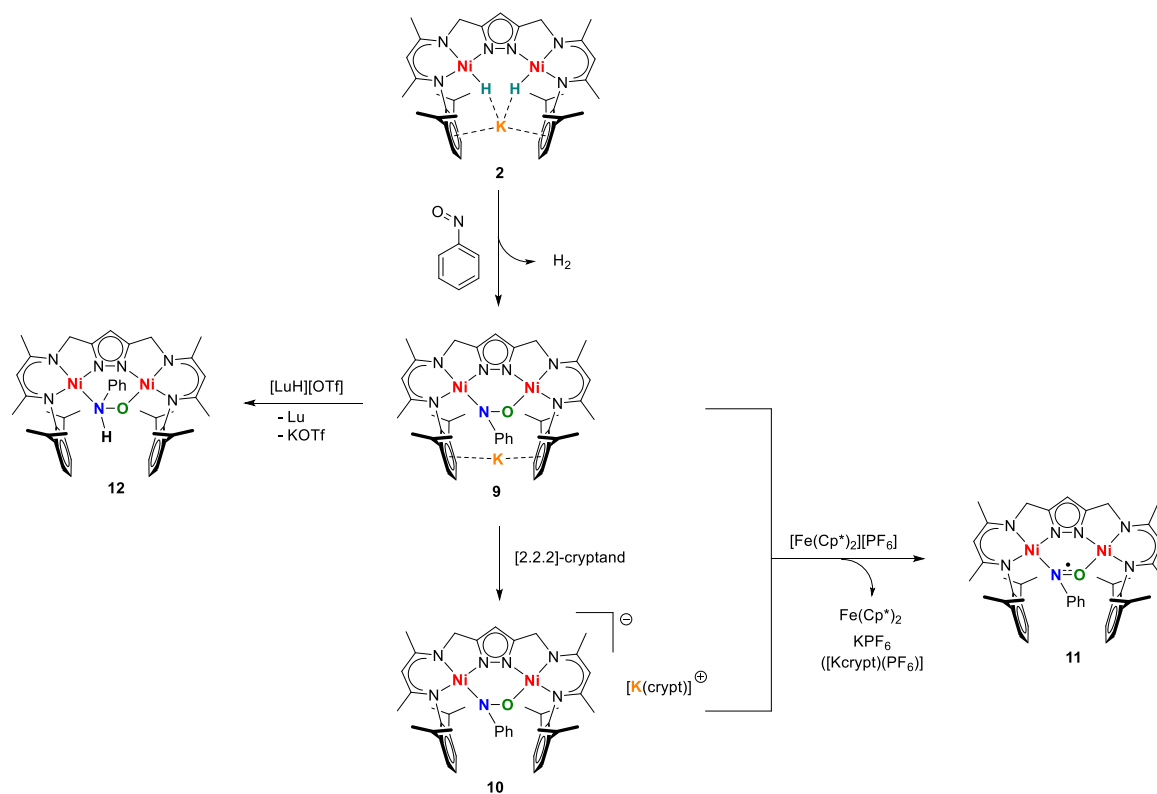
Scheme 46. Overview of the reaction described in this chapter, showing the interconversion of nitrosobenzene on a dinuclear nickel β-diketiminato scaffold.

6 Characterization and Reactivity Studies of a Diiron β-Diketiminate Complex

6.1 Solid State Characterization of a Diiron β-diketiminate Complex

Preliminary work on this project was already conducted by NEUMANN,[196] who was able to isolate and to obtain the molecular structure of the first diiron complex of the ligand **L³⁻**, LFe₂(OTf)₂(THF)₂ **(13)**, by treating the deprotonated ligand **L³⁻** with Fe(OTf)₂·2MeCN. Due to the high reactivity of the compound, a full characterization and subsequent reactivity studies could not be performed. Instead, the optimization of the reaction conditions ans crystallization procedures for the successful synthesis of **13** was pursued within this work.

As reported by NEUMANN, deprotonation of **H₃L** with ⁿBuLi in THF at -78°C and subsequent treatment of the reaction mixture with two equivalents of Fe(OTf)₂·2MeCN led to the isolation of complex **13**, as shown in Scheme 47. In order to minimize the formation of impurities that prevented the crystallization of the compound due to the high sensitivity of the complex towards dioxygen, the synthetic procedure was conducted in a N₂ glovebox at -30°C. Removal of the solvent and subsequent extraction of **13** with dry toluene led to a deep green solution containing the desired compound. Recrystallization at low temperature by layering pentane onto a concentrated THF solution of **13** led to light green rod-shaped crystals suitable for X-ray diffraction analysis.
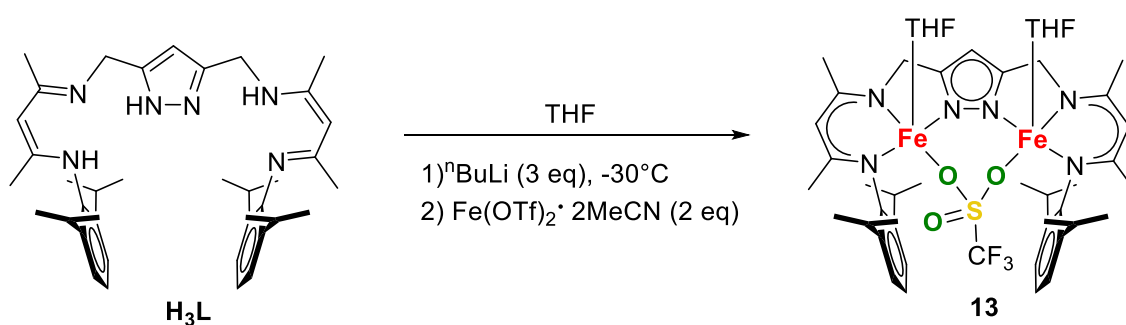
Scheme 47. General scheme for the synthesis of complex **13**.

The molecular structure of **13** is shown in Figure 66, and selected structural parameters are reported in Table 11. Complex **13** crystallizes in the triclinic space group $P\bar{1}$ with two molecules in the unit cell. In contrast to the observations reported for the dinuclear nickel(II) complexes in this thesis work, both metal centers in **13** are found in a square pyramidal environment. The molecular structure reveals that each iron ion is four-fold coordinated by the ligand scaffold with a triflate moiety bridging between the two metal centers which are lying essentially on the same plane. The fifth axial position is occupied by a THF solvent molecule. Charge balance considerations indicate that both iron centers are found in the oxidation state +2. In order to systematize the coordination environment in the vicinity of the iron ions, the structural index parameter τ_5 was used. In a five-fold coordinated system (Scheme 48), τ is defined as $\tau = (\beta - \alpha)/60$ where α and β are the two largest basal angles BMC and DME, respectively.
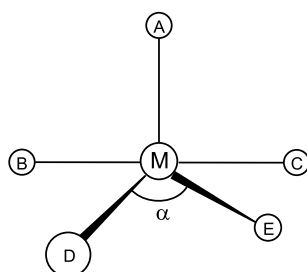
Scheme 48. Representation of a five coordinated system for the definition of the structural parameter τ.

When $\tau = 1$, a perfect trigonal bipyramid is expected, while a tetragonal geometry is associated to $\tau = 0$.[197] Complex **13** shows $\tau_5 = 0.36$ for Fe1 and $\tau_5 = 0.18$ for Fe2, indicating a slight distortion from the tetragonal geometry for both iron ions.

The distance between the metal centers is 4.752 Å, which is rather large for a binuclear pyrazolate-based ligand system.[198] The distances between the iron atoms and the bridging ligand Fe(1)-O(3) and Fe(2)-O(4) are 2.152 Å and 2.137 Å, respectively, while the distance to the pyrazole Fe(1)-N(1) and Fe(2)-N(2) are 2.129 Å and 2.142 Å, respectively. Moreover, the distances between the metal centers and the nacnac side arms fall in the range 2.06 Å - 2.07 Å. Finally, the distance between the iron centers and the THF molecules are 2.130 Å. These values are higher to those found for the nickel analogue but consistent with the longer atomic ratio of iron.
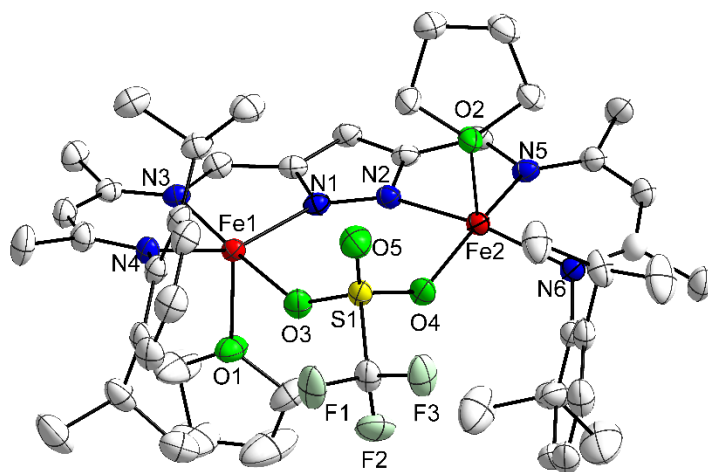
Figure 66. Molecular structure of complex **13**. Hydrogen atoms are omitted for clarity.

Table 11. Selected structural parameters for complex **13** in the solid state.

Bond length / Å		Angle / °	
Fe(1)-N(1)	2.1296(18)	N(1)-Fe(1)-N(3)	81.19(7)
Fe(1)-N(3)	2.0651(18)	N(3)-Fe(1)-N(4)	88.96(7)
Fe(1)-N(4)	2.0632(17)	N(1)-Fe(1)-O(3)	95.52(7)
Fe(1)-O(3)	2.1524(16)	N(3)-Fe(1)-O(3)	176.70(7)
Fe(1)-O(1)	2.1303(17)	N(4)-Fe(1)-N(1)	155.42(7)
Fe(2)-N(5)	2.0649(18)	N(2)-Fe(2)-N(5)	80.68(7)
Fe(2)-N(6)	2.0729(19)	N(2)-Fe(2)-O(4)	94.08(6)
Fe(2)-N(2)	2.1418(19)	N(6)-Fe(2)-O(4)	92.90(7)
Fe(2)-O(4)	2.1370(15)	N(5)-Fe(2)-O(4)	169.02(7)
Fe(2)-O(2)	2.1277(15)	N(6)-Fe(2)-N(2)	157.90(7)
Fe(1)···Fe(2)	4.7524(5)	O(3)-Fe(1)-O(1)	82.60(7)
		O(2)-Fe(2)-O(4)	92.16(6)

6.1.1 NMR Characterization of 13

Further spectroscopic data for the characterization of **13** were reported by NEUMANN, as shown in the Appendix. Mössbauer and SQUID measurements revealed that the electronic configuration of both iron atoms is *hs*-d^6. Therefore, the Fe^{II} ions in **13** possess four unpaired electrons and are paramagnetic. In general, the presence of unpaired electrons leads to considerable line broadening of the NMR signals for nuclei near the paramagnetic center. Nevertheless, the ^{1}H-NMR spectrum of *hs*-Fe^{II} complexes can be recorded,[199] and the signals can be assigned by means of 2D experiments, integrated intensities and relaxation times. Thus, crystals of **13** were dissolved in THF-d$_8$ and the ^{1}H-NMR measurement was attempted, which revealed relatively sharp resonances (Figure 67).
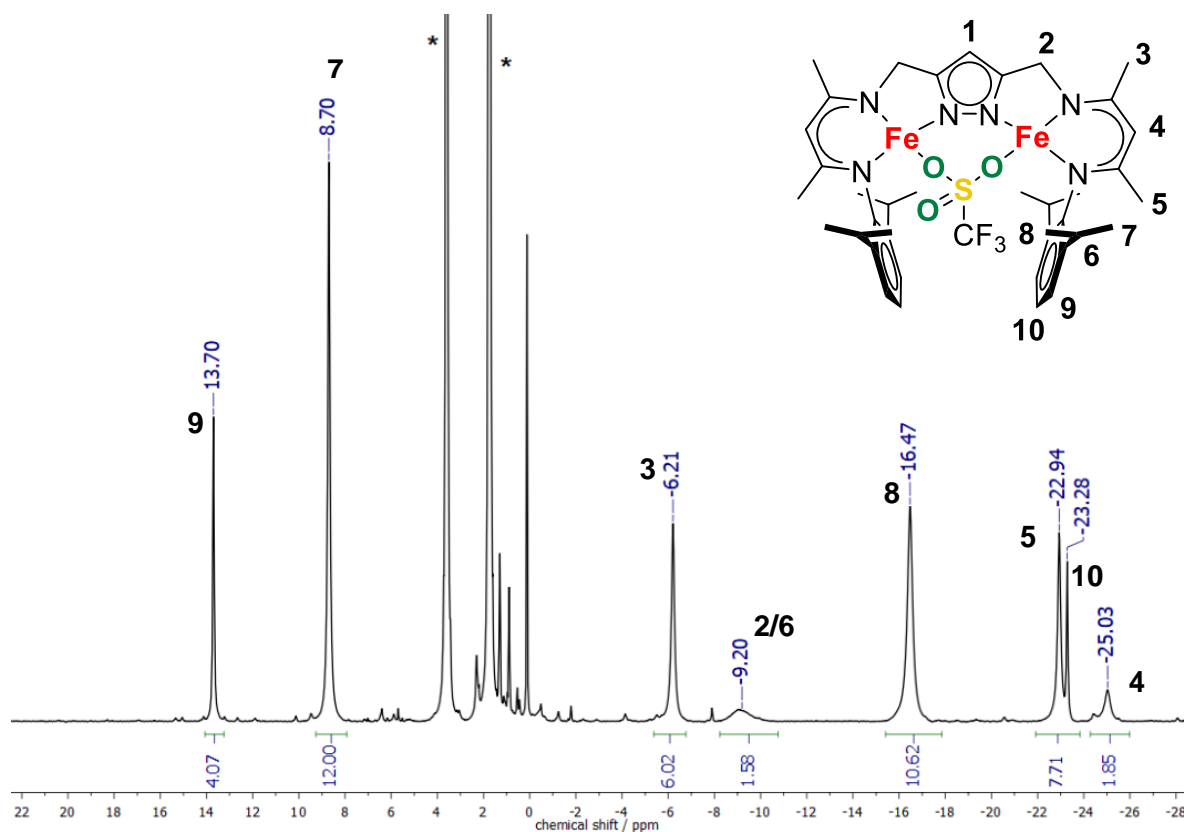
Figure 67. ^{1}H-NMR spectrum of **13** in THF-d$_8$ at room temperature. The residual solvent signals are marked with an asterisk (*).

The spectrum is consistent with the solid state structure, and the number of signals and their integration are characteristic of complexes of the ligand **L**$^{3-}$ in an overall C$_{2v}$ symmetry environment in solution. The signals from all protons in the complex are observed at room temperature, with the exception of the C*H* of the pyrazole group (proton **1**). A broadening effect is also pronounced for the peak at -9.20 ppm corresponding to both C*H*$_2$ and C*H* of

the isopropyl groups in the side arms (protons 2/6); this signal cannot be seen at temperatures below 288 K (Appendix, Figure 10). The rest of the resonances could be assigned on the basis of their relative integration and relaxation time.[200] Thus, the resonance at -25.0 ppm is assigned to the CH of the nacnac backbone (proton 4), and the peak at -23.3 ppm is assigned to *para-H* of the aryl groups (proton 10). Similarly, the signal at 8.7 ppm belongs to one of the inequivalent CH_3 of the isopropyl groups (proton 7). However, no direct correlation from the distance between the protons and the paramagnetic centers was found, as the other set of methyl groups was observed at -16.5 ppm (proton 8).

The presence of the triflate bridging group also allowed for ^{19}F-NMR characterization. As expected, complex **13** shows only one characteristic signal at +88.6 ppm, which indicates that the triflate moiety remains coordinated to the complex in THF solution (Figure 68) since the signal for the corresponding free triflate counterion should be observed at -79.3 ppm.[201]
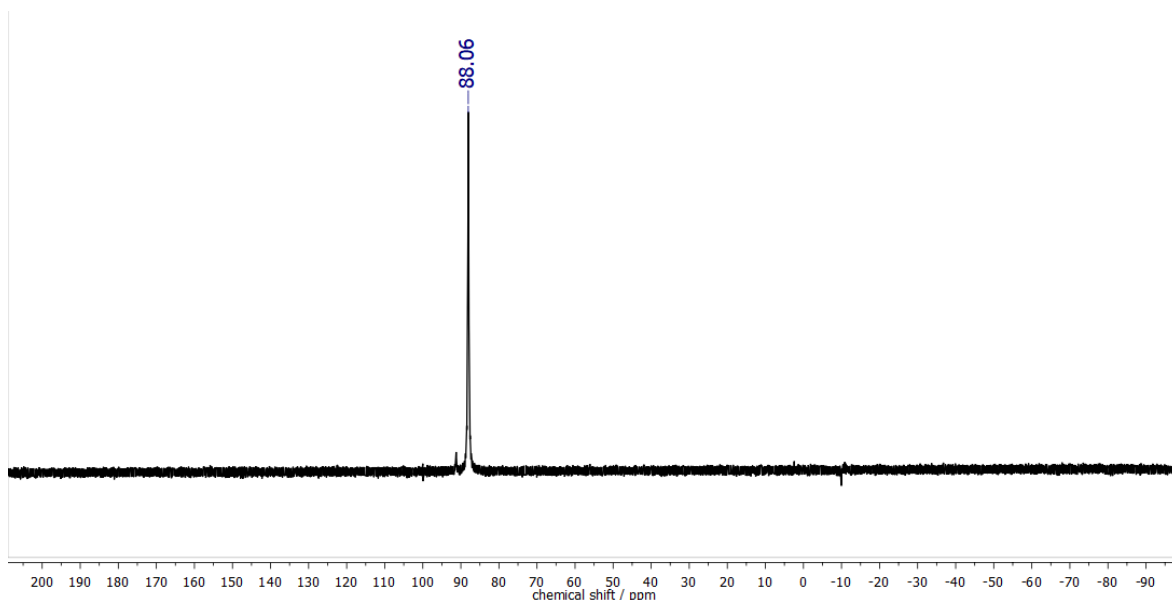
Figure 68. ^{19}F-NMR spectrum of **13** recorded in THF-d$_8$ at room temperature. No signal for the free triflate anion (OTf)$^-$ at -79.3 ppm is observed.

6.2 Attempts to Isolate a Diiron Hydride Species

As described in the general introduction of this work, mononuclear iron hydride complexes were used to gain more insights into the mechanism of nitrogenase. Therefore, the synthesis of analogous dinuclear compounds would be interesting in order to evaluate any potential metal-metal cooperativity. Following the strategy employed by MANZ for the synthesis of

the bimetallic nickel(II) dihydride complex **2**, the isolation of a corresponding iron-based hydride complex of **L**$^{3-}$ was attempted.

Complex **13** was treated with an excess of potassium superhydride (KHBEt$_3$) in THF at room temperature and the mixture was stirred for a few hours. An immediate color change from bright yellow to black was observed, suggesting that a reaction took place quickly. Subsequent workup followed by several crystallization attempts involving different combinations of solvents did not lead to the isolation of any material suitable for structural characterization, and only intractable mixtures of compounds were detected.

The reaction conditions were further modified to avoid the formation of several species that prevented the full characterization of the reaction. In principle, treatment of **13** with at least two equivalents of KHBEt$_3$ would lead to the formation of the desired diiron hydride complex, along with BEt$_3$ as the byproduct, according to Scheme 49. At least two hydrides are expected to bind to the iron compound, as the large metal-metal separation found for **13** in the solid state structure would prevent coordination of only one hydride between the metal centers. When formation of potassium triflate is assumed, the anionic charge of product **14** is -1 and is balanced by the second potassium cation in solution. In this case, each iron ion holds a formal charge of +2, and likely remains in the high spin configuration.
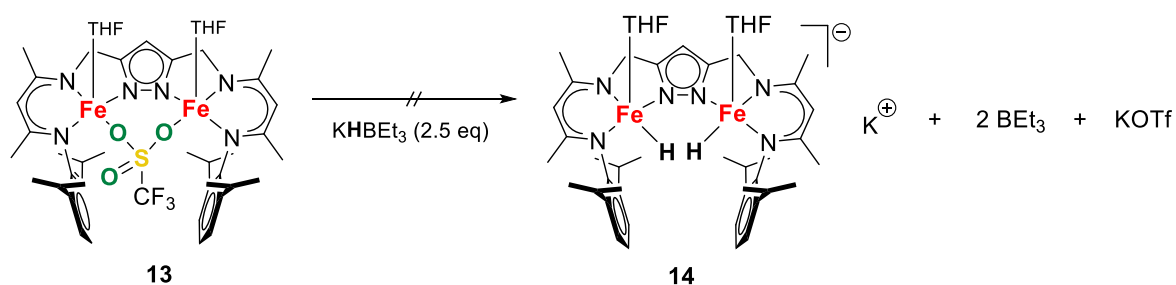
Scheme 49. Suggested reaction pathway for the treatment of **13** with KHBEt$_3$ and subsequent formation of a putative diiron dihydride complex **14**.

Furthermore, it was previously shown by HOLLAND and co-workers that β-diketiminato iron chloride or bromide precursors are capable of reacting with superhydride to form the corresponding iron hydride complex. However, BEt$_3$ forms as the byproduct of the reaction and it further reacts with the synthetized iron hydride when the reaction mixture is stirred longer than 45 minutes.[202] Since a similar reactivity is expected for the putative diiron hydride complex **14**, the starting material **13** was stirred in the presence of KHBEt$_3$ for about 15 minutes in dry toluene at room temperature. A color change from yellow to dark brown was observed, along with the formation of a colorless precipitate. IR spectroscopy of this powder isolated by filtration confirmed the formation of the potassium triflate salt.

In order to determine whether the reactivity pathway proposed in Scheme 49 was feasible, the nature of the resulting iron products was studied by means of Mössbauer (MB) spectroscopy. Mössbauer analysis of the crude product **14** obtained after removal of the solvent showed that at least three species were formed (Figure 69, left). The presence of any starting material was not detected (*hs*-Fe^{II}; IS = 1.08 mm·s^{-1}, QS = 2.32 mm·s^{-1}), but the major species showed an IS = 0.64 mm·s^{-1} with a QS = 1.13 mm·s^{-1}, which is assigned to a different *hs*-Fe^{II} compound. These parameters compare well to a similar diiron dihydride complex that was reported by LIMBERG,[203] which had IS = 0.68 mm·s^{-1} and QS = 1.13 mm·s^{-1}. Similarly, the presence of another unknown impurity with IS = 0.83 mm·s^{-1} and QS = 2.11 mm·s^{-1} was also detected.
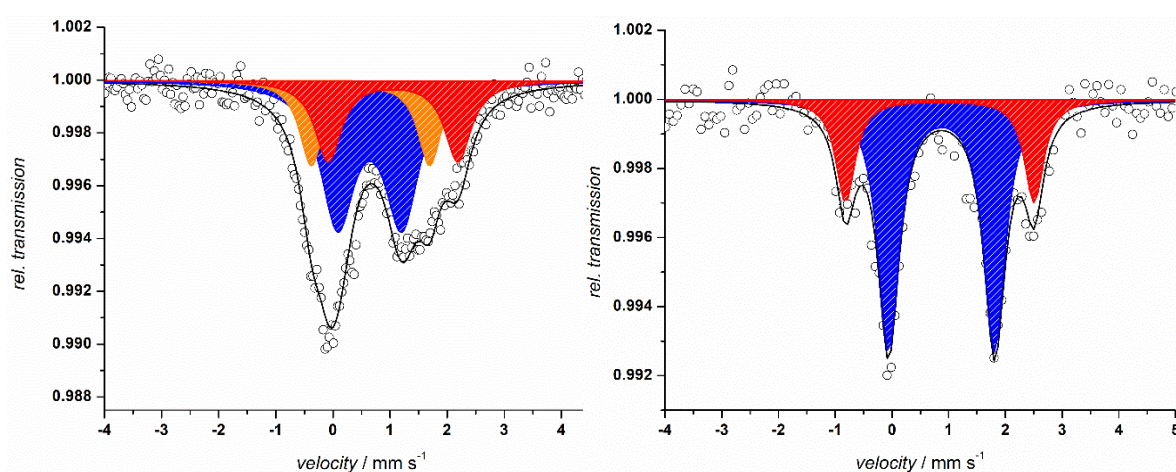
Crude product			After workup		
IS [mm·s^{-1}]	QS [mm·s^{-1}]	%	IS [mm·s^{-1}]	QS [mm·s^{-1}]	%
0.64	1.13	53	0.87	1.87	73
0.66	2.07	23	0.84	3.32	27
1.05	2.27	25	-	-	-

Figure 69. Solid state Mössbauer spectrum recorded at 80 K of the crude product after reaction of **13** with KHBEt₃ (left) and after workup (right). Corresponding spectral parameters are reported in the table.

As mentioned previously, the reaction of **13** with KHBEt₃ led to the formation of several products, as indicated by the red and orange curves in the MB spectrum. The crude powder was then washed several times with hexane and pentane, and a Mössbauer measurement of the product was repeated (Figure 69, right). While the number of species decreased from three to two, the isomer shifts of the new compounds are significantly different compared to the crude product. For instance, two new species with similar IS values of 0.87 mm·s^{-1}

and 0.84 mm·s^{-1}, and QS of 1.87 mm·s^{-1} and 3.32 mm·s^{-1}, respectively, were found in a 70 : 30 ratio. A couple of reasons for this observation could be given.

Firstly, the putative dihydride complex, if formed at all, could decompose either due to its intrinsic instability or due to an insufficient anhydrification/degasification of the solvents. A second explanation could be the high solubility of the complex in apolar solvents, so that it was washed away upon rinsing with pentane or hexane. The different signals detected by Mössbauer spectroscopy could be already present in the crude material, but the general broadness of the spectrum prevented a well resolved fit.

The second assumption was supported by further spectroscopic evidences. The ^{1}H-NMR spectrum of the pale green powder obtained after washing the crude material with pentane showed only the signals in the diamagnetic region belonging to excess KHBEt$_3$ and BEt$_3$. The presence of *hs*-Fe^{II} species was not detected by recording a MB spectrum of the powder. On the other hand, several paramagnetic resonances were detected in the ^{1}H-NMR spectrum in THF-d$_8$ of the solid obtained by extraction of the complex with pentane or hexane followed by removal of the solvent (Figure 70). This confirmed the hypothesis of the high solubility of the desired compound in such solvents.
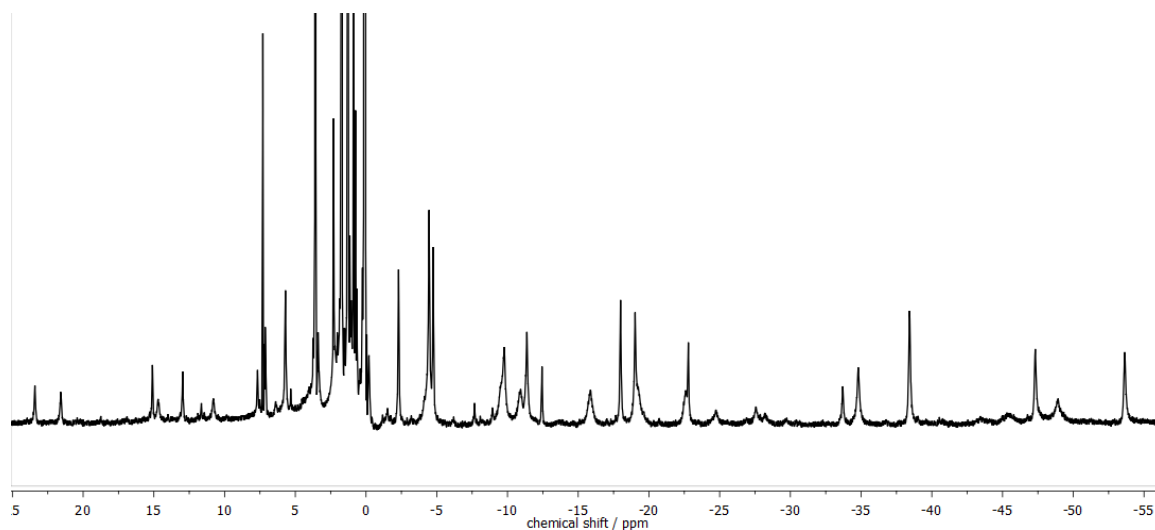
Figure 70. ^{1}H-NMR spectrum in THF-d$_8$ of the pentane extracted phase of the reaction mixture obtained by treating **13** with KHBEt$_3$.

Additionally, a MB spectrum of the solid obtained by removal of the solvent from the pentane extraction was recorded (Figure 71, left). At least three species with very similar spectral parameters were found, suggesting the presence of a mixture of *hs*-Fe^{II} compounds. At the same time, storage of the concentrated extracted pentane phase at -30°C for a few

weeks led to crystalline material that was analyzed again with MB spectroscopy (Figure 71, right). The relative intensity of the major species in the crude material with IS = 0.90 mm·s^{-1} (QS = 2.16 mm·s^{-1}) decreased to 24%, whereas the compound with IS = 0.87 mm·s^{-1} (QS = 1.87 mm·s^{-1}) became the most prominent compound with a relative intensity of 53%. Since *hs*-Fe^{II} complexes are still present, the purification process did not lead to any positive outcome. Several compounds with similar solubility properties and spectral parameters were still present in varying ratios, and they could not be separated either by repeating the same reaction at lower temperatures, or by changing the purification method.

Extracted with pentane			After crystallization		
IS [mm·s^{-1}]	QS [mm·s^{-1}]	%	IS [mm·s^{-1}]	QS [mm·s^{-1}]	%
0.84	1.50	24	0.87	1.87	53
0.79	0.89	26	0.86	0.73	23
0.90	2.16	50	0.82	3.00	24
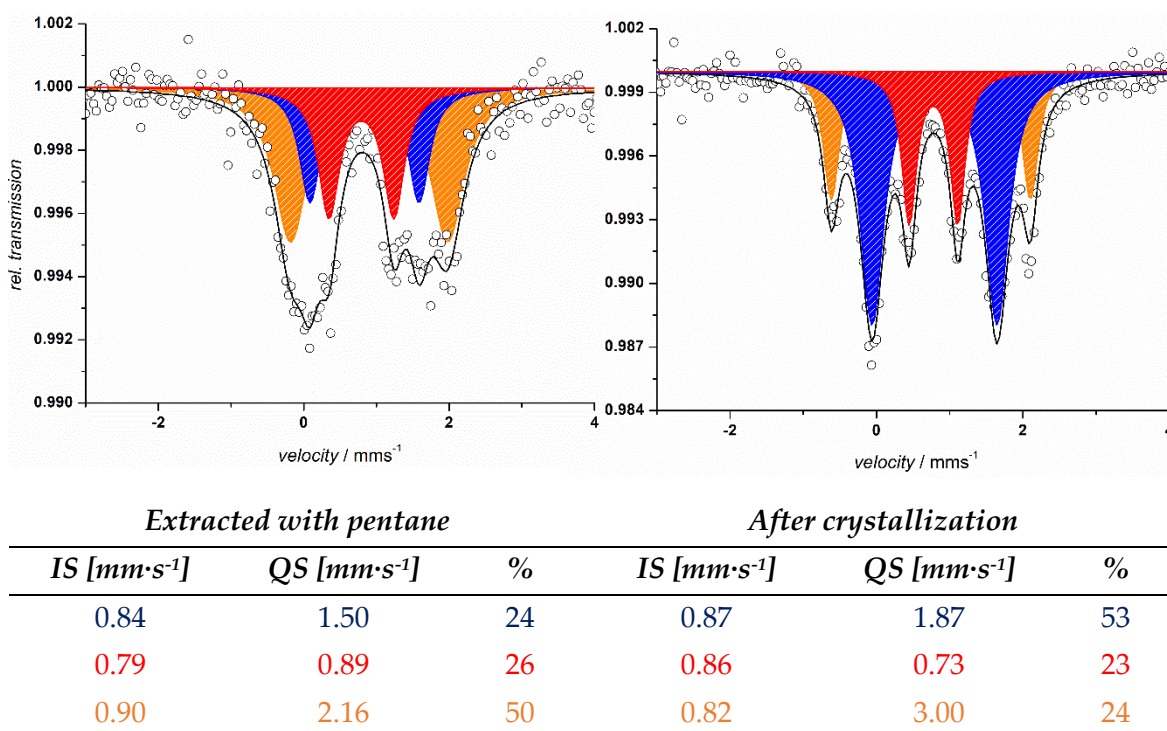
Figure 71. Solid state MB spectrum at 80 K of the pentane extracted phase (left) and the crystallized product (right). Corresponding spectral parameters are reported in the table.

Unfortunately, a similar behavior was also observed when using NaHBEt$_3$ or LiHBEt$_3$. Therefore, a new hydride precursor was chosen, and the same reaction using two equivalents of NaBH$_4$ in a toluene/THF (10 : 1) solvent mixture was attempted. Due to the low solubility of NaBH$_4$ in apolar solvents, the mixture was stirred for one day in order to bring the reaction to completion. The solid was filtered off, followed by removal of the solvent and the resulting solid was washed with cold pentane and dried under vacuum. A MB spectrum of the product was then recorded (Figure 72). Interestingly, formation of an *hs*-Fe^{II} species with IS = 0.88 mm·s^{-1} (QS = 1.03 mm·s^{-1}) was detected in a relative intensity of

84% with respect to a minor species that shows similar MB values as the starting iron precursor **13**.

IS [mm·s⁻¹]	QS [mm·s⁻¹]	%
0.88	1.03	84
0.98	2.32	16
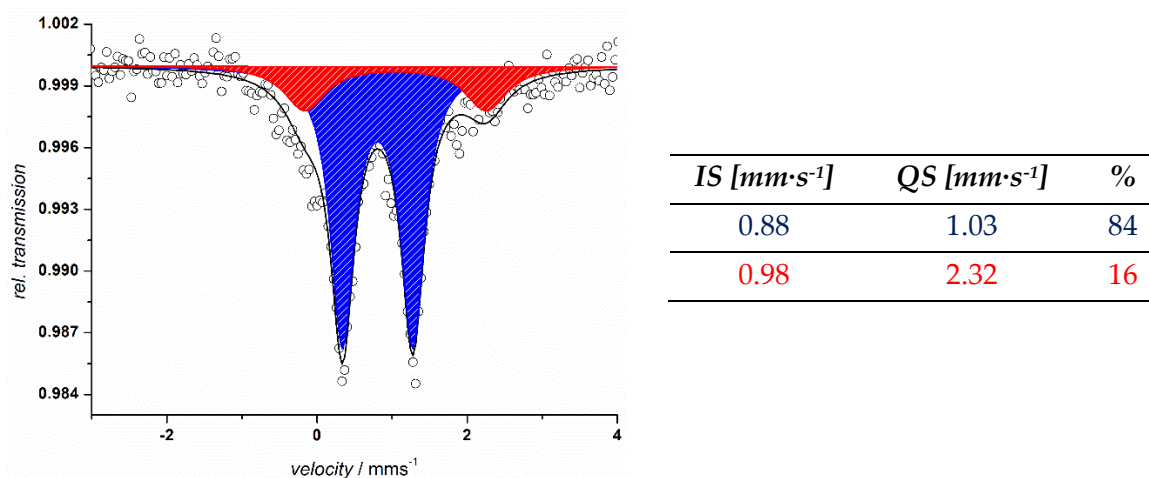
Figure 72. Solid state MB spectrum recorded at 80 K of **13** treated with NaBH₄ after extraction with pentane. Spectral parameters are reported in the table.

When the crude product was extracted with pentane and stored overnight in a freezer at -40°C, rod shaped green crystals were obtained and analyzed by X-ray diffraction (Appendix, Figure 11). Surprisingly, a tetrairon cluster was isolated and the ligand structure seemed to remain stable. However, the ligand moieties showed disorder and despite the fact that the crystal's quality is suitable for X-ray diffraction analysis, it was not possible to discern whether any hydride was present at the iron centers. ¹H-NMR experiments did not lead to any conclusion since the Fe-H resonance is usually not observed for paramagnetic iron hydride compounds. Additional spectroscopic studies, including LIFDI analysis and IR spectroscopy on the complex were inconclusive, and were also prevented by the general instability of the complex at room temperature. Consequently, studies regarding the possibility of obtaining a diiron dihydride species based on **L³⁻** were not continued further.

6.3 Summary

In this chapter, the synthesis of the first dinuclear iron complex supported by the bis(β-diketiminato) ligand L^{3-} was optimized. To minimize the formation of impurities that derive from the high reactivity of the product $LFe_2(OTf)_2(THF)_2$ **13** towards dioxygen, the reaction environment was kept strictly inert.

The compound was characterized by X-ray diffraction analysis, and paramagnetic ^1H-NMR spectroscopy. In combination with the previous data obtained for **13**, it was shown that the iron centers have a +II oxidation state with a *hs*-d^6 electronic configuration.

Reactivity studies with various hydride sources were performed in order to obtain a corresponding dinuclear iron hydride compound. The reaction products were studied by means of paramagnetic ^1H-NMR spectroscopy and Mössbauer spectroscopy. However, a mixture of products mainly containing different *hs*-Fe^{II} species were obtained, and appropriate purification conditions were not achieved. Modification of the hydride source as well as reaction conditions led to similar outcomes. Furthermore, the high reactivity of the products along with the lack of suitable spectroscopic techniques for investigating their properties prevented further studies.

7 Bioinspired Diiron Complexes Relevant for Dinitrogen Fixation

7.1 Preparation of a Novel Diiron Hydrazine-Bridged Complex

When transition metal compounds are involved in the conversion of dinitrogen into ammonia, either biologically or industrially, they should progress through a series of intermediate stages.[204] Insight into the reaction mechanisms are usually supported by the essential features of these metal complexes, and studies regarding their properties helped the scientific community throughout the years to understand how these transformations occur. For instance, it was reported that hydrazine and ammonia form from iron dinitrogen complexes,[205] suggesting that iron compounds of hydrazine or diazene could be possible transient species in the reduction of dinitrogen in such systems. The synthesis of hydrazine complexes containing different metal centers was previously reported,[206] but there are relatively few examples of such iron-based compounds to date. Thus, incorporation of hydrazine into the diiron core of **13** was attempted.

The synthetic strategy that was initially employed followed MANZ's procedure for the preparation of the bimetallic nickel analogue from the bis(nacnac) nickel bromide precursor **1**. The general method used for the diiron complex involved the addition of three equivalents of hydrazine to **13** at room temperature. However, workup of the reaction mixture followed by crystallization attempts led to the following observations. According to the obtained crystal structures (Appendix, Figures 12 and 13), the iron complexes based on **L³⁻** prefer square pyramidal environments for each metal center. When a fifth molecule that can coordinate in the axial position of the iron ions is absent, a structural rearrangement followed by formation of a tetranuclear iron species takes place, and subsequent reactivity studies or synthetic modifications are prevented. On the other hand, numerous exogenous ligand present in solution can potentially bind to the axial position of the iron ions or replace solvent molecules (i.e. THF), if present, so that the presence of impurities should be prevented.

In this particular case, multiple crystallizations of the starting material **13** were typically necessary to remove lithium salts that originated from the ligand deprotonation step since their solubility properties are similar to **13**. Despite being chemically inert, the presence of lithium cations favors the coordination of the other species in the axial position of the iron complex, and in turn prevents the formation of the desired compounds. To that end, ^{7}Li-NMR spectroscopy was used to determine the purity of the precursor **13**. Once sufficient

purity of complex **13** was obtained, hydrazine (N_2H_4) was added in a stoichiometric amount to avoid the substitution of weakly bound solvent molecules at the iron axial positions. Thus, complex **13** was treated with one equivalent of N_2H_4 in THF at room temperature, according to Scheme 50. Substitution of the weakly coordinated triflate bridging unit by hydrazine occurred, and formation of compound $LFe_2(N_2H_4)(OTf)(THF)$ **15** was evidenced by IR spectroscopy and X-ray crystallography. Single crystals suitable for X-ray diffraction of **15** were obtained by layering a green solution of the complex with hexane at -30°C within a few days. The ORTEP diagram of the molecular structure of **15** is presented in Figure 73, and relevant bond lengths and angles are reported in Table 12.
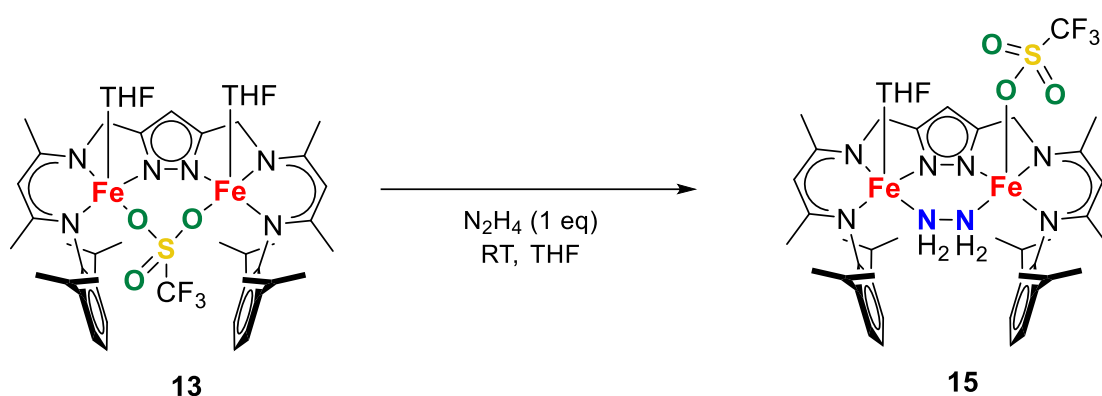
Scheme 50. Synthetic procedure for the synthesis of compound **15**.
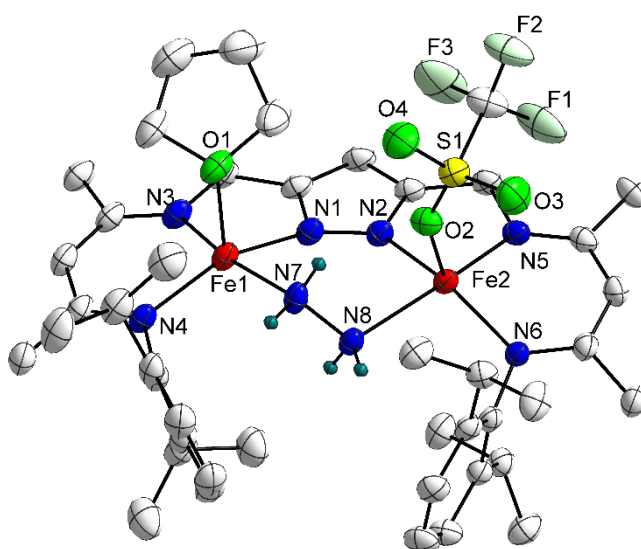
Figure 73. Molecular structure of the diiron hydrazine complex **15**. Hydrogen atoms except for the hydrazine-bridging unit are omitted for clarity.

Table 12. Selected bond lengths and angles for compound **15**.

Bond length / Å		Angle / °	
Fe(1)-N(1)	2.0536(17)	N(3)-Fe(1)-N(1)	79062(7)
Fe(1)-N(3)	2.0703(8)	N(3)-Fe(1)-N(4)	90.39(7)
Fe(1)-N(4)	2.0116(19)	N(4)-Fe(1)-N(7)	99.11(7)
Fe(1)-N(7)	2.2485(19)	N(3)-Fe(1)-N(7)	169.06(7)
Fe(2)-N(2)	2.0748(18)	N(3)-Fe(1)-O(1)	97.40(7)
Fe(2)-N(5)	2.0731(17)	N(2)-Fe(2)-N(5)	78.77(7)
Fe(2)-N(6)	2.0262(17)	N(2)-Fe(2)-N(8)	86.10(7)
Fe(2)-N(8)	2.2603(18)	N(8)-Fe(2)-N(6)	96.3(7)
N(7)-N(8)	1.455(3)	N(8)-Fe(2-N(5)	160.11(8)
Fe(1)-O(1)	2.1691(18)	N(5)-Fe(2-O(2)	111.13(7)
Fe(2)-O(2)	2.1216(16)	N(5)-Fe(2)-N(6)	90.79(7)
Fe(1)···Fe(2)	4.4357(7)	Fe(1)-N(7)-N(8)-Fe(2)	85.40(14)

Compound **15** crystallizes in the monoclinic space group $P2_1/c$ with four molecules in the unit cell. The X-ray diffraction analysis shows that both iron atoms are five-fold coordinated in a square pyramidal environment. One iron atom is coordinated by a THF solvent molecule in the axial position, while a triflate anion is axially bound to the other metal atom. The distances between the iron ions to the nitrogen atoms of the nacnac side arms range from 2.012 Å to 2.073 Å, which are similar to the diiron precursor **13**. Since the N_2H_4 bridging unit replaces the triflate moiety in the starting material **13**, a large decrease in the Fe(1)···Fe(2) distance to 4.306 Å is observed in **15**. Moreover, the coordinated hydrazine displays a N(7)-N(8) distance of 1.455 Å, which agrees with previously reported η^2-hydrazine complexes.[207] The value is also relatively close to that of a structurally characterized *cis*-diiron hydrazine adduct reported by HOLLAND in 2013 (Chapter 1, Figure 10).[126] However, a direct comparison with other systems is not possible since a μ-η^1:η^1-N_2H_4 binding mode for iron complexes was not known so far. The data is consistent with the presence of a N-N single bond, confirmed by the Fe(1)-N(7)-N(8) angle of 114° that agrees with a nitrogen sp^3 hybridization in the bridging ligand. Overall, the steric demand of the N_2H_4 group produces a slight distortion in the system, as suggested from the Fe(1)-N(7)-N(8)-Fe(2) torsion angle of 85.41°.

Binding of the hydrazine between the iron centers was also confirmed by analysis of the N-H stretching vibration using IR spectroscopy (Figure 74). The N-H stretching bands at 3334 cm^{-1} was observed, which differs from the free hydrazine N_2H_4 moiety with a band at roughly 3300 cm^{-1}.[208] This value compares well with other related hydrazine complexes, where the same vibration is found between 3398 cm^{-1} and 3139 cm^{-1}.[116,121] Two other bands

at 3316 cm^{-1} and 3260 cm^{-1} were also observed and can still be assigned to the vibrations of the NH$_2$ unit. Additionally, the bands found in the range 1000 cm^{-1} – 1300 cm^{-1} are consistent with the asymmetric and symmetric SO$_3$ vibrations, and asymmetric and symmetric CF$_3$ stretching of the triflate moiety.[209]
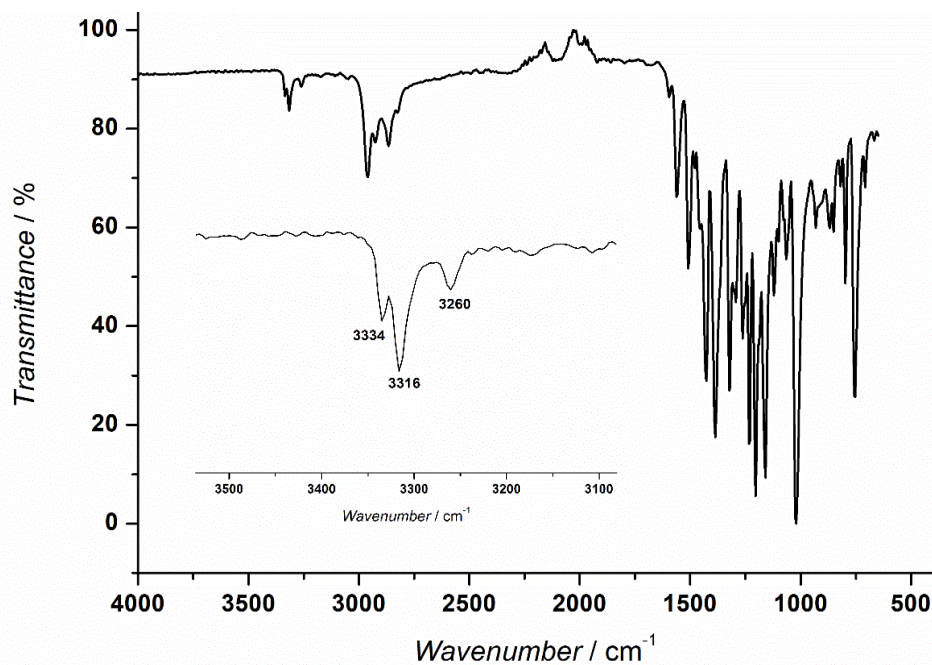
Figure 74. IR spectrum of LFe$_2$(N$_2$H$_4$)(OTf)(THF) **15**. The inset shows the N-H stretching frequencies.

The zero field ^{57}Fe Mössbauer spectrum of crystalline material of **15** revealed only one quadrupole doublet at 80 K with IS = 0.98 mms^{-1} and QS = 2.53 mms^{-1} corresponding to an *hs*-Fe^{II} species, as shown in Figure 75 (left). No distinct subspectra are discernible for the two individual iron atoms, in contrast to what might be expected because of their different coordination environment found in the crystal structure. However, this observation can also be rationalized by the similarities in the coordination sphere, where both the triflate anion and the THF solvent molecule are bound to the metals via an oxygen atom with similar Fe-O bond lengths. As a result, the first coordination sphere on both iron centers is essentially the same and only an averaged signal is detected in the MB experiment. This is consistent with the MB spectra recorded at 7 K and 200 K, where only one doublet was observed with a similar parameters (Appendix, Figure 14).

In order to distinguish between the two different metal centers, another MB experiment was performed on **15** in frozen THF at 80 K (Figure 75, right). In this case, effects that derive from packing or anion effects should be prevented. In these conditions, **15** displays a broader and more asymmetric signal that still corresponds to *hs*-Fe^{II} species. However, two distinct sets of signals in a ratio of roughly 1 : 1 with an IS of 0.97 mms^{-1} (QS = 2.73 mms^{-1}) and 1.04 mms^{-1} (QS = 2.32 mms^{-1}) could be fitted. This behavior may be rationalized by the dissociation of the triflate moiety in solution, affording two distinct iron centers: one bound to the THF molecule and one without a ligand in the axial position. The latter case leads to a modification of the ligand environment on the metal center (from five-fold to four-fold coordinated), which is reflected by a change in the IS and QS values.
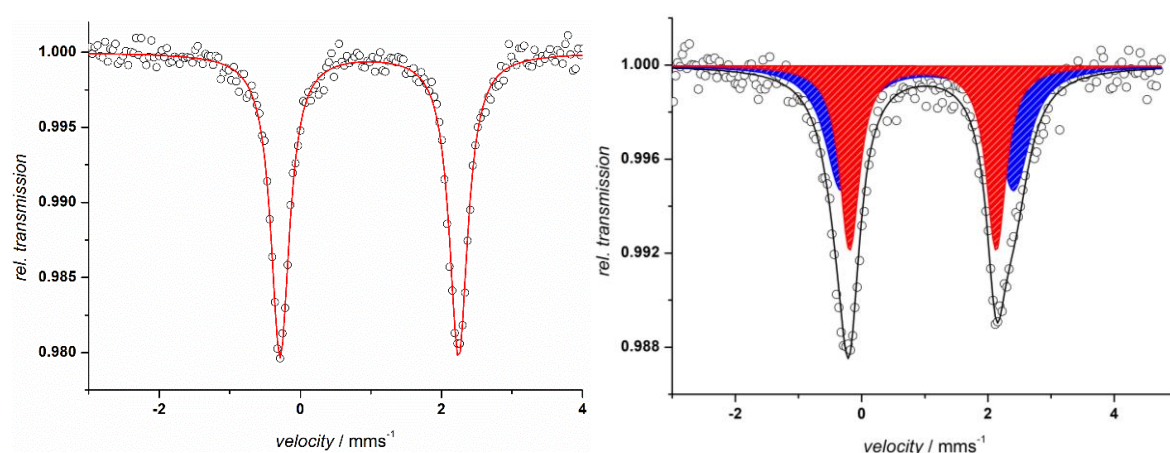
15 (solid state)			*15 (THF)*		
IS [mm·s⁻¹]	*QS [mm·s⁻¹]*	*%*	*IS [mm·s⁻¹]*	*QS [mm·s⁻¹]*	*%*
0.98	2.53	100	0.97	2.73	52
-	-	-	1.04	2.32	48

Figure 75. Solid state (left) and frozen THF solution (right) Mössbauer spectrum of **15** recorded at 80 K. The obtained parameters are reported in the table.

The oxidation and spin state of the iron atoms in **15** was also verified with variable temperature magnetic susceptibility measurements, as shown in Figure 76. The $\chi_M T$ *vs.* T plot shows a $\chi_M T$ value of 5.9 cm³mol⁻¹K in the range from 200 K to 50 K, and it descreases upon lowering the temperature below 50 K. These data match the predicted spin-only value for two *S* = 2 iron centers in the high temperature range, and can be simulated using g = 2.013 and J = −0.071 in the lower temperature range.
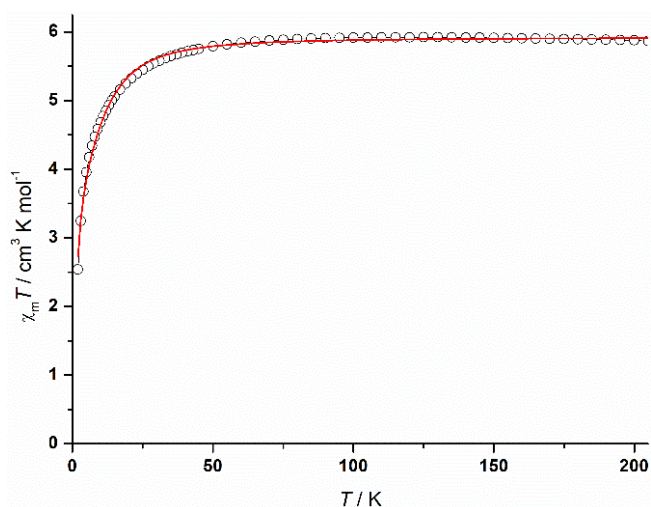
Figure 76. Variable temperature magnetic measurements for complex **15** (black circles). The red line represents for two S = 2 iron centers the simulation using g = 2.013 and J = -0.071.

The ^{1}H-NMR spectrum of **15**, recorded in THF-d$_8$, reflected the *hs* state of the Fe^{II} ions, as it was deduced from previous experiments on **15** in the solid state and in solution (MB). The electronic configuration of the metal atoms is also retained in solution, as seen by the broad and paramagnetically shifted resonances in Figure 77.
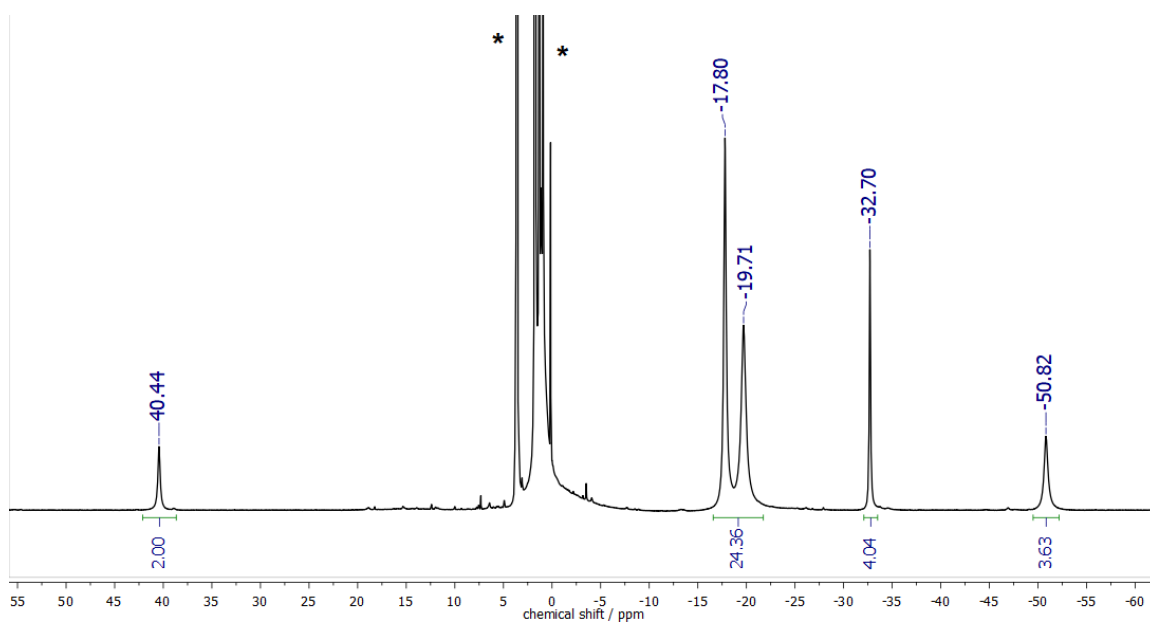
Figure 77. ^{1}H-NMR spectrum of **15** recorded in THF-d$_8$ at room temperature. Solvent signals are marked with an asterisk (*).

Complex **15** exhibits only one set of paramagnetically shifted resonances over a range from -60 ppm to +50 ppm, attributed to the influence of the *hs*-Fe^{II} ions on the local magnetic field and proton relaxation rate.[210] The number of observed resonances is lower than the expected signals consistent with an apparent C$_{2v}$ symmetry in solution. Unfortunately, 2D NMR experiments did not show any cross correlation related to the paramagnetically shifted protons of the signals in the 1D NMR spectrum. Therefore, only the relative intensities could be used to interpret the spectrum. As a result, the signals could not be unambiguously assigned, and a tentative assignment can be made. The signal at +40.44 ppm that integrates for two protons may belong either to the C*H* protons of the nacnac side arms, or to the *para-H* of the aromatic groups. Moreover, the two signals at -32.70 ppm and -50.82 ppm integrate both for four protons and may be assigned to the *meta-H* aryl and isopropyl-C*H* proton groups, respectively, based on a slightly longer distance to the metal center for the latter, as observed in the crystal structure. Unfortunately, two broad peaks at -17.80 ppm and -19.71 ppm integrating for a total of 24 protons could not be accurately interpreted.

To obtain more information, variable temperature ^{1}H-NMR spectra were recorded from 303 K - 263 K, and the results are shown in Figure 78 (left). Overall, the signals shifted upon cooling but the set of peaks corresponding to 24 protons at 298 K did not deconvolute into distinct signals that could be useful for interpretation and assignment. The presence of one set of signals with chemical shifts typical for paramagnetic species is always observed for the recorded spectra, indicating that the *hs*-Fe^{II} state is retained. Additionally, a broad band centered at about 27.5 ppm appeared at temperatures below 278 K. Nevertheless, compound **15** displays typical Curie behavior in solution over the studied temperature range. A linear correlation between the chemical shifts and inverse temperature is illustrated by the Curie plot, shown in Figure 78 (right).
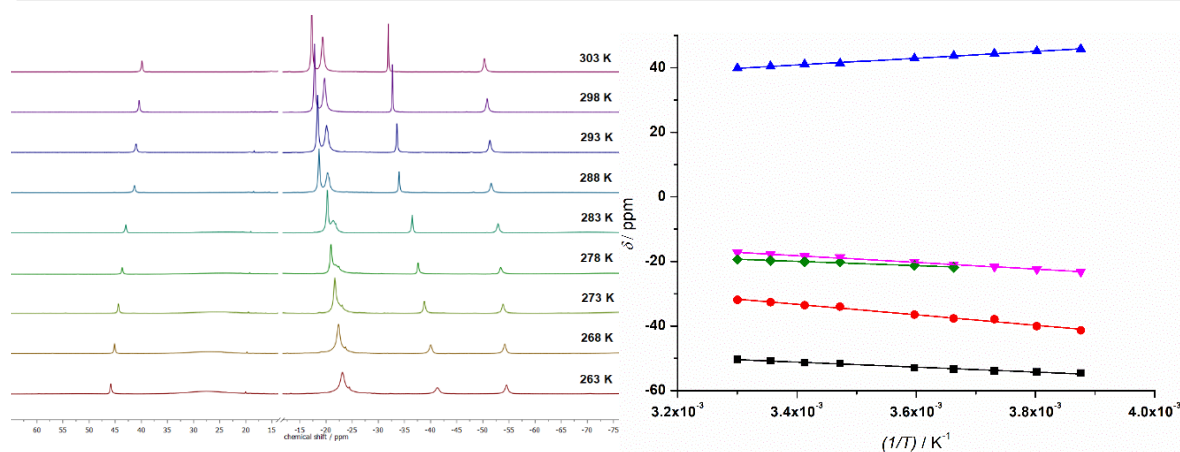
Figure 78. Variable temperature ^{1}H-NMR spectra of **15** (left) in THF-d$_8$ recorded at different temperatures (303 K - 263 K) and Curie plot that shows the linear dependence of ^{1}H resonance shifts on the inverse temperature of **15** (right).

In addition, the NMR characterization was completed by recording the corresponding ^{19}F-NMR spectrum of **15** at room temperature (Figure 79). A single resonance at -53.8 ppm suggests that the triflate moiety bound to the iron center in the axial position found in the solid state mostly retains its position in solution. The presence of free triflate in solution suggested by Mössbauer experiments in frozen solution was not detected, probably due to an equilibrium which is fast on the NMR timescale, and only an averaged signal is detected. Furthermore, it is worth noting that the axial and bridging coordination of this group can be easily distinguished by the resonance value found in the ^{19}F-NMR spectrum. For instance, comparison of the ^{19}F signal found in the starting material **13** ($\delta({}^{19}$F) = +88.6 ppm) with the hydrazine-bridged product shows a dramatic shift of 142.4 ppm.
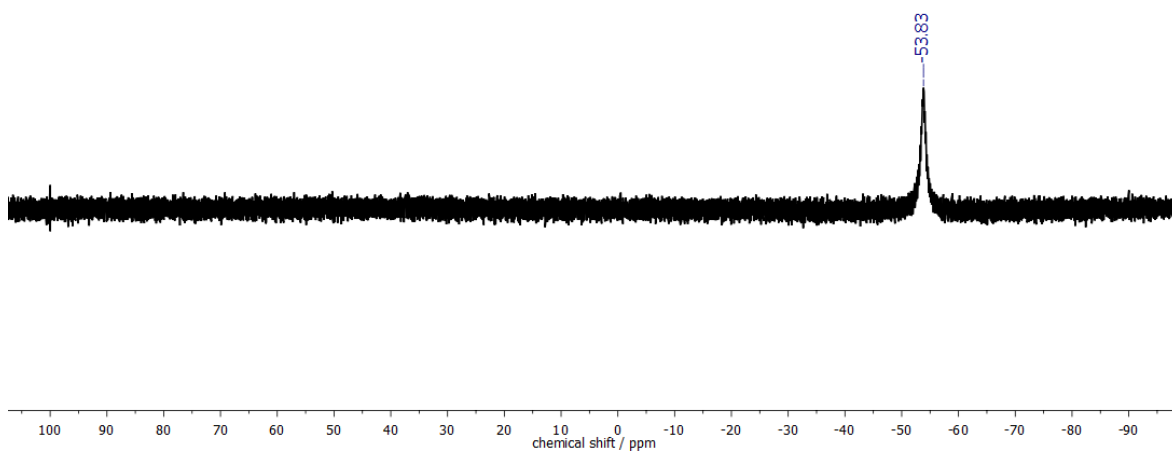
Figure 79. ^{19}F-NMR spectrum of **15** in THF-d$_8$ recorded at room temperature showing that the coordination of the triflate group to the iron center is retained in solution.

7.2 Reactivity of the Hydrazine-Bridged Complex: Deprotonation Attempts

As already described in Chapter 1, an intermediate with Fe/S-bound hydrazine is assumed to occur during the dinitrogen fixation process promoted by nitrogenase. Considering the so-called "alternating pathway" for N_2 reduction, the formation of several species that involve an alternating sequence of protonation and reduction of the N-N bond is suggested. Therefore, reactivity studies on complex **15** were performed in order to investigate the properties of potential intermediates in the activation of dinitrogen.

Deprotonation of the bridging hydrazine unit in **15** was attempted by treating a yellow THF solution of the complex with different equivalents of potassium hydride at room temperature under an atmosphere of dinitrogen, as shown in Scheme 51.

Initially, the reaction was stirred with up to three equivalents of KH for two hours, followed by filtration and subsequent crystallization. However, the complex proved to be relatively stable since decomposition products were not observed, and only starting material was obtained, confirmed by X-ray diffraction analysis. The amount of deprotonating reagent was then increased to five equivalents, and in these conditions, the reaction mixture changed its color to dark green within 30 minutes. When the solution was filtered and crystallization was attempted, a green crystalline solid representing the final product was obtained. The same observations were obtained also when stirring a mixture of **15** in THF with 1.1 equivalents of KH for at least five days.

Unfortunately, the poor solubility of the final complex **16** prevented its characterization in solution, as well as the possibility of obtaining single crystals for X-ray diffraction studies. Several solvents with different polarity such as toluene, THF, MeCN, DMF, MeOH and various combinations of the aforementioned solvents did not lead to any successful result. However, when chlorinated solvents such as DCM or $CHCl_3$ were used, an immediate color change of the suspension was observed, suggestive of the formation of decomposition products within minutes, even at low temperatures.
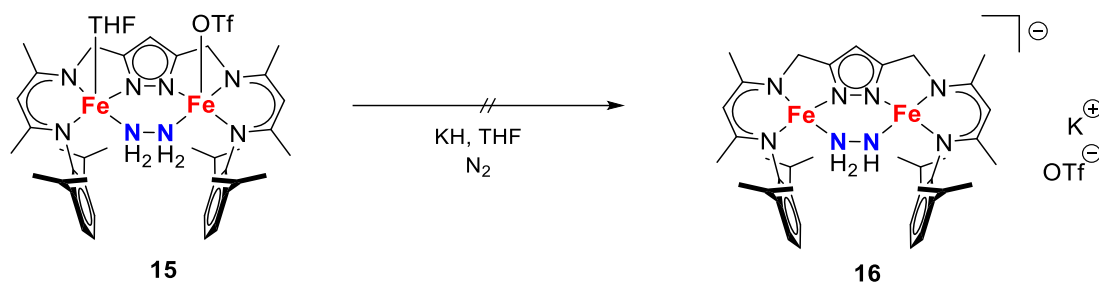
Scheme 51. General scheme for the deprotonation of **15**.

Thus, the formally deprotonated compound **16** was mainly studied in the solid state by means of IR spectroscopy, as shown in Figure 80. The differences in the N-H stretching from the starting material **15** and the final product **16** were taken into account.
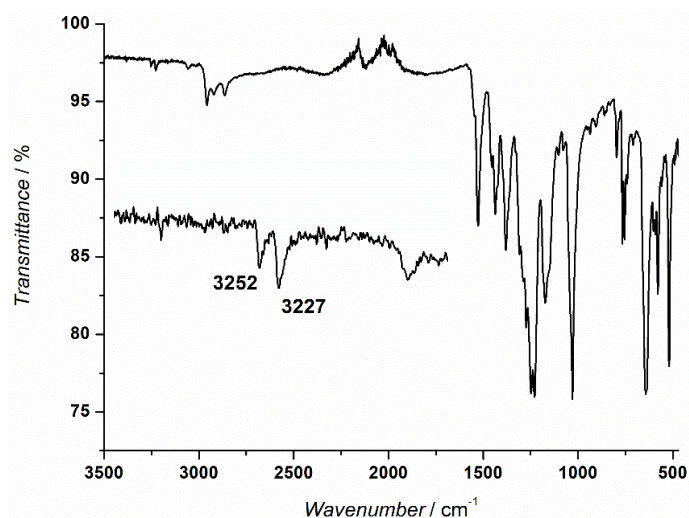
Figure 80. Solid IR-ATR spectrum of complex **16**. The inset shows the N-H stretching bands that belong to the N_2H_x bridging unit.

The IR spectroscopic investigation showed that upon treatment with KH, the bands at 3334 cm^{-1}, 3316 cm^{-1} and 3260 cm^{-1} that belong to the N-H stretching of the N_2H_4 moiety in **15** shifted to 3227 cm^{-1} and 3252 cm^{-1} in complex **16**, along with the disappearance of one band. These changes suggest the formation of a $(N_2H_3)^-$ group, based on comparison with an analogous dinickel hydrazido-bridged complex, previously reported by MANZ (ν(NH) = 3273 cm^{-1}, 3299 cm^{-1}).[145]

Moreover, Mössbauer studies illustrated that when **15** is treated with a slight excess of KH (1.1 equivalents), two distinct signals are detected, which could belong either to two inequivalent iron atoms on the same molecule, or to two different species in a roughly 1 : 1

ratio (Figure 81, left). The signal with IS = 0.95 mm·s^{-1} (QS = 2.19 mm·s^{-1}) undoubtedly corresponds to an *hs*-Fe^{II} compound, and the parameters are very similar to those found for **15**, which may indicate the presence of unreacted starting material.

On the other hand, another quadrupole doublet with IS = 0.36 mms^{-1} and QS = 1.32 mms^{-1} indicates that another species formed, where the nature of the oxidation and spin state of the metal center could be interpreted as either *ls*-Fe^{II}, Fe^{III} or Fe^{I}. Fe^{III} may be safely excluded, as the use of KH as the deprotonating reagent or reducing agent should not lead to the formation of such species.
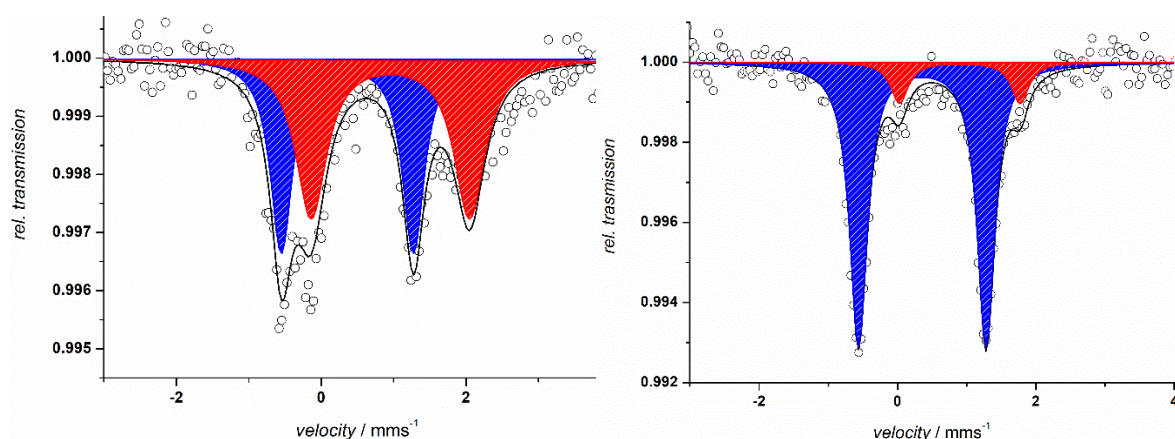
KH (1.1 eq)			KH (excess)		
IS [mm·s^{-1}]	QS [mm·s^{-1}]	%	IS [mm·s^{-1}]	QS [mm·s^{-1}]	%
0.36	1.82	47	0.36	1.85	87
0.95	2.19	53	0.90	1.75	13

Figure 81. MB spectrum recorded at 80 K of **15** treated with a stoichiometric amount of KH (left) and with excess KH (right).

To gain more insights into the identity of **16**, further studies were conducted. Complex **15** was treated with a large excess of KH (> 10 equivalents) and a MB spectrum of the green precipitate was recorded (Figure 81, right). Interestingly, the *hs*-Fe^{II} species decreased significantly, while the other species with and IS of 0.36 mm·s^{-1} increased to 90% from 50%. The same sample was studied by magnetic susceptibility measurements and the results are shown in Figure 82.
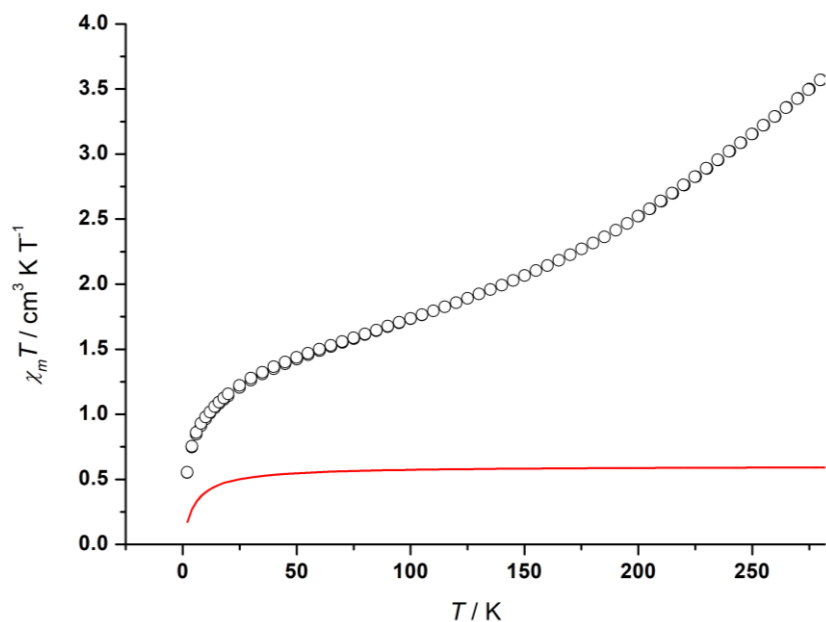
Figure 82. Variable temperature magnetic measurement for complex **15** treated with a large excess of KH. The black circles represent the experimental data, and the red line represent the simulation of paramagnetic *hs*-Fe^{II} dinuclear species with a 10% contribution.

The simulation of the magnetic data highlighted by the red line included the presence of a paramagnetic *hs*-Fe^{II} dinuclear species with a relative concentration of ca. 10%, reflecting the situation observed in the MB spectrum (Figure 80, right). In case that the remaining 90% of the species is *ls*-Fe^{II}, a diamagnetic compound should be detected, whereas if a Fe^{I} species is present, a much higher $\chi_M T$ value should be observed as a result of its intrinsic paramagnetic properties.

Taken these considerations into account, the results obtained by magnetic measurements indicate that a paramagnetic signal is still present when the *hs*-Fe^{II} contribution (10%) is removed. This suggests that upon reaction with excess KH, a Fe^{I} compound could be generated, probably due to the reducing properties of KH. However, several problems regarding the reproducibility of the synthesis of **16** were encountered, so that the amount of material used for magnetic susceptibility measurements was limited. Therefore, only a qualitative interpretation can be given, and quantitative results are characterized by a large error.

It is also worth mentioning that similar results were obtained when another deprotonating agent such as KHMDS was used. In this case, MB experiments showed two quadrupole doublets in a 1 : 1 ratio with IS and QS values in agreement with those found for **15** treated with 1.1 equivalents of KH. Furthermore, no changes in the oxidation and spin state of the

compounds were observed when using an excess of base, confirming that excess of KH could reduce the iron centers.

Considering all these observations, it was not possible to determine whether the reaction was successfully completed and a new complex intermediate in the dinitrogen fixation could be synthetized. Future studies on **15** with different bases will be attempted in hopes to optimize the reaction conditions. Moreover, in order to enhance the solubility of the deprotonated compound, a modification of the ligand scaffold may be a reasonable strategy (for instance, the isopropyl substituents of the aryl groups can be replaced by benzylic moieties). Furthermore, magnetic measurements to identify the nature of the iron centers must be repeated several times in order to gain information about the reproducibility of the results.

7.3 Summary

In this last chapter, further reactivity studies employing the diiron triflate precursor **13** were performed. The goal was to achieve the binding of small molecules to obtain intermediate compounds relevant for dinitrogen fixation. After optimization of the reaction conditions, it was possible to substitute the triflate bridging group in **13** with hydrazine to form the corresponding LFe$_2$(N$_2$H$_4$)(OTf)(THF) **15** complex.

15 could be obtained in high purity and reasonable yields, and it was characterized by means of NMR spectroscopy, IR spectroscopy, Mössbauer spectroscopy and X-ray diffraction analysis. In particular, MB characterization showed that the iron centers have an oxidation state of +2 and retain their *hs* configuration, as expected. Furthermore, ^{19}F-NMR was particularly useful to prove the coordination of the triflate moiety to the iron ion in solution, and to distinguish the coordination mode (i.e. axial *vs.* bridging coordination) by comparing the isomer shift value of the iron precursor **13** with that found for the final product **15**.

Furthermore, deprotonation of the hydrazine-bridged compound **15** was probed. However, reaction with KH gave poorly soluble compounds, which prevented their characterization and consequent reactivity investigations. IR spectroscopy of the product **16** suggested the formation of a (N$_2$H$_3$)$^-$ unit. On the other hand, Mössbauer and SQUID analysis suggested that the iron centers could also change their oxidation state, probably due to the reducing

nature of the KH. Furthermore, preliminary structural data on **16** showed the formation of an iron cluster complex, which is highly susceptible to decomposition.

Ongoing studies aim to employ a modified ligand scaffold in order to improve the solubility of the products, and to facilitate further characterization.

8 Conclusion and Perspectives

This thesis work has presented new insights into the reactivity of dinuclear nickel and iron complexes towards small molecules relevant to the multitude of functions observed in biological systems. Inspired by nature, where enzymes often mediate the conversion of key substrates by taking advantage of metal-metal cooperativity, a novel ligand scaffold that provide two cavities for incorporating two metal centers in close proximity was developed.[146] The corresponding nickel[145,146] and iron[196] complexes were obtained and further reactivity studies were conducted in this work.

In the first part of this thesis, the dinuclear nickel(II) dihydride complex **2** was employed to generate the corresponding $KLNi_2(N_2O_2)$ **3** compound. Two reducing equivalents stored by **2** as hydrides were provided for the successful reduction of two molecules of nitric oxide (NO) upon release of dihydrogen H_2. The process was followed by coupling of the $(NO)^-$ groups to obtain the corresponding $(N_2O_2)^{2-}$ hyponitrite moiety which was trapped at the nickel centers supported by the β-diketiminate scaffold. In contrast to the structural evidences observed for **3** in the solid state, ^{1}H-NMR experiments revealed a symmetric ligation of the bridging unit, as a result of a dynamic process which is fast on the NMR timescale. DFT calculations that aim to shed light into such process are currently ongoing.

The unprecedented *cis* coordination mode of the hyponitrite group in **3** supports the hypothesis of the formation of similar species occurring into the nitric oxide reduction process mediated by natural enzymes such as nitric oxide reductases (NORs). In fact, the reactivity of **3** towards acids was studied. Headspace IR spectroscopy analysis of the reaction mixture confirmed the production of nitrous oxide (N_2O), which amount was quantified to ca. 70% with respect to the hyponitrite compound **3**. On the other hand, ^{1}H-NMR experiments allowed for the detection of water, which forms as byproduct of the reaction, showing the typical resonance for the corresponding dinickel hydroxo complex LNi_2OH **4** at -7.24 ppm. These results emphasize the significance of the formation of hyponitrite moiety in the NO reduction, and they are summarized in Scheme 52.
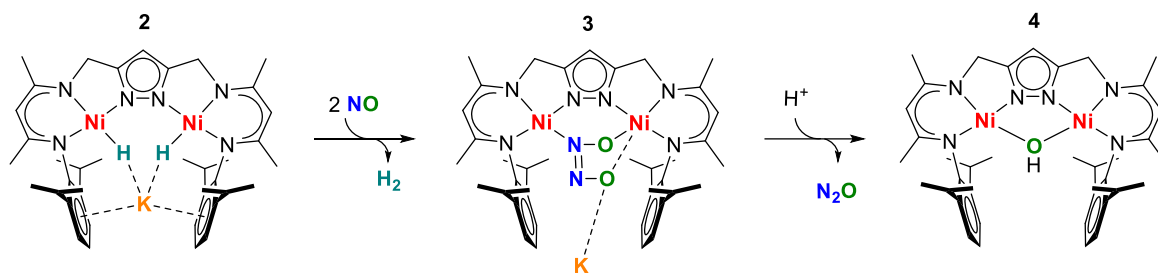
Scheme 52. Reductive binding of two molecules of NO mediated by complex **2** and subsequent protonation of the hyponitrite complex **3** to produce N_2O and water.

To elucidate the mechanism by which the coupling of two NO units at the nickel centers occurs, studies regarding the formation of a mononitrosyl nickel complex were conducted. Direct transfer of two electrons from **2** to one equivalent of NO produces an highly reactive species, which is postulated to be a dianionic $(NO)^{2-}$ complex in light of the fact that only the hyponitrite **3** and complex **4** as decomposition product were isolated from the reaction mixture. To prove the formation of such super-reduced $(NO)^{2-}$ intermediate, a novel nitroxyl NO^- complex **5** was synthetized by a two electron reduction of a NO^+ source mediated by **2**. An unusual coordination mode for the NO moiety was found, and the presence of the NO bridging unit in the complex was confirmed by ^{15}NO labeling experiments. Cyclic voltammetry experiments revealed the possibility of reducing complex **5** at a potential of −2.0 V *vs.* the ferrocene/ferrocenium couple, which is rather low but chemically achievable by using a suitable reagent.

The one-electron chemical reduction of **5** promoted by decamethylcobaltocene $(Co(Cp^*)_2)$ led to the formation of a new species $[LNi_2(NO)]^-$ **6**, as indicated by EPR measurements. Indeed, usage of a bulky reductant led to the formation of a radical anion, whose electron density is mainly located on the metal centers as indicated by the pronounced anisotropy of the g values. Furthermore, labeled ^{15}NO experiments led to analogous results, indicating that the nitrogen atoms of the bridging unit do not affect the multiplicity of the system. Consequently, the spin density on these atoms must give a minor contribution to the total EPR signal.

Reduction of **5** in presence of alkali metal cations – specifically potassium K^+ – significantly influences the electronic structure of the corresponding reduced species. Electrochemistry studies showed that the reduction becomes irreversible and occurs at lower potentials of −2.3 V (*vs.* Fc/Fc^+) with respect to the process in absence of K^+. Reaction of **5** with potassium benzophenone led to the formation of $KLNi_2(NO)$ **7**. Characterization of this new paramagnetic complex revealed an EPR signal consistent with an organic species, indicating that the electron density is localized on the NO bridging unit due to the

interaction with the potassium cation. In fact, preliminary structural determination analysis of **7** showed that the potassium cation is held in the cavity between the aryl groups of the isopropyl side arms of the ligand. The experiments presented in this chapter highlight the importance of such metal cations in the stabilization of a $(NO)^{2-}$ anion at the nickel centers, as well as the possibility of tuning the electron density on specific sites of the complex.

Reaction of compound **6** and **7** with one equivalent of NO led to the formation of the hyponitrite complex **3**, which was detected by ESI-MS experiments, supporting that the first steps of the NO reduction to N_2O pathway can be rationalized by considering a two electron reduction of one molecule of NO followed by coupling to another NO radical species. These conversions are represented in Scheme 53.
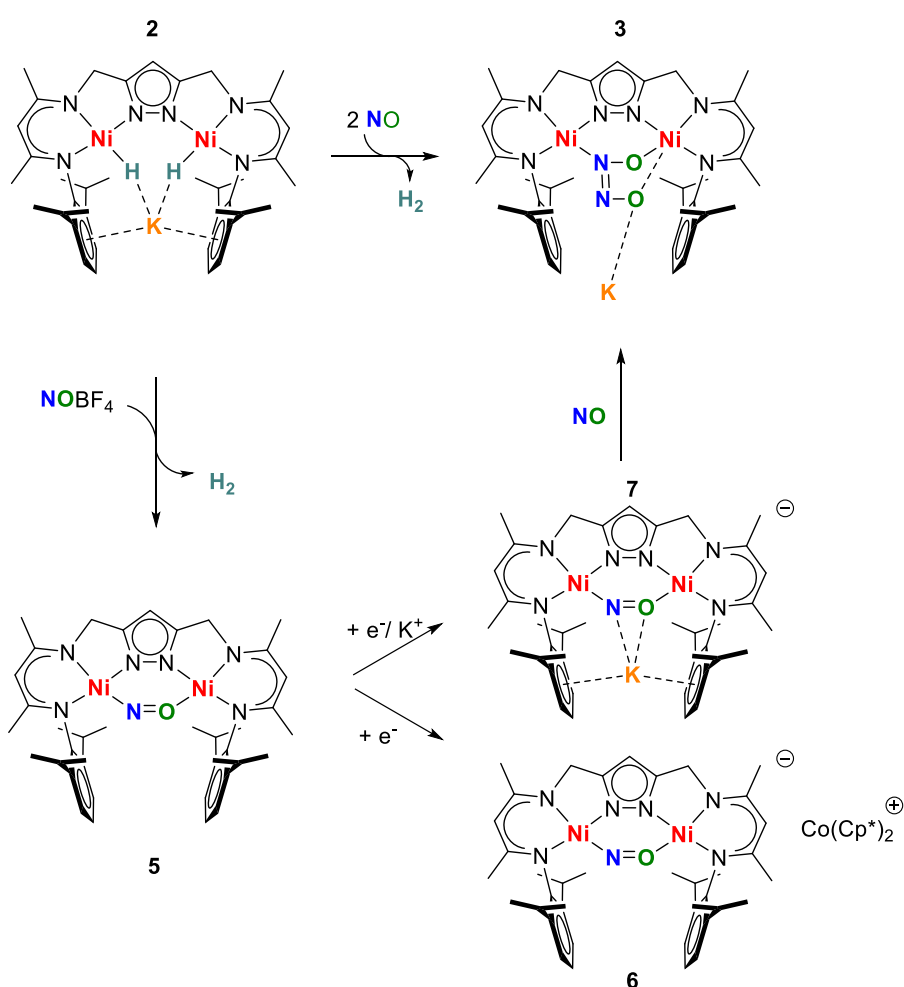
Scheme 53. Redox transformations of nitric oxide on the dinickel dihydride complex **2**.

Finally, the redox transformations of nitrosobenzene (PhNO) mediated by the dinuclear nickel dihydride complex **2** were investigated to gain more insight into the chemistry of such organic molecules, which are thought to be relevant in processes connected to the chemistry of NO (Scheme 54). It was possible to doubly reduce PhNO followed by its binding to the nickel centers to form the corresponding compound KLNi2(PhNO) **9**. Structural analysis revealed once more the presence of the potassium cation held in the ligand cavity. The cation interacts weakly with the PhNO unit, and it can be easily removed by treating **9** with [2.2.2]-cryptand to form [K(crypt)][LNi2(PhNO)] **10**. While compounds **9** and **10** display significant differences with respect to the NO bond strength in the solid state, which are supported by IR experiments, the electronic properties of the compounds analyzed by cyclic voltammetry experiments are similar in solution. Furthermore, it was possible to oxidize these reduced species to obtain the radical LNi2(PhNO) **11**. EPR studies on **11** and the labeled ^{15}NO analogous complex indicated that the electron density is exclusively located on the PhNO bridging unit.

It was also shown that it was possible to protonate complex **9** to obtain a bridging (μ-PhNHO) unit in LNi2(PhNHO) **12**. This complex represents a stable analog of HNO, and was characterized by X-ray diffraction.
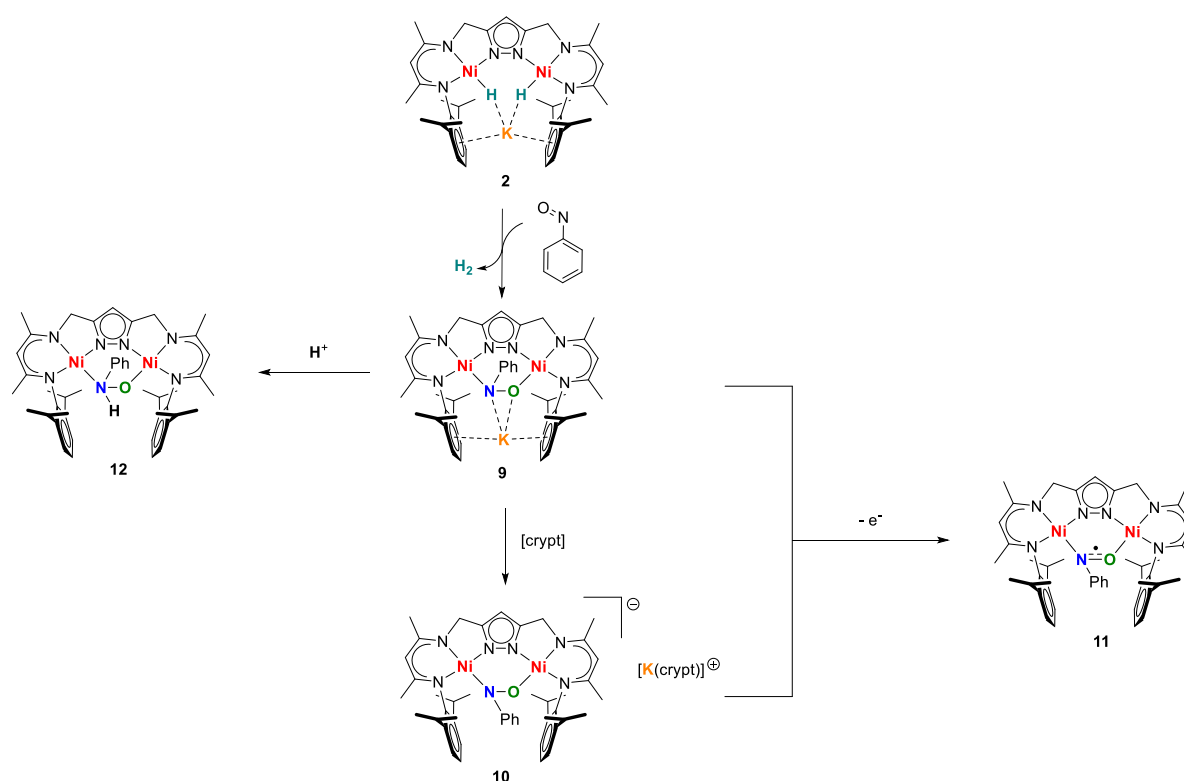
Scheme 54. Interconversions of nitrosobenzene mediated by **2**.

In the second part of this thesis, the properties of the dinuclear iron β-diketiminate complex LFe$_2$(OTf)(THF) **13** were further studied in solution, and paramagnetic ^{1}H-NMR spectroscopy proved to be an useful tool for such investigations. Furthermore, the reactivity of **13** towards hydride donors was explored in order to synthetize the corresponding diiron hydride complex **14**. However, the general instability of the reaction products, as well as the lack of suitable techniques for the characterization of these compounds, prevented the isolation of the desired molecule.

Further reactivity studies aimed to obtain iron complexes as model for intermediates in the biological nitrogen fixation led to the synthesis of an iron hydrazine complex LFe$_2$(N$_2$H$_4$)(OTf)(THF) **15**. The compound displays a novel binding mode for neutral hydrazine at the iron centers, and the possibility of deprotonating such moiety was considered. The poor solubility of the final products interfered with their characterization. Thus, modification of the ligand scaffold to enhance this intrinsic property is considered for future studies.

In conclusion, this thesis has presented several compounds that provide insights into the reactivity of small molecules of biological and industrial relevance. Especially in the nitric oxide chemistry mediated by the dinuclear nickel complex **2**, unprecedented insight into the redox transformations and binding of this molecule to the metal scaffold were obtained. Experiments concerning the reactivity of the nickel nitroxyl compound **5** and its reduced analogues **6** and **7** may be considered with respect to protonation or methylation to isolate highly reactive moieties of relevance. Although this work has shed light on a numbers of reactions, which benefit from metal-metal cooperativity, a great number of open questions still remains for future generation studies.

9 Experimental Part

9.1 Materials and Methods

9.1.1 General Considerations

Unless otherwise noted, all manipulations were performed under an inert atmosphere of dry argon (dried by passing over P_2O_5 on solid support [Sicapent®, Merck]) using standard Schlenk techniques, or in a glovebox (MBRAUN LABmaster) with levels of H_2O and O_2 below 0.5 ppm. All glassware was stored in an oven at 120°C overnight prior use. Solvents were dried and distilled under Ar from the appropriate drying agents (THF, diethyl ether, n-hexane, n-pentane and toluene from sodium/benzophenone; DCM, $CHCl_3$, Et_3N from CaH_2 or P_2O_5; MeOH from Mg) and stored under molecular sieves (3Å) and thoroughly deoxygenated with Ar prior use. Deuterated solvents were treated according to the undeuterated analogous. Available chemicals were purchased from commercial sources and used as received, unless otherwise stated. The ligand precursors **I**, **II**, **III**, **IV**, **V**[211,212,213] and $Ph_3C–S–NO$,[214] nitrosonium tetrafluoroborate ($^{14/15}NO$),[169] labelled $Ph^{15}NO$,[34] $Fe(OTf)_2 \cdot 2MeCN$,[215] $LNi_2(\mu\text{-Br})$ **1** and $KL(NiH)_2$ **2** were synthetized according to published procedures.[146] Nitric oxide gas (NO) was purchased from LINDE and passed through a column filled with Ascarite II and distilled before being added to the reaction mixture. A picture of the reaction setup is depicted in the Appendix (Figure 16).

9.1.2 NMR Spectroscopy

^1H, ^{13}C, ^{19}F, ^{15}N spectra were recorded on a BRUKER AVANCE 400 or 500 MHz spectrometer at 298K, unless otherwise mentioned. Chemical shifts are reported in ppm and are referenced to the corresponding solvent residual signal.[216] ^{13}C NMR spectra were recorded in proton-decoupled mode. Peaks are labeled according to their multiplicity and abbreviated as follows: s (singlet), d (doublet), t (triplet), m (multiplet) and an additional b in case of broad signals that prevent the determination of coupling constants (J [Hz]).

9.1.3 Ultraviolett/visible Spectroscopy and Infrared Spectroscopy

UV/Vis spectra were recorded using a Varian Cary 5000 or Varian Cary 60 with quartz cells (1 cm) in the solvents indicated and the temperature control was performed with a cryostat from UNISOKU SCIENTIFIC INSTRUMENTS (Japan).

Solid state and solution IR spectra were recorded with a Cary 630 FTIR spectrometer with Dial Path Technology and analyzed by FTIR Microlab software. Gas phase IR spectra were recorded with a Bruker Vertex 70 spectrometer and analysed by OPUS 7.5 program. The peaks (ṽ) were labeled according to their relative intensity: vs (very strong), s (strong), m (medium), w (weak), vw (very weak). The calculated isotope shift values were obtained by using the following equations:

$$\nu = \frac{1}{2\pi}\sqrt{\frac{k}{m}}$$

where

ν = vibrational frequency

k = force constant

m = reduced mass = $\frac{m_A m_B}{m_A + m_B}$
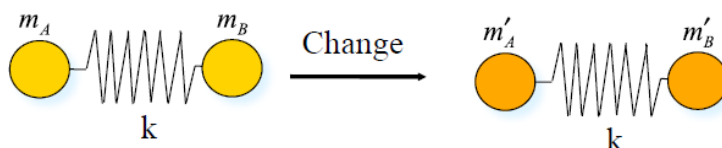
$$\nu' = \nu\sqrt{\frac{m}{m'}} = \nu\sqrt{\frac{m_A m_B}{m_A + m_B}\frac{m'_A + m'_B}{m'_A m'_B}}$$

9.1.4 Mass Spectrometry

ESI MS measurements were performed using a Thermo Finnigan Trace LCQ spectrometer or a Bruker Apex IV (FTICR-MS). The samples were prepared in a glovebox (MBRAUN UNIlab) under argon atmosphere and injected into the instrument via a direct Peek™ tubing connection. LIFDI spectrometry was performed using a Joel AccuTOF spectrometer under inert conditions.

9.1.5 Electrochemistry

Cyclic voltammograms were measured under inert conditions with a Gamry Interface 1000b potentiostat controlled by Gamry Framework software. The samples were measured in THF solutions at a concentration of 1 mM of complex and 0.1 M of Bu_4NPF_6 as conductive salt. A glassy carbon electrode was used as working electrode, a platinum wire as counter electrode and a silver wire as a pseudo-reference electrode. Ferrocene was added as an internal standard and all spectra were referenced to the ferrocene/ferrocenium redox couple (Fc/Fc+).[175]

Electronic spectra during spectro-electrochemical measurements were recorded with the *BWTek Exemplar LS* Spectrophotometer supplied with the quartz dip probe (1 mm, Hellma Analytics). Spectra were analyzed by BWSpek software.

9.1.6 Mössbauer Spectroscopy

Mössbauer spectra were recorded at a given temperature with a ^{57}Co source in a Rh matrix using an alternating constant-acceleration *WissEl* Mössbauer spectrometer operated in the transmission mode and equipped with a *Janis* closed-cycle helium cryostat. Isomer shifts (IS) and the quadrupole splitting (QS) are given in mms^{-1} relative to iron metal at ambient temperature. The Mfit program was used for the simulation of the experimental data.[217]

Solid samples were introduced in sealable PEEK tablets which was mounted in a sample holder. Solution samples were placed in a PEEK cup and required at least 20 mg of solid material dissolved in 1 mL of the respective solvent. Air sensitive samples were prepared in a glovebox and immediately frozen in liquid nitrogen. Data were collected for one day in order to obtain a satisfactory signal-to-noise ratio.

9.1.7 Electron Paramagnetic Resonance Spectroscopy

X-band EPR spectra were obtained with a Bruker E500 ELEXSYS spectrometer equipped with a standard cavity (ER4102ST, 9.45 GHz). The temperature was regulated with an Oxford Instruments Helium flow cryostat (ESP910) and an Oxford temperature controller (ITC-4). The microwave frequency was measured with the built-in frequency counter and the magnetic field was calibrated using an NMR field probe (Bruker ER035M). The final spectra were simulated with Easy-Spin[218] or XSophe software.[219]

9.1.8 Magnetic Susceptibility Measurements

A SQUID magnetometer (Quantum Design MPMS XL-5) was used for measuring temperature-dependent magnetic susceptibilities. Solid samples were placed in a capsule inside a glovebox. In order to avoid orientation of the crystalline material, samples were fixed with the low viscosity perfluoroether based inert oil *Fomblin Y45*. The capsule was then placed in a diamagnetic sample holder (PTFE straw). Each raw data file for the magnetic moment was corrected for diamagnetic contribution of the gelatin capsule according to M_{dia}(caps) = $\chi_g \times m \times H$. The molar susceptibility data were corrected for the diamagnetic contribution using Pascal constants and the increment method according to Haberditzl.[220] The program[221] *julX* was used for the simulation of the magnetic properties using a Heisenberg-Dirac-van-Vleck Hamiltonian (HDvV) including isotropic exchange interaction, zero field and Zeeman splitting. Temperature independent paramagnetism (*TIP*) and paramagnetic impurities (*PI*) were included according to $\chi_{calc} = (1 - PI) \cdot \chi + PI \cdot \chi_{mono} + TIP$. Intermolecular interactions were considered in a mean field approach by using a Weiss temperature θ. The Weiss temperature θ (defined as $\theta = z\,J_{inter}\,S(S+1)/3k$) relates to intermolecular interactions $z\,J_{inter}$, where J_{inter} represents the interaction parameter between two nearest neighbor magnetic centers, k the Boltzmann constant (0.695 cm^{-1} $\cdot$K^{-1}) and z is the number of nearest neighbors.

9.1.9 X-ray Crystallography

X-ray analyses were performed on a STOE IPDS II diffractometer with an area detector (graphite monochromated Mo-K$_\alpha$ radiation, Λ = 0.71.73 Å) by use of ω scans at 133K. The structures were solved by direct methods with SHELXT[222] and refined on F^2 using all reflections with SHELX-2013/14.[223] Non-hydrogen atoms were refined anisotropically unless otherwise noted. Hydrogen atoms were placed in calculated positions and assigned to an isotropic displacement of 1.2/1.5 Ueq(C). Face-indexed absorption corrections were performed by the program X-RED.[224]

9.2 Synthetic Procedures

9.2.1 Ligand Synthesis and Complexes Precursors
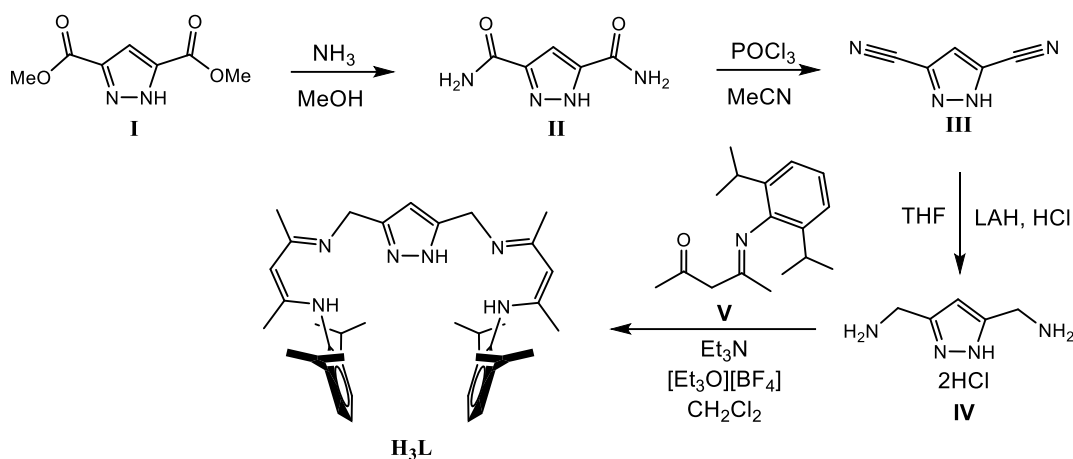
Scheme 55. Synthesis route for the ligand **H₃L**.

The synthesis of the ligand **H₃L** was modified from the literature known procedure.[146]

A colorless solution of 2-[2,6-diisopropylphenyl)imido]-pent-2-en-4-one (16.4 g, 63 mmol, 2 eq) in dry DCM (100 mL) was slowly treated with a solution of triethyloxonium tetrafluoroborate (12.7 g, 67 mmol, 2.1 eq) in DCM (20 mL). The resulting mixture was stirred overnight at room temperature. Dry triethylamine (9.3 mL) was added and after 20 minutes of stirring, the red solution was added to a suspension of bis(3,5-aminomethyl)pyrazole **IV** (4.0 g, 32 mmol, 1 eq) in dry triethylamine (20 mL). The mixture was stirred for 3 days at room temperature under argon. The solvents were removed under reduced pressure and the resulting orange residue was extracted with toluene (100 mL). The suspension was filtrated and the solvent was completely removed under reduced pressure. The orange solid was washed with water (3 × 30 mL) and dried under vacuum. The product was recrystallized from ethanol, dried overnight under reduced pressure and stored under inert atmosphere. Yield = 9.7 g, 43%.

Molecular weight: 608.92 g/mol ($C_{39}H_{56}N_6$)

¹H-NMR (CDCl₃, 300 MHz) δ = 7.12-6.98 (m, 6H, Ar), 5.94 (s, 1H, *H*-Pz), 4.64 (s, 2H, C*H*), 4.32 (s, 2H, C*H₂*), 2.77 (s, 2H, iPr-C*H*), 1.87 (s, 6H, C*H₃*), 1.56 (s, 6H, C*H₃*), 1.08 (d, 12H, C*H₃*-Ar), 0.97 (C*H₃*-Ar) ppm.

¹³C-NMR (CDCl₃, 75 MHz) δ = 166.0, 155.6, 146.3, 138.0, 123.6, 122.8, 101.3, 40.1, 23.8, 22.8, 21.6, 19.2.

ATR-IR ṽ/cm⁻¹ = 3192 (br, NH), 3131 (m, NH), 3105 (m, NH), 3060 (w), 3025 (w), 2962 (m), 2928 (w), 2859 (w), 1622 (vs), 1552 (vs), 1501 (w), 1455 (m), 1433 (m), 1377 (m), 1361 (m),

1290 (m), 1284 (m), 1266 (m), 1179 (m), 1158 (m), 1095 (m), 1046 (m), 1026 (m), 1003 (w), 934(w), 818 (w), 805 (w), 788 (s), 752 (s), 694 (m), 664 (w), 608 (w), 586 (w), 518 (w), 498 (w).
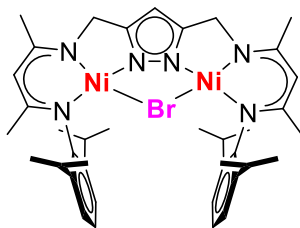
1

Complex **1** was synthetized by following the literature known procedure.[146]

Molecular Weight: 803.17 g/mol ($C_{39}H_{53}N_6Ni_2Br$)

¹H-NMR (CDCl₃, 300 MHz) δ = 6.91-6.80 (m, 2H, Ar), 6.75-6.73 (d, J_{H-H} = 6 Hz, 4H, Ar), 5.46 (s, 1H, *H*-Pz), 4.68 (s, 2H, C*H*), 4.07 (s, 4H, C*H₂*), 3.30-3.20 (m, 4H, iPr-C*H*), 1.95 (s, 6H, C*H₃*), 1.39 (s, J_{H-H} = 6 Hz, 12H, C*H₃*), 1.26 (s, 6H, C*H₃*-Ar), 0.95 (d, J_{H-H} = 6 Hz, 12H, C*H₃*-Ar) ppm.

¹³C-NMR (CDCl₃, 75 MHz) δ = 159.7 (s, CH*C*Me), 153.2 (s, Pz) 147.6 (s, Ar), 141.5 (s, Ar), 125.4 (s, Ar), 123.3 (s, Ar), 97.2 (s, CH₂), 91.5 (s, 4*C*-Pz), 54.4 (s, *C*H), 28.1 (s, *C*H₃-iPr), 24.8 (*C*H₃-iPr, 23.7 (s, Me), 21.5 (s, Me) ppm.

ATR-IR ṽ/cm⁻¹ = 3058 (w), 2959 (m), 2923 (m), 2862 (m), 1555 (m), 1532 (vs), 1462 (vs), 1435 (s), 1399 (s), 1381 (s), 1369 (vs), 1313 (s), 1279 (s), 1252 (s), 1236 (m), 1186 (m), 1175 (s), 1093 (s), 1052 (s), 1032 (m), 1012 (m), 957 (m), 935 (m), 795 (vs), 759 (vs), 745 (vs), 542 (m).
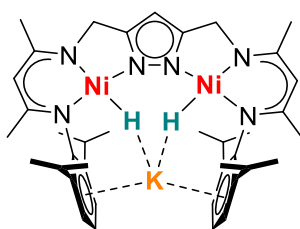
2

Complex **2** was synthetized by following the literature known procedure.[146]

Molecular Weight: 763.44 g/mol ($C_{39}H_{55}N_6Ni_2K$)

¹H-NMR (THF-d₈, 400 MHz) δ = 6.88−6.77 (m, 6H, Ar), 5.56 (s, 1H, *H*-Pz), 4.56 (s, 2H, CH), 4.23 (s, 4H, CH₂), 3.48−3.43 (sept, 4H, *H*-iPr), 1.83 (s, 6H, Me), 1.22 (s, 6H, Me), 1.12 (d, J_{H-H} = 6 Hz, 12H, Me-iPr), 1.03 (d, J_{H-H} = 6 Hz, 12H, Me-iPr), −24.17 (s, 2H, Ni*H*) ppm.

¹³C-NMR (THF-d₈, 100 MHz) δ = 158.6 (C_q-Me), 157.6 (C_q-Me), 157.1 (C_q-Me), 156.6 (C_q-Me), 140.3 (Pz), 123.9 (Ar), 123.2 (Ar), 97.0 (CH), 92.2 (*C*HPz), 53.3 (CH₂), 28.3 (Me-iPr), 24.5 (Me-iPr), 23.9 (Me-iPr), 22.7 (Me).

ATR-IR ṽ/cm^{-1} = 3054 (w), 2955 (m), 2858 (m), 1961 (Ni–H) (m), 1562 (s), 1518 (vs), 1461 (s), 1431 (vs), 1398 (vs), 1355 (m), 1315 (s), 1272 (s), 1254 (m), 1230 (m), 1196 (m), 1159 (m), 1097 (m), 1057 (w), 1028 (m), 935 (w), 861 (m), 804 (m), 773 (m), 731 (m), 720 (m), 644 (m), 546 (m), 516 (m), 458 (m), 422 (m).
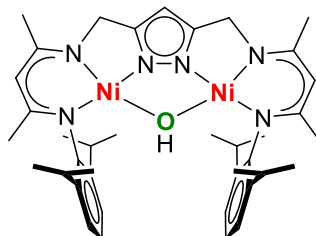
4

Complex **4** was synthetized by following the known procedure.[145]

Molecular Weight: 740.29 g/mol ($C_{39}H_{54}N_6Ni_2O$)

^{1}H-NMR (THF-d$_8$, 400 MHz) δ = 6.98−6.94 (t, 4H, Ar), 6.82−6.80 (d, 2H, Ar), 5.48 (s, 1H, H-Pz), 4.60 (s, 2H, CH), 4.01 (s, 4H, CH$_2$), 3.37−3.32 (sept, 4H, *H*-iPr), 1.86 (s, 6H, Me), 1.61 (s, 12H, J$_{H-H}$ = 4 Hz, Me), 1.08 (s+d, 18H, Me+Me-iPr), -7.26 (s, 1H, OH) ppm.

^{13}C-NMR (THF-d$_8$, 100 MHz) δ = 161.2 (C$_q$-Me), 159.3 (C$_q$-Me), 145.5 (Ar), 142.4 (Ar), 126.1 (Ar), 125.3 (Ar), 98.2 (CH), 91.6 (Pz), 55.14 (CH$_2$), 29.2 (Me), 25.9 (Me), 23.7 (Me), 21.4 (Me).

ATR-IR ṽ/cm^{-1} = 3608 (m, OH), 3058 (w), 2955 (m), 2864 (m), 1553 (m), 1529 (vs), 1462 (s), 1436 (s), 1394 (vs), 1381 (vs), 1323 (m), 1314 (m), 1271 (m), 1251 (m), 1234 (m), 1196 (w), 1159 (w), 1104 (w), 1082 (w), 1060 (m), 1018 (m), 946 (m), 874 (m), 799 (s), 756 (vs), 732 (vs), 709 (w), 649 (m).

9.2.2 Complexes Syntheses and Reactivity Studies

KLNi$_2$(N$_2$O$_2$) (3): In a glovebox, a 25 mL Schlenk flask was charged with a solution of **2** (10 mg, 1.3 · 10^{-2} mmol, 1 eq) in THF (3 mL) and sealed with a septum. The flask was transferred out of the glovebox and dry NO$_{(g)}$ (0.64 mL, 2.6 · 10^{-2} mmol, 2.0 eq) was purged into the solution with a gas tight Hamilton syringe. The mixture was stirred for 10 minutes, during which the color changed to dark red. The solvent was removed under reduced pressure and the flask was transferred again into the glovebox. The compound was extracted with Et$_2$O (3 × 3 mL) and the solution was stored overnight at -30°C. The crystalline powder was then recrystallized by layering a concentrated THF solution of **3** with hexane. Storage of a solution of **3** in Et$_2$O/pentane at -30°C afforded single crystals suitable for X-Ray diffraction.

Molecular Weight: 1718.94 g/mol ($C_{39}H_{53}N_6Ni_2K$)$_2$ · ($C_4H_{10}O$)

^{1}H-NMR (THF-d$_8$, 400 MHz) δ = 6.74 (m, 2H, Ar-*H*^{m}), 6.64 (m, 4H, Ar-*H*^{P}), 5.79 (s, 1H, *H*-Pz) 4.65 (s, 2H, C*H*), 3.96 (s, 4H, C*H*$_2$), 3.61 (m, 4H, iPr-C*H*), 1.92 (s, 6H, Me) 1.27 (s, 12H, iPr-Me) 0.97 (s, 12H, iPr-Me) 0.87 (s, 6H, Me) ppm.

ATR-IR ṽ/cm^{-1} = 3055 (w), 2955 (m), 2920 (m), 2856 (m), 1584 (vw), 1550 (m), 1528 (s), 1492 (vw), 1460 (m), 1435 (s), 1401 (vs), 1379 (m), 1367 (m), 1362 (m), 1314 (s), 1277 (m), 1244, (m), 1230 (m), 1182 (w), 1134 (w), 1098 (m), 1089 (m), 1067 (w), 1050 (m), 1024 (m), 952 (vw), 934 (w), 856 (m), 794 (m), 757 (s), 732 (m), 715 (m), 642 (w), 619 (vw), 541 (vw), 521 (vw), 498 (w), 436 (m).

UV-Vis (THF) λ$_{max}$/nm (ε/M^{-1}cm^{-1}) = 245 (53800), 350 (19300), 396 (19000).

MS (ESI$^-$, THF) *m/z* (%) = 781.4 [LNi$_2$(N$_2$O$_2$)]$^-$

Reactivity of 3 in presence of excess NO: A solution of **3** (5 mg, 6.39 · 10^{-3} mmol, 1 eq) in THF (2 mL) was added to a two-neck 25 mL Schlenk flask. NO (1 mL, 4.09 · 10^{-2} mmol, 6.5 eq) was then slowly injected into the flask through a septum at room temperature. The solution was stirred for 20 minutes and the headspace was allowed to diffuse into a fully evacuated gas phase IR-cell (10 cm path length). The IR spectrum of the gas phase was then recorded.

IR ṽ/cm^{-1} = 2224 (N$_2$O), 1876 (NO).

Reactivity of 2 towards N$_2$O: A J. Young NMR tube was charged with **2** (8 mg, 1.05 · 10^{-1} mmol) and dissolved in THF-d$_8$ in a glovebox. The tube was taken out of the glovebox and a slight vacuum was applied on it. N$_2$O (excess) was used to replace the atmosphere and the color of the solution changed from red to green. A ^{1}H-NMR spectrum was recorded, showing exclusive formation of the correspondent hydroxo-bridged complex **4**.

^{1}H-NMR (THF-d$_8$, 400 MHz) δ = 6.95 (t, 2H, Ar-*H*^{o}), 6.81 (d, 4H, Ar-*H*^{P}), 5.47 (s, 1H, *H*-pz), 4.59 (s, 2H, C*H*), 4.01 (s, 4H, C*H*$_2$), 3.36 (m, 4H, iPr-C*H*), 1.86 (s, 6H, Me), 1.60 (d, 12H, iPr-C*H*$_3$), 1.07 (m, 24H, Me+ iPr-C*H*$_3$), -7.26 (s, 1H, O*H*) ppm.

Procedure for the quantification of N$_2$O: The calibration plot for the quantification of the N$_2$O released upon protonation of complex **3** was obtained as follows: in a glovebox, a two-neck 25 mL Schlenk flask was equipped with a gas IR cell (KBr windows) previously evacuated in a Schlenk line to 4.0 · 10^{-2} mmHg and a magnetic stirrer (A picture of the described system is given in the Appendix, Figure 16). The system was filled with THF (3 mL) and the Schlenk tube was closed with a septum. The set up was taken out of the glovebox, and the valve to the IR cell was opened for 90 seconds. After that, the valve was closed and a blank spectrum was recorded. The system was assembled again as previously described, taken out of the glovebox and a known amount of N$_2$O$_{(g)}$ was injected through the septum via a gas tight Hamilton syringe. After two minutes of stirring, the valve to the

IR cell was opened for exactly 90 seconds and an IR spectrum was recorded. The procedure was repeated for 5 different volumes of N_2O. The measure for each volume was repeated three times and the arithmetic mean for each point was taken.

Detection of evolved N_2O upon protonation of 3: A two-neck 25 mL Schlenk tube was filled with THF (2 mL) and complex **3** (5 mg, $2.9 \cdot 10^{-6}$ mmol, 1 eq). The system was set up exactly as previously described for the quantification of N_2O procedure. [LutH][OTf] (1.6 mg, $6.1 \cdot 10^{-6}$ mmol, 2.1 eq) was dissolved in THF (1 mL) and injected through the septum into the Schlenk flask. The mixture was stirred for two minutes and the valve to the IR cell was opened. After 90 seconds the valve was closed and an IR spectrum was recorded. The solvents were removed under reduced pressure and the brownish solid was dried in vacuo.

IR $\tilde{v}$/cm^{-1} = 2224 (N_2O, 68.4%).

^{1}H-NMR (THF-d$_8$, 400 MHz) δ = 7.41 (t, 1H, Lut), 7.30 (d, 2H, Lut), 6.95 (t, 2H, Ar-H^o), 6.81 (d, 4H, Ar-H^p), 5.47 (s, 1H, H-pz), 4.59 (s, 2H, CH), 4.01 (s, 4H, CH_2), 3.36 (m, 4H, iPr-CH), 1.86 (s, 6H, Me), 2.41 (s, 6H, Lut), 1.60 (d, 12H, iPr-CH_3), 1.07 (m, 24H, Me + iPr-CH_3), -7.26 (s, 1H, OH) ppm.

LNi$_2$(NO) (5): Compound **5** can be synthetized by following two different strategies.

a) A solution of Ph$_3$CSNO (6.1 mg, $2.2 \cdot 10^{-2}$ mmol, 1.1 eq) in THF (1 mL) was added dropwise to a solution of **2** (15.2 mg, $2.0 \cdot 10^{-2}$ mmol, 1.0 eq) in THF (1 mL) at -20°C. The solution was stirred overnight at -30°C and then pentane (10 mL) was added. The mixture was stored for additional 3 hours at -30°C during which the product precipitated. The solution was discarded and the red-purple solid was washed with pentane (3 × 2 mL) and dried under vacuum. Single crystals suitable for X-Ray diffraction were obtained by layering a concentrated THF solution of **5** with hexane/Et$_2$O. Yield = 5.8 mg , 39%.

b) Complex **2** (17 mg, $2.2 \cdot 10^{-5}$ mmol, 1 eq) was suspended in DME (2 mL) and treated with [NO][BF$_4$] (2.8 mg, $2.45 \cdot 10^{-5}$ mmol, 1.1 eq) at room temperature. After stirring for 15 minutes, the solvent was removed under reduced pressure and the solid was washed with pentane (3 × 2 mL). The product **5** was recrystallized by layering a concentrated THF solution of **5** with hexane/Et$_2$O. Yield = 7.9 mg , 46%.

Molecular Weight: 751.30 g/mol (C$_{39}$H$_{53}$N$_7$Ni$_2$O)

^{1}H-NMR (THF-d$_8$, 400 MHz) δ = 6.95−6.68 (m, 6H, Ar), 5.80 (s, 1H, H-Pz), 5.33 (s, 1H, CH), 5.10 (s, 1H, CH), 4.32 (s, 1H, CH_2), 4.23 (s, 1H, CH_2), 3.61 (sept, 4H, CH-iPr), 3.22 (sept, 4H, CH-iPr), 2.09 (s, 3H, CH_3), 2.05 (s, 3H, CH_3) 1.93 (s, 3H, CH_3), 1.62 (s, 3H, CH_3), 1.09 (m, 12H, CH_3-Ar), 0.84 (d, 6H, CH_3-Ar), 0.51 (d, 6H, CH_3-Ar) ppm.

^{13}C-NMR (THF-d$_8$, 100 MHz) δ = 163.3 (C-Me), 162.0 (C-Me), 161.2 (C-Me), 159.9 (C-Me), 153.4 (Ar), 151.6 (Ar), 145.6 (Ar), 144.7 (Ar), 142.5 (Ar), 142.3 (Ar), 125.4 (Ar), 124.4 (Ar), 122.8 (Ar), 122.2 (Ar), 101.4 (CH), 99.2 (CH), 93.0 (Pz), 54.5 (CH$_2$), 51.3 (CH$_2$), 27.9 (Me), 27.4 (Me), 25.7 (Me), 25.4 (Me), 23.2 (Me), 23.0 (Me), 21.5 (Me) ppm.

ATR-IR $\tilde{v}$, cm^{-1} = 3055 (w), 2959 (m), 2922 (m), 2864 (m), 1786 (w), 1552 (m), 1532 (s), 1458 (s), 1435 (m), 1395 (s), 1306 (m), 1252 (sh, s)1230 (vs), 1184 (w), 1095 (m), 1057 (w), 1008 (sh, m), 978 (s), 932 (s), 909 (w), 871 (m), 793 (vs), 757 (m), 745 (s), 714 (s), 642 (w).

UV-Vis (THF) λ_{max}/nm (ε/M^{-1}cm^{-1}) = 261 (12200), 367 (5400), 500 (2700).

MS (HR-ESI$^+$, THF/MeOH) m/z (%) = 752.4 [LNi$_2$(NO) + H]$^+$

LNi$_2$(^{15}NO) (5-^{15}NO): The synthesis of the ^{15}NO labelled analogue of **5** was performed as described for **5** by employing [^{15}NO][BF$_4$].

ATR-IR $\tilde{v}$/cm^{-1} = 1745 (w, NO).

^{15}N-NMR (THF-d$_8$, 50 MHz) δ = 734.75 (s, ^{15}NO) ppm.

[LNi$_2$(NO)][Co(Cp*)$_2$] (6): A solution of Co(Cp*)$_2$ (4.4 mg, 1.3 · 10^{-2} mmol, 1 eq) in THF (1 mL) was added dropwise to a solution of complex **5** (10 mg, 1.3 · 10^{-2} mmol, 1 eq) in THF (0.5 mL) at 0°C. An immediate color change from deep red to brown was observed. The mixture was stirred for about 10 minutes and filtered. The solvent was removed and the resulting dark brown powder was washed with cold hexane (3 × 2 mL) and dried under vacuum. The product was recrystallized by layering hexane on a concentrated solution of **6** in THF at -30°C. Yield = 4 mg, 27%.

Molecular Weight: 1080.79 g/mol (C$_{59}$H$_{83}$N$_7$Ni$_2$OCo)

ATR-IR $\tilde{v}$/cm^{-1} = 1776 (w, NO).

EPR (THF, 153 K, X-band) g(A(^{14}N/MHz)) = 2.171 (40), 2.058 (65), 2.007 (1); organic impurity g = 2.085 (3%).

[LNi$_2$(^{15}NO)][Co(Cp*)$_2$] (6-^{15}NO): The synthesis of the ^{15}NO labelled analogue of **6** was performed as described for **6** by employing **5-^{15}NO** as starting material.

ATR-IR $\tilde{v}$/cm^{-1} = 1735 (m, ^{15}NO).

EPR (THF, 153 K, X-band) g(A(^{15}N/MHz)) = 2.175 (40), 2.058 (65), 2.007 (1); organic impurity g = 2.060 (1%).

KLNi$_2$(NO) (7): A purple solution of freshly prepared potassium benzophenone (1 mL, 2.1 · 10^{-2} mmol, 2 eq, 0.02 M in THF) was added dropwise to a red solution of **5** (8 mg, 1.0 · 10^{-2} mmol, 1 eq) in THF (0.3 mL) at -10°C. The color changed to dark green and the mixture was stirred for additional 5 minutes at room temperature. The resulting solution of **7** was

layered with a mixture of Et$_2$O/hexane (1 : 1) and crystals of **7** were obtained in about 3 days. Yield = 3.7 mg, 44%.

Molecular Weight: 790.59 g/mol (C$_{39}$H$_{53}$N$_7$Ni$_2$OK)

ATR-IR (ṽ, cm^{-1}) = 1193 (m, NO).

EPR (THF, 153 K, X-band) = g(A(^{14}N/MHz)) = 2.125 (50), 2.045 (5), 2.001 (80).

LNi$_2$(^{15}NO) (7-^{15}NO): The synthesis of the ^{15}NO labelled analogous of **7** was performed as described for **7** by employing **5-^{15}NO** as starting material.

ATR-IR ṽ/cm^{-1} = 1175 (m, ^{15}NO).

EPR (THF, 153 K, X-band) = g(A(^{15}N/MHz)) = 2.047 (15), 2.011 (25), 2.001 (70).

Conversion of LNi$_2$(NO) 5 to [LNi$_2$(N$_2$O$_2$)]$^-$ (3–K$^+$)$^-$: In a glovebox, a solution of **5** (5 mg, 6.6 · 10^{-3} mmol, 1 eq) in THF (0.5 mL) was added dropwise to a solution of Co(Cp*)$_2$ (2.2 mg, 6.6 · 10^{-3} mmol, 1 eq) in THF (1 mL) at 0°C in a Schlenk flask equipped with a septum. After 10 minutes of stirring, the flask was transferred out of the glovebox and NO (0.16 mL, 6.6 · 10^{-3} mmol, 1 eq) was slowly bubbled in the solution through the septum. The solution was stirred for additional 5 minutes and the solvent was removed under reduced pressure. The same results were obtained by starting from complex **6**.

MS (HR-ESI$^-$, THF/MeOH) m/z (%) = 781.4 [LNi$_2$(N$_2$O$_2$)]$^-$

LNi$_2$(NO$_2$) (8): In a glovebox, a 25 mL Schlenk flask was charged with **5** (11 mg, 1.4 · 10^{-2} mmol, 1 eq) dissolved in THF (2 mL) and the system was closed with a septum. The flask was transferred out of the glovebox and NO (1.80 mL, 7.32 · 10^{-2} mmol, 5 eq) was bubbled through the septum in the solution. After a few minutes of stirring, the solvent was removed under reduced pressure and the resulting brown powder was washed with hexane (3 × 2 mL) and crystallized by layering a THF solution of **8** with a mixture Et$_2$O/hexane 1 : 1.

Molecular Weight = 767.4 g/mol (C$_{39}$H$_{53}$N$_7$Ni$_2$O$_2$)

LIFDI (THF) = 767.3 [LNi$_2$(NO$_2$)]

KLNi$_2$(μ-PhNO) (9): A solution of PhNO (4.1 mg, 3.8 · 10^{-2} mmol, 1 eq) in THF (1 mL) was added dropwise to an orange solution of KL(NiH)$_2$ (29 mg, 3.8 · 10^{-2} mmol, 1 eq) in THF (2 mL) at 0°C. The color turned immediately to black and the mixture was stirred for 2 hours at room temperature. The volatile materials were removed under reduced pressure. The resulting black solid was washed with pentane (3 × 2 mL) and crystallized by layering a THF solution of **9** with Et$_2$O. Single crystals suitable for X-ray diffraction were obtained by diffusion of Et$_2$O into a concentrated solution of **9** in THF/MeCN. Yield = 19 mg, 60%.

Molecular Weight: 868.46 g/mol (C$_{45}$H$_{57}$KN$_7$Ni$_2$O)

ATR-IR ṽ/cm⁻¹ = 3036 (w), 2660 (m), 2922 (m), 2861 (m), 1576 (m), 1560 (m), 1537 (w), 1519 (vs), 1462 (s), 1428 (s), 1402 (vs), 1366 (w), 1337 (w), 1312 (s), 1290 (w), 1273 (m), 1244 (m), 1227 (m), 1213 (m), 1187 (m), 1163 (s), 1088 (m), 1069 (m), 1052 (m), 1030 (m), 1023 (s), 1013 (m), 976 (s), 948 (w), 933 (w), 911 (w), 907 (w, NO), 853 (w), 804 (s), 772 (s), 754 (m), 746 (w), 734 (vs), 693 (s), 656 (w), 634 (w), 597 (w), 549 (m), 522 (s), 492 (w), 473 (w), 464 (w), 458 (w), 447 (w), 439 (w), 432 (s).

UV-Vis (THF, λ/nm (ε/M⁻¹cm⁻¹)) = 271 (20400), 374 (9800), 611 (2000), 721 (1400).

MS (ESI⁺, THF/MeOH) m/z (%) = 867.3 [LNi₂(PhNO) + K]⁺, 851.3 [LNi₂(PhNO) + Na]⁺

KLNi₂(μ-Ph¹⁵NO) (9-¹⁵NO): The synthesis of the ¹⁵NO labelled analogue of **9** was performed as described for **9** by employing Ph¹⁵NO.

ATR-IR ṽ/cm⁻¹ = 894 (m, ¹⁵NO).

[LNi₂(μ-PhNO)][K(crypt)] (10): Complex **9** (15 mg, 1.7 · 10⁻⁵ mmol, 1 eq) was dissolved in THF (1 mL) and treated with [2.2.2]-cryptand (6.8 mg, 1.8 · 10⁻⁵ mmol, 1.05 eq) at room temperature. After stirring for 2 hours, the solution was layered with hexane and kept at -30°C for 3 days. The product was then isolated as dark green powder that was washed with pentane (3 × 2 mL). Single crystals suitable for X-ray diffraction were obtained by diffusion of pentane into a concentrated solution of **10** in THF at -30 °C. Yield = 12 mg, 58 %.

Molecular Weight: 1244.95 g/mol (C₆₃H₉₃N₉Ni₂O₇K)

¹H-NMR (THF-d₈, 400 MHz) δ = 9.73 (br, Ph-H°), 6.88−6.44 (m, 8H, Ph + Ar), 5.91 (t, J_{H-H} = 7 Hz, 1H, Ph-Hᴾ), 5.22 (s, 1H, H-Pz), 4.59 (sept, 1H, CH-iPr), 4.39 (s, 1H, CH), 4.36 (s, 1H, CH), 4.00−3.73 (m, 4H, CH₂), 3.41 (sept, 1H, CH-iPr), 3.11 (sept, 1H, CH-iPr), 3.02 (sept, 1H, CH-iPr), 2.17 (d, J_{H-H} = 7 Hz, 3H, CH₃-Ar), 1.77 (s, 3H, CH₃), 1.63 (s, 3H, CH₃), 1.42 (d, J_{H-H} = 7 Hz, 3H, CH₃-Ar), 1.63 (s, 3H, CH₃), 1.42 (d, J_{H-H} = 7 Hz, 3H, CH₃-Ar), 1.23 (s, 3H, CH₃), 1.18 (s, 3H, CH₃),1.05 (d, J_{H-H} = 7 Hz, 3H, CH₃-Ar), 0.98 (d, J_{H-H} = 7 Hz, 3H, CH₃-Ar), 0.85 (d, J_{H-H} = 4 Hz, 3H, CH₃-Ar), 0.82 (d, J_{H-H} = 4 Hz, 3H, CH₃-Ar) ppm.

¹³C-NMR (THF-d₈, 100 MHz) δ = 180.4 (C-H°), 165.2 (C-CHᴾ), 160.4 (C-Pz), 158.4 (C-Me), 157.3 (C-Me), 156.6 (C-Me), 150.5 (C-Pz), 148.8 (Ar), 146.0 (Ar), 145.0 (C-Me), 142.5 (Ar), 141.9 (Ar) 126.0 (Ar), 125.0 (Ar), 124.3 (Ar), 122.6 (Ar), 122.3 (Ar), 122.1 (Ar), 121.8 (Ar), 121.2 (Ar), 114.1 (C-Hᵐ), 111.7 (Ar), 105.6 (C-Hᴾ), 96.0 (CH), 95.3 (CH), 89.1 (C-Pz), 54.4 (CH₂), 50.9 (CH₂), 31.6 (Me), 28.5 (CH-iPr), 28.1 (CH-iPr), 27.8 (CH-iPr), 26.7 (CH-iPr), 26.2 (CH₃), 26.0 (CH₃), 25.8 (CH₃), 25.1 (CH₃), 25.0 (CH₃), 24.7 (CH₃), 24.3 (CH₃), 23.9 (CH₃), 23.8 (CH₃), 23.2 (CH₃), 23.1 (CH₃) ppm.

ATR-IR ṽ/cm⁻¹ = 2953 (w), 2922 (m), 2865 (m), 2814 (m), 1580 (m), 1550 (m), 1521 (m), 1468 (m), 1443 (m) 1403 (m), 1354 (m), 1298 (m), 1233 (m), 1134 (m), 1101 (vs), 1081 (m), 1061 (m),

1022 (w), 982 (m), 973 (m, NO), 949 (s), 933 (m), 833 (m), 799 (m), 759 (m), 723 (m), 694 (w), 568 (w), 524 (m), 508 (m), 480 (w), 464 (w), 452 (w), 444 (w), 435 (w), 425 (vs).

UV-Vis (THF, λ/nm (ε/M^{-1}cm^{-1})) = 270 (19607), 378 (7826).

MS (ESI$^+$, THF/MeOH) m/z (%) = 867.3 [LNi$_2$(PhNO) + K]$^+$

[LNi$_2$(μ-Ph^{15}NO)][K(crypt)] (10-^{15}NO): The synthesis of the ^{15}NO labelled analogue of **10** was performed as described for **10** by employing Ph^{15}NO.

ATR-IR $\tilde{v}$/cm^{-1} = 954 (m, ^{15}NO).

^{15}N-NMR (THF-d$_8$, 50 MHz) δ = -213.8 (s, ^{15}NO) ppm.

LNi$_2$(μ-PhNO) (11): Complex **9** (20 mg, 2.3 · 10^{-2} mmol, 1 eq) was dissolved in THF (1 mL) and treated with [Fe(Cp*)$_2$][PF$_6$] (12 mg, 2.5 · 10^{-2} mmol, 1.1 eq) at room temperature. After stirring for 2 hours, the resulting red suspension was filtrated and stored at -30°C overnight. The solution was filtrated again cold and the solvent was removed under reduced pressure. The obtained dark red powder was washed with cold pentane (2 × 2 mL) and the final product was dried under vacuum. Yield = 6.5 mg, 34 %.

Molecular Weight: 829.43 g/mol (C$_{45}$H$_{57}$N$_7$Ni$_2$O)

ATR-IR $\tilde{v}$/cm^{-1} = 3055 (w), 2953 (m), 2929 (m), 2887 (m), 2857 (m), 1661 (w), 1546 (m), 1532 (s), 1549 (m), 1434 (m), 1396 (s), 1369 (m), 1311 (m), 1275 (m) 1248 (m), 1185 (w), 1139 (w), 1080 (m, NO), 1073 (m), 1054 (m), 1027 (m), 887 (sh, m), 853 (vs), 796 (m), 760 (m), 747 (m), 740 (m), 717 (m), 676 (w), 592 (w), 558 (s), 508 (w), 450 (m).

UV-Vis (THF, λ/nm (ε/M^{-1}cm^{-1})) = 270 (19607), 378 (7826).

EPR (THF, RT, X-band) g_{iso}(A(^{14}N/MHz)) = 2.040 (40).

EPR (THF, 150 K, X-band) g(A(^{14}N/MHz)) = 2.051 (15), 2.036 (30), 2.024 (83).

LNi$_2$(μ-Ph^{15}NO) (11-^{15}NO): The synthesis of the ^{15}NO labelled analogue of **11** was performed as described for **11** by employing **9-^{15}NO** as starting material.

ATR-IR $\tilde{v}$/cm^{-1} = 1053 (m, ^{15}NO).

EPR (THF, RT, X-band) g_{iso}(A(^{15}N/MHz)) = 2.039 (49).

EPR (THF, 150 K, X-band) g(A(^{15}N/MHz)) = 2.054 (14), 2.042 (20), 2.022 (80).

LNi$_2$(μ-PhNHO) (12): Complex **9** (15 mg, 1.72 · 10^{-5} mmol, 1 eq) was dissolved in THF (1 mL) and treated with [LuH][OTf] (4.8 mg, 1.89 · 10^{-5} mmol, 1.1 eq) at room temperature. After stirring for one hour, the resulting red suspension was filtered and the solvent was removed under reduced pressure. The product was extracted with hexane (3 × 2 mL) and the solvent was removed again under reduced pressure. Single crystals of **12** suitable for X-ray diffraction were grown by diffusion of hexane into a concentrated THF solution of **12** at room temperature. Yield = 7 mg, 47 %.

Molecular Weight: 830.43 g/mol ($C_{45}H_{58}N_7Ni_2O$)

ATR-IR $\tilde{\nu}$/cm^{-1} = 3147 (w), 3142 (w), 2981 (w), 2955 (m), 2921 (m), 2863 (m), 1644 (vw), 1553 (s), 1523 (s), 1492 (w), 1454 (s), 1433 (s), 1398 (vs), 1377 (s), 1309 (s), 1276 (m), 1251 (m), 1227 (m), 1182 (m), 1175 (m), 1137 (w), 1086 (m), 1052 (w), 1026 (s, NO), 981 (m), 953 (w), 933 (m), 920 (m), 880 (m), 864 (w), 794 (s), 784 (m), 758 (vs), 731 (vs), 714 (s), 694 (m), 632 (m), 600 (m), 522 (m), 492 (s).

LNi$_2$(μ-Ph^{15}NHO) (12-^{15}NO): The synthesis of the ^{15}NO labelled analogue of **12** was performed as described for **12** by employing **9-^{15}NO** as staring material.

ATR-IR $\tilde{\nu}$/cm^{-1} = 1018 (s, ^{15}NO).

LFe$_2$(OTf)(THF)$_2$ (13): The synthetic strategy reported by NEUMANN[196] was modified in order to obtain clean crystals of **13** in higher yields. A yellow solution of **H$_3$L** (1.0 g, 1.64 mmol, 1 eq) in THF (5 mL) was cooled at -30°C and treated with ^{n}BuLi (1.99 mL, 3.03 eq, 2.5 M in hexane). The color changed to deep red and the solution was stirred at room temperature for 15 minutes. A solution of Fe(OTf)$_2 \cdot$ 2MeCN (1.45 g, 3.3 mmol, 2.02 eq) in THF (3 mL) was then added and the mixture was stirred for additional 18 h. The volatile materials were removed under reduced pressure and the product was extracted with toluene (3 × 20 mL). The solvent was removed under vacuum and the resulting dark green solid was washed with pentane (3 × 15 mL). The solid was dissolved in THF (5 mL) and diffusion of hexane into the solution yielded yellow-green crystals that were washed with pentane and dried under vacuum. Yield: 1.11 g, 65%.

Molecular weight: 1046.90 g/mol ($C_{50}H_{73}F_3Fe_2N_6O_{5.5}S$)

^{1}H-NMR (THF-d$_8$, 400 MHz) δ = 13.72 (s, 4H, Ar-H^m), 8.57 (s, 12H, Me-iPr), 2.95 (s, 1H, H-Pz), -6.09 (s, 6H, Me), -8.90 (br, CH_2/CH-iPr), -16.33 (s, 12H, Me-iPr), -22.55 (s, 6H, Me), -23.04 (s, 2H, Ar-H^p), -25.13 (s, 2H, CH) ppm.

^{19}F-NMR (THF-d$_8$, 376 MHz) δ = 88.0 (s, OTf) ppm.

ATR-IR $\tilde{\nu}$/cm^{-1} = 1549 (w), 1521 (m), 1460 (w), 1430 (m), 1384 (m), 1307 (vs), 1254 (m), 1218 (s), 1178 (s), 1095 (w), 1032 (s), 1019 (s), 936 (w), 916 (w), 881 (m), 847 (w), 817 (vw), 793 (w), 761 (m), 747 (m), 632 (s), 577 (w), 513 (m).

UV-Vis (THF, λ [nm], ε [M^{-1}cm^{-1}]) = 323 (23500), 372 (7580), 412 (3250).

Mössbauer (80 K) (IS/mms^{-1} (QS/mms^{-1}), %) = 1.08 (2.52), 100%

LIFDI (toluene) = 866.2 [LFe$_2$(OTf)].

Elemental analysis (%) calc. for $C_{48}H_{69}N_6Fe_2O_5F_3S$: C 57.03, H 6.88, N 8.31, S 3.17; found C 55.41, H 7.31, N 8.21, S 3.64.

LFe$_2$(N$_2$H$_4$)(OTf)(THF) (15): A yellow solution of **13** (50 mg, 4.7· 10^{-2} mmol, 1.0 eq) in THF (2 mL) was cooled at 0°C and treated with N$_2$H$_4$ (0.47 mL, 4.7· 10^{-2} mmol mmol, 1.0 eq, 1M

in THF). The color immediately turned dark green and the mixture was stirred for 15 minutes at room temperature. Green crystals suitable for X-Ray diffraction were obtained by layering the resulting solution with hexane. Yield: 26 mg, 53%.

Molecular weight: 1042.9 g/mol ($C_{48}H_{73}F_3Fe_2N_8O_5S$)

^{1}H-NMR (THF-d$_8$, 400 MHz) δ = 40.44 (s, 4H, CH_2), -17.80 − -19.71 (m, 36H, *H*-Pz/C*H*/C*H*-iPr), -32.70 (s, 6H, C*H*-Me), -50.82 (s, 6H, C*H*-Me) ppm.

^{19}F-NMR (THF-d$_8$, 376 MHz) δ = 53.83 (s, OTf) ppm.

ATR-IR ṽ/cm^{-1} = 3336 (w, NH), 3318 (w, NH), 3260 (w, NH), 2957 (m, CH), 2925 (m, CH), 2866 (m, CH), 2822 (m, CH), 1560 (m), 1510 (m), 1455 (m), 1429 (s), 1381 (s), 1322 (s), 1291 (m), 1260 (m), 1231 (vs), 1201 (vs), 1160 (vs), 1122 (m), 1098 (m), 1063 (m), 1021 (vs), 929 (w), 870 (w), 848 (w), 817 (vw), 795 (m), 752 (s), 708 (w).

UV-Vis (THF, λ/nm (ϵ/M^{-1}cm^{-1})) = 325 (34672), 414 (4465).

LIFDI (THF) *m*/*z* (%) = 717.1 [LFe$_2$(N$_2$H$_4$)(OTf)(THF) – (N$_2$H$_4$) – (THF) – (OTf)]

Mössbauer (80 K) (IS/mms^{-1} (QS/mms^{-1}), %) = 1.08 (2.79), 100%.

Elemental analysis (%) calc. for $C_{39}H_{57}N_8Fe_2OF_3S(C_4H_8O)$: C 54.40, H 6.50, N 11.50, S 3.30; found C 54.67, H 7.08, N 9.91, S 3.58.

9.3 Crystallographic Details

Table 13. Crystal data and refinement details for **3**.

Compound	KLNi$_2$(N$_2$O$_2$) **(3)**
empirical formula	C$_{82}$ H$_{116}$ K$_2$ N$_{16}$ Ni$_4$ O$_5$
formula weight	1718.94
crystal size [mm^3]	0.400 x 0.290 x 0.190 mm^3
crystal system	monoclinic
space group	*C* 2/*c*
a [Å]	30.0806(9)
b [Å]	20.7584(4)
c [Å]	21.5283(6)
α [°]	90
β [°]	117.828(2)
γ [°]	90
V [Å^3]	11888.2(6)
Z	4
ρ [g/cm^3]	0.960
F(000)	3640
μ [mm^{-1}]	0.736
T$_{min}$ / *T*$_{max}$	0.774, 0.942
Ө-range [°]	1.244-25.774
hkl-range	±36, -25 - 22, -26 - 22
measured refl.	31508
unique refl. [*R*$_{int}$]	11241 [0.0591]
Data/restrains/param.	11241 / 0 / 506
Goodness-of-fit *F*^{2}	1.100
*R*1, w*R*2 [*I*>2σ(*I*)]	0.0886, 0.2037
*R*1, w*R*2 (all data)	0.1155, 0.2155
resid. el .dens [e/Å^3]	0.591/-0.647

Figure 83. Plot of the molecular structure of **3** (50% probability thermal ellipsoids; only monomer represented; hydrogen atoms and solvent omitted for clarity).

Table 14. Crystal data and refinement details for **5**.

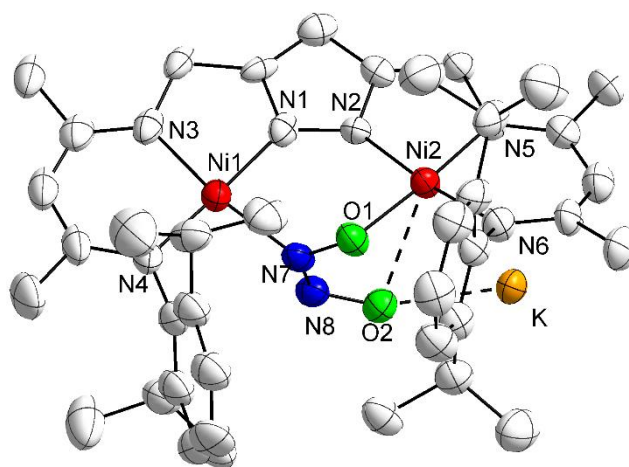| Compound	LNi$_2$(NO) **(5)**
empirical formula	C$_{39}$ H$_{53}$ N$_7$ Ni$_2$ O
formula weight	753.30
crystal size [mm^3]	0.190 x 0.110 x 0.050 mm^3
crystal system	monoclinic
space group	$P\,2_1$/c
a [Å]	17.4726(5)
b [Å]	14.1366(5)
c [Å]	17.2721(6)
α [°]	90
β [°]	113.539(2)
γ [°]	90
V [Å^3]	3911.3(2)
Z	4
ρ [Mg/cm^3]	1.279
F(000)	1600
μ [mm^{-1}]	1.001
T_{min} / T_{max}	0.9417, 0.7543
Θ-range [°]	1.921-26.867
hkl-range	-22,18 ±17 ±21
measured refl.	33852
unique refl. [R_{int}]	8302 [0.0955]
Data/restrains/param.	8302 / 68 / 474
Goodness-of-fit F^2	1.046
R1, wR2 [$I>2\sigma(I)$]	0.0533, 0.0932
R1, wR2 (all data)	0.1140, 0.1159
resid. el .dens [e/Å^3]	0.449/-0.421
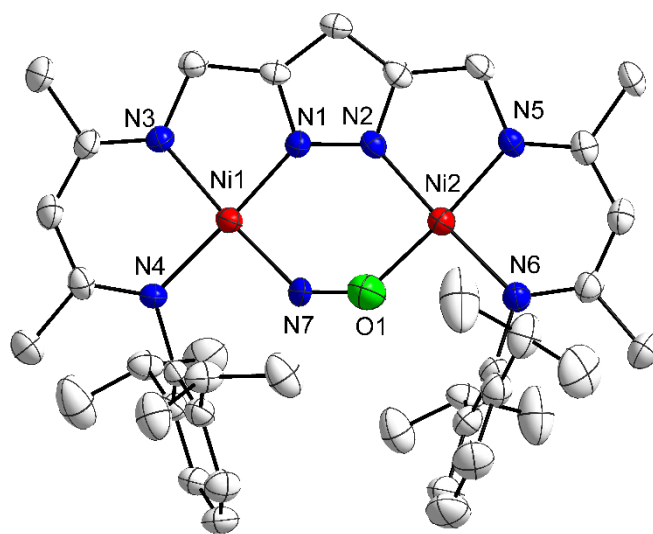
Figure 84. Plot of the molecular structure of **5** (50% probability thermal ellipsoids; hydrogen atoms and solvent omitted for clarity).

Table 15. Crystal data and refinement details for **8**.

Compound	$LNi_2(NO_2)$ **(8)**
empirical formula	$C_{41} H_{57.40} N_{6.60} Ni_2 O_{2.10}$
formula weight	793.75
crystal size [mm^3]	0.174 x 0.134 x 0.079 mm^3
crystal system	Monoclinic
space group	$P\,2_1/c$
a [Å]	17.2658(6)
b [Å]	14.1209(5)
c [Å]	17.2391(6)
α [°]	90
β [°]	112.247(2)
γ [°]	90
V [Å^3]	3890.2(3)
Z	4
ρ [Mg/cm^3]	1.355
$F(000)$	1690
μ [mm^{-1}]	1.012
T_{min} / T_{max}	0.9738, 0.8998
Θ-range [°]	1.925-27.018
hkl-range	±21 ±17 -22,21
measured refl.	38066
unique refl. [R_{int}]	8304 [0.0997]
Data/restrains/param.	8304 / 48 / 517
Goodness-of-fit F^2	1.104
$R1$, w$R2$ [$I>2\sigma(I)$]	0.0639, 0.1102
$R1$, w$R2$ (all data)	0.1318, 0.1374
resid. el .dens [e/Å^3]	0.546/-0.400
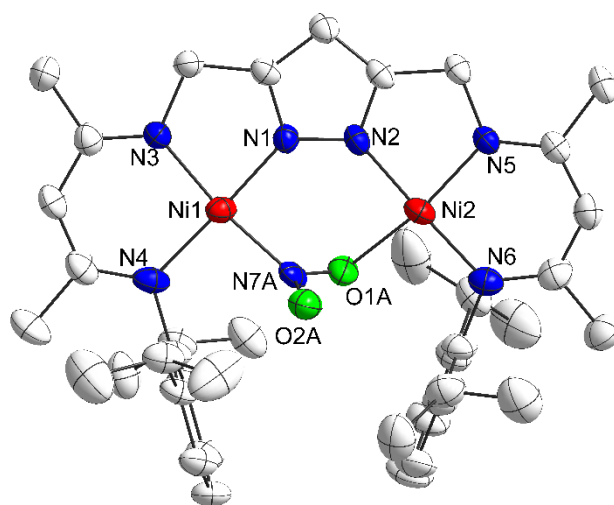
Figure 85. Plot of the molecular structure of **8** (50% probability thermal ellipsoids; the compound co-crystallizes with **4**, which is not represented here; hydrogen atoms and solvent omitted for clarity).

Table 16. Crystal data and refinement details for **9** and **10**.

Compound	KLNi$_2$(μ-PhNO) **(9)**	[K(crypt)][LNi$_2$(μ-PhNO)] **(10)**
empirical formula	C$_{47}$ H$_{61}$ K N$_8$ Ni$_2$ O	C$_{71}$ H$_{110}$ K N$_9$ Ni$_2$ O$_9$
formula weight	910.55	1390.19
crystal size [mm^3]	0.360 x 0.340 x 0.280 mm^3	0.255 x 0.252 x 0.187 mm^3
crystal system	Monoclinic	Monoclinic
space group	$P\,2_1$/m	$P\,2_1$/c
a [Å]	11.6350(7)	25.3445(7)
b [Å]	18.2506(13)	12.9108(5)
c [Å]	11.6398(9)	22.8413(8)
0α [°]	90	90
β [°]	91.616(6)	106.782(2)
γ [°]	90	90
V [Å^3]	2470.7(3)	7155.8(4)
Z	2	4
ρ [Mg/cm^3]	1.244	1.290
F(000)	964	2984
μ [mm^{-1}]	0.887	0.645
T_{min} / T_{max}	0.8708, 0.6692	0.8782, 0.729
Θ-range [°]	1.750-25.775	1.750-25.775
hkl-range	±14 ±22 ±14	±90 ±15 -27, 23
measured refl.	27929	69092
unique refl. [R_{int}]	4854 [0.1346]	13156 [0.1435]
Data/restrains/param.	4854 / 36 / 305	13156 / 158 / 916
Goodness-of-fit F^2	1.099	0.918
R1, wR2 [I>2σ(I)]	0.0825 0.1799	0.0627 0.0797
R1, wR2 (all data)	0.0962, 0.1873	0.1281, 0.0930
resid. el .dens [e/Å^3]	1.839/-0.484	0.482/-0.280
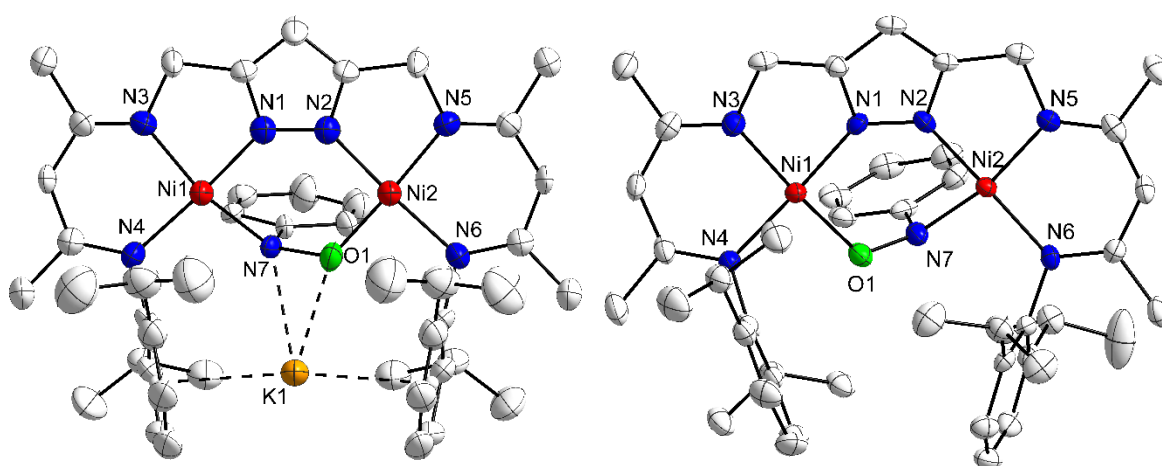
Figure 86. Plot of the molecular structure of **9** (left) and the anionic part of **10** (right) (50% probability thermal ellipsoids; hydrogen atoms and solvent omitted for clarity).

Table 17. Crystal data and refinement details for **12**

Compound	LNi$_2$(PhNHO) **(12)**
empirical formula	C$_{45}$ H$_{59}$ N$_7$ Ni$_2$ O
formula weight	831.41
crystal size [mm^3]	0.486 x 0.314 x 0.173 mm^3
crystal system	Monoclinic
space group	$P\,2_1/n$
a [Å]	10.6925(3)
b [Å]	23.5112(7)
c [Å]	16.6922(4)
α [°]	90
β [°]	101.387(2)
γ [°]	90
V [Å^3]	4113.7(2)
Z	4
ρ [Mg/cm^3]	1.342
F(000)	1768
μ [mm^{-1}]	0.959
T_{min} / T_{max}	0.8278, 0.5781
Θ-range [°]	1.516-25.785
hkl-range	-11,12 ±28 ±20
measured refl.	37123
unique refl. [R_{int}]	7701 [0.0301]
Data/restrains/param.	7701 / 0 / 512
Goodness-of-fit F^2	1.084
$R1$, w$R2$ [$I>2\sigma(I)$]	0.0287, 0.0702
$R1$, w$R2$ (all data)	0.0378, 0.0754
resid. el .dens [e/Å^3]	0.606/-0.422

Figure 87. Plot of the molecular structure of **12** (50% probability thermal ellipsoids; hydrogen atoms and solvent omitted for clarity).

Table 18. Crystal data and refinement details for **13**.

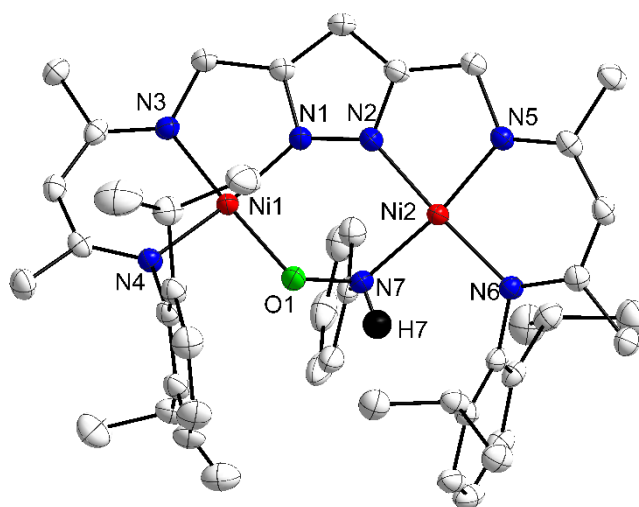| Compound	$LFe_2(OTf)(THF)$ **(13)**
empirical formula	$C_{50.50} H_{75} N_6 Fe_2 O_5 F_3 S$
formula weight	1046.92
crystal size [mm^3]	0.500 x 0.400 x 0.160 mm^3
crystal system	Triclinic
space group	$P\bar{1}$
a [Å]	11.5110(6)
b [Å]	15.1672(7)
c [Å]	15.9216(8)
α [°]	86.726(4)
β [°]	87.752(4)
γ [°]	70.828(4)
V [Å^3]	2629.8(2)
Z	2
ρ [Mg/cm^3]	1.322
$F(000)$	1110
μ [mm^{-1}]	0.652
T_{min} / T_{max}	0.8993, 0.6004
Ө-range [°]	1.423-26.772
hkl-range	-13,14 ±19 ±20
measured refl.	39156
unique refl. [R_{int}]	11182 [0.0704]
Data/restrains/param.	11182 / 53 / 675
Goodness-of-fit F^2	0.952
$R1$, w$R2$ [$I>2\sigma(I)$]	0.0413, 0.0937
$R1$, w$R2$ (all data)	0.0616, 0.0993
resid. el .dens [e/Å^3]	0.600/-0.268

Figure 88. Plot of the molecular structure of **13** (50% probability thermal ellipsoids; hydrogen atoms and solvent omitted for clarity).

Table 19. Crystal data and refinement details for **15**.

Compound	LFe$_2$(N$_2$H$_4$)(OTf)(THF)·THF **(15)**
empirical formula	C$_{48}$ H$_{73}$ N$_8$ Fe$_2$ O$_5$ F$_3$ S
formula weight	1042.90
crystal size [mm^3]	0.500 x 0.490 x 0.320 mm^3
crystal system	Monoclinic
space group	$P\,2_1$/c
a [Å]	11.8734(3)
b [Å]	16.4472(5)
c [Å]	26.5357(6)
α [°]	90
β [°]	90.273(2)
γ [°]	90
V [Å^3]	5181.9(2)
Z	4
ρ [Mg/cm^3]	1.337
F(000)	2208
μ [mm^{-1}]	0.663
T_{min} / T_{max}	0.8674, 0.7447
Θ-range [°]	1.457-26.765
hkl-range	-15,14 ±20 -32,33
measured refl.	65549
unique refl. [R_{int}]	10985 [0.0664]
Data/restrains/param.	10985 / 15 / 672
Goodness-of-fit F^2	1.046
R1, wR2 [I>2σ(I)]	0.0427, 0.1042
R1, wR2 (all data)	0.0560, 0.1102
resid. el .dens [e/Å^3]	0.527/-0.358
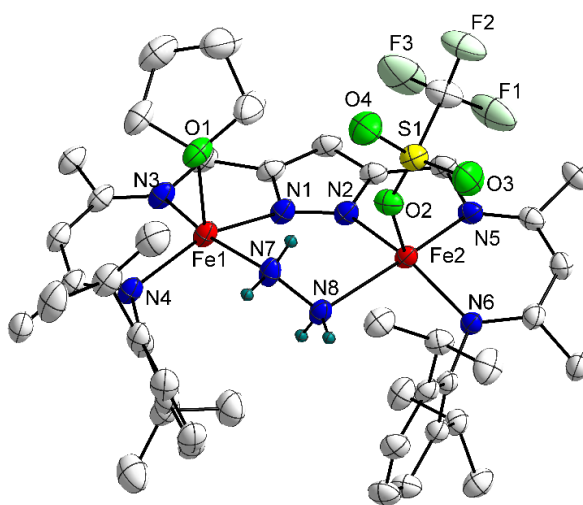
Figure 89. Plot of the molecular structure of the cationic part of **15** (50% probability thermal ellipsoids; hydrogen atoms except those that belong to the N$_2$H$_4$ bridging unit and solvent omitted for clarity).

9.4 DFT Calculations

9.4.1 Optimization of the Molecular Structures

Calculation for the geometrical optimizations of the reported complexes were performed using the ORCA software[225] package 3.0.3 with BP86[226] or B3LYP functional,[227] RI or RIJCOSX approximation, def2-tzvp or def2-txvp/j basis sets,[228] respectively. The initial coordinates were taken from the X-ray structure of the complexes, and charges were modified for the respective calculations on the oxidized or reduced species.

Table 20. Coordinates for the energy optimized structure of the anionic part of **3** (**3⁻**).

Ni	1.9453751139	-0.9886324441	0.4704366065
Ni	-1.8845842173	-1.2139274947	-0.0754114468
O	0.385455158	-0.0171233602	2.6778102186
O	0.5514589471	0.2325371953	0.1017055079
N	3.2244175153	0.3975236141	0.3029988115
N	3.2123077411	-2.3459731922	0.8513883278
N	-3.2255155461	0.0901135239	-0.3355796523
N	-2.9437552361	-2.6983141078	-0.6125479861
N	0.7510843831	-2.4212728994	0.4032272633
N	-0.5491234918	-2.5003095497	0.0758847381
N	-0.6917077895	-0.1449519145	2.0326093359
N	-0.6262178941	-0.0183905727	0.706027517
C	2.9622506643	3.3018148202	2.5690946481
C	0.5007234045	3.0851649206	2.0369160956
C	4.5202157682	0.7624975776	-3.7523857223
C	2.5205835817	-0.5519866484	-2.9344558937
C	2.2038018902	3.8814535591	-1.8504706655
C	1.9072034396	2.5657419659	1.7270122527
C	1.9151539947	3.7963411412	-0.4905503992
C	3.6580461458	0.404677093	-2.5364168102
C	2.7795463051	2.7926918512	-2.5060907245
C	-5.1883824549	1.0099379744	2.4420842191
C	-3.0428322761	1.3800253611	3.723255606
C	-2.7236510431	2.5644030234	-3.5723530835
C	-0.567572782	1.6373840364	-2.6321191958
C	-2.4657758096	4.1619306009	0.4825880661
C	2.2201345568	2.6441657045	0.2457853713
C	3.0949824813	1.6196497573	-1.8125242581
C	5.4535749749	1.4528471539	0.3816985678
C	5.333725718	-3.3209857542	1.6305469469
C	5.0965199277	-0.8889403672	1.1291976668
C	-3.6527471029	1.0392516028	2.359526012

C	-2.9438688868	3.3219459797	1.4882484305
C	-2.0877503664	1.7360392036	-2.4452447282
C	-2.1829280037	3.6400016689	-0.7773009743
C	2.8367803098	1.568108061	-0.4226961191
C	4.5169397535	0.2866179379	0.6252362073
C	4.4831173289	-2.151108708	1.1874694
C	2.7016370007	-3.7248192813	0.8183720886
C	-3.1627736337	1.9600511967	1.2529243047
C	-2.4118617599	2.288785294	-1.0676636628
C	-5.3574949595	0.9979855296	-1.1888745624
C	-4.9400581113	-3.9281131504	-1.3665699669
C	-4.9026697899	-1.4409658775	-1.1802720322
C	0.2415349753	-4.5981461932	0.1760320352
C	1.2553131871	-3.6709687021	0.4739846653
C	-2.9197911735	1.4602115639	-0.0458913139
C	-4.4309293742	-0.1566584691	-0.8632826013
C	-4.2038618747	-2.6492872056	-1.0330300182
C	-2.3048625237	-4.0169849577	-0.4659524708
C	-0.8870884998	-3.7996052898	-0.0713218234
H	3.9632548835	2.8657072625	2.4413002714
H	3.017307067	4.3683269767	2.2935049934
H	2.7040820131	3.2384947448	3.6378384045
H	0.4107449641	4.1729249792	1.8829742271
H	-0.2421573336	2.5907204894	1.4011421495
H	0.2458223798	2.8683213043	3.0836410662
H	3.9214410041	1.2111082818	-4.560081597
H	5.3174299667	1.4737381264	-3.48915709
H	4.9886222572	-0.1456663771	-4.1611813136
H	1.9604494642	-0.8773254373	-2.0448415935
H	1.8169501425	-0.052222165	-3.6165255842
H	2.9236586151	-1.4456068487	-3.4361506503
H	1.9558898577	4.7869883429	-2.4087124708
H	1.9143339325	1.5018005217	2.0024955842
H	1.4309378604	4.6340607237	0.0140371059
H	4.2961390094	-0.1392875241	-1.8240659276
H	2.9751855197	2.8549226977	-3.5774892088
H	-5.6398051706	0.6426570633	1.5116344562
H	-5.5127965563	0.3432920294	3.2564188041
H	-5.5915115626	2.0157305535	2.6447935089
H	-1.9470611565	1.3810259656	3.6628043821
H	-3.3855386356	2.357955599	4.0984845184
H	-3.3404853109	0.6221121284	4.463553301
H	-3.8132861843	2.6579417866	-3.4496166717
H	-2.3030071661	3.5806890061	-3.606075459
H	-2.5272393308	2.0934626616	-4.5481636954

|			
H	-0.1060203727	2.6347469683	-2.5970552883
H	-0.1075902065	1.0376285218	-1.834741675
H	-0.3254132648	1.1859077751	-3.6073198966
H	-2.2818719332	5.2172872039	0.693106557
H	5.7477639144	1.49648058	-0.678898747
H	4.9826359855	2.4148500809	0.6151635395
H	6.3643015294	1.3363098074	0.9823120929
H	6.3443898982	-2.9824499411	1.8858492
H	4.8998955781	-3.8177022436	2.5131632781
H	5.4162683325	-4.0859452726	0.8413980136
H	6.1422806082	-0.8339767044	1.4261041776
H	-3.302914353	0.0303899985	2.0950827071
H	-3.1217986217	3.726543025	2.4853471282
H	-2.4990916701	0.7177931063	-2.4962286775
H	-1.7708591752	4.2908778395	-1.5512544549
H	3.2566817858	-4.3284356356	0.0748086444
H	2.8453257628	-4.2242013935	1.7956783583
H	-5.3526515625	1.7663074151	-0.406552832
H	-5.0322236972	1.492747488	-2.1168752275
H	-6.3817180513	0.6334802317	-1.3356755825
H	-4.4290871776	-4.4948436803	-2.1613773442
H	-5.0012622771	-4.591888502	-0.4892071166
H	-5.9598237551	-3.7067008444	-1.7015434771
H	-5.9143450467	-1.5026995177	-1.5762346499
H	0.3155920994	-5.6807828177	0.1396420338
H	-2.3582048263	-4.5887795517	-1.4110109531
H	-2.8357654639	-4.6210890229	0.2951482249
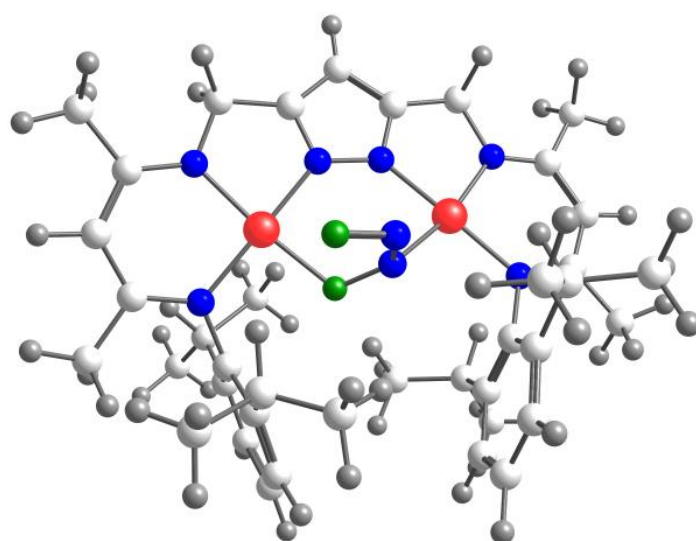
Figure 90. DFT calculated molecular structure of the anionic part of the hyponitrite complex (**3**⁻).

Table 21. Coordinates for the energy optimized structure of the anionic part of **10** (**10⁻**).

Ni	1.883981	1.184839	0.31317
Ni	-1.893298	1.011558	-0.27403
O	-0.513183	-0.238924	-0.36654
N	3.167394	-0.199747	0.59379
N	2.963156	2.582856	1.05688
N	0.585338	2.491841	0.31979
N	0.735648	0.152759	-0.78584
N	-3.191921	-0.380041	-0.41423
N	-3.209026	2.392984	-0.25152
N	-0.75347	2.426827	0.12591
C	5.252337	-2.036884	-1.98854
C	3.102373	-1.952761	-3.22613
C	2.209043	-2.11344	4.02444
C	0.176205	-1.26689	2.84669
C	2.058785	-4.270012	0.2542
C	3.787543	-1.648519	-1.90364
C	2.737002	-3.648731	-0.78424
C	1.679919	-1.454189	2.76726
C	1.71691	-3.547418	1.35945
C	-2.793587	-3.767979	-2.54082
C	-0.467762	-2.971413	-2.04765
C	-2.354609	-3.87282	1.78489
C	3.083454	-2.293467	-0.71067
C	2.063629	-2.205569	1.49494
C	5.193525	-1.195798	1.59006
C	4.951575	3.687669	1.98287
C	4.863974	1.247682	1.52519
C	1.049601	1.180392	-4.87907
C	-5.163292	-0.945575	3.26218
C	2.066354	1.457691	-3.96768
C	-1.947737	-2.717408	-1.792
C	-1.995301	-3.80731	0.46627
C	-3.034761	-2.8116	2.36645
C	2.748174	-1.581718	0.44081
C	4.349941	-0.01575	1.18628
C	4.206919	2.464592	1.48065
C	2.335006	3.920871	1.06754
C	-0.111016	0.610579	-4.40395
C	-4.041356	-0.509086	2.33171
C	1.935948	1.158554	-2.6366
C	-2.279233	-2.685579	-0.30818
C	-3.336864	-1.664687	1.64538
C	-5.371827	-1.376317	-0.94666

C	-5.339148	3.510085	-0.77279
C	-4.981714	1.06972	-1.12009
C	-0.280459	4.467454	0.89776
C	0.881272	3.723629	0.77199
C	-0.268961	0.304586	-3.04794
C	-3.051852	0.393111	3.06399
C	0.773587	0.532823	-2.1398
C	-2.929846	-1.609668	0.29802
C	-4.436097	-0.187006	-0.84472
C	-4.438451	2.297473	-0.71927
C	-2.748451	3.696583	0.27409
C	-1.283994	3.606476	0.47427
H	5.721341	-1.712683	-1.19203
H	5.327377	-3.014022	-2.03888
H	5.650228	-1.637614	-2.78939
H	3.4763	-1.380282	-3.92694
H	3.248139	-2.893303	-3.4599
H	2.140463	-1.780757	-3.14277
H	1.982956	-1.563688	4.80346
H	1.804987	-3.000449	4.12189
H	3.18279	-2.203108	3.96144
H	-0.139109	-0.807705	2.04008
H	-0.258692	-2.141936	2.9156
H	-0.044751	-0.730418	3.63543
H	1.835756	-5.191746	0.19576
H	3.750246	-0.657838	-1.77146
H	2.969085	-4.148965	-1.55617
H	2.091377	-0.54412	2.71177
H	1.230422	-3.972429	2.05629
H	-2.563781	-3.754095	-3.49362
H	-2.609287	-4.657345	-2.17249
H	-3.743664	-3.561647	-2.4304
H	0.067064	-2.311959	-1.55638
H	-0.233447	-3.87324	-1.74265
H	-0.282789	-2.890774	-3.00568
H	-2.139602	-4.641608	2.29947
H	4.826965	-1.595621	2.40542
H	5.19147	-1.861484	0.87086
H	6.113124	-0.899318	1.7565
H	4.511019	4.03058	2.78865
H	5.876034	3.445104	2.19547
H	4.94853	4.381161	1.28951
H	5.766092	1.268283	1.82019
H	1.153979	1.379089	-5.80277
H	-5.720663	-1.612485	2.80943

H	-4.781399	-1.335116	4.07455
H	-5.710748	-0.168954	3.4998
H	2.868872	1.86217	-4.27651
H	-2.171746	-1.820502	-2.17297
H	-1.543111	-4.543686	0.07046
H	-3.298083	-2.871066	3.27728
H	2.451271	4.347377	1.95268
H	2.750196	4.501057	0.38068
H	-0.819107	0.419509	-5.00967
H	-4.459334	0.044959	1.61091
H	-6.157529	-1.131264	-1.4789
H	-4.906489	-2.123053	-1.37705
H	-5.65612	-1.645836	-0.04838
H	-4.91225	4.211292	-1.30776
H	-6.195415	3.263627	-1.18168
H	-5.493918	3.841585	0.13596
H	-5.789207	1.094377	-1.61961
H	-0.369278	5.361839	1.20275
H	-3.512149	1.201856	3.37083
H	-2.68372	-0.086172	3.83612
H	-2.962211	4.418793	-0.3671
H	-3.199413	3.896689	1.13346
H	2.639752	1.377939	-2.03781
H	-1.090492	-0.058148	-2.74015
H	-2.324759	0.640988	2.45683
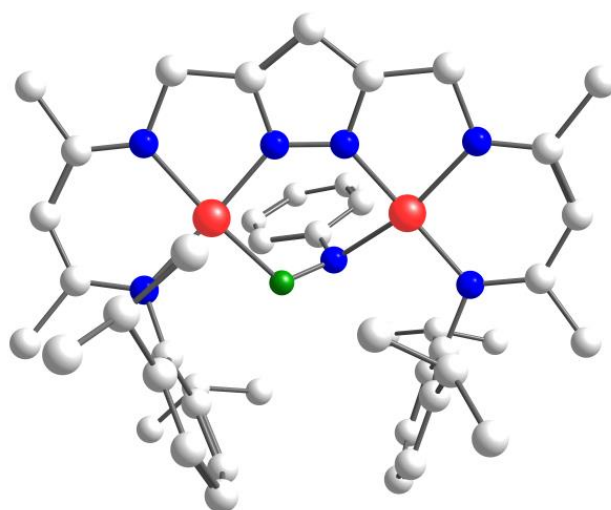
Figure 91. DFT calculated molecular structure of the anionic part of the nitrosobenzene compound (**10**⁻).

162

Table 22. Coordinates for the energy optimized structure of the radical complex **11.**

Ni	1.856962	1.107377	0.405221
Ni	-1.898595	0.950892	-0.345597
O	-0.471644	-0.317124	-0.341629
N	3.118523	-0.282551	0.689167
N	2.894466	2.490926	1.217653
N	0.544387	2.411699	0.36888
N	0.742042	0.109948	-0.783297
N	-3.188135	-0.447001	-0.385514
N	-3.192641	2.354705	-0.532396
N	-0.743255	2.378009	-0.01122
C	5.080634	-1.881761	-1.966214
C	2.901523	-1.844581	-3.23971
C	1.909665	-2.442192	4.108392
C	0.364839	-0.91524	2.819416
C	1.922008	-4.302454	0.203273
C	3.577309	-1.564353	-1.893127
C	2.534377	-3.629185	-0.850983
C	1.758908	-1.557584	2.86436
C	1.667684	-3.631164	1.397822
C	-2.835949	-3.727414	-2.530949
C	-0.478897	-2.906449	-2.199502
C	-2.039865	-3.880297	1.789035
C	2.90814	-2.284869	-0.735271
C	2.045167	-2.295183	1.567356
C	5.127888	-1.322304	1.682939
C	4.914438	3.598749	2.089757
C	4.820492	1.139412	1.669408
C	0.959778	1.46171	-4.782506
C	-4.774215	-1.005592	3.521101
C	1.998867	1.712214	-3.873071
C	-1.946952	-2.684412	-1.831692
C	-1.768497	-3.802809	0.426815
C	-2.726794	-2.8402	2.418032
C	2.68103	-1.631131	0.494387
C	4.300604	-0.112377	1.295798
C	4.152426	2.375501	1.628569
C	2.257414	3.817985	1.247825
C	-0.186998	0.805753	-4.317007
C	-3.826474	-0.548347	2.405224
C	1.908168	1.299144	-2.549874
C	-2.167539	-2.694746	-0.331351
C	-3.122299	-1.70363	1.706465
C	-5.407323	-1.478172	-0.663569

C	-5.285328	3.414659	-1.2786
C	-5.026859	0.932583	-1.137911
C	-0.279088	4.482136	0.626761
C	0.856215	3.664898	0.764329
C	-0.295365	0.387456	-2.993927
C	-2.809681	0.474206	2.937992
C	0.770054	0.591246	-2.079698
C	-2.826136	-1.63278	0.322041
C	-4.467716	-0.294211	-0.746422
C	-4.434824	2.200706	-0.972601
C	-2.708347	3.71225	-0.239497
C	-1.267663	3.614492	0.129298
H	5.605994	-1.559147	-1.057814
H	5.246464	-2.963904	-2.092083
H	5.539636	-1.363061	-2.822015
H	3.363021	-1.23058	-4.02649
H	3.000942	-2.901243	-3.534772
H	1.836363	-1.59119	-3.202814
H	1.807868	-1.831235	5.018433
H	1.130999	-3.219855	4.150744
H	2.889769	-2.942511	4.137665
H	0.230754	-0.303045	1.915853
H	-0.414692	-1.690309	2.798318
H	0.205205	-0.280158	3.70471
H	1.624796	-5.346676	0.087407
H	3.475886	-0.489892	-1.691831
H	2.705826	-4.151259	-1.79399
H	2.488339	-0.738213	2.946701
H	1.162772	-4.153258	2.211285
H	-2.702823	-3.674671	-3.623094
H	-2.5704	-4.74586	-2.205931
H	-3.903045	-3.574713	-2.311062
H	0.161998	-2.198426	-1.666246
H	-0.152954	-3.923703	-1.936325
H	-0.330277	-2.773435	-3.281539
H	-1.713876	-4.748685	2.364905
H	4.735135	-1.762879	2.613296
H	5.093406	-2.114784	0.926104
H	6.170811	-1.030087	1.859326
H	4.416862	4.086535	2.943337
H	5.932016	3.326752	2.392915
H	4.982818	4.351753	1.287979
H	5.828817	1.143257	2.079339
H	1.0343	1.790618	-5.820086
H	-5.48674	-1.764621	3.163493

H	-4.225739	-1.434441	4.374041
H	-5.347462	-0.147311	3.902825
H	2.891097	2.25246	-4.199741
H	-2.247626	-1.689527	-2.188119
H	-1.226664	-4.614453	-0.062312
H	-2.939867	-2.907828	3.486112
H	2.267677	4.239408	2.271164
H	2.815457	4.531793	0.611556
H	-1.023297	0.622892	-4.996914
H	-4.434302	-0.026796	1.651163
H	-6.313205	-1.285955	-1.251933
H	-4.934832	-2.402777	-1.016556
H	-5.708864	-1.656544	0.380505
H	-4.808465	4.055616	-2.037949
H	-6.271239	3.111245	-1.649299
H	-5.431956	4.038379	-0.381822
H	-6.052256	0.912009	-1.502555
H	-0.372997	5.538871	0.856735
H	-3.323387	1.36523	3.330732
H	-2.208119	0.033166	3.746787
H	-2.840111	4.378599	-1.112939
H	-3.293498	4.16158	0.586362
H	2.705906	1.534215	-1.841055
H	-1.196204	-0.104299	-2.636792
H	-2.128021	0.795578	2.134875
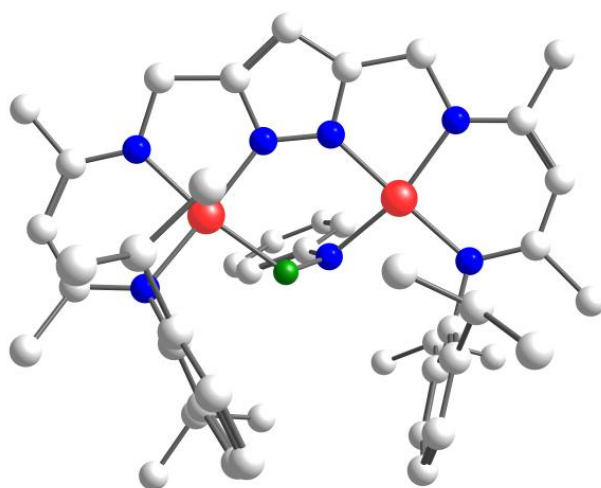
Figure 92. DFT calculated molecular structure of the anionic part of the nitrosobenzene radical compound **11**.

9.4.2 Calculation of IR spectra
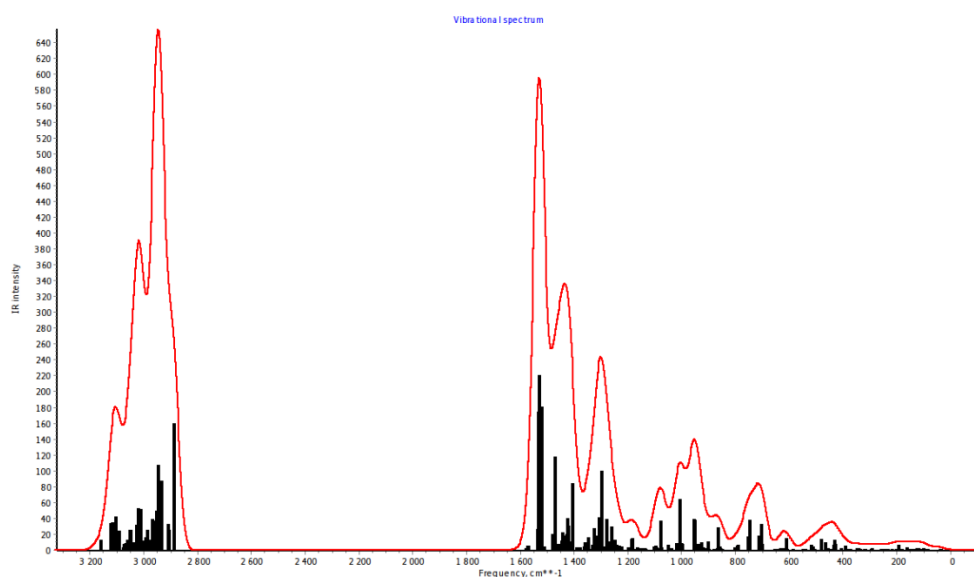
Figure 93. IR calculated spectrum of the anionic part of the hyponitrite compound **3**. Predicted NO stretching: 1006 cm^{-1} (μ-NO); 1299 cm^{-1} (terminal NO).
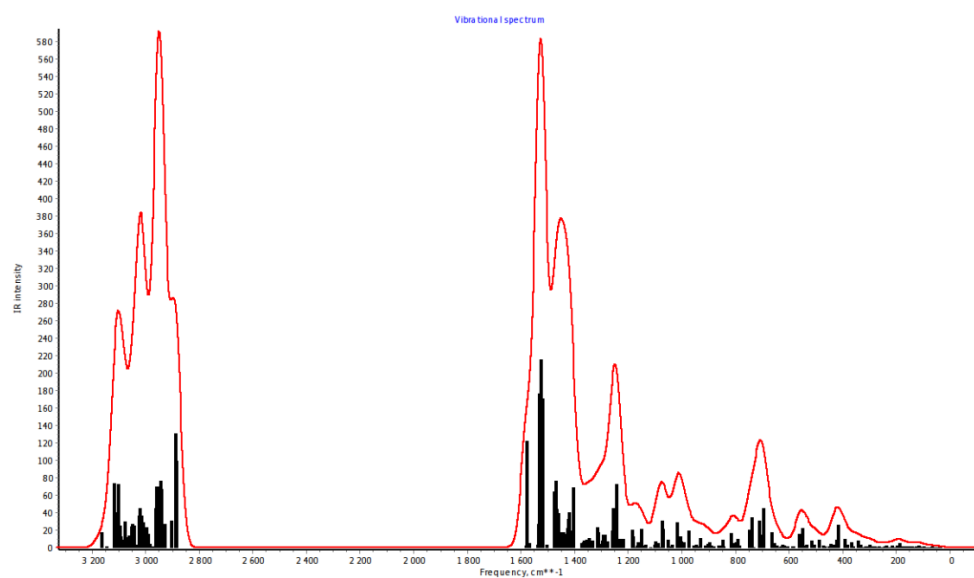
Figure 94. IR calculated spectrum of the anionic part of the nitrosobenzene compound **10**. Predicted NO stretching: 1007 cm^{-1}.
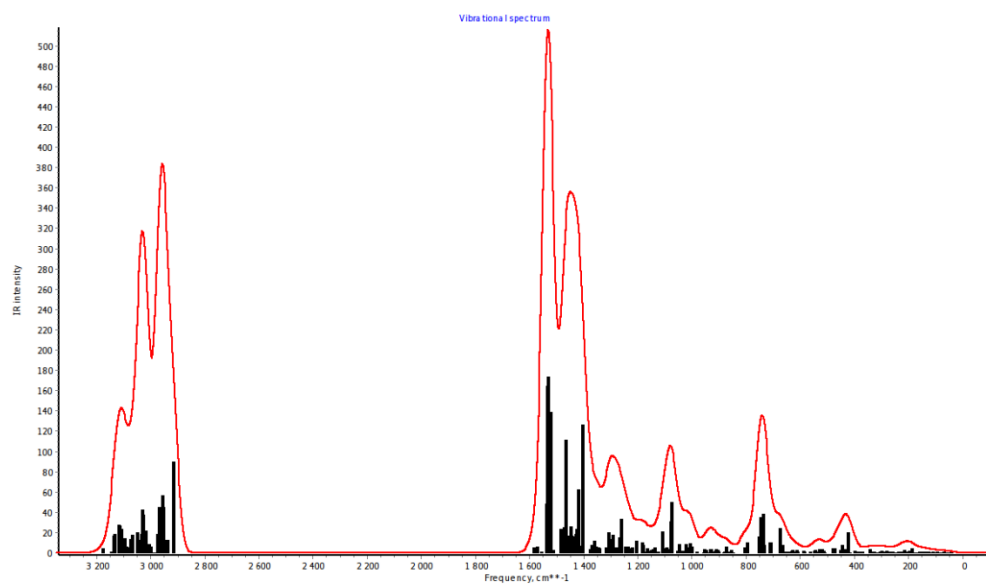
Figure 95. IR calculated spectrum of the nitrosobenzene radical compound, **11**. Predicted NO stretching: 1110 cm^{-1}.

10 Appendix

10.1 Further Analytical Data
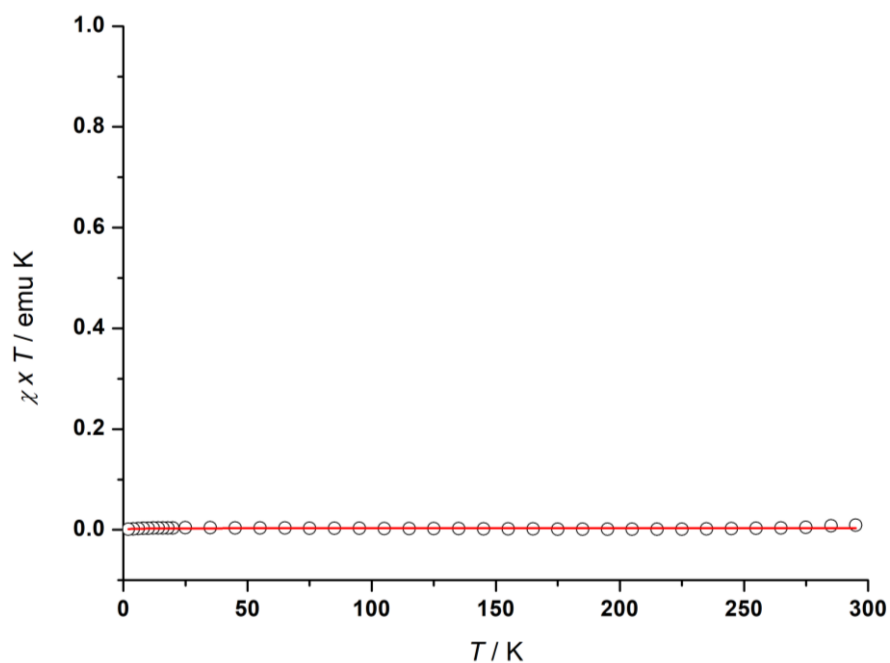
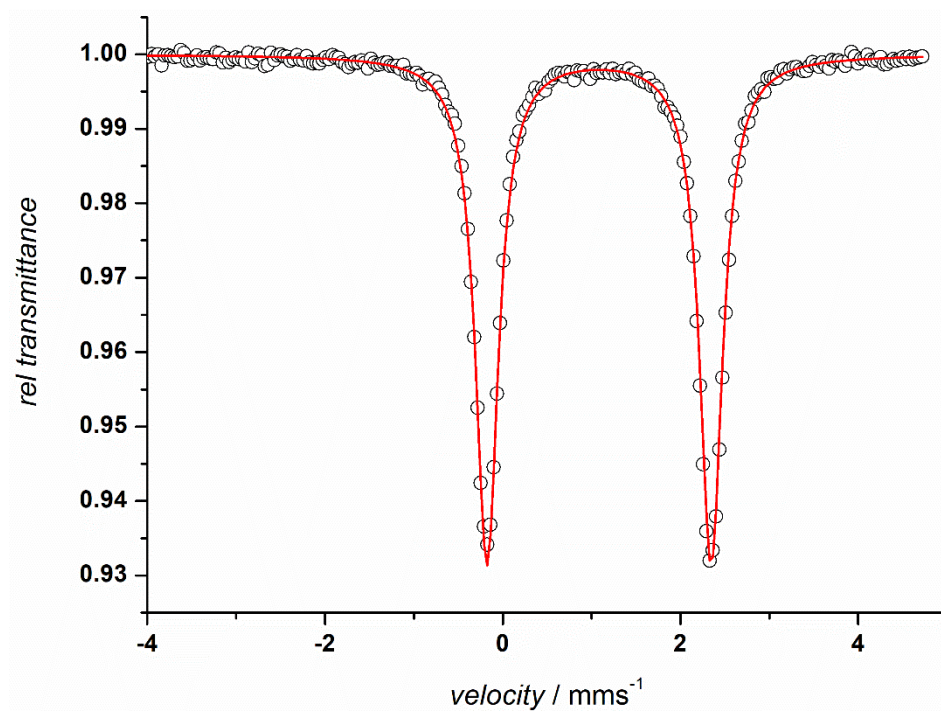**Appendix. Figure 1.** SQUID magnetic measurement for complex $KLNi_2(N_2O_2)$ **3**.
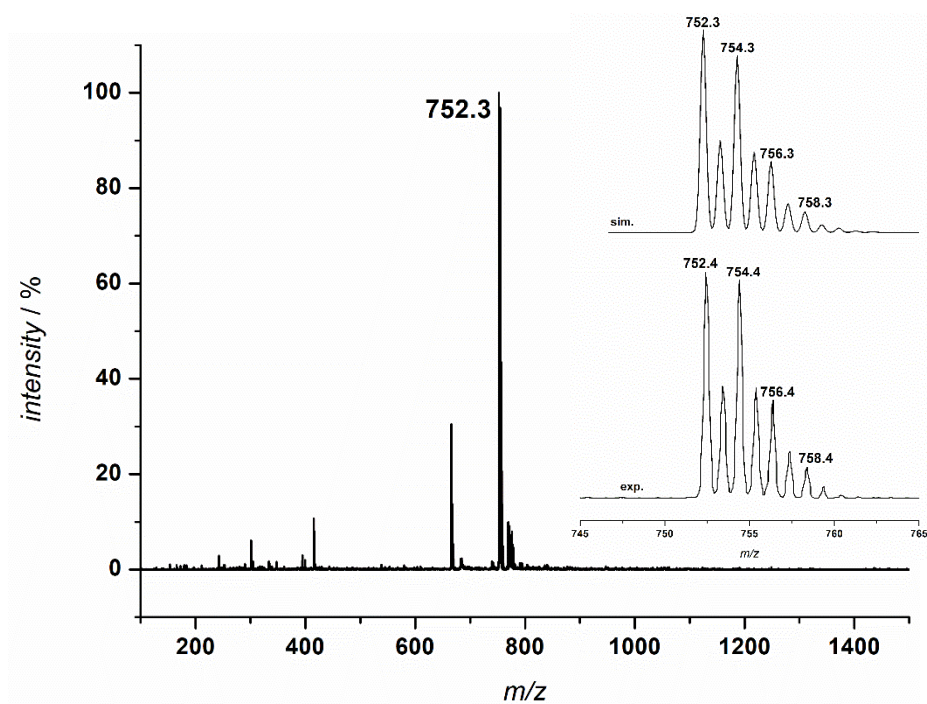
Appendix. Figure 2. ESI-MS(+)of **5** and the isotopic distribution of the molecular peak corresponding to $[LNi_2(NO) + H]^+$ with simulation.
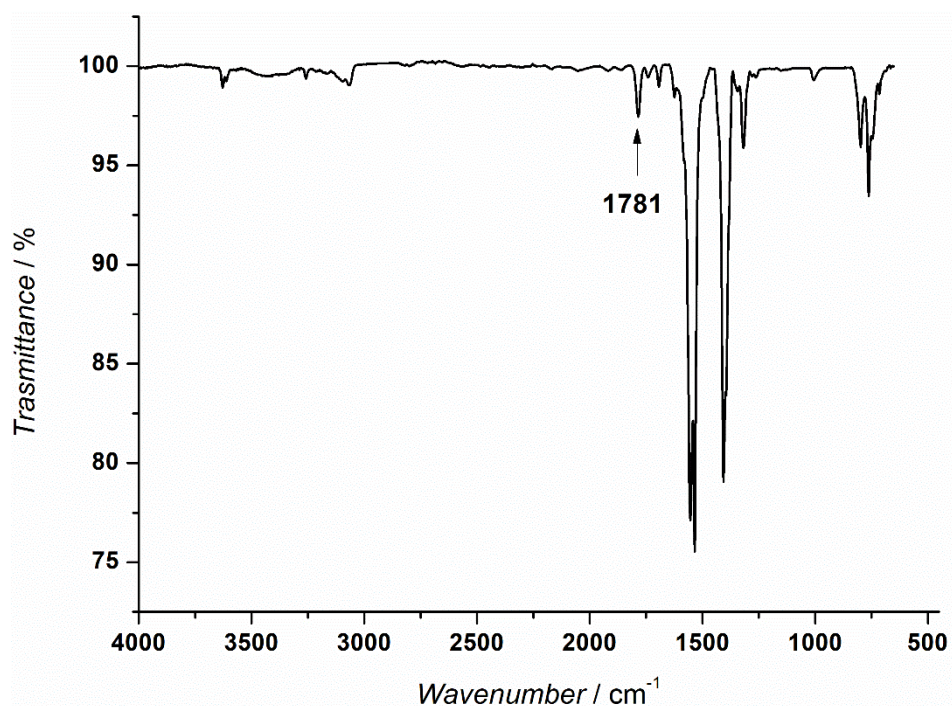
**Appendix. Figure 3.** IR spectrum of LNi₂(NO) **5** recorded in THF solution at room temperature.
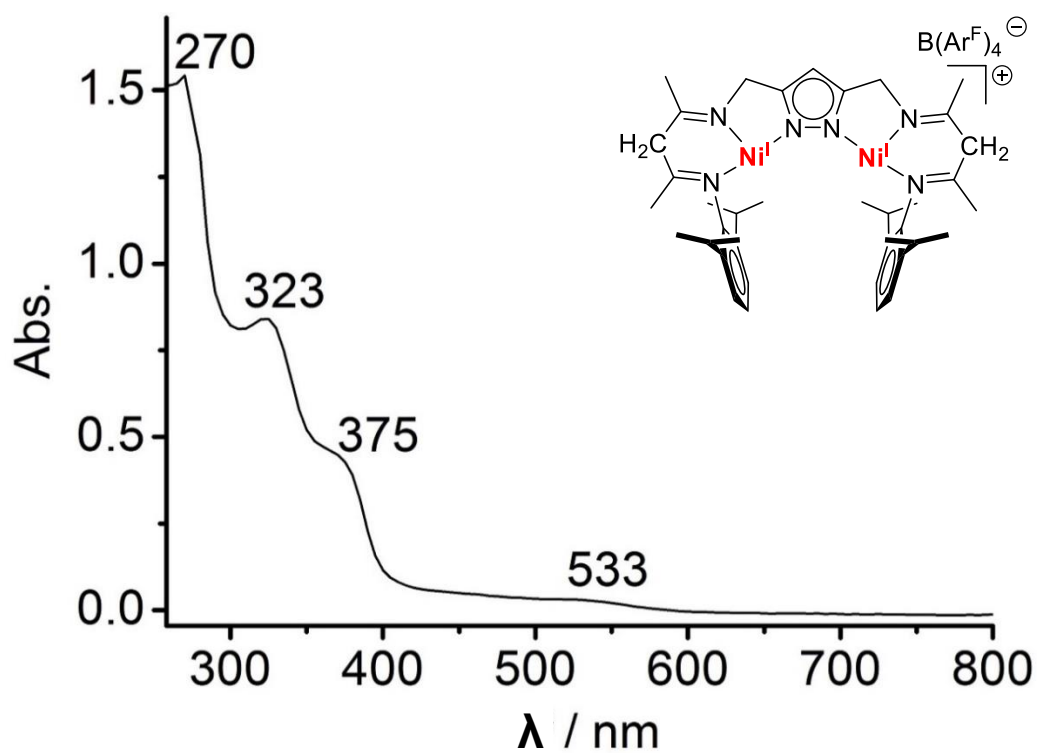
Appendix. Figure 4. UV/vis spectrum of a dinickel(I) complex based on **L³⁻** recorded in THF at room temperature. Data obtained by DUAN.[229]
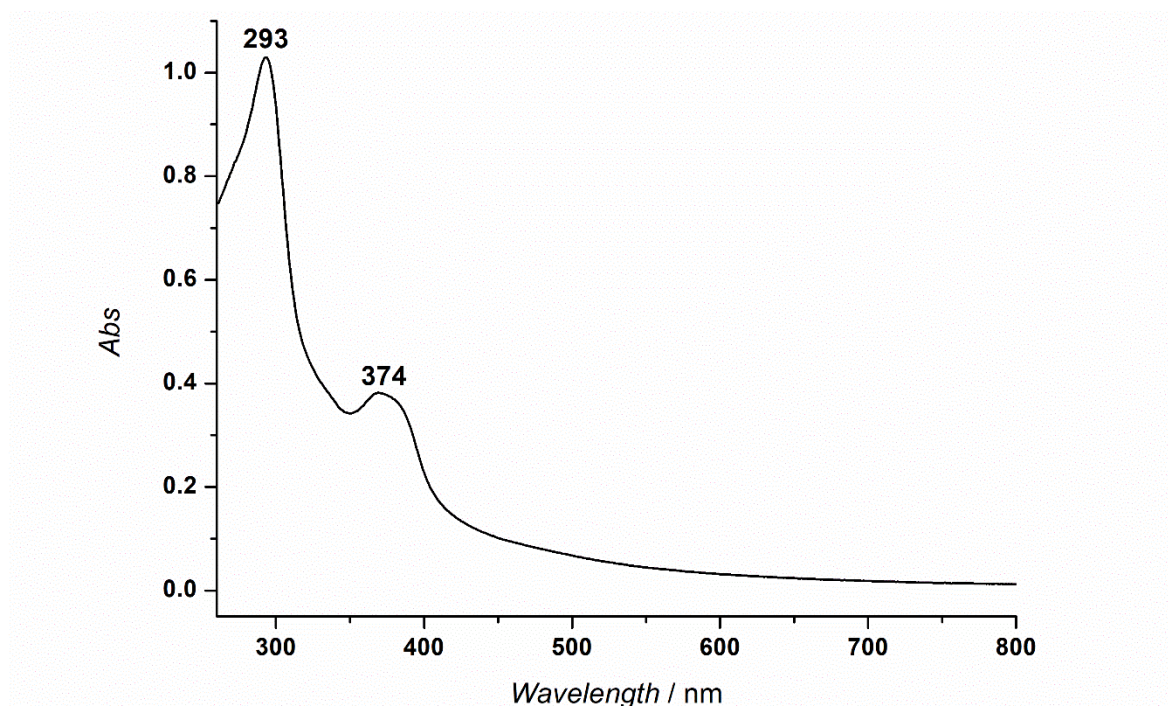
Appendix. Figure 5. UV/vis spectrum of [LNi2(NO)][Co(Cp*)2] **6** recorded in THF solution at room temperature. The presence of the decamethylcobaltocenium cation with $\lambda_{max} = 293$ nm prevented the assignment of the bands which belong to **6**.
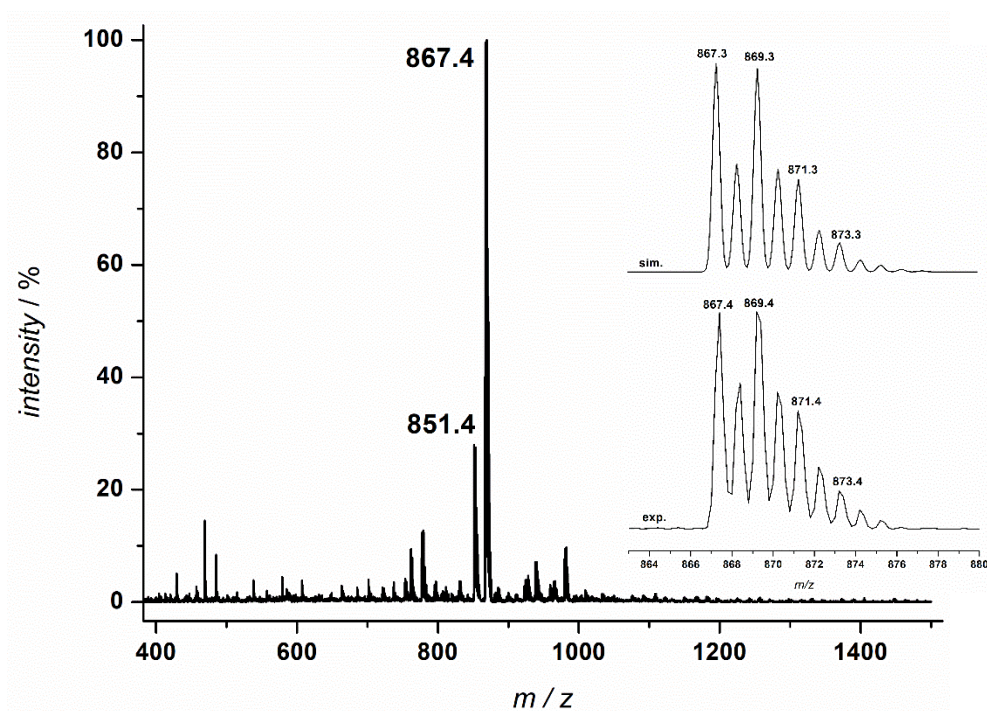
Appendix. Figure 6. ESI-MS(+) spectrogram of **9** and the isotopic distribution of the molecular peak corresponding to [LNi2(PhNO) + K]+ with simulation.
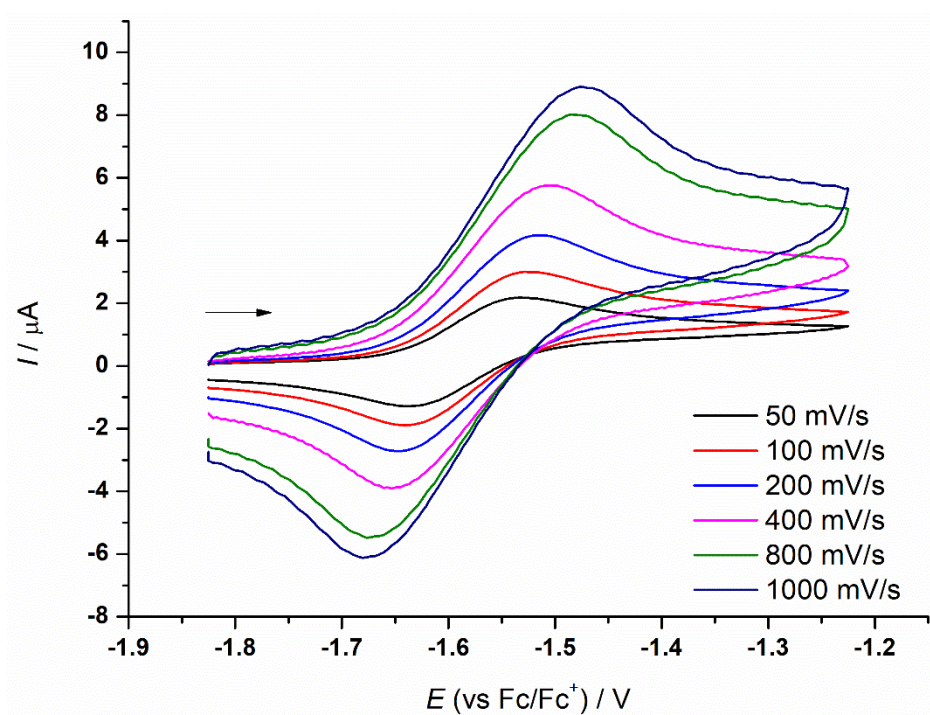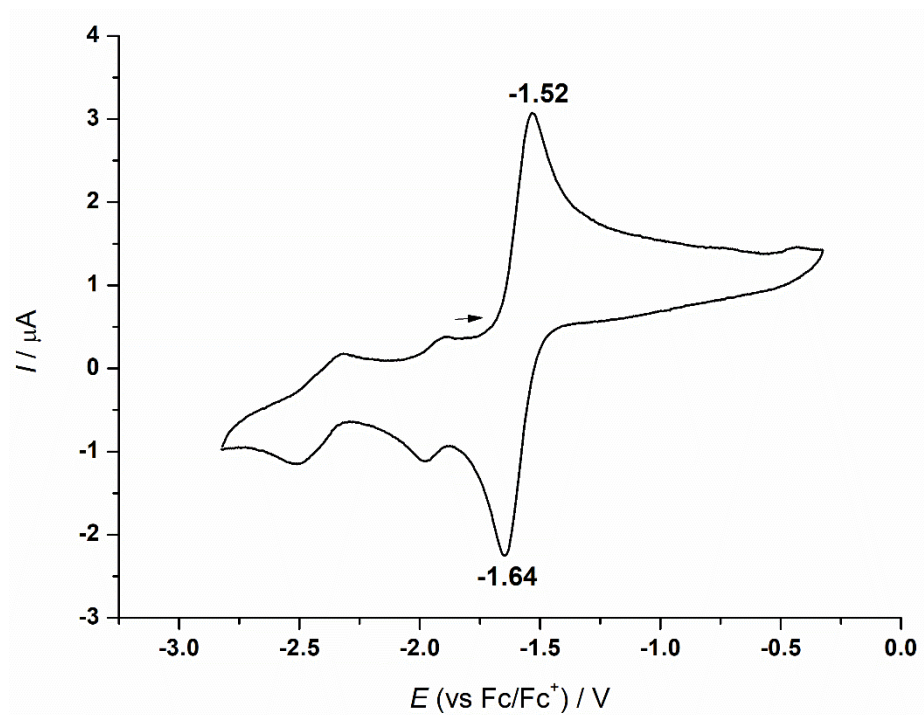
Appendix. Figure 7. Cyclic voltammogram of compound **10** (top) recorded in THF at room temperature, showing a main reversible wave centered at −1.58 V *vs.* Fc/Fc⁺. Bottom: peak centered at −1.58 V measured at different scan rates.
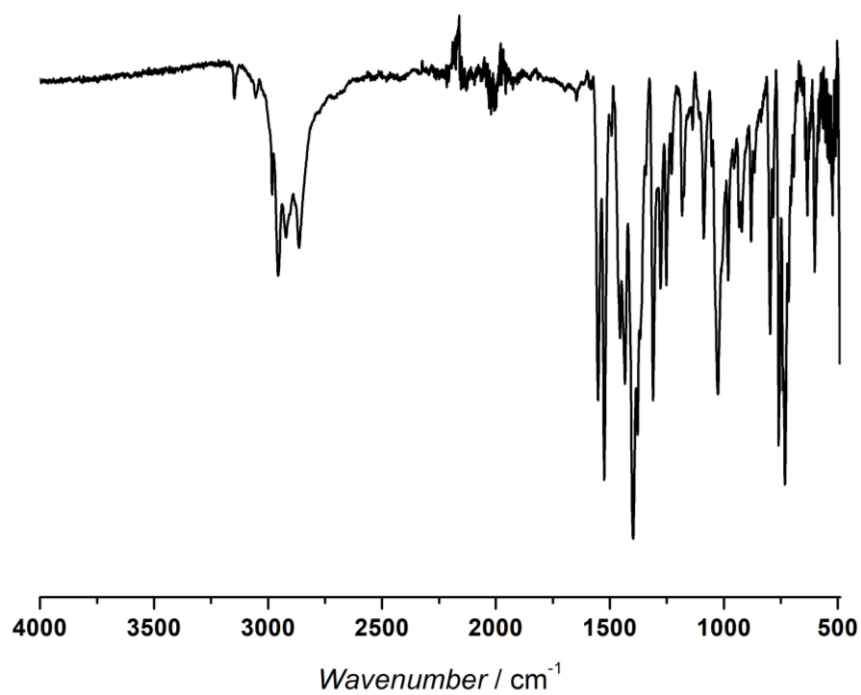
Appendix. Figure 8. IR-ATR spectrum of solid **12**. The N-H stretching was not observed.
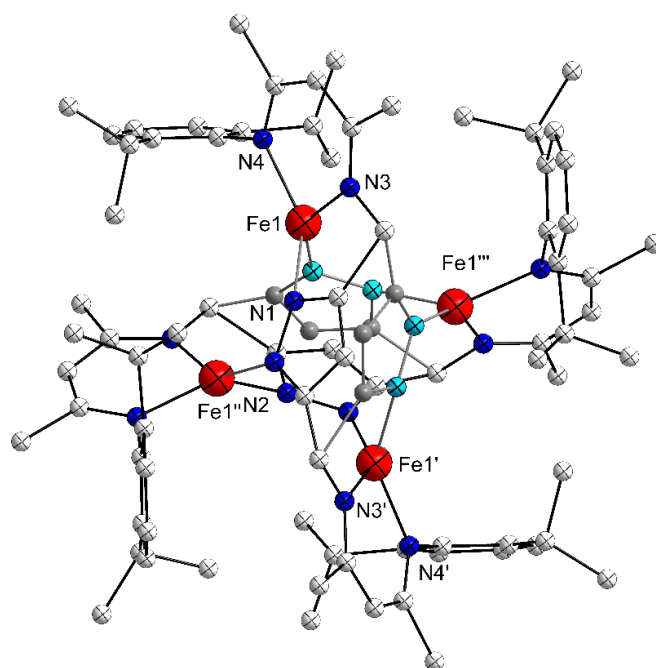
**Appendix. Figure 9.** Mössbauer spectrum of a solid sample of complex LFe$_2$(OTf)(THF) **13**.
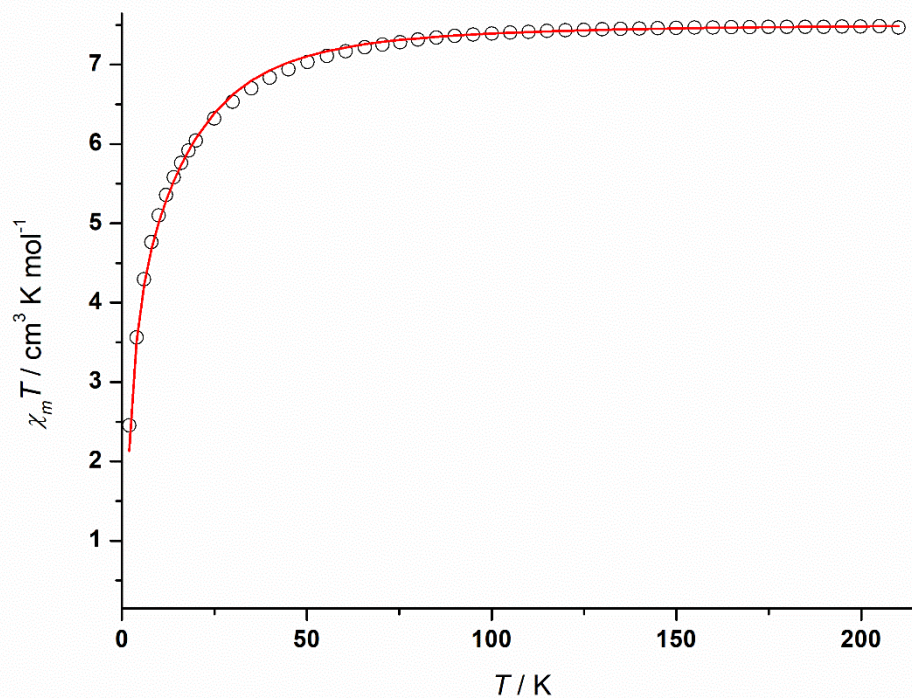
Appendix. Figure 10. SQUID measurements for complex LFe$_2$(OTf)(THF)$_2$ **13** (black dots) at 0.5 T and simulation (red line) with S$_1$ = S$_2$ = 2; g = 2.24; J = -0.13 cm^{-1}; D = -15 cm^{-1}.
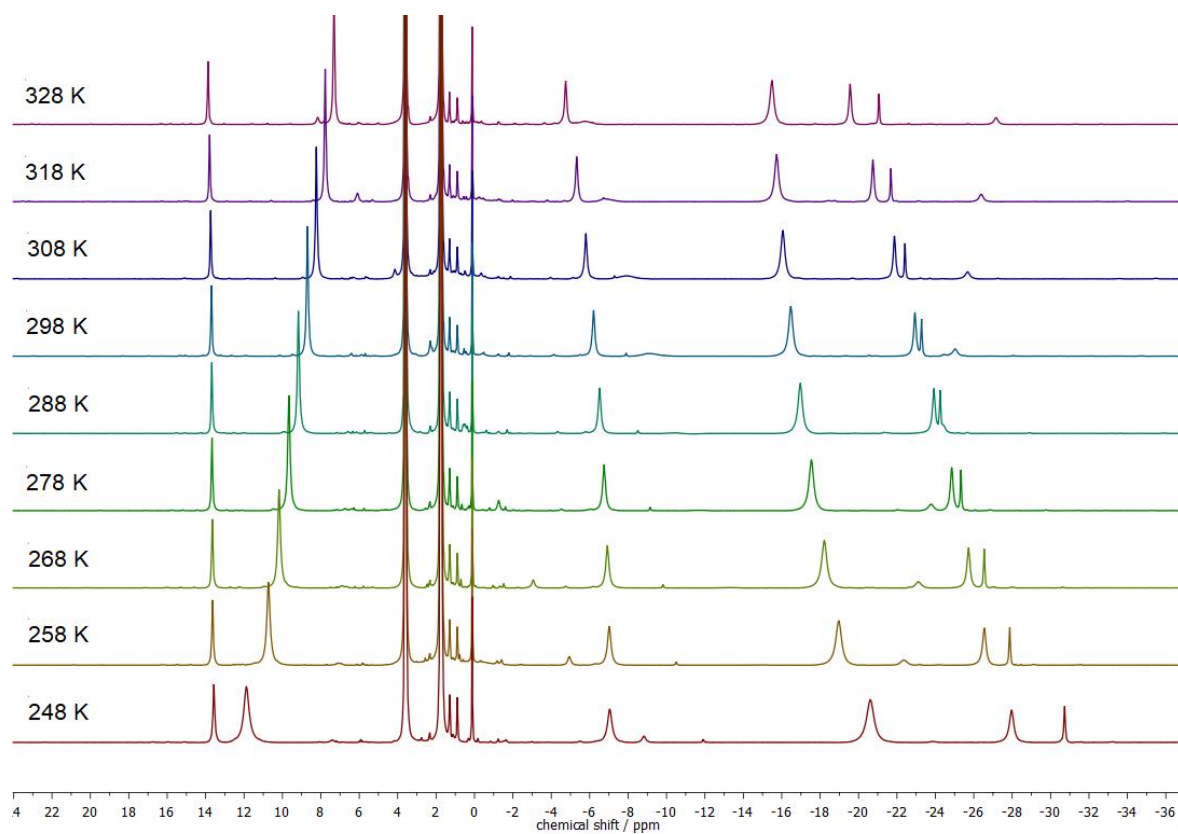
Appendix. Figure 11. Variable temperature ^{1}H-NMR spectrum of **13** recorded in THF-d$_8$ in the range 328 K–248 K.


Appendix. Figure 12. Molecular structure of the product obtained from treating **13** with KHBEt$_3$. The X-ray crystallographic data are of poor quality, and due to high disorder, it was not possible to characterize the bridging unit.
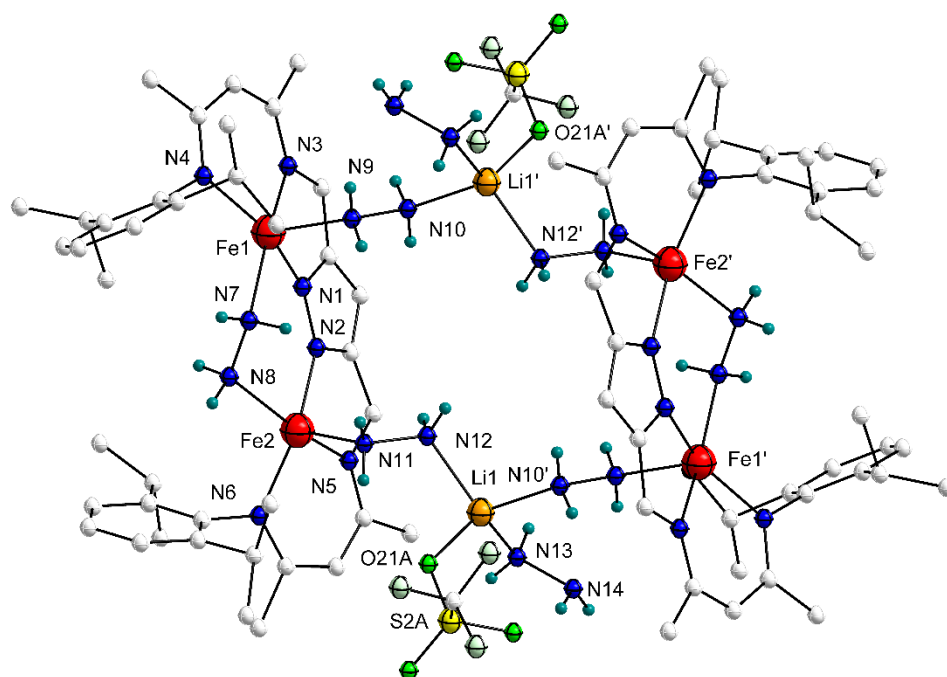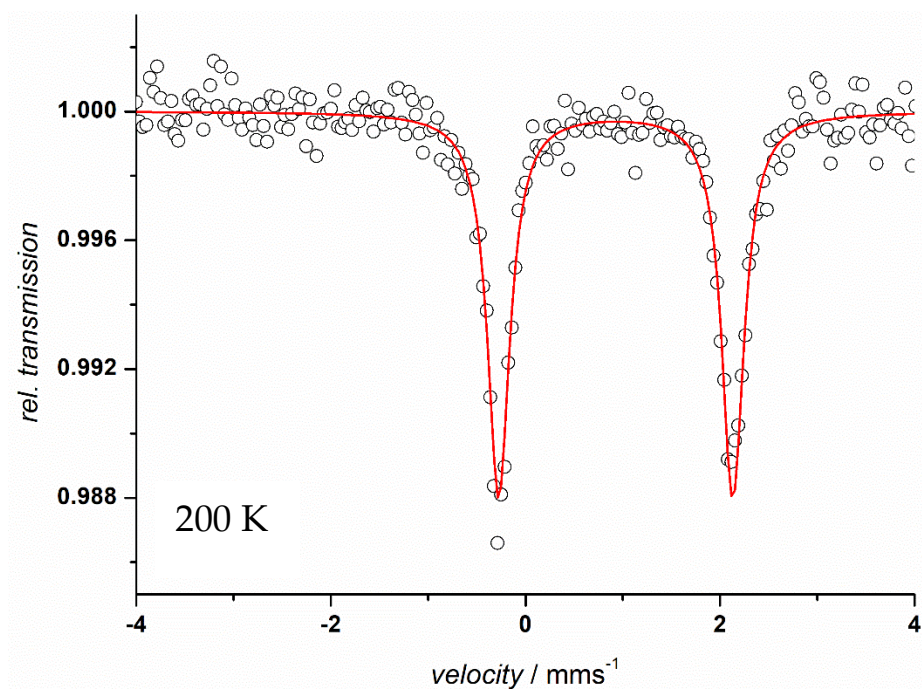
Appendix. Figure 13. Molecular structure of the product obtained by treating **13** (not purified from lithium salts) with a slight excess of hydrazine.
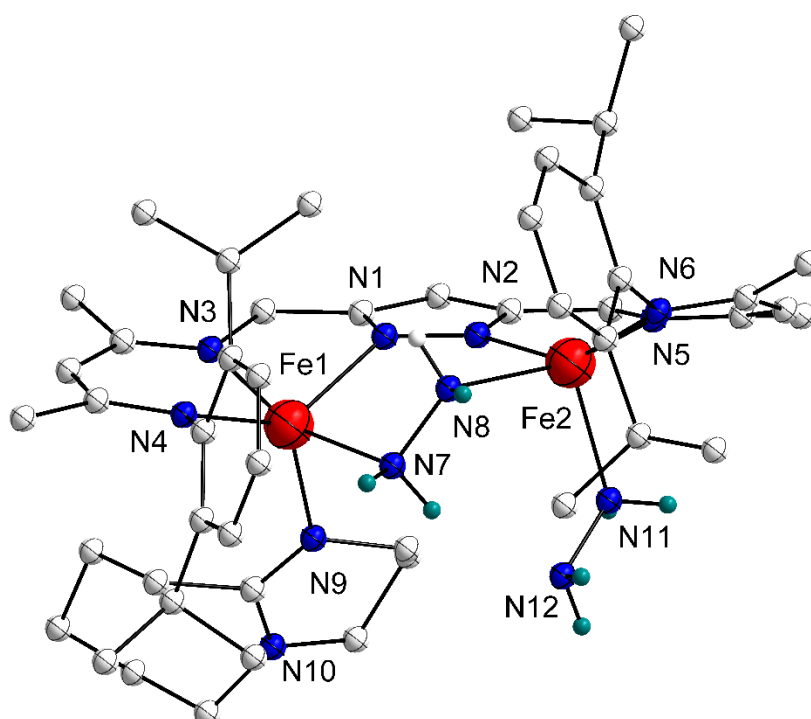
Appendix. Figure 14. Molecular structure of the product obtained by treating **13** with a slight excess of hydrazine in presence of DBU.
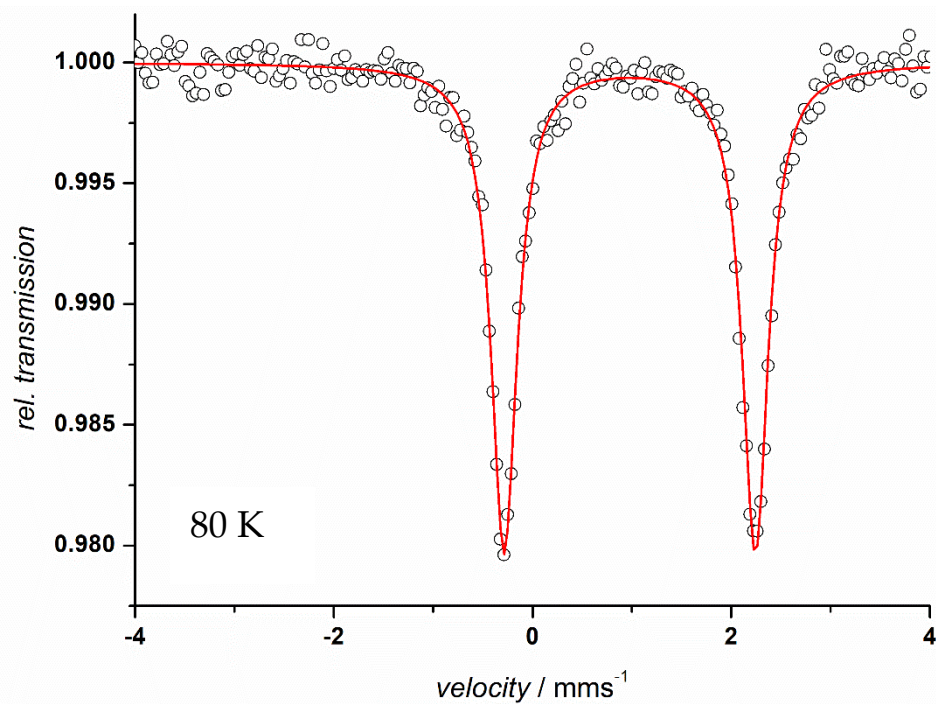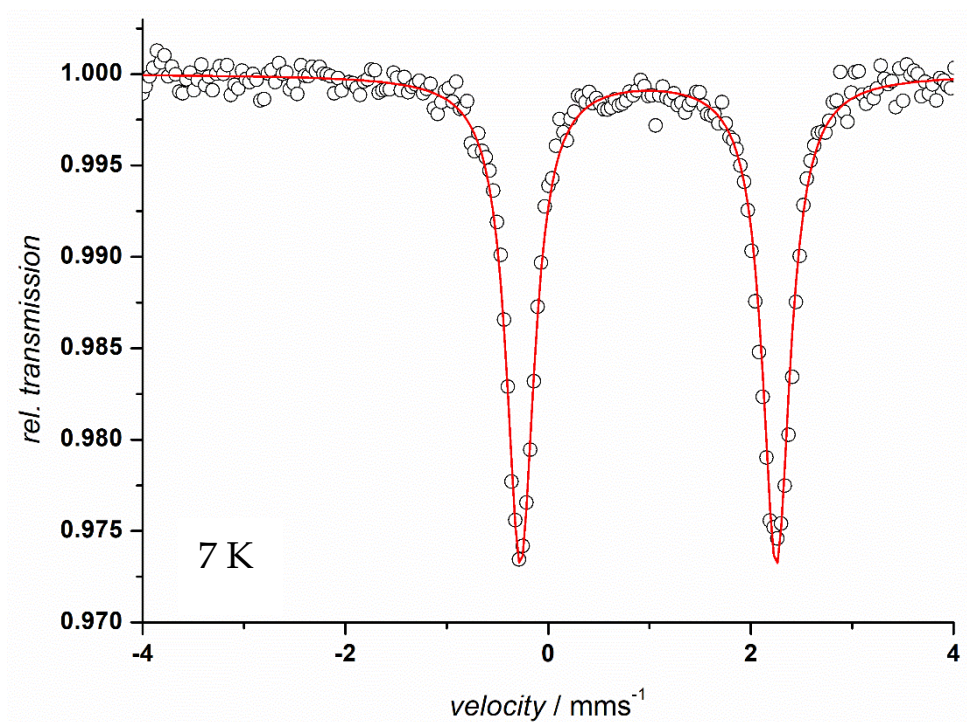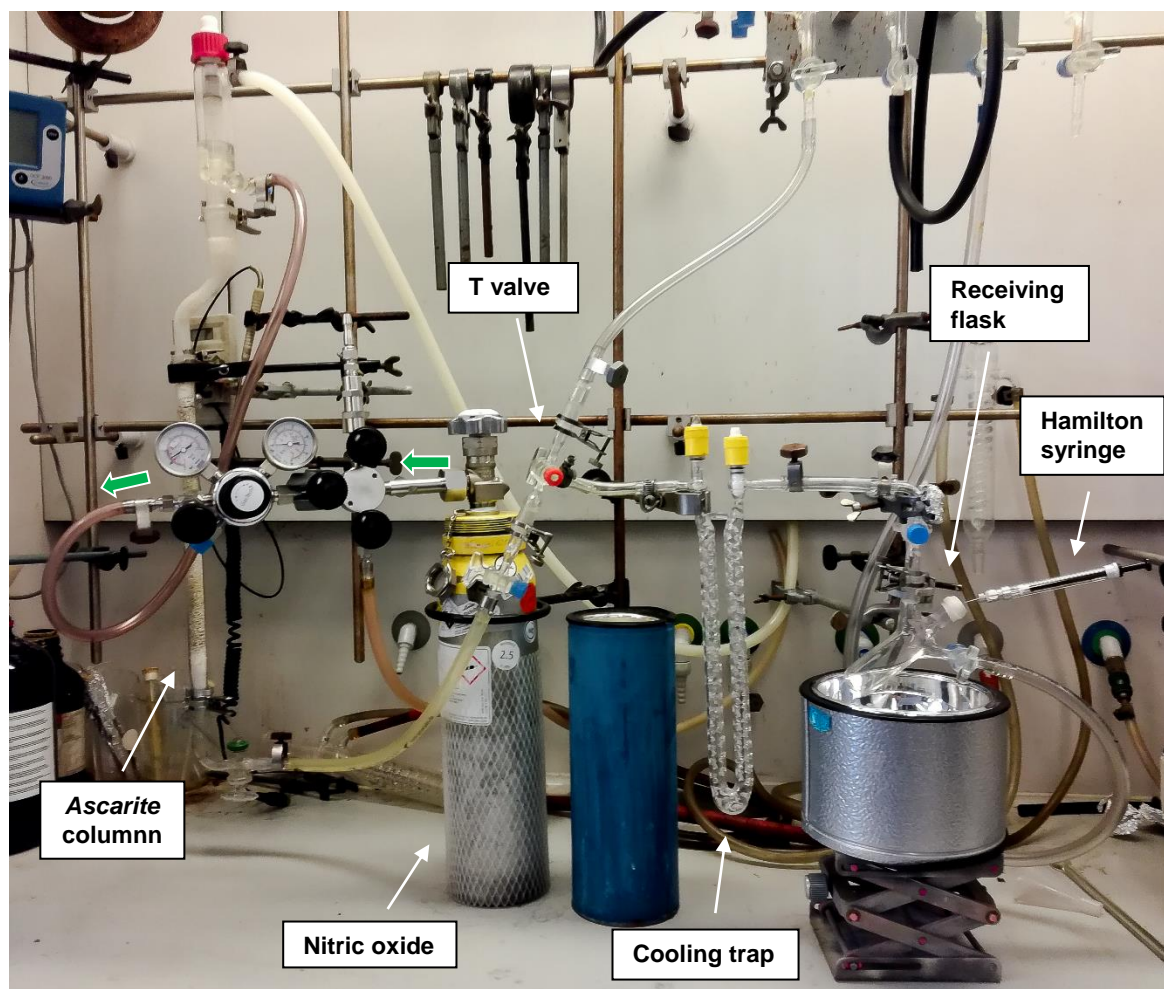
LFe$_2$(N$_2$H$_4$)(OTf)(THF) **15**

	7 K	**80 K**	**200 K**
IS / mm s^{-1}	0.99	0.98	0.93
QS / mm s^{-1}	2.53	2.53	2.41

Appendix. Figure 15. Mössbauer spectra recorded for a solid sample of complex **15** at three different temperatures. Simulated parameters are displayed in the table.

10.2 Nitric Oxide Purification Setup

Appendix. Figure 16. Setup for purification of nitric oxide. The green arrows show the direction of the gas flow.

In a typical experiment, NO was passed through a purification column of *Ascarite* and condensed in a cooling trap with liquid nitrogen. Afterwards, the Dewar containing liquid nitrogen was replaced with an acetone/dry ice cooling bath. The NO gas was distilled in the receiving flask (equipped with a septum and a valve to release the overpressure) cooled with liquid nitrogen. Finally, the liquid nitrogen was replaced with an acetone/dry ice cooling bath and the pure NO gas was collected from the headspace with a gas tight Hamilton syringe.

10.3 Experimental Setup for Headspace IR Spectroscopy
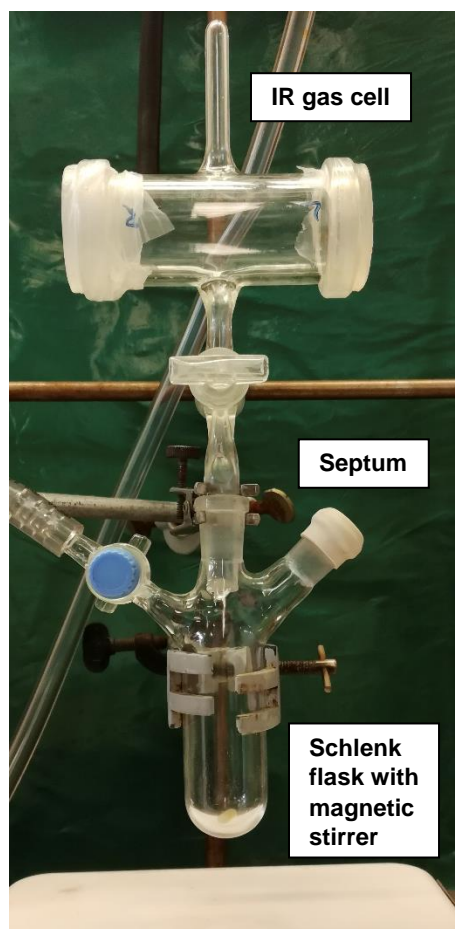
Appendix. Figure 17. Experimental setup used for the quantification of N_2O.

10.4 List of the Synthetized Compounds

I II III IV

H₃L 1 2

3 4 5

6 7

8 9 10
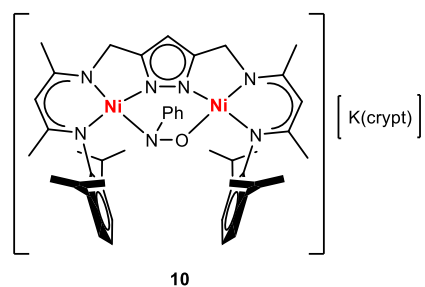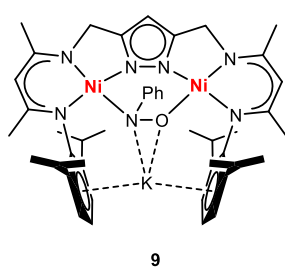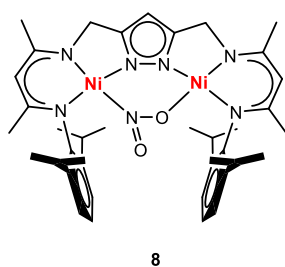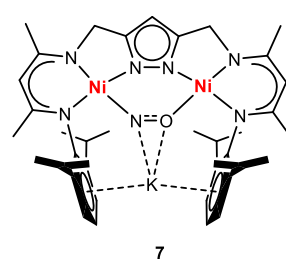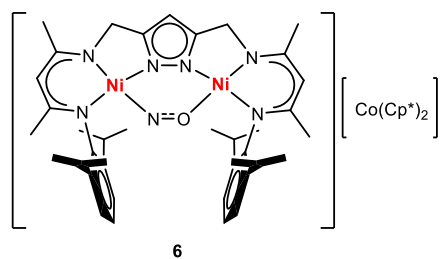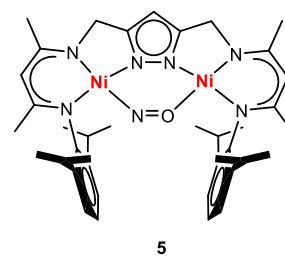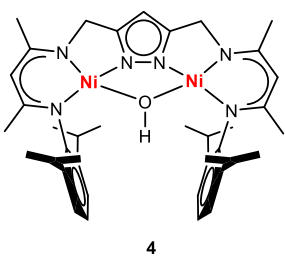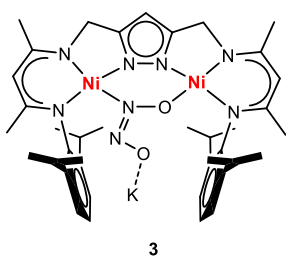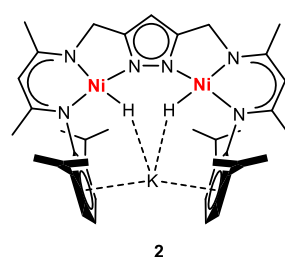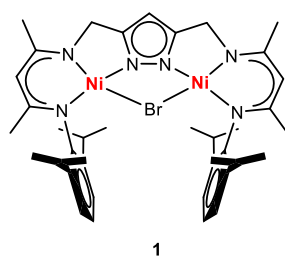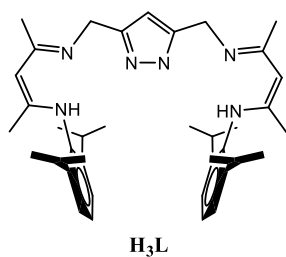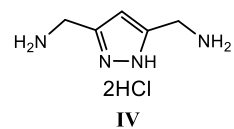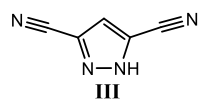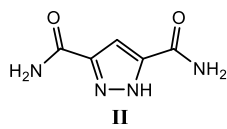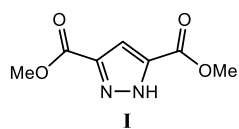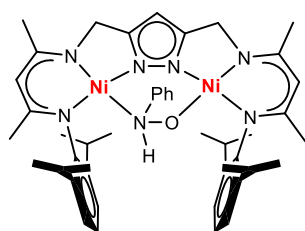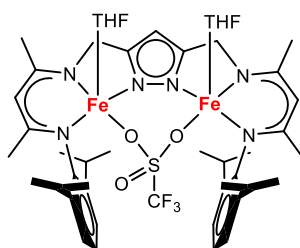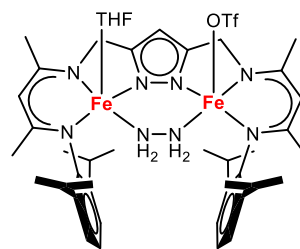
12   **13**   **15**

10.5 List of Abbreviations

THF	Tetrahydrofuran
THF-d_8	Deuterated tetrahydrofuran
DCM	Dichloromethane
DMF	Dimethylformamide
MeOH	Methanol
MeCN	Acetonitrile
pz	Pyrazole
OTf	Triflate; trifluoromethanesulfonate
$\tilde{v}$	Wavenumber
IR	Infrared
UV/vis	Ultraviolet/visible
ε	Molar extinction coefficient
λ	Wavenumber
NMR	Nuclear Magnetic Resonance
δ	Chemical shift
ppm	Parts per million
COSY	Correlated spectroscopy
HSQC	Heteronuclear single quantum correlation
HMBC	Heteronuclear multiple-bond correlation
VT	Variable temperature
Å	Angstrom
d	Distance
ESI	Electrospray ionization
GC	Gas chromatography
m/z	Mass per charge
MS	Mass Spectrometry
KC$_8$	Potassium graphite

KHBEt$_3$	Potassium superhydride
BEt$_3$	Triethylborane
KH	Potassium hydride
TEMPO	(2,2,6,6-tetramethylpiperidine-1-oxyl)
Ar	Aryl
Me	Methyl
Ph	Phenyl
EPR	Electron Paramagnetic Resonance
SQUID	superconducting quantum interference device
CV	Cyclic voltammetry
FeCp$_2$/Fc	bis(η5-cyclopentadienyl)iron(II); ferrocene
Fe(Cp*)$_2$/Fc*	bis(η5-pentamethylcyclopentadienyl)iron(II); decamethylferrocene
EA	Elemental analysis
DFT	Density Functional Theory
RT	Room temperature, 25°C
L	Ligand
M	Metal (ion)
MB	Mössbauer
IS	Isomer shift
QS	Quadrupole splitting
S	Spin
hs	High spin
ls	Low spin
vs.	Versus
et al.	*Et alia*

11 References

[1] D. C. Adriano, Trace Elements in Terrestrial Environments, 2nd ed., Springer, New York, **2001**, 1–867.

[2] R. K. Thauer, *Science* **2001**, 293, 1264–1265.

[3] P. M. Vignais, B. Billoud, J. Meyer, *FEMS Microbiol. Rev*. **2001**, *25*, 455–501.

[4] H. S. Shafaat, O. Rüdiger, H. Ogata, W. Lubitz, *Biochim. Biophys. Acta* **2013**, *1827*, 986–1002.

[5] a) D.-H. Kim, M.-S. Kim, *Bioresour. Technol.* **2011**, *102*, 8423–8431; b) H. Atomi, T. Sato, T. Kanai, *Curr. Opin. Biotechnol.* **2011**, *22*, 618–626.

[6] B. Friedrich, J. Fritsch, O. Lenz, *Curr. Opin. Biotechnol.* **2011**, *22*, 358–364.

[7] L. Florin, A. Tsokoglou, T. Happe, *J. Biol. Chem*. **2001**, *276*, 6125–6132.

[8] T. Matsumoto, S. Eguchi, H. Nakai, T. Hibino, K. S. Yoon, S. Ogo, *Angew. Chem. Int. Ed.* **2014**, *53*, 8895–8898.

[9] D. Schomburg, I. Schomburg, Springer Handbook of Enzymes, *30*, 459–466.

[10] P. D. Weitzman, *Biochem. Soc. Symp.* **1987**, *25*, 33–43.

[11] T. I. Doukov, T. Iverson, J. Seravalli, S. W. Ragsdale, C. L. Drennan, *Science* **2002**, 298, 567–572.

[12] C. Darnault, A. Volbeda, E. J. Kim, P. Legrand, X. Vernede, P. A. Lindahl, J. C. Fontecilla-Camps, *Nat. Struct. Biol.* **2003**, *10*, 271–279.

[13] D. J. Evans, *Coord. Chem. Rev.* **2005**, *249*, 1582–1595.

[14] M. Can, F. A. Armstrong, S. W. Ragsdale, *Chem. Rev.* **2014**, *114*, 4149–4174.

[15] S. W. Ragsdale, *Chem. Rev.* **2006**, *106*, 3317–3337.

[16] P. A. Lindahl, *J. Biol. Inorg. Chem.* **2004**, *9*, 516–524.

[17] J. Shearer, *Acc. Chem. Res.* **2014**, *47*, 2332–2341.

[18] D. C. Wallace, *Science* **1992**, *256*, 628-632.

[19] V. Pelmenschikov, *J. Am. Chem. Soc.* **2006**, *128*, 7466–7475.

[20] W. C. Barrette, D. T.Sawyer, J. A. Fee, K. Asada, *Biochem.* **1983**, *22*, 624–627.

[21] a) J. Wuerges, J.-W. Lee, Y.-I. Yim, H.-S.Yim, S.-O. Kang, K. D. Carugo, *Proc. Natl. Acad. Sci.* **2004**, *101*, 8569–8574; b) D. P. Barondeau, C. J. Kassmann, C. K. Bruns, J. A. Tainer, E. D. Getzoff, *Biochem.* **2004**, *43*, 8038–8047.

[22] D. E. Jr Koshland, *Science* **1992**, *258*, 1861.

[23] M. D. Bartberger, W. Liu, E. Ford, K. M. Miranda, C. Switzer, J. M. Fukuto, P. J. Farmer, D. A. Wink, K. N. Houk, *Proc. Natl. Acad. Sci.* **2002**, *99*, 10958–10963.

[24] A. R. Butler, D. L. H. Williams, *Chem. Soc. Rev.* **1993**, *22*, 233–241.

[25] I. M. Wasser, S. de Vries, P. Moënne-Loccoz, I. Schröder, K. D. Karlin, *Chem. Rev.* **2002**, *102*, 1201–1234.

[26] A. C. Montenegro, V. T. Amorebieta, L. D. Slep, D. F. Martín, F. Roncaroli, D. H. Murgida, S. E. Bari, J. A. Olabe, *Angew. Chem. Int. Ed.* **2009**, *48*, 4213–4216.

[27] J. S. Stamler, D. J. Singel, J. Loscalzo, *Science* **1992**, *258*, 1898–1902.

[28] R. Eisenberg, C. D. Meyer, *Acc. Chem. Res.* **1974**, 8, 26–34.

[29] J. A. McCleverty, *Chem. Rev.* **2004**, *104*, 403–418.

[30] A. L. Feig, M. T. Bautista, S. J. Lippard, *Inorg. Chem.* **1996**, *35*, 6892–6898.

[31] J. H. Enemark, R. D. Feltham, *Coord. Chem. Rev.* **1974**, *13*, 339–406.

[32] A. M. Wright, G. Wu, T. W. Hayton, *J. Am. Chem. Soc.* **2012**, *134*, 9930–9933.

[33] S. C. Puiu, T. H. Warren, *Organometallics* **2003**, *22*, 3974–3976.

[34] S. Wiese, P. Kapoor, K. D. Williams, T. H. Warren, *J. Am. Chem. Soc.* **2009**, *131*, 18105–18111.

[35] J. A. McCleverty, *Chem. Rev.* **1979**, *79*, 53–76.

[36] A. M. Wright, H. T. Zaman, G. Wu, T. W. Hayton, *Inorg. Chem.* **2013**, *52*, 6, 3207–3216.

[37] A. M. Wright, G. Wu, T. W. Hayton, *Inorg. Chem.* **2011**, *50*, 11746–11753.

[38] A. Meltzer, C. Präsang, C. Milsmann, M. Driess, *Angew. Chem. Int. Ed.* **2009**, *48*, 3170–3173.

[39] B. C. Fullmer, M. Pink, H. Fan, X. Yang, M.-H. Baik, K. G. Caulton, *Inorg. Chem.* **2008**, *47*, 3888–3892.

[40] V. K. Landry, G. Parkin, *Polyhedron* **2007**, *26*, 4751–4757.

[41] L. S. Maffett, K. L. Gunter, K. A. Kreisel, G. P. A. Yap, D. Rabinovich, *Polyhedron* **2007**, *26*, 4758–4764.

[42] Y.Arikawa, M. Onishi, *Coord. Chem. Rev.* **2012**, *256*, 468–478.

[43] N. Xu, J. Yi, G. B. Richter-Addo, *Inorg. Chem.* **2010**, *49*, 6253–6266.

[44] W. Zumft, *J. Inorg. Biochem.* **2005**, *99*, 194–215.

[45] C. J. White, A. L. Speelman, C. Kupper, S. Demeshko, F. Meyer, J. P. Shanahan, E. E. Alp, M. Hu, J. Zhao, N. Lehnert, *J. Am. Chem. Soc.* **2018**, *140*, 2562–2574.

[46] C. Van Stappen, N. Lehnert, *Inorg. Chem.* **2018**, *57*, 4252-4269.

[47] P. Granger, V. I. Parvulescu, *Chem. Rev.* **2011**, *111*, 3155–3207.

[48] R. M. Bullock, Catalysis without Precious Metals, WileyVCH: Weinheim, Germany, **2010**.

[49] Z.-P. Liu, S. J. Jenkins, D. A. King, *J. Am. Chem. Soc.* **2004**, *126*, 7336–7340.

[50] S. Roy, M. S. Hegde, G. Madras, *Appl. Energy* **2009**, *86*, 2283–2297.

[51] Y. H. Hu, K. Griffiths, P. R. Norton, *Surf. Sci.* **2009**, *603*, 1740–1750.

[52] A. M. Wright, T. W. Hayton, *Inorg. Chem.* **2015**, *54*, 9330–9341.

[53] a) S. Cenini, R. Ugo, G. La Monica, S. D. Robinson, *Inorg. Chim. Acta* **1972**, *6*, 182–184; b) S. Bhaduri, B. F. G. Johnson, A. Pickard, P. R. Raithby, G. M. Sheldrick, C. I. Zuccaro, *Chem. Commun.* **1977**, 354–355.

[54] B. Jezowska-Trzebiatowska, J. Hanuza, M. Ostern, J. Ziolkowski, *Inorg. Chim. Acta* **1972**, *6*, 141–144.

[55] F. Doctorovich, D. Bikiel, J. Pellegrino, S. A. Suarez, A. Larsen, M. A. Martí, *Coord. Chem. Rev.* **2011**, *255*, 2764–2784.

[56] a) V. Shafirovich, S. V. Lymar, *Proc. Natl. Acad. Sci.* **2002**, *99*, 7340–7345; b) M. D. Bartberger, W. Liu, E. Ford, K. M. Miranda, C. Switzer, J. M. Fukuto, P. J. Farmer, D. A. Wink, K. N. Houk, *Proc. Natl. Acad. Sci.* **2002**, *99*, 10958–10963.

[57] J. F. DuMond, S. B. King, *Antioxid. Redox Signal.* **2011**, *14*, 1637–1648.

[58] P. Eyer, M. Ascherl, *Biol. Chem. Hoppe-Seyler* **1987**, 368, 285–294.

[59] a) S. R. Srivastava, M. A. Khan, K. M. Nicholas, *J. Am. Chem. Soc.* **2005**, *127*, 72–78; b) S. R. Srivastava, N. R. Tarver, K. M. Nicholas, *J. Am. Chem. Soc.* **2007**, *129*, 15250–15258.

[60] X. Dai, P. Kapoor, T. H. Warren, *J. Am. Chem. Soc.* **2004**, *126*, 4798–4799.

[61] J. Lee, L. Chen, A. H. West, G. B. Richter-Addo, *Chem. Rev.* **2002**, *102*, 1019–1066.

[62] S. Kundu, S. C. Stieber, M. G. Ferrier, S. A. Kozimor, J. A. Bertke, T. H. Warren, *Angew. Chem. Int. Ed.* **2016**, *55*, 10321 –10325.

[63] S. Yao, E. Bill, C. Milsmann, K. Wieghardt, M. Driess, *Angew. Chem. Int. Ed.* **2008**, *47*, 7110–7113.

[64] S. Yao, Y. Xiong, M. Vogt, H. Grîtzmacher, C. Herwig, C. Limberg, M. Driess, *Angew. Chem. Int. Ed.* **2009**, *48*, 8107–8110.

[65] O. Tenaillon, D. Skurnik, B. Picard, E. Denamur, *Nature Rev. Microbiol.* **2010**, *8*, 207–217.

[66] J. L. Steegmann-Olmedillas, *Clin. Transl. Oncol.* **2011**, *13*, 71–76.

[67] J. F. Berry, E. Bill, E. Bothe, S. D. George, B. Mienert, F. Neese, K. Wieghardt, *Science* **2006**, *312*, 1937–1941.

[68] M. F. Perutz, M. G. Rossmann, A. F. Cullis, H. Muirhead, G. Will, A. C. North, *Nature* **1960**, *185*, 416–422.

[69] J. C. Kendrew, R. E. Dickerson, B. E. Strandberg, R. G. Hart, D. R. Davies, D. C. Phillips, V. C. Shore, *Nature* **1960**, *185*, 422–427.

[70] J.C. Fontecilla-Camps, A. Volbeda, C. Cavazza, Y. Nicolet, *Chem Rev.* **2007**, *107*, 4273–4303.

[71] L.C. Seefeldt, B. M. Hoffman, D.R. Dean, *Annu. Rev. Biochem.* **2009**, *78*, 701–722.

[72] J. Postgate, Nitrogen Fixation, 3rd ed., Cambridge University Press, Cambridge UK, **1998**.

[73] B. M. Hoffman, D. R. Dean, L.C. Seefeldt, *Acc. Chem. Res.* **2009**, *42*, 609–619.

[74] J. C. Fontecilla-Camps, P. Amara, C. Cavazza, Y. Nicolet, A. Volbeda, *Nature* **2009**, *460*, 814–822.

[75] S. Shima, D. Chen, T. Xu, M. D. Wodrich, T. Fujishiro, K. M. Schultz, J. Kahnt, H. Kenichi, X. Hu, *Nature Chem.* **2015**, *12*, 995–1002.

[76] M. W. W. Adams, *Biochim. Biophys. Acta* **1990**, *1020*, 115–145.

[77] S. Shima, U. Ermler, *Eur. J. Inorg. Chem.* **2011**, 7, 963–972.

[78] T. Xu, C. M. Yin, M. D. Wodrich, S. Mazza, K. M. Schultz, R. Scopelliti, X. Hu, *J. Am. Chem. Soc.* **2016**, *138*, 3270–3273.

[79] W. Lubitz, H. Ogata, O. Rüdiger, E. Reijerse, *Chem. Rev.* **2014**, *114*, 4081–4148.

[80] N. Khadka, R. D. Milton, S. Shaw, D. Lukoyanov, D. R. Dean, S. D. Minteer, S. Raugei, B. M. Hoffman, L. C. Seefeldt, *J. Am. Chem. Soc.* **2017**, *139*, 13518–13524.

[81] I. Dance, *Biochem.* **2006**, *45*, 6328–6340.

[82] R. A. Kinney, C. T. Saouma, J. C. Peters, B. M. Hoffman, *J. Am. Chem. Soc.* **2012**, *134*, 12637–12647.

[83] W. Wang, M. J. Nilges, T. B. Rauchfuss, M. Stein, *J. Am. Chem. Soc.* **2013**, *135*, 3633–3639.

[84] a) Editorial comment, *Nature* **2013**, *501*, 6; b) B. E. Smith, *Science* **2002**, *297*, 1654–1655.

[85] L. E. Roth, F. A. Tezcan, *ChemCatChem* **2011**, *3*, 1549–1555.

[86] B. M. Ho, D. Lukoyanov, Z. Yang, D. R. Dean, L. C. Seefeldt, *Chem. Rev.* **2014**, *114*, 4041–4062.

[87] I. Djurdjevic, O. Einsle, L. Decamps, *Chem. Asian J.* **2017**, *12*, 1447–1455.

[88] a) R. R. Schrock, *Angew. Chem. Int. Ed.* **2008**, 47, 5512–5522; b) D. Sippel, M. Rohde, J. Netzer, C. Trncik, J. Gies, K. Grunau, I. Djurdjevic, L. Decamps, S. L. A. Andrade, O. Einsle, *Science* **2018**, *359*, 1484–1489.

[89] B. M. Hoffman, D. Lukoyanov, D. R. Dean, L. C. Seefeldt, *Accounts of Chemical Research* **2013**, 46, 587–595.

[90] B. M. Hoffman, D. Lukoyanov, Z. Yang, D. R. Dean, L. C. Seefeldt, *Chem. Rev.* **2014**, *114*, 4041–4062.

[91] M. M. Rodriguez, E. Bill, W. W. Brennessel, P. L. Holland, *Science* **2011**, *334*, 780–783.

[92] J. S. Anderson, J. Rittle, J. C. Peters, *Nature* **2013**, *501*, 84–87.

[93] R. H. Holm, E. I. Solomon, *Chem. Rev.* **2004**, *104*, 347–348.

[94] J. A. Ibers, R. H. Holm, *Science* **1980**, *209*, 223–235.

[95] R. Poli, Paramagnetic Mono- and Polyhydrides of the Transition Metals. In: M. Peruzzini, R. Poli, editors. Recent Advances in Hydride Chemistry. Elsevier; New York: **2001**, 139–188.

[96] Two examples of paramagnetic iron-hydride complexes: (a) M. Gargano, P. Giannoccaro, M. Ross, G. Vasapollo, A. Sacco, *Dalton Trans* **1975**, 9–12. (b) M. C. Rakowski, D. H. Busch, *J. Am. Chem. Soc.* **1975**, *97*, 2570–2571.

[97] W. Wang, M. J. Nilges, T. B. Rauchfuss, M. Stein, *J. Am. Chem. Soc.* **2013**, *135*, 3633–3639.

[98] J. M. Smith, R. J. Lachicotte, P. L. Holland, *J. Am. Chem. Soc.* **2003**, *125*, 15752–15753.

[99] Y. Yu, A. R. Sadique, J. M. Smith, T. R. Dugan, R. E. Cowley, W. W. Brennessel, C. J. Flaschenriem, E. Bill, T. R. Cundari, P. L. Holland, *J. Am. Chem. Soc.* **2008**, *130*, 6624–6638.

[100] T. R. Dugan, E. Bill, K. C. MacLeod, W. W. Brennessel, P. L. Holland, *Inorg. Chem.* **2014**, *53*, 2370–2380.

[101] Y. Lee, K. J. Anderton, F. T. Sloane, D. M. Ermert, K. A. Abboud, R. García-Serres, L. J. Murray, *J. Am. Chem. Soc.* **2015**, *137*, 10610–10617.

[102] D. Yang, Y. Li, B. Wang, X. Zhao, L. Su, S. Chen, P. Tong, Y. Luo, J. Qu, *Inorg. Chem.* **2015**, *54*, 10243–10249.

[103] N. A. Arnet, T. R. Dugan, F. S. Menges, B. Q. Mercado, W. W. Brennessel, E. Bill, M. A. Johnson, P. L. Holland, *J. Am. Chem. Soc.* **2015**, *137*, 13220–13223.

[104] J. G. Rebelein, Y. Hu, M. W. Ribbe, *Angew. Chem. Int. Ed.* **2014**, *53*, 11543–11546.

[105] C. C. Lee, Y. Hu, M. W. Ribbe, *Angew. Chem. Int. Ed.* **2015**, *54*, 1219–1222.

[106] S. E. Creutz, J. C. Peters, *J. Am. Chem. Soc.* **2015**, *137*, 7310–7313.

[107] a) P. L. Holland, *Can. J. Chem.* **2005**, *83*, 296–301. b) J. C. Peters, M. P. Mehn, Bio-organometallic approaches to nitrogen fixation chemistry. In: W. B. Tolman, editor. Activation of Small Molecules. Wiley; Weinheim, Germany **2006**, 81–119.

[108] (a) H. Andres, E. Bominaar, J. M. Smith, N. A. Eckert, P. L. Holland, E. Münck, *J. Am. Chem. Soc.* **2002**, *124*, 3012–3025 (b) P. L. Holland, T. R. Cundari, L. L. Perez, N. A. Eckert, R. J. Lachicotte, *J. Am. Chem. Soc.* **2002**, *124*, 14416–14424 (c) S. A. Stoian, Y. Yu, J. M. Smith, P. L. Holland, E. L. Bominaar, E. Münck, *Inorg Chem* **2005**, *44*, 4915–4922. (d) S.A. Stoian, J. Vela, J. M. Smith, A. R. Sadique, P. L. Holland, E. Münck, E.L. Bominaar, *J. Am. Chem. Soc.* **2006**, *128*, 10181–10192.

[109] J. Vela, J. M. Smith, Y. Yu, N. A. Ketterer, C. J. Flaschenriem, R. J. Lachicotte, P. L. Holland, *J. Am. Chem. Soc.* **2005**, *127*, 7857–7870.

[110] M. M. Rodriguez, E. Bill, W. W. Brennessel, P. L. Holland, *Science* **2011**, *334*, 780–783.

[111] K. C. MacLeod, P. L. Holland, *Nat. Chem.* **2013**, *5*, 559–565.

[112] S. E. Creutz, J. C. Peters, *J. Am. Chem. Soc.* **2014**, *136*, 1105–1115.

[113] G. Ung, J. C. Peters, *Angew. Chem. Int. Ed.* **2015**, *54*, 532–535.

[114] J. Rittle, J. C. Peters, *Proc. Natl. Acad. Sci.* **2013**, *110,* 15898–15903.

[115] M.-E. Moret, J. C. Peters, *J. Am. Chem. Soc.* **2011**, *133*, 18118–18121.

[116] Y. Lee, N. P. Mankad, J. C. Peters, *Nat. Chem.* **2010**, *2*, 558–565.

[117] J. S. Anderson, G. E. Cutsail, J. Rittle, B. A. Connor, W. A. Gunderson, L. Zhang, B. M. Hoffman, J. C. Peters, *J. Am. Chem. Soc.* **2015**, *137*, 7803–7809.

[118] J. Rittle, J. C. Peters, *J. Am. Chem. Soc.* **2016**, *138*, 4243–4248.

[119] T. J. Del Castillo, N. B. Thompson, J. C. Peters, *J. Am. Chem. Soc.* **2016**, *138,* 5341–5350.

[120] C. T. Saouma, R. A. Kinney, B. M. Hoffman, J. C. Peters, *Angew. Chem. Int. Ed.* **2011**, *50*, 3446–3449.

[121] C. T. Saouma, P. Müller, J. C. Peters, *J. Am. Chem. Soc.* **2009**, *131*, 10358–10359.

[122] D. Sellmann, W. Soglowek, F. Knoch, M. Moll, *Angew. Chem. Int. Ed. Engl.* **1989**, *28*, 1271–1272.

[123] D. Sellmann, J. Sutter, *Acc. Chem. Res.* **1997**, *30*, 460–469.

[124] Y.-H. Chang, P.-M. Chan, Y.-F. Tsai, G.-H. Lee, H.-F. Hsu, *Inorg. Chem.* **2014**, 53, 664–666.

[125] Y. Chen, Y. Zhou, P. Chen, Y. Tao, Y. Li, J. Qu, *J. Am. Chem. Soc.* **2008**, *130*, 15250–15251.

[126] B. D. Stubbert, J. Vela, W. W. Brennessel, P. L. Holland, *Z. Anorg. Allg. Chem.* **2013**, *639*, 1351–1355.

[127] J. Vela, S. Stoian, C. J. Flaschenriem, E. Münck, P. L. Holland, *J. Am. Chem. Soc.* **2004**, *126*, 4522–4523.

[128] C. Camp, J. Arnold, *Dalton Trans.* **2016**, *45*, 14462–14498.

[129] D. L. Mindiola, *Angew. Chem. Int. Ed.* **2009**, *48*, 6198–6200.

[130] L. Bourget-Merle, M. F. Lappert, J. R. Severn, *Chem. Rev.* **2002**, *102*, 3031–3066.

[131] a) H. Gornitzka, D.Stalke, *Organometallics* **1994**, *13*, 4398–4405; b) B.-J. Deelman, P. B. Hitchcock, M. F. Lappert, H.-K. Lee, W.-P. Leung, *J. Organomet. Chem.* **1996**, *513*, 281–285.

[132] K. P. Chiang, S. M. Bellows, W. W. Brennessel, P. L. Holland, *Chem. Sci.* **2014**, *5*, 267–274.

[133] C. Köthe, R. Metzinger, C. Limberg, *Eur. J. Inorg. Chem.* **2013**, 3937–3942.

[134] S. Yao, M. Driess, *Acc. Chem. Res.* **2012**, *45*, 276–280.

[135] a) D. Drees, J. Magull, *Z. Anorg. Allg. Chem.* **1994**, 620, 814–818. B) D. Drees, J. Magull, *Z. Anorg. Allg. Chem.* **1995**, *621*, 948–952.

[136] R. J. Wright, P. P. Power, B. L. Scott, L. Brian, J. L. Kiplinger, *Organometallics* **2004**, *23*, 4801–4803.

[137] a) S. G. McGeachin, *Can. J. Chem.* **1968**, *46*, 1903–1912; b) J. E. Parks, R. H. Holm, *Inorg. Chem.* **1968**, *7*, 1408–1416.

[138] J. M. Smith, A. R. Sadique, T. R. Cundari, K. R. Rodgers, G. Lukat-Rodgers, R. J. Lachicotte, C. J. Flaschenriem, J. Vela, P. L. Holland, *J. Am. Chem. Soc.* **2006**, *28*, 756–769.

[139] N. A. Eckert, J. M. Smith, R. J. Lachicotte, P. L. Holland, *Inorg. Chem.* **2004**, *43*, 3306–3321.

[140] D. V. Vitanova, F. Hampel, K. C. Hultzsch, *Dalton Trans.* **2005**, *0*, 1565–1566.

[141] D. F. Piesik, S. Range, S. Harder, *Organometallics* **2008**, 27, 6178–6187.

[142] a) J. Spielmann, D. E. J. Piesik, S. Harder, *Chem. A Eur. J.* **2010**, *16*, 8307–8318; b) J. Spielmann, J. Intemann, S. Harder, *Dalton Trans.* **2014**, *43*, 14284–14290.

[143] H. Gehring, R. Metzinger, C. Herwig, J. Intemann, S. Harder, C. Limberg, *Chem. Eur. J.* **2013**, *19*, 1629–1636.

[144] H. Gehring, R. Metzinger, B. Braun, C. Herwig, S. Harder, K. Ray, C. Limberg, *Dalton Trans.* **2016**, *45*, 2989–2996.

[145] D. H. Manz, Preorganized Bimetallic Nickel Complexes of Pyrazolate-Bridged Ligands for Cooperative Substrate Transformation, PhD Thesis, Göttingen **2016**.

[146] D. H. Manz, P. C. Duan, S. Dechert, S. Demeshko, R. Oswald, M. John, R. A. Mata, F. Meyer, *J. Am. Chem. Soc.* **2017**, *139*, 16720–16730.

[147] B. M. Hoffman, D. R. Dean, L. C. Seefeldt, *Acc. Chem. Res.* **2009**, *42*, 609–619.

[148] J. Klingele, S. Dechert, F. Meyer, *Coord. Chem. Rev.* **2009**, *253*, 2698–2741.

[149] P. C. Duan, D. H. Manz, S. Dechert, S. Demeshko, F. Meyer, *J. Am. Chem. Soc.* **2018**, 140, 4929–4939.

[150] S. Zheng, T. C. Berto, E. W. Dahl, M. B. Hoffman, A. L. Speelman, N. Lehnert, *J. Am. Chem. Soc.* **2013**, *135*, 4902–4905.

[151] M. Jana, N. Pal, C. J. White, C. Kupper, F. Meyer, N. Lehnert, A. Majumdar *J. Am. Chem. Soc.* **2017**, *139*, 14380–14383.

[152] C. J. White, A. L. Speelman, C. Kupper, S. Demeshko, F. Meyer, J. P. Shanahan, E. E. Alp, M. Hu, J. Zhao, N. Lehnert, *J. Am. Chem. Soc.* **2018**, 140, 2562–2574.

[153] Y. Jiang, T. Hayashi, H. Matsumura, L. H. Do, A. Majumdar, S. J. Lippard, P. Moenne-Loccoz, *J. Am. Chem. Soc.* **2014**, *136*, 12524–12527.

[154] C. Kupper, J. A. Rees, S. Dechert, S. DeBeer, F. Meyer, *J. Am. Chem. Soc.* **2016**, *138*, 7888–7898.

[155] N. Kindermann, A. Schober, S. Demeshko, N. Lehnert, F. Meyer, *Inorg. Chem.* **2016**, *55*, 11538–11550.

[156] A. R. Schober, Activation of Nitric Oxide and Dioxygen at Diferrous Complexes with Compartmental Pyrazolate Ligand Scaffolds, PhD Thesis, Göttingen **2016**.

[157] P. C. Ford, D. A. Wink, D. M. Stanbury, *FEBS Lett* **1993**, *326*, 1–3.

[158] N. Arulsamy, D. S. Bohle, J. A. Imonigie, E. S. Sagan, *Inorg. Chem.* **1999**, *38*, 2716–2725.

[159] R. Bau, I. H. Sabherwal, A. B. Burg, *J. Am. Chem. Soc.* **1971**, *93*, 4926–4928.

[160] H.-C. Böttcher, M. Graf, K. Mereiter, K. Kirchner, *Organometallics* **2004**, *23*, 1269–1273.

[161] L. H. Chen, J. Laane, *J. Raman Spectr.* **1983**, *14*, 284–287.

[162] L. Kuhn, E. L. Lippincott, *J. Am. Chem. Soc.* **1956**, *78*, 1820–1821.

[163] V. Daskalakis, T. Ohta, T. Kitagawa, C. Varotsis, *Biochim. Biophys. Acta* **2015**, *1847*, 1240–1244.

[164] N. B. Colthup, L. H. Daly, S. E. Wiberley, Introduction to Infrared and Raman Spectroscopy, Academic Press Inc. 2nd ed, **2012**, 331.

[165] a) P. Gans, *J. Chem. Soc. (A)* **1967**, 943–946; (b) B. F. Hoskins, F. D. Whillans, *Chem. Commun.* **1969**, 69–70; (c) B. F. Hoskins, F. D. Whillans, *Dalton Trans.* **1973**, 607–611; (d) M. E. Chacon Villalba, A. Navaza, J. A. Guida, E. L. Varetti, P. J. Aymonino, *Inorg. Chim. Acta* **2006**, 359, 707–712.

[166] D. L. H. Williams, Nitrosation Reactions and the Chemistry of Nitric Oxide, Elsevier Science **2004**

[167] C. Köthe, R. Metzinger, C. Limberg, *Eur. J. Inorg. Chem.* **2013**, 3937–3942.

[168] P. C. Duan, A Dinuclear Dihydride Complex for Bimetallic Reductive Activation and Transformation of a Range of Inert Substrates, PhD Thesis, Göttingen **2017**.

[169] N. G. Connelly, P. T. Draggett, M. Green, T. A. Kuc, *Dalton Trans.* **1977**, 70–73.

[170] G. Elbaze, F. Dahan, M. Dartiguenave, Y. Dartiguenave, *Inorg. Chim. Acta* **1984**, 87, 91–97.

[171] A. M. Wright, H. T. Zaman, G. Wu, T. W. Hayton, *Inorg. Chem.* **2013**, *52*, 3207–3216.

[172] J. Mason, L. F. Larkworthy, E. A. Moore, *Chem. Rev.* **2002**, *102*, 913–934.

[173] S. Fukuzumi, K. Ohkubo, Y. Lee, W. Nam, *Chem. Eur. J.* **2015**, *21*, 17548–17559.

[174] L. Carreras, L. Rovira, M. Vaquero, I. Mon, E. Martin, J. Benet-Buchholz, A. Vidal-Ferran, *RSC Adv.* **2017**, *7*, 32833–32840.

[175] N. G. Connelly, W. E. Geiger, *Chem. Rev.* **1996**, *96*, 877–910.

[176] W. J. Evans, M. Fang, J. E. Bates, F. Furche, J. W. Ziller, M. D. Kiesz, J. I. Zink, *Nature Chem.* **2010**, *2*, 644–647.

[177] F. A. Cotton, G. Wilkinson, Advanced Inorganic Chemistry, 5th ed.; John Wiley & Sons: New York, **1988**.

[178] T. W. Hayton, P. Legzdins, W. Brett Sharp, *Chem. Rev.* **2002**, *102*, 935–992.

[179] C. Gaviglio, J. Pellegrino, D. Milstein, F. Doctorovich, *Dalton Trans.* **2017**, *46*, 16878–16884.

[180] K. J. Franz, S. L. Lippard, *J. Am. Chem. Soc.* **1999**, *121*, 10504–10512.

[181] K. J. Franz, S. L. Lippard, *J. Am. Chem. Soc.* **1998**, *120*, 9034–9040.

[182] K. Kobayashi, A. Koppenhöfer, S. J. Ferguson, N. J. Watmough, S. Tagawa, *Biochem.* **2001**, *40*, 8542–8547.

[183] F. Doctorovich, D. E. Bikiel, J. Pellegrino, S. A. Suàrez, M. A. Martì, *Acc. Chem. Res.* **2014**, 47, 2907–2916.

[184] M. Cameron, B. G. Gowenlock, G. Vasapollo, *Chem. Soc. Rev.* **1990**, *19*, 355–379.

[185] (a) S. Cenini, M. Pizzotti, C. Crotti, In Aspects of Homogeneous Catalysis; R. Ugo, Ed.; Reidel: Dordrecht, **1988**, 97–198; (b) F. Ragaini, S. Cenini, *J. Mol. Catal. A: Chem.* **1996**, *109*, 1–25. (c) S. J. Skoog, W. L. Gladfelter, *J. Am. Chem. Soc.* **1997**, *119*, 11049–11060; (d) F. Paul, J. Fischer, P. Ochsenbein, J. A. Osborn, *Organometallics* **1998**, *17*, 2199–2206.

[186] H. Gehring, R. Metzinger, C. Herwig, J. Intemann, S. Harder, C. Limberg, *Chem. Eur. J.* **2013**, *19*, 1629–1636.

[187] D. W. Hoard, P. R. Sharp, *Inorg. Chem.* **1993**, *32*, 612–620.

[188] T. Iwasa, H. Shimada, A. Takami, H. Matsuzaka, Y. Ishii, M. Hidai, *Inorg. Chem.* **1999**, *38*, 2851–2859.

[189] S. Stella, C. Floriani, A. Chiesa-Villa, C. Guastini, *Dalton Trans.* **1988**, *0*, 545–547.

[190] K. Ohkita, H. Asano, H. Kurosawa, T. Hirao, Y. Miyaji, I. Ikeda, *Can. J. Chem.* **1996**, *74*, 1936–1944.

[191] F. P. Gasparro, N. H. Kolodny, *J. Chem. Ed.* **1977**, *54*, 258–261.

[192] B. G Gowenlock, K. G. Orrell, V. Šikb, G. Vasapollo, *Polyhedron* **1998**, *17*, 3495–3500.

[193] D. A. Fletcher, B. G. Gowenlock, K. G. Orrell, V. Šikb, *Magn. Reson. Chem.* **1995**, *33*, 561–569.

[194] M. Calligaris, T. Yoshida, S. Otsuka, *Inorg. Chim. Acta* **1974**, *11*, 15–16.

[195] O. Burghaus, M. Rohrer, T. Gotzinger, M. Plato, K. Mobius, *Meas. Sci. Technol.* **1992**, *3*, 765–774

[196] S. Neumann, Bimetallische Eisenkomplexe für die kooperative Aktivierung kleiner Moleküle, M. Sc. Thesis, Göttingen **2015**.

[197] A W. Addison, T. N. Rao, J. Reedijk, J. van Rijn, G. C. Verschoor, *Dalton Trans.* **1984**, 1349–1356.

[198] A. L. Gavrilova, B. Bosnich, *Chem. Rev.* **2004**, *104*, 349–384.

[199] I. Bertini, C. Luchinat, G. Parigi, Solution NMR of Paramagnetic Molecules: Applications to Metallobiomolecules and Models, Elsevier, Amsterdam, **2001**.

[200] L.-J. Ming, In Physical Methods in Bioinorganic Chemistry; L. Que, Jr. Ed.; University Science Books: Sausalito, CA, **2000**, 375–464.

[201] N. V. Ignat'ev, P. Barthen, A. Kucheryna, H. Willner, P. Sartori, *Molecules* **2012**, *17*, 5319–5338.

[202] Y. Yu, W. W. Brennessel, P. L. Holland, *Organometallics* **2007**, *26*, 3217–3226.

[203] H. Gehring, R. Metzinger, B. Braun, C. Herwig, S. Harderb, K. Ray, C. Limberg, *Dalton Trans.* **2016**, *45*, 2989–2996.

[204] Y. Tanabe, Y. Nishibayashi, *Chem. Rec.* **2016**, *16*, 1549–1577.

[205] S. Kuriyama, K. Arashiba, K. Nakajima, Y. Matsuo, H. Tanaka, K. Ishii, K. Yoshizawa, Y. Nishibayashi, *Nature Commun.* **2016**, *7*, 1–9.

[206] B. T. Heaton, C. Jacob, P. Page, *Coord. Chem. Rev.* **1996**, *154*, 193–229.

[207] F. H. Allen, O. Kennard, D. G. Watson, L. Brammer, A. G. Orpen, R. J. Taylor, *Chem. Soc., Perkin Trans. II* **1987**, 1–9.

[208] M. Fang, D. S. Lee, J.W. Ziller, R. J. Doedens, J. E. Bates, F. Furche, W. J. Evans, *J. Am. Chem. Soc.* **2011**, *133*, 3784–3787.

[209] D. H. Johnston, D. F. Shriver, *Inorg. Chem.* **1993**, *32*, 1045–1047.

[210] I. Bertini, C. Luchinat, *Coord. Chem. Rev.* **1996**, *150*, 1–292.

[211] J. L. Chou, J. P. Chyn, F. L. Urbach, D. F. Gervasio, *Polyhedron* **2000**, *19*, 2215–2223.

[212] B. C. Askew, C. J. Mclntyre, C. A. Hunt, D. A. Claremon, R. J. Gould, R. J. Lynch, D. J. Armstrong, *Bioorg. Med. Chem. Lett.* **1995**, *5*, 475–480.

[213] D. Ruiz Plaza, J. C. Alvarado-Monzon, G. A. Andreu de Riquer, G. Gonzalez-Garcia, H. Hoepfl, Herbert, L. M. de Leon-Rodriguez, J. A. Lopez, *Eur. J. Inorg. Chem.* **2016**, *6*, 874–879.

[214] N. Arulsamy, D. S. Bohle, J. A. Butt, G. J. Irvine, P. A. Jordan, E. Sagan, *J. Am. Chem. Soc.* **1999**, *121*, 7115–7123.

[215] K. S. Hagen, *Inorg. Chem.* **2000**, *39*, 5867–5869.

[216] H. E. Gottlieb, V. Kotlyar, A. Nudelman, *J. Org. Chem.*, **1997**, *62*, 7512–7515.

[217] E. Bill, Max Planck Institute for Chemical Energy Conversion, Mühlheim/Ruhr, Germany.

[218] S. Stoll, A. Schweiger, *J. Magn. Reson.* **2006**, *178*, 42–55.

[219] G. R. Handson, K. E. Gates, C. J. Noble, M. Griffin, A. Mitchell, S. Benson, *J. Inorg. Biochem.* **2004**, *98*, 903–916.

[220] G. A. Bain, J. F. Berry, *J. Chem. Educ.* **2008**, *85*, 532–536.

[221] E. Bill, julX - Simulation of Molecular Magnetic Data, Max Planck Institute for Chemical Energy Conversion, Mülheim/Ruhr, Germany.

[222] G. M. Sheldrick, *Acta Crystallogr. A Found Adv.* **2015**, *71*, 3–8.

[223] G. M. Sheldrick, *Acta Crystallogr. C Struct. Chem.* **2015**, *71*, 3–8.

[224] X-RED, STOE & CIE GmbH, Darmstadt, Germany, **2002**.

[225] a) F. Neese, ORCA: An ab initio, DFT and semiempirical SCF-MO package, Max-Planck Institute for Chemical Energy Conversion, Mülheim an der Ruhr, Germany, **2013**; b) F. Neese, *Wiley Interdiscip. Rev.: Comput. Mol. Sci.* **2012**, *2*, 73–78.

[226] a) A. D. Becke, *Phys. Rev. A* **1988**, *38*, 3098–3100; b) J. P. Perdew, *Phys. Rev. B* **1986**, 33, 8822–8824.

[227] A. D. Becke, *J. Chem. Phys.* **1993**, *98*, 1372–1377.

[228] a)http://libint.valeyev.net; b) H - Kr: A. Schaefer, H. Horn, R. Ahlrichs, *J. Chem. Phys.* **1992**, *97*, 2571; c) F. Weigend, R. Ahlrichs, *Phys. Chem. Chem. Phys.* **2005**, *7*, 3297; d) https://orcaforum.cec.mpg.de/.

[229] P.-C. Duan, B. Van Kuiken, A. Römer, R. A. Schulz, S. Dechert, S. Demeshko, G. E. Cutsail III, R. A. Mata, S. DeBeer, F. Meyer, manuscript in preparation.

Curriculum Vitae

PERSONAL DATA

Eleonora Ferretti
Weender Str. 68
37073 Göttingen
eleonora.ferretti@chemie.uni-goettingen.de

Date and Place of Birth: 26/12/1988 in Pisa, Italy

ACADEMIC EDUCATION

09/2014–09/2018   PhD candidate, Advisor: Prof. Dr. Franc Meyer

Thesis: *Bioinspired Small Molecule Activation with Pyrazole-Supported Binuclear Nickel and Iron β-Diketiminate Complexes*

10/2011–10/2013   M. Sc. in Inorganic Chemistry, Advisor: Prof. Fabio Marchetti

Thesis (Title translated): *Synthesis of New Niobium Complexes with Bulky NHC Ligands*

10/2007–10/2011   B. Sc. in Chemistry, Advisor: Prof. Daniela Belli Dell'Amico

Thesis (Title translated): *Some Aspects Regarding the Synthesis and Characterization of Dinuclear Platinum(II) Complexes*

TEACHING EXPERIENCE

Method Course "Methoden der Chemie III"
Teaching assistant (EPR spectroscopy, Mössbauer spectroscopy, Cyclic Voltammetry, Electrocatalysis)

Practical Course "Anorganisch-Chemisches Synthesepraktikum"
Laboratory assistant (Inorganic Synthesis)

Practical Course "Enzyme Catalysis and Biological Chemistry"
Laboratory assistant (Inorganic Synthesis and Characterization Methods)

Exercise Course "Methoden der Chemie II"
Teaching assistant (UV/vis spectroscopy)

COURSES AND LECTURES

Method Courses	Introduction to X-Ray Spectroscopy – mainly XAS and a little bit of XES, Prof. Serena DeBeer, MPI for Chemical Energy Conversion, Mülheim an der Ruhr, **2014**
	Solid State NMR Spectroscopy and Functionalization of Surfaces Towards Single-Site Catalyst, Christophe Copéret, ETH Zurich, **2016**
	Summer School "Molecular Methods in Energy Research: Theory and Spectroscopy" (Organized by Max-Planck Institute for Chemical Energy and Conversion), Gelsenkirchen, **2014**
	NMR practical course, Dr. Michael John, Göttingen Universität, **2014/2015**
Soft Skill Courses	Project Management, Anna Royon-Weigelt, Golin Wissenschaftsmanagement, Hamburg, **2017**
	Basics in Business Competence, Cedric Ronsöhr, Klein Consult, Duderstadt, **2017**
	Industrial Property Rights, Dr. Thomas Doerper, BASF, Ludwigshafen, **2015**
Languages	Italian (Mothertongue) English (C1 of European Reference framework) German (B1/B2 of European Reference framework)
IT	Origin, MestreNova, Easyspin for Matlab, MS Office package, Photoshop

Prize for the best poster at the Final ECOSTbio meeting, Berlin, Germany, **9-11/04/2018**

Prize for the best poster at the 4th EuChemMS Inorganic Chemistry Conference, Copenhagen, Denmark, **2-5/07/2017.**

Prize for the best poster at the 9. Göttinger Chemie Forum, Göttingen, Germany, **22/06/2017.**

Research grant by the University of Pisa, **11/2013-05/2014** *"Reactivity of high valent transition metals with small organic molecules"*

List of Scientific Contributions

Publications

E. Ferretti, S. Dechert, S. Demeshko, M. C. Holthausen, F. Meyer, *Angew. Chem. Int. Ed.* **2019**, *58*, 1705-1709. *Reductive Nitric Oxide Coupling at a Dinickel Core: Isolation of a Key cis-Hyponitrite Intermediate en route to N2O Formation*

L. Biancalana, M. Bortoluzzi, E. Ferretti, M. Hayatifar, F. Marchetti, G. Pampaloni, S. Zacchini, *RSC Advances* **2017**, *7*, 10158−10174. *The Reactions of alfa-Amino Acids and alfa-Amino Acid Esters with High Valent Transition Metal Halides: Synthesis of Coordination Complexes, Activation Processes and Stabilization of alfa-Ammonium acylchloride cations*

M. Bortoluzzi, E. Ferretti, F. Marchetti, G. Pampaloni, S. Zacchini, *J. Coord. Chem.* **2016**, *69*, 2766−2774. *A crystallographic and DFT study on a NHC complex of niobium oxide trifluoride*

M. Bortoluzzi, E. Ferretti, M. Hayatifar, F. Marchetti, G. Pampaloni, S. Zacchini, *Eur. J. Inorg Chem.* **2016**, 3838−3845. *One-Pot Intermolecular C–S Self-Coupling of Dimethyl Sulfoxide Promoted by Molybdenum Pentachloride*

M. Bortoluzzi, E. Ferretti, F. Marchetti, G. Pampaloni, C. Pinzino, S. Zacchini, *Inorg. Chem.* **2016**, *55*, 4173−4182. *Coordination Compounds of Niobium(IV) Oxide Dihalides Including the Synthesis and the Crystallographic Characterization of NHC Complexes*

M. Bortoluzzi, E. Ferretti, F. Marchetti, G. Pampaloni, S. Zacchini, *Dalton Trans* **2016**, *45*, 6939−6948. *Coordination Complexes of Niobium and Tantalum Pentahalides with a Bulky NHC Ligand*

E. Ferretti, M. Hayatifar, F. Marchetti, G. Pampaloni, S. Zacchini, *Polyhedron* **2015**, *100*, 400−403. *Molybdenum(V) and Molybdenum(IV) Coordination Compounds from the Reactions of MoCl5 with Sulfones*

M. Bortoluzzi, E. Ferretti, F. Marchetti, G. Pampaloni, S. Zacchini, *Chem. Commun.* **2014**, *50*, 4472−4474. *A structurally-characterized NbCl5–NHC adduct*

Presentations at Conferences and Workshops

10. Göttinger Chemie Forum, Göttingen, Germany, **31/05/2018**. *"Reductive Binding and Redox Transformations of Nitric Oxide at a Dinuclear Nickel(II) Dihydride Complex"* (Talk)

Final ECOSTbio meeting, Berlin, Germany, **9-11/04/2018.** *"Reductive Binding and Redox Transformations of Nitric Oxide on a Dinuclear Nickel(II) Dihydride Complex"* (Poster)

14. Koordinationschemie-Treffen, Heidelberg, Germany, **11-13/03/2018**. *"Reductive Binding and Redox Transformations of Nitric Oxide at a Dinuclear Nickel(II) Dihydride Complex"* (Talk)

Anglo-German Inorganic Chemistry Meeting (AGICHEM), Göttingen, Germany, **6-9/08/2017.** *"Cooperative Activation and Redox Transformation of Nitric Oxide and Nitrosobenzene at a Dinickel(II) Dihydride Complex"* (Poster)

4th EuChemMS Inorganic Chemistry Conference (EICC-4), Copenhagen, Denmark, **2-5/07/2017.** *"Cooperative Activation and Redox Transformation of Nitric Oxide and Nitrosobenzene at a Dinickel(II) Dihydride Complex"* (Poster)

9. Göttinger Chemie Forum, Göttingen, Germany, **22/06/2017.** *"Cooperative Activation and Reductive Coupling of Nitric Oxide at a Dinickel(II) Dihydride Complex"* (Poster)

IRTG Final Symposium, Göttingen, Germany, **27-28/08/2015.** *"A Pyrazole-Bridged Bis(β-diketiminato) Ligand and Its Dinuclear Iron Complexes"* (Poster)

Acknowledgments

I would like to thank the many people, in many countries, who guided me during this journey. This thesis work would not have been possible without your support.
First of all, I am grateful to my mentor Prof. Dr. Franc Meyer for the scientific freedom and the opportunity to work on this inspiring topic. Thanks to his endless optimism, expertise, and the excellent laboratory equipment I could grow during these years as a scientist. I would further like to address a special thank to Prof. Dr. Inke Siewert for her constructive comments to my project and for overtaking the position of second supervisor.

I also would like to acknowledge all my colleagues and external collaborators who contributed to this thesis work: Prof. Dr. Max Holthausen for the DFT calculations on the hyponitrite complex, Dr. Claudia Stückl for the EPR measurements, Dr. Sebastian Dechert and Anna Kölpin for X-ray diffraction measurements and refinement of the obtained molecular structures, Dr. Serhiy Demeshko for magnetic measurements and for teaching me how to use the Mössbauer spectrometer, Dr. Michael John and Ralf Schöne for the assistance in the NMR department, Andreas Schwarz and Jörg Teichgräber for the distribution of chemicals and laboratory materials, the Analytics Department for the FD measurements, Massimiliano Morganti for his continuous support during electrochemical analyses, the workshops and the facility management. A special thank also to Dr. Peng-Cheng Duan for the effective teamworking and Dr. Dennis Manz for the helpful discussions about our similar topics.

I am grateful to Dr. Claudia Stückl, Britta Müller and Petra Unger and the rest of the staff for taking care of the amministrative tasks.

I would like to thank my past and present labmates Dr. Alexander Gers-Barlag and Roland Alexander Schultz for the nice working atmosphere. I also thank Joanne, Anna, Pierre, Massimiliano, Giuseppe, Vandana, Mattia, Jann, Alex, Anastasia, Marten, Markus, Kristian and the rest of the group members who were around over the last few years, during fun evenings in town or weeks of hard work in the lab.

I am in debt with Joanne Wong, Pierre Goursot, Hendrik Stevens and Jana Lücken for their comments and linguistic improvements during proofreading of this thesis.

I also thank all my Italian friends, especially Maddalena, Marta, Francesca, Daria, Margherita, Rachele, Benedetta, Betta, Sara, Alessio and Andrea for their love and encouragement. I would like to say also 'thank you' to Giorgio for his support in good times and bad times, for keeping me sane over the past few months and for providing a homey place to write.

Finally, last but not least, I will always be deeply thankful to my mum, my brother, my grandparents and my dad for their unconditional love and unwavering belief in me.